International Committee for Future Accelerators

Sponsored by the Particles and Fields Commission of IUPAP

Beam Dynamics Newsletter

No. 60

Issue Editor:
G. R. Neil

Editor in Chief:
W. Chou

April 2013

Contents

1 FOREWORD....9

1.1 FROM THE CHAIR....9

1.2 FROM THE EDITOR....11

2 LINEAR COLLIDERS....12

2.1 FROM THE LINEAR COLLIDER DIRECTOR....12

2.2 EIGHTH INTERNATIONAL ACCELERATOR SCHOOL FOR LINEAR COLLIDERS....13

3 THEME: FEL OSCILLATORS....15

3.1 INTRODUCTION TO AN X-RAY FEL OSCILLATOR....15

- 3.1.1 Introduction....15
- 3.1.2 An X-Ray FEL in Oscillator Configuration....15
- 3.1.3 Scientific Applications....19
- 3.1.4 Accelerator System....19
- 3.1.5 X-ray Optics....20
- 3.1.6 Nuclear-Resonance-Stabilized XFELO for Fundamental Science....21
- 3.1.7 Conclusions....23
- 3.1.8 Acknowledgments....23
- 3.1.9 References....23

3.2 SCIENTIFIC OPPORTUNITIES FOR HIGH RESOLUTION INELASTIC X-RAY SCATTERING WITH AN XFELO SOURCE....24

- 3.2.1 Introduction to Inelastic X-ray Scattering....24
- 3.2.2 Description of Inelastic X-ray Scattering....26
  - 3.2.2.1 *Non- resonant IXS....26*
  - 3.2.2.2 *Resonant Inelastic X-ray Scattering (RIXS)....27*
- 3.2.3 Advantages of an X-ray Free Electron Laser Oscillator (XFELO) Source..27
  - 3.2.3.1 *Medium Resolution Measurements....28*
  - 3.2.3.2 *High Resolution Measurements with an XFELO....28*
- 3.2.4 Summary....29
- 3.2.5 References....29

3.3 PROSPECTS FOR NEW SCIENCE USING X-RAY PHOTON CORRELATION SPECTROSCOPY AT AN XFELO....30

3.4 OPPORTUNITIES FOR A FREE ELECTRON LASER OSCILLATOR IN NANOMATERIAL PHONON CHARACTERIZATION AND COMPLEX OXIDE DYNAMICS....39

- 3.4.1 Introduction....39
- 3.4.2 Nanomaterial Phonon Characterization....39
- 3.4.3 Dynamics in Complex Oxides....41
- 3.4.4 References....42

3.5 MÖßBAUER SCIENCE AND NUCLEAR QUANTUM OPTICS WITH X-RAY FREE ELECTRON LASER OSCILLATORS 44

3.5.1 Introduction 44
3.5.2 Nuclear Quantum Optics 45
    3.5.2.1 *Motivation* *45*
    3.5.2.2 *State of the Art* *45*
    3.5.2.3 *Significance of the Light Source* *46*
    3.5.2.4 *Future Perspectives* *48*
3.5.3 Perspectives for Mößbauer Science 49
3.5.4 References 49

3.6 SCIENTIFIC POSSIBILITIES FOR NUCLEAR RESONANT SCATTERING WITH AN XFEL-OSCILLATOR 51

3.6.1 Introduction 51
3.6.2 Dynamics of Artificially Structured Materials 51
3.6.3 Exploring the Dynamical Origins of Friction 53
3.6.4 Nuclear Inelastic Pump-Probe Experiments 54
3.6.5 Nuclear Quantum Optics 55
3.6.6 Conclusion 56
3.6.7 References 56

3.7 NUCLEAR-RESONANCE-STABILIZED XFELO FOR FUNDAMENTAL PHYSICS AND PRECISION METROLOGY 56

3.7.1 Introduction 56
3.7.2 The Comb Structure of an XFELO and Tolerance Requirements 57
3.7.3 Cavity Stabilization 59
    3.7.3.1 *Schematic* *59*
    3.7.3.2 *Sources of Phase Noise* *61*
3.7.4 Applications 63
    3.7.4.1 *Time and Length Standard* *63*
    3.7.4.2 *Coherent Control in Quantum Optics* *64*
    3.7.4.3 *Matter-wave Interferometry* *65*
    3.7.4.4 *Decoherence in Mesoscopic Quantum Physics* *66*
3.7.5 Summary 67
3.7.6 Acknowledgments 67
3.7.7 References 67

3.8 FEASIBILITY OF X-RAY CAVITIES FOR FREE ELECTRON LASER OSCILLATORS 68

3.8.1 Introduction 68
3.8.2 Optical Schemes of X-Ray Cavities 69
    3.8.2.1 *Two-Crystal Cavity* *69*
    3.8.2.2 *Tunable Four-Crystal Cavity* *71*
    3.8.2.3 *Tunable Multi-User Compact Cavity* *71*
3.8.3 Diamond Crystals as Bragg Reflecting Mirrors 72
    3.8.3.1 *Reflectivity of Diamond Crystals* *73*
    3.8.3.2 *Wavefront Distortions upon Bragg Reflection* *75*
    3.8.3.3 *Heat Load Problem and Thermal Stability* *76*
    3.8.3.4 *Dynamical Response of Crystals to Instantaneous Heating* *77*

3.8.3.5 *Radiation Damage*..*77*
3.8.4 Focusing and Collimating Optics 79
3.8.5 Stability of the Optical Cavity..79
3.8.6 Conclusions and Outlook 80
3.8.7 Acknowledgments 80
3.8.8 References 81

3.9 NANOPOSITIONING STAGES TO ENABLE XFELO OPTICS MOUNTING AND MANIPULATING CAPABILITIES 83

3.9.1 Introduction 83
3.9.2 Basic Nanopositioning Techniques Developed at the APS..........83
3.9.3 Linear Weak-link Stages for Hard X-ray Nanoprobe....................84
3.9.3.1 *Linear Weak-link Stages with Ultrahigh Positioning Resolution ..84*
3.9.3.2 *Linear Weak-link Stages with Extended Travel Range 84*
3.9.3.3 *Linear Flexure Stage with Centimeter Travel Range..................85*
3.9.4 Angular Flexure Stages at the APS 86
3.9.4.1 *Horizontal Axis Angular Weak-link Stages................................86*
3.9.4.2 *Vertical Axis Angular Weak-link Stages 87*
3.9.4.3 *Multi-dimensional Alignment Apparatus 87*
3.9.5 Prototype of Tip-tilting Stage with Resolution in Nanoradian Scale 88
3.9.6 Summary..89
3.9.7 Acknowledgments 89
3.9.8 References 90

3.10 BINP FREE ELECTRON LASER FACILITY – CURRENT STATUS AND FUTURE PROSPECTS...91

3.10.1 Introduction 91
3.10.2 Accelerator Design...91
3.10.3 The First Stage FEL 94
3.10.3.1 *Design and Basic Parameters 94*
3.10.3.2 *Operation Experience...94*
3.10.4 The Second Stage FEL 95
3.10.5 Third Stage ERL and FEL...97
3.10.6 Future Prospects 98
3.10.7 References 98

3.11 A PROGRAM FOR OPTIMIZING SRF LINAC COSTS.......................................98

3.11.1 Introduction 98
3.11.2 Software Description..99
3.11.2.1 *General structure 99*
3.11.2.2 *Input / Output Parameters...99*
3.11.2.1 *Calculating* Q_0...*101*
3.11.2.2 *Calculating Loaded-Q and RF Power.......................................102*
3.11.2.3 *Cryogenic Facility Costs..103*
3.11.3 Results 104
3.11.3.1 *Cost as a Function of Frequency 104*
3.11.3.2 *Cost as a Function of Gradient...105*
3.11.4 Model Deficiencies and Future Improvements. 106
3.11.5 Conclusions 106

3.11.6 References 107

3.12 SIMULATIONS OF A FREE-ELECTRON LASER OSCILLATOR AT JEFFERSON LAB LASING IN THE VACUUM ULTRAVIOLET 107

3.12.1 Introduction 108
3.12.2 FEL accelerator 108
3.12.2.1 *Present Accelerator Configuration* *108*
3.12.2.2 *Proposed Upgrades* *108*
3.12.3 FEL Oscillator 108
3.12.3.1 *FEL Modeling* *108*
3.12.4 Optics Considerations 111
3.12.5 Conclusions 112
3.12.6 Acknowledgements 112
3.12.7 References 112

4 ICFA BEAM DYNAMICS WORKSHOP REPORT – ACCELERATORS FOR A HIGGS FACTORY: LINEAR VS. CIRCULAR (HF2012) 113

4.1 EXECUTIVE SUMMARY 113

4.2 HIGGS PHYSICS 118

4.2.1 Physics Case 118
4.2.2 The LHC as a Higgs Factory 119
4.2.3 Higgs Physics of Electron-Positron Colliders 120
4.2.4 Physics of $\mu^+\mu^- \rightarrow$ Higgs 122
4.2.5 Physics of $\gamma\gamma \rightarrow$ Higgs 123
4.2.6 Higgs Physics Summary 124

4.3 LINEAR e^+e^- COLLIDERS 126

4.3.1 Introduction 126
4.3.2 ILC-based Higgs Factory 128
4.3.3 CLIC-based Higgs Factory 130
4.3.4 X-band Klystron-based Higgs Factory 132
4.3.5 Machine-Detector Interface 132

4.4 CIRCULAR e^+e^- COLLIDERS 132

4.4.1 Introduction 132
4.4.2 Circular e^+e^- Colliders Considered 133
4.4.3 Technical Challenges 134
4.4.3.1 *Energy Reach and Upgradability* *134*
4.4.3.2 *Synchrotron Radiation* *135*
4.4.3.3 *RF System* *135*
4.4.3.4 *Vacuum System* *136*
4.4.3.5 *Beam-beam Effects* *136*
4.4.3.6 *Beamstrahlung* *137*
4.4.3.7 *Lattice Design* *137*
4.4.3.8 *Emittance Control* *138*
4.4.3.9 *Top-up Injection* *138*
4.4.3.10 *Polarization* *138*

4.5 MUON COLLIDER 139
4.5.1 Introduction 139
4.5.2 The Muon Collider as a Higgs Factory 140
4.6 PHOTON COLLIDERS 141
4.6.1 Introduction 141
4.6.2 Required R&D for Photon Colliders 144
4.7 ACKNOWLEDGMENTS 146
4.8 APPENDICES 147
4.8.1 Appendix 1 – Agenda 147
4.8.2 Appendix 2 – Parameter Comparison Tables 150
4.8.3 Appendix 3 – Timelines 155
4.9 REFERENCES 156

5 WORKSHOP AND CONFERENCE REPORTS 158

5.1 XFELO 2013 WORKSHOP REPORT – PART A: SCIENCES 158
5.1.1 Introduction 158
5.1.2 Possible Scientific Area 158
5.1.2.1 *High Resolution Spectroscopy: Inelastic X-ray Scattering* *158*
5.1.2.2 *High Resolution Spectroscopy: Mössbauer Spectroscopy* *158*
5.1.2.3 *Hard X-Ray Photoemission Spectroscopy (HXPS, HAXPES)*......*159*
5.1.2.4 *X-ray Microscopy and Phase Contrast Imaging* *159*
5.1.2.5 *Dynamics and Imaging with Coherent X-rays* *159*
5.1.2.6 *Time-Resolved Studies* *159*
5.1.3 Insights to New Scientific Areas 160
5.1.4 Conclusions 160
5.1.5 Acknowledgement 160
5.2 XFELO 2013 WORKSHOP REPORT – PART B: XFELO R&D ISSUES (ACCELERATOR AND X-RAY OPTICS) 161
5.2.1 Introduction 161
5.2.2 Components 161
5.2.2.1 *Accelerator* *161*
5.2.2.2 *SRF* *161*
5.2.2.3 *Gun* *161*
5.2.3 Magnet and Vacuum 162
5.2.4 Optics 162
5.2.4.1 *Mirrors* *162*
5.2.4.2 *Stabilization* *162*
5.2.4.3 *Tests* *162*
5.2.5 Scale 162
5.2.6 Participants in the XFELO Workshop 163
5.3 WORKSHOP ON ACCELERATOR R&D FOR ULTIMATE STORAGE RINGS 165
5.3.1 Introduction 165
5.3.2 Charge to the Workshop 165

5.3.3 Scientific Program 166
5.3.4 Conclusion 166

6 RECENT DOCTORIAL THESES ABSTRACTS 167

6.1 Optics Design of Intrabeam Scattering Dominated Damping Rings 167

7 FORTHCOMING BEAM DYNAMICS EVENTS 168

7.1 SLAC Summer School on Electron and Photon Beams 168

7.2 53rd ICFA Advanced Beam Dynamics Workshop (ABDW) Energy Recovery Linacs (ERL) 2013 168

7.3 The 14th International Conference on Accelerator and Large Experimental Physics Control Systems (ICALEPCS 2013) 169

7.4 COOL'13 170

7.5 SRF 2013 171

7.6 ICFA Mini-Workshop on Space Charge (SPACE CHARGE 2013) 172

7.7 35th International Free-Electron Laser Conference (FEL'13) 172

7.8 The 17th Pan-American Synchrotron Radiation Instrumentation Conference 173

7.9 The Third Low Emittance Ring Workshop 174

7.10 First Circular for PSTP2013 175

7.10.1 Workshop Introduction 175
7.10.2 Program 175
7.10.3 Registration 176
7.10.4 Travel and Accommodation 176
7.10.5 Visas 176
7.10.6 Local Organizing Committee Members 176
7.10.7 International Spin Physics Committee (ISPC) 177

8 ANNOUNCEMENTS OF THE BEAM DYNAMICS PANEL 177

8.1 ICFA Beam Dynamics Newsletter 177

8.1.1 Aim of the Newsletter 177
8.1.2 Categories of Articles 177
8.1.3 How to Prepare a Manuscript 178
8.1.4 Distribution 178
8.1.5 Regular Correspondents 179

8.2 ICFA Beam Dynamics Panel Members 180

1 Foreword

1.1 From the Chair

Weiren Chou, Fermilab
Mail to: chou@fnal.gov

The International Committee for Future Accelerators (ICFA) met on February 21-22, 2013 at TRIUMF, Vancouver, Canada. Pier Oddone, Fermilab Director and ICFA Chair chaired the meeting. This meeting was preceded by a joint ILC Steering Committee (ILCSC) and Linear Collider Board (LCB) meeting earlier on February 21 in the same place.

This meeting was a milestone on the long road towards the next big accelerator in our field – the International Linear Collider (ILC). The ILC GDE, led by Barry Barish from Caltech, has completed its mission by delivering a *Technical Design Report* (TDR) to the ILCSC. The TDR includes a cost estimate for a 500 GeV (E_{CM}) linear e+e- collider – US$ 7.8 billion plus 23 million person-hours. The TDR has been reviewed by outside experts and is currently under revision. The official release of this document is scheduled during the LP2013 conference in June 2013 in San Francisco. Meanwhile, the ILCSC was replaced by a new ICFA panel, the Linear Collider Board (LCB). The LCB consists of 15 members, 5 each from the three regions – Asia, Europe and North America – and is chaired by Sachio Komamiya from Tokyo University. Under the LCB, there is a Linear Collider Directorate, which has a director (Lyn Evans from CERN), a deputy director (Hotoshi Murayama from IPMU), and three associate directors (Mike Harrison from BNL for the ILC, Steinar Stapnes from CERN for the CLIC and Hitoshi Yamamoto from Tohoku University for physics and detectors). The main goal of this new organization is to turn the ILC from a paper machine into a construction project in the next several years, with the CLIC as an option for higher energy (> 1 TeV). At this moment, Japan is a strong candidate for hosting the ILC. The Japanese HEP community has proposed to build a 250 GeV (E_{CM}) linear e+e- collider as the first stage of the ILC to serve as a Higgs factory. The cost of such a machine is about 70% of a 500 GeV machine.

In Evans' article in Section 2.1, he emphasizes that "*the main thrust of the effort must now move to a diplomatic campaign to convince governments to participate in the construction of a first-rate laboratory*" (for the ILC).

Tatsuya Nakada from EPFL gave a report on a draft of the European Strategy Updates for particle physics. The draft says: "*Europe looks forward to a proposal from Japan to discuss a possible participation*" in construction of the ILC in Japan.

As Oddone retires as Fermilab Director and ICFA Chair on July1, 2013, the ICFA approved a proposal that the incoming Fermilab Director will become the ICFA chair for the remainder of Pier's term, which ends on December 31, 2014.

Several ICFA panels presented reports at the meeting. I gave a report on behalf of the Beam Dynamics Panel about the panel activities in the past year. One important activity was the organization of an ICFA workshop on "*Accelerators for a Higgs Factory: Linear vs. Circular*" (HF2012), which took place from November 14 to 16, 2012 at Fermilab. (http://conferences.fnal.gov/hf2012/) At this workshop various proposals were presented and discussed that claim to be able to reach the required energy and luminosity of a Higgs factory: a linear e^+e^- collider, either cold or warm (e.g., x-band), a circular e^+e^- collider; a muon collider and a photon collider. The workshop compared the pros and cons of these candidates mainly from the accelerator point of view but did not recommend any specific machine, which is only possible with further physics input. Also it is not excluded that multiple facilities may be required to complement one another in addressing the entire breadth of Higgs physics. The comparison included:

- physics reach
- performance (energy and luminosity)
- upgrade potential
- technology maturity and readiness
- technical challenges requiring further R&D

Cost was not included because it was too early for such a comparison at this stage. A summary report has been published and can be found in Section 4 of this newsletter.

In 2012, our panel organized two Advanced Beam Dynamics Workshops (51st ABDW on *Future Light Sources FLS2012*, March 5-9 at JLab, USA; 52nd ABDW on *High Intensity High Brightness Hadron Beams HB2012*, Sept. 17-21 in Beijing, China) and three mini-workshops (*Breakdown Science and High Gradient Technology*, April 18-20 at KEK, Japan; *High Order Mode Diagnostics and Suppression in SC Cavities*, June 25-27 at the Cockcroft Institute, UK; and *Deflecting/Crab Cavity Applications in Accelerators*, July 11-13 in Lanzhou, China).

In 2013, the BD panel held a mini-workshop *Beam-Beam Effects in Hadron Colliders*, March 18-22 at CERN, Switzerland; and will organize the 53rd ABDW on *Energy Recovery Linacs ERL2013*, Sept. 9-13 at BINP, Russia as well as the mini-workshop, *Space Charge 2013*, April 15-19 at CERN.

The BD panel also published three issues of the *ICFA Beam Dynamics Newsletter* in 2012: No. 57 edited by Y. Cai (SLAC, USA), No. 58 by E. Metral (CERN, Switzerland) and No. 59 by J.M. Byrd (LBNL, USA).

The Eighth International Accelerator School for Linear Colliders will be held from December 4 to 15, 2013 at Antalya, Turkey. The Institute of Accelerator Technologies (IAT) of Ankara University will be the host of this school. (http://www.linearcollider.org/school/2013/) Please see Section 2.2 for the details.

The editor of this issue is Dr. George Neil, a panel member and a senior scientist at JLab, USA. George collected 12 well-written articles in the theme section "*FEL Oscillators*." These articles give a comprehensive review of this important branch of free electron laser, a rapidly growing field in accelerator science and technology. In this issue there are also three workshop reports (Part A and B of *XFELO13*, *USR2012*), one recent PhD thesis abstract (F. Antoniou of National Technical U. of Athens) and ten workshop and event announcements (*SLAC Summer School, 53rd ICFA ABDW ERL2013, ICALEPCS2013, COOL'13, SRF2013, SpaceCharge2013, FEL'13, SRI2013, LER2013* and *PSTP2013*). I thank George for editing and producing a newsletter of great value to our community.

1.2 From the Editor

George R. Neil
Thomas Jefferson National Accelerator Facility
Mail to: neil@jlab.org

For this 60th Issue of the Beam Dynamics Newsletter I have selected FEL Oscillators as a special focus topic. This may seem a little odd at first given the huge advances made by SASE FEL amplifiers in the last few years with breakthrough performance in peak brightness achieved in the x-ray region. This will continue to be a major push at a number of facilities internationally in the years to come. Nonetheless the role of ICFA is to try to remain one step ahead with forward-thinking studies. The idea of using the continuous or long macropulse beam from a superconducting linac to provide a repetitive source of gain for an x-ray oscillator is intriguing because it could provide single-mode narrow-band output at an average brightness significantly exceeding the SASE systems of today. Use of such a system for scientific studies is explored in this newsletter as well as practical considerations for building such machines. To provide a connection to existing technology I have accepted a few papers on the technology of existing or nearer term FEL oscillators operating in longer wavelength regimes. These FELs are even now providing a fertile ground for scientific discovery in a range of condensed matter science.

The bulk of the papers in this volume were contributed based on presentations at a workshop sponsored by Pohang Accelerator Laboratory, Postech, held at the POSCO International Center in Pohang, Korea, February 14-15, 2013, entitled “Science Outlook and R&D Issues for an X-Ray Free Electron Laser Oscillator (XFELO)”. The two-day workshop featured lively exchanges on the applications of such an advance as well as serious discussions on the required technological developments to ensure success. In **Sections 5.1 and 5.2, Workshop and Conference Reports,** of this newsletter you will find a summary of the workshop in two parts. First the science applications of such an oscillator and then the technological considerations of building such a machine are summarized in the XFELO2013 Workshop Report Parts A and B. Further details on those subjects can be found in the contributed papers to this volume. The Workshop organizers also did an excellent job of letting the attendees enjoy Korean food and culture. I am grateful to the organizers of that workshop, **Moohyun Yoon**, Chair of Physics Department, POSTECH, **Moohyun Cho**, Director of Pohang Accelerator Laboratory, and **Kwang-Je Kim**, Chair of Program Committee, for permitting me to solicit contributions for this newsletter. An additional workshop report comprises **Section 5.3,** Workshop on Accelerator R&D for Ultimate Storage Rings.

The first group of contributed papers to this newsletter presents the range of the scientific opportunities possible with the development of an XFELO. We start with an Introduction to the X-ray FEL Oscillator by **Kwang-Je Kim** who has worked hard to develop and promote the idea. The first application paper is High Resolution Inelastic X-ray Scattering by **Clement Burns**, followed by a study of New Science in X-ray Photon Correlation Spectroscopy from **Laurence Lurio**. The next topic presented by **Paul Evans** highlights the Nanomaterial Photonic Studies that would be enabled by this development. Mößbauer Science and Nuclear Quantum Optics by **Jörg Evers** is a perspective on exciting new science enabled by the brightness of such sources. Studies of the capability for Nuclear Resonant Scattering are given a thorough treatment by

Ralf Röhlsberger. Finally, the exciting prospect for a Nuclear-Resonance-Stabilized XFELO for Fundamental Physics and Precision Metrology by **Bernhard Adams and Kwang-Je Kim** rounds out the application talks for this source.

Technical feasibility discussions then take the fore. We treat the critical issue of technical Feasibility of X-ray Cavities for FELO in a paper by **Yuri Shvyd'ko**, followed by a discussion of the nanopositioning approach in Nanopositioning Stages to Enable XFELO Optics, Mounting and Manipulation Capabilities by **Deming Shu**. An update on the ERL performance advances by the Budker team in the Budker INP FEL Facility – Current Status and Future Prospects is contributed by **O. A. Shevchenko**.

Papers not presented at the XFELO Workshop but appropriate to this discussion include A Program for Optimizing SRF Linac Costs, crucial for XFELO design, is submitted in an original submission by **Tom Powers**. **Michelle Shinn** contributes Simulations of a FEL Oscillator based on the JLab ERL representing an intermediate step between existing FEL oscillator operation and our aspirations in the x-ray region. I am grateful to all the contributors for their work in providing an excellent discussion on the topic of FEL Oscillators.

2 Linear Colliders

2.1 From the Linear Collider Director

Lyn Evans
Director of the Linear Collider Collaboration
Mail to: lyn.evans@cern.ch

(*Reprinted from "LC Newsline" March 7, 2013 with author's permission*)

Let me take this opportunity to acknowledge the enormous achievement of the very small GDE team, led by Barry Barish. They have produced the *Technical Design Report* (TDR), which has been favourably reviewed by an independent expert committee. The TDR also contains a detailed cost estimate which has also been independently reviewed and has proved to be robust – see Barry's Corner for more detail on the cost review. I would also like to acknowledge the work of the physics and detector community, led by Sakue Yamada. They are in the process of finalising the *Detailed Baseline Design* (DBD) report.

The mandate of the Linear Collider Collaboration (LCC) is strongly supported by the recent update of the proposed European Strategy for Particle Physics (still to be endorsed by the CERN Council). For CLIC, "*CERN should undertake design studies for accelerator projects in a global context, with emphasis on proton-proton and electron-positron high-energy frontier machines. These design studies should be coupled to a vigorous accelerator R&D programme, including high-field magnets and high-gradient accelerating structures, in collaboration with national institutes, laboratories and universities worldwide.*"

For ILC, "*There is a strong scientific case for an electron-positron collider, complementary to the LHC, that can study the properties of the Higgs boson and other particles with unprecedented precision and whose energy can be upgraded. The*

Technical Design Report of the International Linear Collider (ILC) has been completed with large European participation. The initiative of the Japanese particle physics community to host the ILC in Japan is most welcome, and European groups are eager to participate. Europe looks forward to a proposal from Japan to discuss a possible participation". The next step in developing a world consensus is the "Snowmass" process which is now underway. Hopefully the result of these discussions will lend as strong support to the ILC from the US HEP community as has been shown by the European Strategy Group.

The new structure of the LCC Directorate is very light. Hitoshi Murayama will be my deputy, who will mainly be responsible for explaining the scientific case for the ILC to governments and the public. Steinar Stapnes will continue in his role as Director of the CLIC effort and Mike Harrison will take over the ILC. Hitoshi Yamamoto, as Detector Director, will take on the difficult task of bringing the experimental community together so that they are capable of building two state-of-the-art detectors. Regional representation and coordination will be strengthened by appointing regional members (of the directorate?) for Europe and the Americas. For the moment it is considered that the representation from Japan is adequate and regional advice will be sought case by case as the ILC project develops.

The GDE has left the ILC in very good shape. Although continuing R&D is still needed to try to further reduce the cost and to prepare for a possible construction project, the main thrust of the effort must now move to a diplomatic campaign to convince governments to participate in the construction of a first-rate laboratory that will further the world's efforts in understanding the fundamental nature of matter.

2.2 Eighth International Accelerator School for Linear Colliders

Lyn Evans (LCC/CERN), Weiren Chou (Fermilab), Omer Yavas (Ankara U.)
Mail to: lyn.evans@cern.ch, chou@fnal.gov, yavas@ankara.edu.tr

We are pleased to announce the *Eighth International Accelerator School for Linear Colliders*. This school is a continuation of the series of schools which began seven years ago. The first school was held in 2006 at Sokendai, Japan, the second in 2007 at Erice, Italy, the third in 2008 at Oakbrook Hills, USA, the fourth in 2009 at Huairou, China, the fifth in 2010 at Villars-sur-Ollon, Switzerland, the sixth in 2011 at Pacific Grove, USA, and the seventh at Indore, India. The school is organized by the Linear Collider Collaboration (LCC including ILC and CLIC) and the International Committee for Future Accelerators (ICFA) Beam Dynamics Panel.

The school this year will take place in Antalya, Turkey from December 4 to 15, 2013. It will be hosted by the Institute of Accelerator Technologies (IAT) of Ankara University. The school is sponsored by a number of funding agencies and institutions including the U.S. National Science Foundation (NSF), Fermilab, SLAC, CERN, DESY, INFN, IN2P3, CEA, CPAN, KEK, IHEP and RRCAT.

The 11-day program includes 8-1/2 days of lectures, an excursion, a site visit and an examination. The first three days will be an introductory course with an overview of proposed future lepton colliders (ILC, CLIC and the muon collider) as well as introductions to linac basics and beam instrumentation. This will be followed by two elective courses, one on accelerator physics and the other on RF technology to run in parallel for 6 days. Each student is required to take the introductory course and one of the two electives. A complete description of the program will soon be published on the school web site (www.linearcollider.org/school/2013/). There will be homework assignments and a final examination but no university credits.

We encourage young physicists (graduate students, post doctoral fellows, junior researchers) to apply. We welcome those physicists who are considering changing to a career in accelerator physics. This school is adopting an in-depth approach. Therefore, former students are welcome to apply if they have a compelling reason to do so. The school will accept a maximum of 60 students from around the world. Students will receive full or partial financial aid covering their expenses for attending including travel. There will be no registration fee. Each applicant should complete the online registration form (which can be found on the school web site) and submit a curriculum vita as well as a letter of recommendation from his/her supervisor (in electronic form, either PDF or MS WORD). The application deadline is July 20, 2013. For more information, please contact: Dr. Avni Aksoy, Ankara University, Institute of Accelerator Technologies, 06830, Gölbaşı, Ankara, Turkey, telephone: +90-312-4851377, ext. 5016, mobile: +90-533-3827864, fax: +90-312-4847456, email: lcs2013@ankara.edu.tr

Organizing Committee
- Lyn Evans (LCC/CERN, Chair)
- Alex Chao (SLAC)
- Hesheng Chen (IHEP)
- Weiren Chou (ICFA BD Panel/Fermilab)
- Paul Grannis (Stony Brook Univ.)
- P. D. Gupta (RRCAT)
- Mike Harrison (BNL)
- In Soo Ko (PAL)
- Shin-ichi Kurokawa (KEK)
- Hermann Schmickler (CERN)
- Nick Walker (DESY)
- Kaoru Yokoya (KEK)

Curriculum Committee
- Weiren Chou (Fermilab, Chair)
- William Barletta (USPAS)
- Alex Chao (SLAC)
- Jie Gao (IHEP)
- Srinivas Krishnagopal (BARC)
- Carlo Pagani (INFN/Milano)
- Joerg Rossbach (DESY)
- Hermann Schmickler (CERN)
- Nobuhiro Terunuma (KEK)
- Kaoru Yokoya (KEK)

Local Committee
- Omer Yavas (IAT, Ankara University, Chair)
- Avni Aksoy (IAT, Ankara University)
- Ozlem Karsli (IAT, Ankara University)
- Sinan Kuday (IAT, Ankara University)
- Suat Ozkorucuklu (IAT & S. Demirel University)

3 Theme: FEL Oscillators

3.1 Introduction to an X-ray FEL Oscillator

Kwang-Je Kim
Argonne National Laboratory, Argonne, IL 60439, USA
Mail to: kwangje@aps.anl.gov

3.1.1 **Introduction**

A hard x-ray free-electron laser in oscillator configuration—an FEL oscillator (XFELO)—will produce highly stable x-ray beams of ultra-high spectral purity and high average brightness, offering unique scientific opportunities complementary to those provided by high-gain x-ray amplifiers. The x-ray optics issues for the oscillator cavity are challenging but appear feasible. An XFELO is well-suited for an energy recovery linac (ERL) employing a cw superconducting linac. A super x-ray facility can be envisaged in which XFELOs are combined with a high-gain amplifier, possibly with harmonic generation, producing x-ray beams of extraordinary capabilities. In addition, by stabilizing the x-ray cavity relative to a narrow nuclear resonance, the XFELO output can be made to exhibit sharp comb structure as in a mode-locked optical laser. A nuclear-resonance-stabilized XFELO may offer exciting opportunities in areas outside of traditional x-ray physics, such as developing an x-ray time/length standard and studying fundamental questions in quantum mechanics and gravitation. This workshop is to explore the scientific opportunities for an XFELO and technical challenges for realizing the machine.

3.1.2 **An X-Ray FEL in Oscillator Configuration**

The recently successful LCLS [1] is the first x-ray free-electron laser operating in a self-amplified spontaneous emission (SASE) mode [2,3], in which the gain is so high that the initial spontaneous emission is amplified to intense, quasi-coherent radiation in a single pass. High-gain XFELs are currently under vigorous development; several additional facilities are under construction, the self-seeding scheme has been developed successfully to improve the temporal coherence [4,5], and a large-scale soft x-ray facility utilizing seeded high-gain devices is in the conceptual design phase [6]. An x-ray FEL oscillator (XFELO) [7,8] is a qualitatively different device from high-gain single-pass x-ray FELs, and thus promises to further enrich the era of x-ray FELs.

3.1.2.1 ***FEL Oscillator Principles***

An oscillator FEL is a low-gain device and was successfully operated [9] soon after the invention of the FEL concept [10]. Since then, several devices around the world have been operated for many years in the UV and lower photon energy regions, where low-loss, normal-incidence reflectors and accelerators meeting the required beam qualities are readily available [11].

The principle of an FEL oscillator is illustrated in Figure 1. Electron bunches from an accelerator (normally an rf type) pass through an undulator located inside a high-Q optical cavity. The spontaneous emission pulse from the first pass is reflected back into the undulator by the cavity mirrors. In the second pass, the spontaneous emission pulse meets the second electron pulse at the entrance of the undulator. The radiation pulse out of the undulator in the second pass consists of spontaneous emission from the first and second pass as well as an amplified part. The process will repeat if the round-trip loss is smaller than the gain. The amplified part increases exponentially as the pass number increases. At high intra-cavity power the gain starts to decrease, and the system eventually reaches a steady state when the gain becomes just enough to replenish the loss. Part of the cavity loss appears as the useful FEL output power.

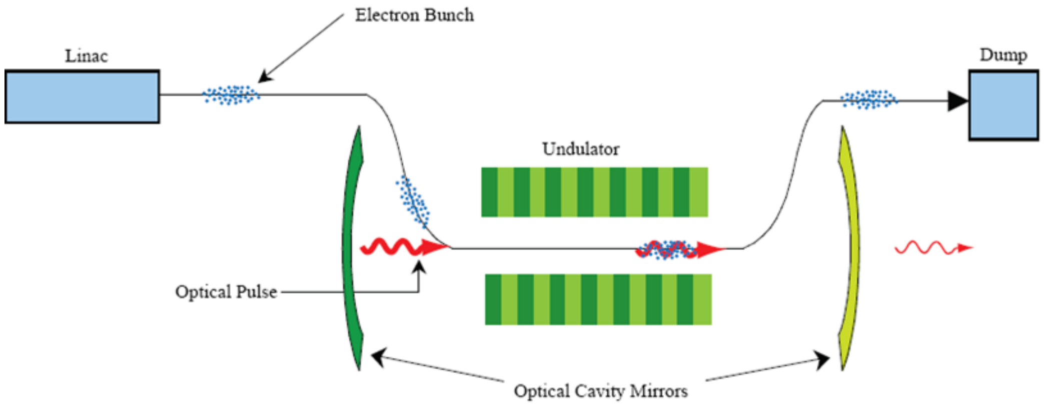

Figure 1: FEL oscillator principle

A subtle but important phenomenon is the lethargy [12]—the fact that the later part of the optical pulse receives more gain since the gain is due to the electron beam developing a density modulation and it takes time for the initially un-modulated electron beam to develop modulation. A consequence of this effect is that the electron bunch spacing does not need to be exactly the same as the round-trip time of the radiation pulse; the cavity length should actually be slightly shorter than that determined from the synchronism condition, and there is a little room around the optimum de-synchronism. The round-trip time of the pulse envelope is in general different from the round-trip time of the phase, the latter being determined essentially by the cavity length. This fact will be important later when we discuss a nuclear-resonance-stabilized XFELO in section 1.1.6.

Temporal coherence in an FEL oscillator is achieved by the gain narrowing as well as filtering by the cavity mirrors if they are of a narrow-band type.

An FEL oscillator can operate in pulsed accelerator as long as the duration of the macro-pulse is longer than the time to reach steady state from the initial spontaneous emission regime. With a cw accelerator, however, the oscillator can be maintained at a steady state, a desirable mode of operation since it provides higher stability and higher average power.

Finally we note that an FEL oscillator is inherently more stable than a single-pass amplifier since the circulating intra-cavity at any time is evolved from the initial spontaneous emission by interacting with many previous electron bunches.

3.1.2.2 *X-ray Cavity Configurations*

The concept for an XFELO that uses crystals as low-loss reflectors was first proposed in 1983 [7], at the same time that the x-ray SASE was first proposed in the West [3]. However, the concept did not receive its due attention until a recent, detailed study showed that an XFELO would be feasible with low-intensity, ultra-low-emittance electron bunches contemplated for ERLs [8].

The basic insight realizing a high-Q optical cavity in the hard x-ray region is to note the high reflectivity of the Bragg reflection within the narrow Darwin width. Both aspects are important—high reflectivity has high Q and narrow Darwin width for efficient spectral filtering.

The simplest configuration is illustrated in Figure 2, consisting of two Bragg crystals at near-normal incidence configuration and a grazing incidence, curved mirror for controlling the transverse mode shape.

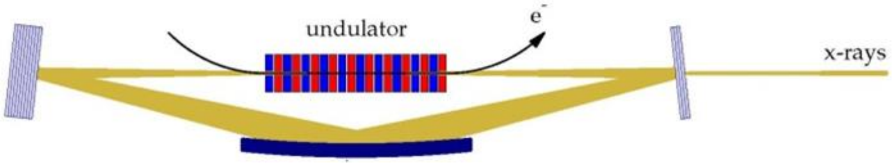

Figure 2: A basic scheme for optical cavities for an XFELO that is not tunable.

The tuning range of the two-crystal scheme is severely limited because the grazing angle of incidence at the curved mirror should be kept to less than a few mrad for high reflectivity.

Tunable cavity configurations were invented more than forty years ago [13]. Figure 3 shows a tunable four-crystal scheme adopted for an XFELO [14]. Here, the four crystals' Bragg angles are changed in unison while keeping a constant round-trip path length by a coordinated translation of the crystals. The four-crystal scheme also allows the use of one crystal material for all spectral regions of interest—an important advantage since we can then choose diamond, taking advantage of its excellent thermo-mechanical properties, as will be explained later.

More agile schemes are possible by employing more crystals [15].

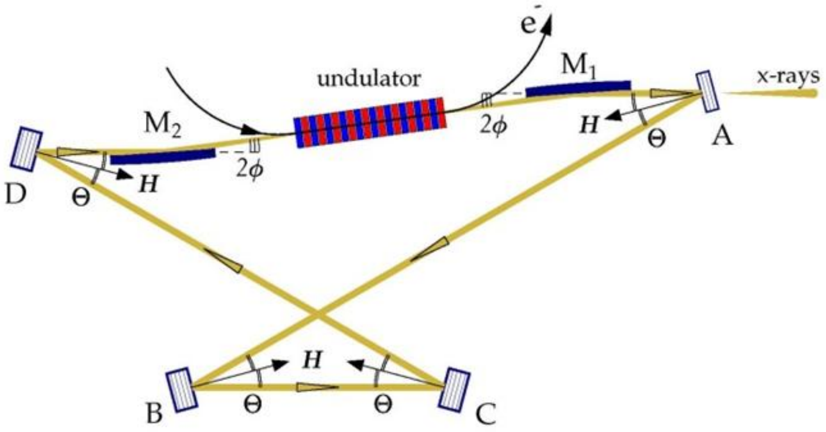

Figure 3: A tunable cavity configuration in terms of four crystals.

3.1.2.3 *Major Parameters and Performances*

The major parameters of an example XFELO system from reference [16] are listed in Table 1. The electron beam parameters considered here are relatively conservative. XFELO parameters with higher beam qualities, lower bunch charge, and lower electron beam energy may also be feasible [17]. The XFELO operation with Bragg reflectors will be difficult below 5 keV due to the enhanced photo-absorption in the crystal and above 20 keV due to the small crystal bandwidth. Although the four-crystal configuration is tunable over a wider range, the practical tuning range for a specific Bragg plane is limited to 2 – 6% because the angular acceptance can become smaller than the x-ray beam divergence at lower Bragg angles. We note that a few % is in fact a huge tuning range in view of the very narrow bandwidth of ~10^{-7}.

The profiles of the radiation output near the energy of 14.4 keV are shown in Figure 4 [16]. In panel (a) the output radiation power as a function of time is indicated in red, with the electron beam current envelope in green for reference. In panel (b) we plot the corresponding output spectrum with a red line, showing that the spectral FWHM is approximately 1.8 meV, corresponding to a relative FWHM of ~1.3×10^{-7}. Note that this bandwidth is much narrower than the reflectivity width of the Bragg crystals (the blue line). The spectral profile is roughly the Fourier transform of the electron current profile. These steady state profiles are reached after 1000 passes.

Table 1: Major Parameters

Electron Beam	
Energy	5 – 7 GeV
Bunch charge	25 – 50 pC
Bunch length (rms)	0.1 – 1 ps
Normalized rms emittance	0.2– 0.3 mm-mrad
Energy spread (rms)	2×10^{-4}
Bunch repetition rate	~ 1 MHz (constant)
Undulator	
Period length	~ 2 cm
Deflection parameter K	1.0 – 1.5
Total length	30 – 60 m
Optical Cavity	
Configuration	2 – 4 diamond crystals and focusing mirrors
Total roundtrip reflectivity	> 85% (50% for 100-A peak current)
XFELO Output	
Photon energy coverage	5 – 25 keV (plus the third harmonic)
Spectral purity	1 – 10 meV (10^{-6} –10^{-7} in relative BW)
Coherence	Fully coherent transversely and temporally
X-ray pulse length	0.1 – 1.0 ps
Tuning range	2 – 6 %
Number of photons/pulse	~ 10^{9}
Pulse repetition rate	~ 1 MHz
Peak spectral brightness	10^{32} – 10^{34} ph/[s*mm^2*mrad^2*(0.1% BW)]
Average spectral brightness	10^{26} – 10^{28} ph/[s*mm^2*mrad^2*(0.1% BW)]

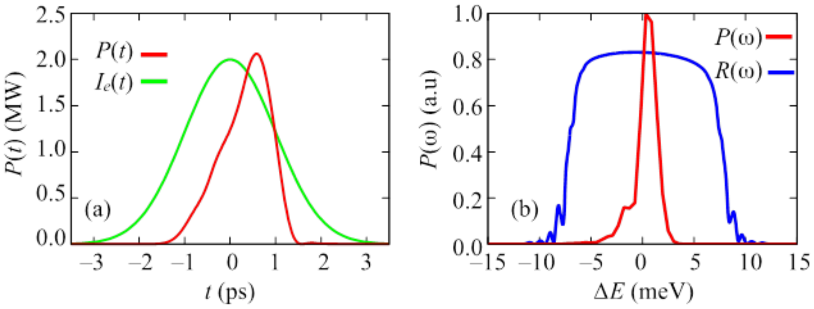

Figure 4: (a) The red line plots the temporal power profile of the XFELO output at 14.4 keV, showing peak powers ~ 2 MW; the electron beam current is shown as a green line. (b) Spectrum of the XFELO output as a red line. The FWHM ~1.8 meV is much narrower than that of the crystal reflectivity, shown in blue.

3.1.3 Scientific Applications

An XFELO may be regarded to be a more natural extension of the third-generation x-ray sources compared to the high-gain devices. Currently the APS, one of the brightest sources in the hard x-ray range, produces 10^9 photons per second in the meV bandwidth, which will be increased a million-fold by an XFELO. Inelastic x-ray scattering and nuclear resonance scattering techniques, which are currently limited by the available flux in the desired bandwidth, can be revolutionized by an XFELO. Hard x-ray imaging will be feasible with nanometer resolution using multilayer Laue lenses that require an x-ray bandwidth of less than 10^{-5}. The intensity of an XFELO will also enable hard x-ray photoemission spectroscopy for time-resolved study of Fermi surfaces in bulk material. The temporally coherent photons at an average rate of 10^{15} photons per second will be a game changer for x-ray photon correlation spectroscopy.

Some of these applications were discussed during the workshop “Science Opportunities with an XFELO” held at the APS at Argonne National Laboratory, on May 5, 2010. More science cases are presented during this workshop. This issue of the ICFA Beam Dynamics Newsletter contains papers from the 2010 workshop as well as this workshop.

3.1.4 Accelerator System

At the level of an individual bunch, the electron beam characteristics required for an XFELO (Table 1) have already been demonstrated, for example, by the LCLS accelerator system in its low-charge mode [18]. Producing ultra-low emittance bunches at a constant and high repetition rate is a challenge currently being actively addressed by several research groups, in particular those pursuing an ERL-based light source [19,20]. These studies indicate that an injector with the bunch characteristics of Table 1 and a repetition rate in the MHz to GHz range is feasible. A variety of approaches based on laser-driven photocathodes employing either a DC voltage [19,20] or a low-frequency radio frequency (rf) cavity [21] are in various stages of development.

The main accelerator for an XFELO should be of a cw superconducting type to accommodate a constant bunch repetition rate, with one or more recirculation paths to save cost. An XFELO is therefore a natural fit for a multi-GeV ERL-based light source facility. Various technical issues on ERL accelerator systems have been addressed in the proceedings of ERL workshops, including the design of high-current, low-emittance injectors; beam mergers for the recirculation loop; cw superconducting linacs; and recirculation optics that preserve the electron beam quality [22].

The KEK-JAEA collaboration plans to construct a one-loop ERL with a 3-GeV superconducting linac in the first step. An XFELO operation is envisaged in the second step by adjusting the rf phase of the recirculation path to double the final energy to 6-7 GeV, as shown in Figure 5 [23]. Note that energy recovery is not necessary for an XFELO due to its low average current.

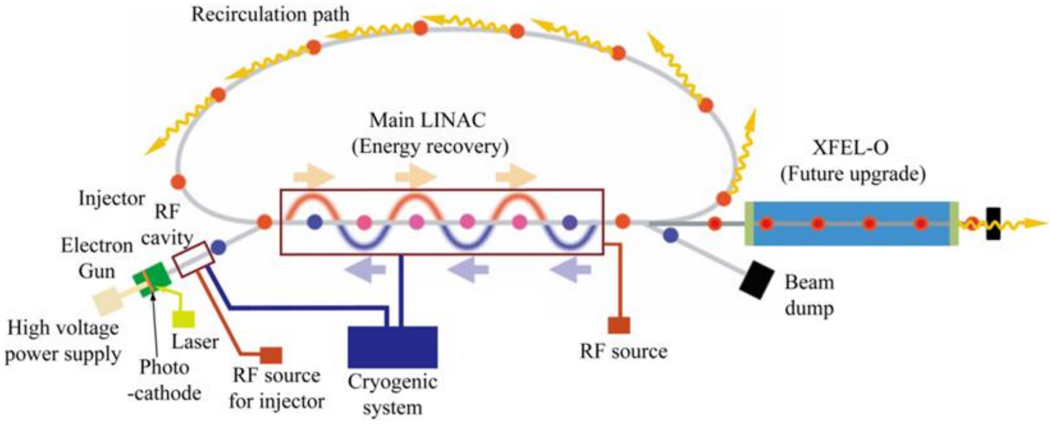

Figure 5: XFELO plan for the future KEK-JAEA 3-GeV ERL (courtesy of S. Sakanaka).

A pulsed superconducting linac such as that being used for the European XFEL can operate an XFELO in a pulsed mode [24]. The macropulses in this linac are 1–2 ms long, accommodating 1000–2000 micropulses at a 1-MHz repetition rate, sufficient to drive an XFELO to saturation level.

3.1.5 X-ray Optics

A comprehensive discussion of the x-ray optics for an XFELO and recent progress can be found in Yuri Shvyd'ko's article in this Newsletter [15]. In the following we give a brief summary.

Diamond is a material whose superb physical qualities are well suited for an XFELO cavity: high mechanical hardness, high thermal conductivity, high radiation hardness, low thermal expansion, and chemical inertness. An exceptionally high $\geq 99\%$ reflectivity is predicted in x-ray Bragg diffraction, higher than that from any other crystal due to the uniquely small ratio of the extinction length to the absorption length. The issue then is whether synthetic diamond crystals of sufficient size (active volume ~1 mm^3) and crystalline perfection required for high reflectivity can be manufactured. Working with several crystal growers, we found that modern techniques can grow high-quality diamonds containing defect-free regions suitable for an XFELO. Experiments with 13.9-keV and 23.7-keV x-ray photons have established that the predicted reflectivity greater than 99% at near normal incidence is feasible [25, 26].

Temperature gradients that lead to gradients in the crystal lattice spacing can diminish the reflectivity. The simulation shows that the radiation heat load produced by an XFELO requires that the diamond crystal be cryogenically cooled to a temperature $T \leq 100$ K. In this case, the diamond has sufficient time to conduct away the heat, so that the crystal temperature becomes homogeneous before the subsequent radiation pulse arrives. Low temperatures are favorable because diamond has an unmatched thermal diffusivity and an extremely small coefficient of thermal expansion for $T < 100$ K as measured recently [27].

High radiation hardness is another desirable feature of diamond. The power density incident on diamond crystals in the XFELO cavity is ~ 4 kW/mm^2, which is about 30 times higher than that of the undulator radiation used to test the first crystal at the APS. While it is encouraging that the APS crystals have survived one year of operation without an apparent decrease in performance, additional studies should be performed to understand the degree of irreversible radiation damage in diamond and how this damage affects its reflectivity.

Deviations of the crystal and focusing mirror surface from its ideal will disturb the x-ray wavefront, producing mode distortions and large-angle scattering. For diamond crystals, the surface error height δh should be a fraction of the x-ray wavelength times the difference of the index of refraction from unity δn. Since δn for hard x-rays is of the order of 10^{-6}, the tolerance on δh is about a micron, which should be achievable. The tolerance of the grazing incidence mirror on the height error (contributing to diffusion) is about $\delta h \leq 1$ nm, while the tolerance on figure error (contributing to mode distortion) is about 0.1 μr. These tolerances are tight but are current state of the art.

The requirements to stabilize the crystals and the mirrors in the cavity are stringent—better than 10-nrad (rms) angular stability and 3-m (rms) positional stability. The null-detection feedback technique employed at the Laser Interferometer Gravitational-Wave Observatory (LIGO) can stabilize several optical axes with a single detector and therefore appears to be a promising approach. A pilot experiment with a high-resolution, six-crystal x-ray monochromator at the APS Sector 30 beamline succeeded in achieving an angular stability of 13 nrad (rms) [28]. We will need to improve the scheme to meet the XFELO requirements—a multiple-axis system with better than 10-nrad stability.

The stages for optical elements need to be precisely engineered to enable manipulations meeting the tight tolerances. These issues are discussed by Deming Shu's article in this ICFA Newsletter [29].

3.1.6 Nuclear-Resonance-Stabilized XFELO for Fundamental Science

Since the XFELO output pulses are essentially copies of a single intra-cavity pulse circulating inside the x-ray cavity, the output pulses can be coherent with each other if the cavity length can be held fixed. The output spectrum then consists of a comb of sharp lines spaced at about 10 neV from each other. If left to itself, however, the cavity length will fluctuate, and other phase errors will also accumulate, so the comb lines will be effectively broadened up to their spacing, and inter-pulse coherence is lost. This can be prevented by locking the cavity length to an external reference to obtain an inter-pulse coherence commensurate with the stability of that reference. A convenient external reference is nuclear resonances. Thus we will refer to such an extreme stabilized device as a nuclear-resonance-stabilized XFELO, or NRS-XFELO [30, 31].

The output of an ideal XFELO at a fixed location consists of pulses that are identical but displaced in time. The electric field of the n-th pulse as a function of time can be written as

$$E_n(t) = e^{-i\omega_{FEL}(t-nT_c)} A(t-nT_e) \quad .$$

Here $A(t)$ is the radiation envelope, ω_{FEL} is the XFELO frequency in the middle of its bandwidth, $T_c = L / c$ is the round-trip time of the EM field in the cavity, and T_e is the electron bunch spacing. The above equation is in accord with the discussion in section 1.1.2.1, namely, that the phase advance per period is T_c while the envelope advance per period is T_e. (We are neglecting here the small index of refraction during the FEL interaction.)

The tolerance on electron bunch spacing T_e is not as stringent since it appears in the field envelope rather than in the phase. A detailed analysis shows that the fluctuation in T_e should be much less than the electron bunch length, a requirement for an XFELO without NRS stabilization.

On the other hand, the fluctuation in cavity length gives rise to fluctuation in comb lines. Thus the cavity length fluctuation should be much less than the FEL wavelength. Although very stringent, the desired stabilization appears to be feasible by a feedback system referenced by, for example, ^{57}Fe nuclear resonance, since the resonance width and the comb spacing is comparable (~ 10 neV). The feedback principle is illustrated in Figure 6 and works as follows. The comb line moves one comb spacing if the cavity length changes by one FEL wavelength. With one of the comb lines overlapping with the ^{57}Fe resonance well inside the FEL bandwidth, the cavity length is scanned by one wavelength (~0.8 Å) and held fixed where the fluorescence signal is maximum. Note that it is not necessary to identify which comb line overlaps with the nuclear resonance. It is only necessary that one of the lines does overlap, and we are keeping that line at that position.

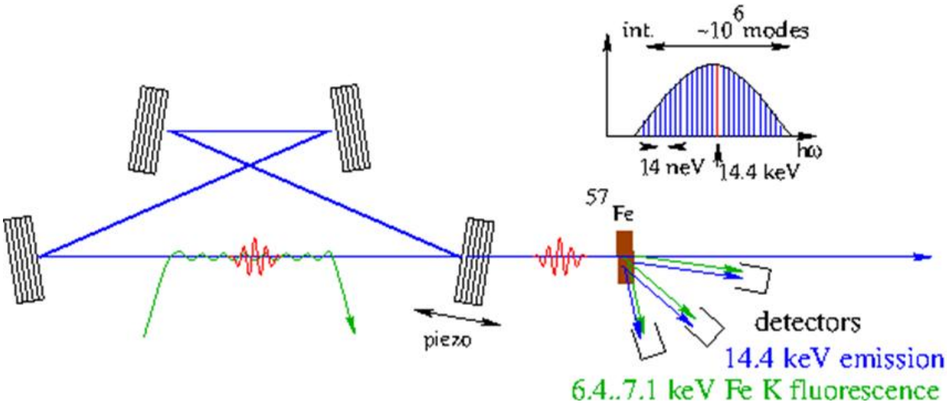

Figure 6: Schematic of the cavity-stabilization scheme. A nuclear-resonant sample (here ^{57}Fe) is placed into the XFELO output, and the nuclear-resonant and K-shell electronic fluorescence are monitored as functions of cavity tuning with a piezoelectric actuator. A feedback loop keeps one of the ca. 10^6 longitudinal modes of the XFELO on resonance with the sample.

Realizing an NRS-XFELO appears to be within the current state of the art, at least with ^{57}Fe resonance. Extending the stabilization to narrower resonances by an order of magnitude may also be feasible. NRS-XFELOs for even narrower resonances will be quite challenging but worthwhile as they provide new scientific techniques hitherto not available in hard x-ray wavelengths. The principles and applications of NRS-XFELO are discussed in greater detail in another paper in this issue of the ICFA Newsletter [31].

3.1.7 Conclusions

The accelerator technology for an XFELO is essentially available in view of the recent advances in connection with various future light source projects. Recent advances in x-ray optics towards realizing an x-ray cavity meeting the XFELO specifications are encouraging. The output characteristics of an XFELO are complementary to those of high-gain type x-ray FELs, thus enriching the era of hard x-ray FELs. It might also be feasible to stabilize an XFELO cavity using the narrow nuclear resonances, vastly extending the coherence length with fundamental applications outside the traditional realm of x-ray physics.

3.1.8 Acknowledgments

I thank Ryan Lindberg, Deming Shu, and Yuri Shvyd'ko for collaboration on XFELO, and Bernhard Adams for collaboration on NRS-XFELO. The support for this workshop by POSTECH and PAL is greatly acknowledged. This work was supported by the U.S. Department of Energy, Office of Science, under Contract No. DE-AC02-06CH11357.

3.1.9 References

1. P. Emma for the LCLS Team, Proc. of the 2009 Part. Accel. Conf., TH3PBI01, p. 315 (2011).
2. K. Kondratenko and E. Saldin, "Generation of Coherent Radiation by a relativistic electron beam in an undulator," Part. Acc. 10, 207 (1980)
3. R. Bonifacio, N. Narducci, and C. Pellegrini, Opt. Commun. 50, 373 (1984).
4. G. Geloni, V. Kocharyan, and E.L. Saldin, J. Modern Optics 58, 1391 (2011); G. Geloni, V. Kocharyan, and E.L. Saldin, "Cost-effective way to enhance the capabilities of the LCLS baseline," DESY 10-133, August 2010.
5. J. Amman et al., "Demonstration of self-seeding in a hard X-ray free electron laser," Nature Photonics 6, 693 (2012); doi: 10.1038/nphoton.2012.180.
6. J.N. Corlett et al., "A next generation light source facility at LBNL," http://escholarship.org/uc/item/ 81t3h97w
7. R. Colella and A. Luccio, Optics Comm. 50, 41 (1984).
8. K.-J. Kim, Y. Shvyd'ko, and S. Reiche, Phys. Rev. Lett. 100, 244802 (2008).
9. D.A.G. Deacon, et al., Phys. Rev. Lett. 38, 892 (1977).
10. J.M.J. Madey, J. App. Phys. 42, 1906 (1971).
11. For a review, see C. Brau, *Free-Electron Lasers* (Academic Press, New York, NY, 1990).
12. H. Al-Abawi, et al, Opt. Commun. **30**, 235 (1979)
13. R. M. J. Cotterill, Appl. Phys. Lett., **12**, 403(1968)
14. K.-J. Kim and Yu.V. Shvyd'ko, Phys. Rev. ST Accel. Beams 12, 030703 (2009).
15. Y. Shvyd'ko, "Feasibility of X-ray Cavities for XFELO," this Newsletter,
16. R. R. Lindberg et al., Phys. Rev. ST Accel. Beams 14, 010701 (2011).
17. R. Hajima and N. Nishimori, Proc. of the FEL2009 (2009).
18. Y. Ding et al., PRL 102, 254801 (2009).
19. I. Bazarov et al., Proc. of the 2009 Part. Accel. Conf., TU2GRI01, p. 683 (2011).
20. N. Nishimori et al., Proc. of the 2009 FEL Conf., TUPC17, p. 277 (2009).
21. F. Sannibale et al., Proc. of the 2010 FEL Conf., WEPB36, p. 475 (2010).
22. See presentations of the ERL Workshop, Tsukuba, Japan (October, 2011); http://erl2011.kek.jp/

23. K. Harada and ERL Project Team, J. of the Japanese Soc. for Synch. Rad. Res., 24(5), 256 (2011) [in Japanese].
24. J. Zemella et al., presented at FLS2010 (SLAC, 2010).
25. Yu. V. Shvyd'ko et al., Nature Physics 6, 96 (2010).
26. Yu. V. Shvyd'ko, S. Stoupin, V. Blank, and S. Terentyev, Nat. Photonics 5, 539 (2011).
27. S. Stoupin and Yu. V. Shvyd'ko, Phys. Rev. Lett. 104, 085901 (2010); S. Stoupin and Yu. V. Shvyd'ko, Phys. Rev. B 83, 104102 (2011).
28. S. Stoupin et al., Rev. Sci. Instrum. 81, 055108 (2010).
29. D. Shu, "Nanopositioning Stages to Enable XFELO Optics Mounting and Manipulation Capabilities," this Newsletter.
30. B. W. Adams and K.-J. Kim, in preparation.
31. B.W. Adams and K.-J. Kim, "Nuclear-Resonance-Stabilized XFELO for Fundamental Physics and Precision Metrology," this Newsletter.

3.2 Scientific Opportunities for High Resolution Inelastic X-ray Scattering with an XFELO Source

Clement A. Burns
Western Michigan University, Dept. of Physics, Mail Stop 5252
1903 W. Michigan Ave, Kalamazoo, MI, USA 49008
Mail to: clement.burns@wmich.edu

3.2.1 Introduction to Inelastic X-ray Scattering

Scattering measurements have provided much of the microscopic information that we have about a variety of systems. In particular, these measurements have helped determine the excitation spectrum for phonons, magnons, excitons, band transitions, and plasmons. Scattering studies have helped explain phenomenon as commonplace as heat transfer in solids, and as exotic as superfluidity. Due to the wide variation in the energy and momenta of these excitations, a variety of probes such as visible light, x-rays, neutrons, and electrons are needed. Fig. 1 shows a schematic picture of some of the different probes and the approximate range of energies and wavevectors which they can access. For certain combinations of wavevectors and energies, inelastic x-ray scattering (IXS) is the only suitable probe. Good overviews of using IXS to study electronic excitations are given in the recent book by Schülke [1] and the review article by Ament et al. [2] An overview of the use of IXS to study phonons is given by Krisch and Sette. [3]

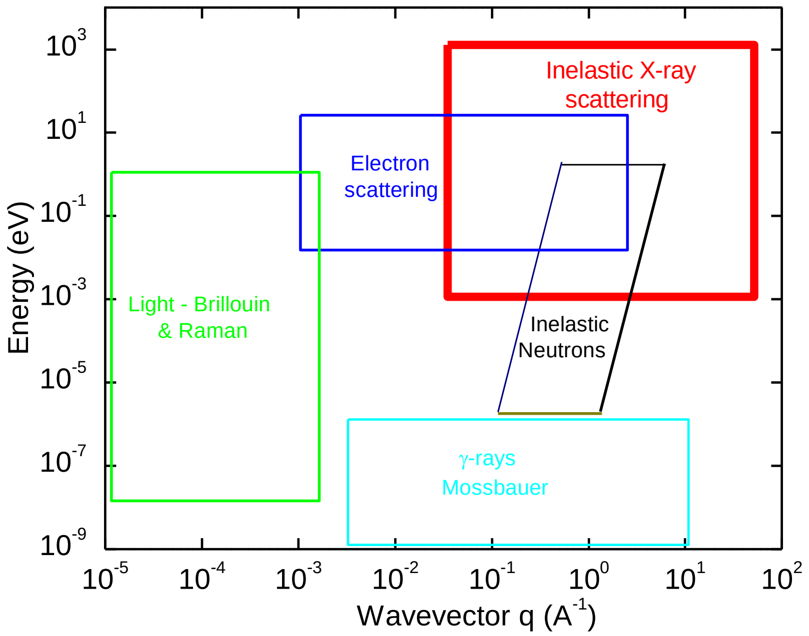

Figure 1: Energy and momentum space for different scattering techniques.

As Fig. 1 shows, IXS offers the ability to probe a variety of excitations at moderate energies and high momentum transfers *q* that cannot be studied with other techniques. For instance, light scattering with an energy of ~ 1 eV has a maximum momentum transfer of about 10^5/cm; this is much smaller than a typical Brillouin zone boundary which is ~10^8/cm. While neutrons can reach higher *q* values, they have only an extremely weak coupling to electronic excitations [4] and are therefore not ideal probes of these excitations. IXS is complementary to electron scattering; it probes the bulk, and thus is not sensitive to surface effects which are seen in electron scattering. IXS also allows studies of materials under a wide range of conditions (e.g., liquid and high pressure states) that are difficult to study with electron scattering. The ability to focus the x-ray beam to ~10 micron spot size allows the study of samples which are too small for techniques such as neutron scattering.

Since inelastic x-rays can probe a wide range of energy and momentum values it would seem that IXS should be a widely used probe. However, the scattered intensity is very weak, and it is only in the last decade with the use of third generation x-ray synchrotron sources and synchrotron insertion devices that there has been sufficient intensity to make these experiments viable. With these new sources, inelastic x-ray scattering has begun to attack a wide variety of problems in systems including liquids, liquid metals, glasses, polymers, high temperature superconductor parent compounds, and ladder compounds. [1-3] IXS has helped solved some long standing questions (e.g., fast sound in water [5]) and enabled new areas of study. All of the third generation x-ray synchrotron sources have multiple beam lines dedicated to IXS.

3.2.2 **Description of Inelastic X-ray Scattering**

The typical scattering event involves an incoming x-ray with a well-defined energy, momentum, and polarization, $(h\omega_i, \mathbf{k}_i, \boldsymbol{\varepsilon}_i)$ which scatters into a new state described by $(h\omega_f, \mathbf{k}_f, \boldsymbol{\varepsilon}_f)$. The energy loss of the x-ray photon is $\Delta E = h\omega_f - h\omega_i$, while the wavevector transfer is $\mathbf{q} = h\mathbf{k_f} - h\mathbf{k_i}$. The differential scattering cross section, to second order in perturbation theory for energies near a resonance is defined by the equation [6]

$$\frac{d^2\sigma}{d\omega_f d\Omega} \cong r_0^2 \left(\frac{\omega_f}{\omega_i} \right) \left| \left\langle f \left| e^{i\mathbf{q}\cdot\mathbf{r}} \right| i \right\rangle [\hat{\boldsymbol{\varepsilon}}_f \cdot \hat{\boldsymbol{\varepsilon}}_i] + \frac{1}{m} \sum_l \left[\frac{\left\langle f \middle| \hat{\boldsymbol{\varepsilon}}_f \cdot \mathbf{p} \middle| l \right\rangle \left\langle l \middle| \hat{\boldsymbol{\varepsilon}}_i \cdot \mathbf{p} \middle| i \right\rangle}{E_g - E_l + h\omega_i - i\Gamma_l} \right]^2 \right|^2 \tag{1}$$

where $r_0^2 = 7.95 \times 10^{-26}\ \mathrm{cm}^2$ is the Thompson cross section for an electron, i stands for the incident x-ray, f is the final x-ray, E_g is the ground state energy of the atom, l is the intermediate state , m is the mass of an electron and the summation is over intermediate states.

The second order term provides a negligible contribution unless the incident energy $h\omega_i$ is equal to the difference in energies of the ground state and one of the excited states E_l. In this case the denominator becomes small and the second order term becomes significant. This is called resonant x-ray scattering, and will be discussed in detail below. It is important since the scattering cross section is often greatly increased for this type of scattering.

For non-resonant scattering, the process is very weak, and can be analyzed using the first Born approximation. Non-relativistic x-rays (that is $E_i << 5\text{x}10^5$ eV) have a scattering cross section which can be related [7] to the dynamic structure factor $S(\mathbf{q},\omega)$

$$\frac{d^2\sigma}{d\omega d\Omega} = r_0^2 (\boldsymbol{\varepsilon}_f \cdot \boldsymbol{\varepsilon}_i) \frac{\omega_f}{\omega_i} S(\mathbf{q}, \omega) \tag{2}$$

The dynamic structure factor is related to the dielectric response function of the medium. The dynamic structure factor can be related to the imaginary part of the dielectric response function using the fluctuation dissipation theorem [8]

$$S(\mathbf{q}, \omega) = \frac{q^2}{4\pi^2 e^2} \frac{1}{e^{-\beta\omega} - 1} \mathrm{Im}\left[\varepsilon(\mathbf{q}, \omega)^{-1} \right] \tag{3}$$

Here β is $1/kT$ and e is the charge of an electron. Information about the real part of the dielectric function may also be determined using the Kramers-Kronig relationship, assuming that the data is accurate enough over a wide range of frequencies. Note in particular that the scattering cross section will show peaks where the real part of the response function becomes small.

3.2.2.1 ***Non- resonant IXS***

Unless the incident x-ray energy is near an absorption edge, non-resonant scattering dominates and IXS can be used to determine the dynamic structure factor shown in Eq. (3). For this case, IXS is in principle able to observe a wide variety of electronic excitations in the system. This scattering typically has small cross sections since the electrons of interest are usually valence electrons, which are only a small percentage of the total number of electrons except in materials with low atomic numbers. So often only low *Z* materials, for which large volumes can be studied, are suitable for study.

In addition to the ability to study electronic excitations, non-resonant inelastic x-ray scattering is widely used to measure phonon properties. The basic principle is the same as has been described above. In order to get the energy resolution needed (on the order of 1-2 meV) it is typical to use high order reflections of high quality crystals, which necessitates higher incident energies, on the order of 20 keV. Higher energy gives large penetration into the sample. Recently, however, another scheme that works at lower energies has been devised [9], which is currently being implemented at the Advanced Photon Source and at the National Synchrotron Light Source II. The higher energy resolution required for phonons reduces allowable x-ray bandwidth, and so the incident flux is much lower. However, since the phonons involve the motion of all the electrons (and not just the valence electrons) there is still a significant signal.

3.2.2.2 *Resonant Inelastic X-ray Scattering (RIXS)*

RIXS has become an important technique for studying the electronic excitations over the last decade or so. Resonant inelastic x-ray scattering (sometimes called x-ray resonant Raman scattering) occurs when the incident energy is tuned to the energy of an atomic transition (absorption edge). For our purposes, this will typically be the excitation of a core electron with an energy on the order of keV. The first measurements of this effect were carried out by Sparks [10], and Eisenburger, Platzman, and Winick [11]. Equation 1 shows that when the incident photon energy is equal to the energy difference between states, the second term can become large. In this case an electron is promoted from a core state to a state at or above the Fermi surface. The final excited state is therefore similar to the final state found in non-resonant scattering. However, the intermediate state involves the system with a core hole in it, and this hole interacts with the rest of the system through the coulomb interaction. These interactions can cause additional effects such as the excitation of electron-hole pairs (shakeup).

For resonant scattering, the simple relationship between the scattering cross section and the dynamic structure factor (Eq. 2) is no longer valid. As a result, the detailed explanation of these measurements is more complicated. However, there are many experimental advantages including the following:

1) Scattering intensities for inelastic events increase greatly for resonant scattering, often by one to two orders of magnitude. Since the weak scattering rate is the greatest disadvantage of inelastic x-ray scattering, resonant enhancement is a useful tool.
2) This technique can be used to determine whether the electronic transition is a dipole or quadrupolar transition.
3) The technique is element selective, that is one can study excitations involving one particular element in a crystal by choosing the appropriate atomic resonance.
4) Different intermediate states couple differently to different final states, allowing different excitations to be emphasized.
5) Magnons and their dispersion can be measured.

3.2.3 Advantages of an X-ray Free Electron Laser Oscillator (XFELO) Source

While IXS has become a useful technique for studies of electronic and vibrational states of matter, it remains a flux-limited technique. Typically, scans last for hours, and a complete characterization of a material at a given set of conditions (pressure, temperature, etc.) may take several days. A proposed XFELO source [12] would provide an enormous increase in scattering signal over current sources and therefore be of great benefit to the technique. We discuss the advantages of an XFELO source for medium and high resolution studies below.

3.2.3.1 *Medium Resolution Measurements*

Measurements of the electronic excitations are critical for understanding the properties of virtually all materials, and a wide variety of probes (Raman, optical absorption, EELS, photoemission, etc.) are used for this work. IXS is in principle an excellent probe of the electronic excitations as well, but is limited by low count rates and few available beamlines. A typical medium energy resolution IXS measurement will have a flux ~ 10^{12} photons/second, and an energy resolution of 100 meV. This lower resolution, compared to the phonon measurements, is used to increase the incident flux to compensate for the lower cross sections.

Electronic excitations of interest may have count rates of 0.25 counts per second or lower. Low count rates are often on top of a large background signal from elastic scattering, adding to the time required to take data. An XFELO IXS spectrometer with 10 meV resolution would provide an increase in resolution of a factor of 10, and also an increase in flux by a factor of ~500 over current instruments. These improvements would have a profound influence on studies of electronic excitations in condensed matter. An XFELO source would enable important studies including:

1) Rapid RIXS scans as a function of incident energy, scattered energy, and wavevector. Currently the large number of different variables makes RIXS measurements quite time consuming.
2) Studies of the evolution of electronic excitations as a function of pressure in small samples.
3) Studies of surface electronic excitations. Currently techniques to study such excitations require high vacuum, but IXS is capable of studies under liquid or ambient conditions.
4) Direct measurement of excitations across a superconducting gap. This would allow for determination of the nature of the superconductivity in many systems.
5) Non-resonant inelastic x-ray scattering on systems of interest. Currently, the signal rate for non-resonant IXS studies is small and measurements are only possible on low Z materials. With an XFELO source the electronic structure of many materials of interest in physics, biology, geology, and materials science would be observable. Most importantly, the scattering could easily be compared with theoretical models. Currently most work uses RIXS due to its higher count rate, but theoretical modeling is more difficult due to the effects of the intermediate state.

3.2.3.2 *High Resolution Measurements with an XFELO*

Phonon spectra from a sample will often take days for collection. Currently, most third generation sources operate at an energy resolution of ~1 meV with an incident flux of approximately 2 x 10^9 photons/second in the appropriate energy bandwidth. An XFELO would provide 10^9 photons per pulse, and a repetition rate of about 10 MHz. This is an improvement in incident flux by a factor of over 10^5. To put this in perspective, a series of measurements which required a day to measure could in principle be carried out in under a second. This would enable a large number of possible studies. First, small samples or samples that were rapidly changing in time could be studied. This opens up the possibility of studying the evolution of excitations in rapid phase transitions. Perhaps as importantly, it would be possible to further monochromatize the beam to allow for higher resolution studies. There are a large number of important scientific questions which require improved resolution. Some examples include the following:

1) Studies of the excitation of water in restricted geometries, which are important for many industrial and biological systems.
2) Studies of liquids at intermediate energy and momentum scales. Liquids are known to undergo a transition in their sound speeds from low to high as a function of momentum transfer, but it is difficult for current and planned sources to study this change.
3) Studies of the excitations in biological systems. There is great interest in the dynamics of biological systems, but such systems require improved resolution to study. For instance, studies of the excitations in DNA in solution [13] are of great interest, but the excitations are difficult to distinguish from the elastic background. Also, the enormous number of biological systems and the wide variety of conditions they exist in makes it important to be able to study the systems rapidly.
4) Studies of the surface phonons [14] offer the exciting possibility to access changes in vibrational modes under realistic conditions; currently, the surface probes such as He scattering require ultra-high vacuum. IXS is not limited to these conditions; however, a large improvement in signal rate is needed to make this a useful probe. Buried interfaces can also be studied in a similar fashion.

3.2.4 **Summary**

IXS is a valuable probe whose usefulness is mainly limited by current x-ray sources. An XFELO would allow a gain in resolution of a factor of 10 with a concurrent improvement in flux by a factor of ~ 500 for medium resolution studies. For high resolution work, the flux gain would be $\sim 10^5$. These improvements would turn a useful technique into one of the most powerful probes of condensed matter systems.

3.2.5 **References**

1. W. Schulke, *Electron Dynamics by Inelastic X-ray Scattering*, Oxford Series on Synchrotron Radiation 7, Oxford, New York, (2007).
2. Luuk J. P. Ament, Michel van Veenendaal, Thomas P. Devereaux, John P. Hill, Jeroen van den Brink, “Resonant inelastic x-ray scattering studies of elementary excitations”, Rev. Mod. Phys. 83, 705 (2011).
3. M. Krisch and F. Sette, “Inelastic X-Ray Scattering from Phonons”, in Light Scattering in Solids IX, Topics in Applied Physics 108, Springer-Verlag, Berlin, (2007).
4. W. Marshall and S. W. Lovesey, *Theory of Thermal Neutron Scattering*, Claredon Press (1971).
5. F. Sette, G. Ruocco, M. Krisch, U. Bergmann, C. Masciovecchio, V. Mazzacurati, G. Signorelli, and R. Verbeni, “Collective Dynamics in Water by High Energy Resolution Inelastic X-Ray Scattering”, Phys. Rev. Lett. 75, 850 (1995).

6. J. P. Rueff and A. Shukla, “Inelastic x-ray scattering by electronic excitations under high pressure”, Rev. Mod. Phys. 82, 847, (2010).
7. P. Nozières and D. Pines, *The Quantum Theory of Liquids,* W. A. Benjamin, New York (1966).
8. P. M. Platzman and P.A. Wolff, *Waves and Interactions in Solid State Plasmas*, Academic Press, New York (1973).
9. Yu. V. Shvyd’ko, M. Lerche, U. Kuetgens, H. D. Rüter, A. Alatas, and J. Zhao, “X-Ray Bragg Diffraction in Asymmetric Backscattering Geometry”, Phys. Rev. Lett. 97, 235502 (2006).
10. C. J. Sparks, “Inelastic Resonance Emission of X Rays: Anomalous Scattering Associated with Anomalous Dispersion”, Phys. Rev. Lett. 33, 262 (1972).
11. P. Eisenburger, P. M. Platzman, and H. Winick, “Resonant x-ray Raman scattering studies using synchrotron radiation”, *Phys. Rev. B* 13, 2377 (1976).
12. Kwang-Je Kim, Yuri Shvyd’ko, and Sven Reiche, “A Proposal for an X-Ray Free-Electron Laser Oscillator with an Energy-Recovery Linac”, Phys. Rev. Lett. 100, 244802 (2008).
13. M. Krisch, A. Mermet, H. Grimm, V. T. Forsyth, and A. Rupprecht “Phonon dispersion of oriented DNA by inelastic x-ray scattering”, Phys. Rev. E 73, 061909 (2006).
14. Murphy et al., “Phonon Modes at the 2H-NbSe$_2$ Surface Observed by Grazing Incidence Inelastic X-Ray Scattering”, Phys. Rev. Lett. 95**,** 256104 (2005).

3.3 Prospects for New Science Using X-ray Photon Correlation Spectroscopy at an XFELO

Laurence Lurio
Department of Physics, Northern Illinois University, DeKalb, IL 60115
Mail to: llurio@niu.edu

Coherent x-ray scattering provides information on equilibrium dynamics in condensed matter which is not normally available from scattering performed using an incoherent beam. Consider the x-ray scattering intensity, $I(\vec{Q})$, from a material of electron density $\rho_e(r)$ given by;

$$I(Q) \sim \iint e^{i\vec{Q}\cdot\vec{r}} \rho_e\left(\vec{r}+\vec{r}'\right)\rho_e\left(\vec{r}'\right) d\vec{r} d\vec{r}' . \tag{1}$$

Here $\vec{Q}=\vec{k}_{out}-\vec{k}_{in}$, with $\vec{k}$ the wavevector of the incoming or outgoing x-rays. In a scattering experiment with an incoherent beam, the intensity at the detector represents the sum over scattering from many incoherent regions within a sample. In this case it is appropriate to make the replacement in eq. (1) of

$$\rho_e\left(\vec{r}+\vec{r}'\right)\rho_e\left(\vec{r}'\right) \Rightarrow \left\langle \rho_e\left(\vec{r}+\vec{r}'\right)\rho_e\left(\vec{r}'\right)\right\rangle \equiv g\left(\vec{r}\right). \tag{2}$$

The x-ray scattering intensity can then be used to obtain the average spatial correlation function. This quantity does not change in equilibrium and thus it does not give any information about equilibrium dynamics. For the situation of coherent x-ray scattering, the replacement of the exact density distribution with the density correlation function $g(\vec{r})$ is no longer appropriate. In this case, the average scattering pattern is the same as the incoherent scattering, but a speckle pattern is superimposed on the scattering. The speckles result from coherent interference over the full extent of the sample. An example of speckle from a region of coherent scattering is given in Fig. 1.

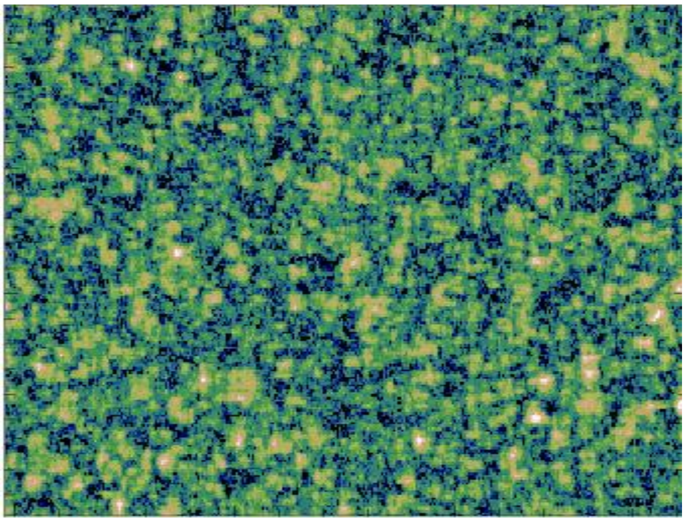

Figure 1: Speckle pattern resulting from the illumination of a silica aerogel by a coherent x-ray beam.

The speckle pattern produced using coherent x-rays provides information about the exact configuration of the density within the sample at a specific moment in time, rather than the average density distribution. The speckle pattern will fluctuate in time when the density distribution is changing in time,. Measurements of the rate of fluctuations of a speckle at a particular wavevector, $\vec{Q}$ gives information about the dynamics within the sample with the corresponding wavevector. This provides information on structural fluctuations of the density about its equilibrium configuration which can be difficult to obtain via other methods. It can also provide unique information about non-equilibrium systems, such as fluctuations about a quasi-equilibrium state. XPCS can yield information regarding a wide range of dynamics including diffusion, linear susceptibilities, the approach to equilibrium and glassy behaviour.

As an example of how a typical XPCS measurement is carried out, consider measurements of the dynamics of a colloidal suspension using XPCS (see for example Lurio *et. al.* [1]). Figure 2 shows a schematic of scattering from a suspension of particles undergoing diffusive motion. The scattering from each of these particles will interfere at the position of the detector with a relative phase depending on its position. As these particles move, their relative phases will change, and the intensity of the scattering pattern in the detector will fluctuate with time.

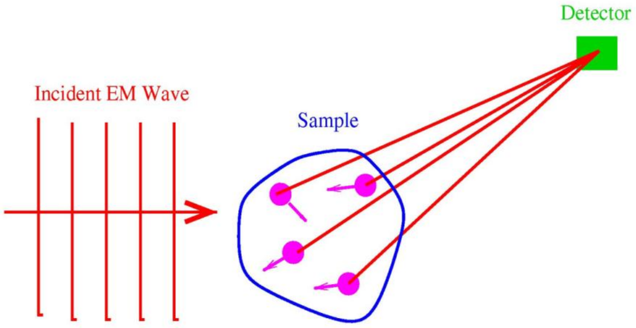

Figure 2. Schematic of scattering from a suspension of particles undergoing diffusive motion.

The normalized intensity-intensity correlation function at a given scattering vector, $\vec{Q}$, is defined by

$$g_2(\vec{Q},\tau) = \frac{\left\langle I(\vec{Q},t)I(\vec{Q},t+\tau)\right\rangle}{\left\langle I(\vec{Q},t)\right\rangle^2}. \tag{3}$$

Here, t is the time of the first intensity measurement and $t+\tau$ is the time of the second measurement. This correlation function can be related to the intermediate scattering function $f(\vec{Q},\tau)$ of the sample via:

$$g_2(\vec{Q},\tau) = 1+\beta\left[f(\vec{Q},\tau)\right]^2. \tag{4}$$

Here β is the contrast of the incident beam. The intermediate scattering function is defined by $f(\vec{Q},\tau) = S(\vec{Q},\tau)/S(\vec{Q},0)$, with

$$S(\vec{Q},\tau) = \frac{1}{\rho_e V}\int e^{i\vec{Q}\cdot(\vec{r}-\vec{r}')}\rho_e(\vec{r},0)\rho_e(\vec{r}',\tau)d^3\vec{r}d^3\vec{r}'. \tag{5}$$

For the case of Brownian motion in a dilute suspension, the intermediate scattering function takes the particularly simple form

$$f(q,t) = \mathrm{e}^{-\tau DQ^2}. \tag{6}$$

Here $D = k_B T/6\pi\eta R$ is the diffusion constant of the particles, with η the viscosity, R the particle radius, T the temperature and k_B Boltzmann's constant. Measured data for 72 nm Latex spheres in glycerol at -25C as a function of wavevector are shown in figure 3. Figure 4 shows the decay rate of the correlation function vs. wavevector. The exponential form of the decay functions and the Q^2 dependence of the relaxation times both indicate that the measured XPCS follows the theory of Brownian motion quite accurately.

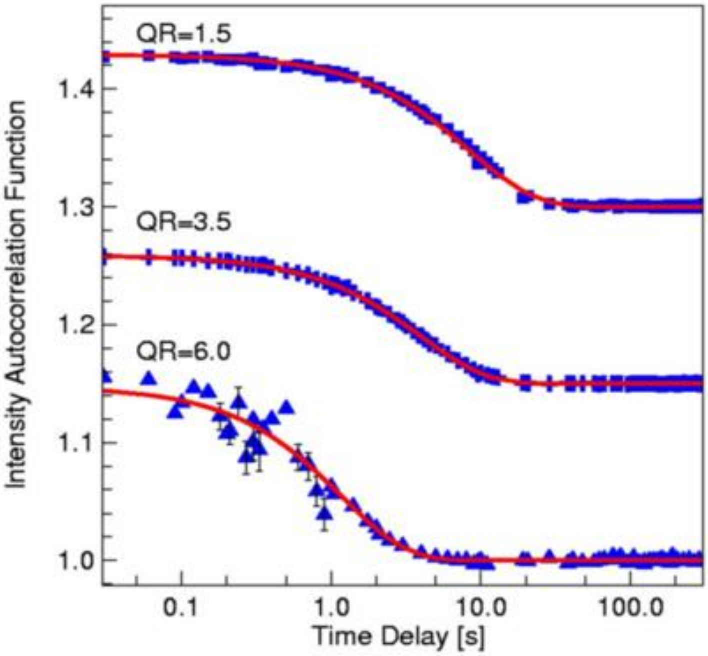

Figure 3. Intensity correlation functions g_2 as a function of wavevector for particles of radius R .

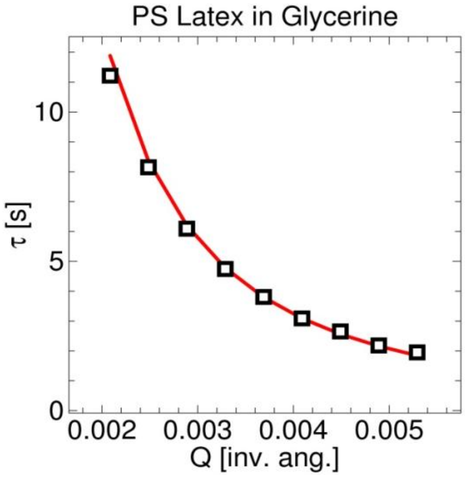

Figure 4. Measured relaxation time obtained from exponential fits to the $g_2(Q,\tau)$ as a function of Q using eq. (6).

A summary of various techniques for measuring dynamics in condensed matter physics has been made by Dierker [2] and later updated by Brian Stephenson *et. al.* [3] and G. Grübel *et. al.* [4]. XPCS at third generation synchrotron sources is unique in its ability to measure dynamics at length scales smaller than can be accessed with visible light and time scales longer than can be resolved with neutron scattering or inelastic x-ray scattering. Some representative examples of XPCS experiments are given below. In the small wavevector regime Gutt *et. al.* [5] obtained microsecond dynamics from capillary waves at $Q \sim 10^{-4}\text{nm}^{-1}$. In the large wavevector regime, atomic scale dynamics were measured by Leitner *et. al.* [6] in CuAu alloys. However, due to the weaker scattering at larger wavevectors, the measured time scales were in the range of hours. At intermediate scales, colloidal dynamics have been measured at millisecond dynamics in the range of $Q \sim 0.01\,\mathrm{nm}^{-1}$[7] to $Q \sim 0.1\,\mathrm{nm}^{-1}$[8]. It has not been possible, however, with third generation sources to simultaneously look at the interesting regime of short times and small length scales so as to obtain overlap with techniques such as inelastic x-ray scattering or neutron spin echo.

Studies of potential science at recent SASE free electron laser sources [3] have indicated that with the increase in instantaneous brightness achievable at these sources, XPCS should be able to measure dynamics into the pico-second regime and thus overlap with inelastic x-ray scattering and neutron spin echo measurements. This opens up a wide range of new science studies such as measurements of atomic diffusion, dynamics of polymers in the Rausse regime, dynamics of biomaterials in water, glassy dynamics at the atomic scale, dynamic critical behaviour, dynamics of liquid surfaces at short wavevectors and dynamics of magnetic materials. Using heterodyne techniques it is also possible to measure velocity fields in materials [9]. Thus XPCS at XFEL's and XFELO's can provide an important window on nanofluidics.

An XFELO source would have several distinct advantages over current third generation sources for performing traditional XPCS measurements. The beam will be fully coherent in the transverse direction. This yields the maximum possible contrast and also the least sample damage. Current designs for XFELO's anticipate a coherent flux of order $\phi \approx 10^{15}$ photons/s as compared with current values of $\phi \approx 10^{9}$ photons/s. This increase in coherent flux will increase the range of length scales and time scales which can be studied. While the average brightness of an XFELO is comparable to that of current XFELs the megahertz timing of the pulse structure allows measurements of dynamics in the microsecond to millisecond time ranges.

Consider the dynamics of colloidal particles diffusing through a fluid. For spherical particles of radius R the scattering cross section goes as the square of the volume; $\sigma \sim R^{6}$. For constant volume fraction of particles, the number of scatterers scales as $N \sim R^{-3}$ and thus the total cross section will go as $\sigma \sim R^{3}$. The relevant time scale for dynamics is the time required for a particle to diffuse over its own radius, which for Brownian motion scales as $\tau \sim 1/R$. The signal to noise ratio (SNR) is given by [10]

$$SNR \sim \phi \tau^{1/2} \sigma \sim \phi R^{-3.5} \qquad (7)$$

Hence the length scales accessible with XPCS should scale roughly as

$$R_{min} \sim \phi^{-0.29} \qquad (8)$$

An increase of 10^{6} in flux should allow a decrease of the smallest measurable particle by a factor of 60, assuming all other conditions are comparable. Thus, for example, current studies of millisecond dynamics of 100 nm particles in glycerol could be extended to microsecond dynamics of 2 nm particles. This would allow study of the anomalous thermal conductivity recently found in nanofluid suspensions by Eastman and collaborators [11].

One may also want to look at faster dynamics without changing the particle size. For example, it would be useful to extend current studies of diffusion of colloidal suspensions in glycerol to diffusion of similar size proteins in aqueous suspension. The change from glycerol to water would yield a consequent decrease in viscosity of a factor of 10^{4}. This measurement would require an increase in flux of only a factor of 100, and should be easily feasible for an XFELO source. For identical values of wavevector and scattering cross section, dynamics should be measurable at a factor of 10^{12} times faster than currently possible. Dynamics at very fast times are, however, ultimately limited to the picosecond regime due to the pulse structure of the source and also limited by the availability of fast area detectors; currently limited to ms time scales.

The longitudinal coherence of XFELO's is considerably enhanced relative to that from current third generation sources. The longitudinal coherence length is defined by the energy bandwidth of the source as

$$\Lambda \approx \lambda(E/\Delta E)\,. \qquad (9)$$

Here E is the energy and ΔE the bandwidth. The longitudinal coherence length of current 3rd generation undulators is proportional to the number of periods in the undulator, $E/\Delta E \approx N$. For a typical APS undulator $N = 72$ yielding $\Lambda \approx 10$ nm. For small angle scattering these short coherence lengths can be acceptable. The longitudinal coherence length can also be increased by using a monochromater. Si-111 gives $\Lambda \sim 1\mu\text{m}$. For an XFELO $E/\Delta E \approx 10^7$ yielding longitudinal coherence lengths on the scale of millimeters. The longer coherence length of XFELO's implies that much thicker samples can be used even in the wide angle scattering regime. Furthermore, heterodyne measurements, in which the scattering from a sample is mixed with a reference signal, would become much easier, since the source of the reference signal must be held within the longitudinal coherence length of the sample.

Even if there is sufficient x-ray flux to measure sample dynamics with XPCS it may not be possible to measure samples if the damage from the x-ray beam destroys the sample during the measurement. Current XPCS measurements are close to the threshold of damage so it is a serious concern whether the higher fluxes available at an XFELO would make measurements impossible. The relevant quantity to consider when evaluating damage is what is the minimum x-ray exposure required for a specified value of the signal to noise ratio (SNR). Consider a sample which has a correlation time T_{corr}. The intensity measured within this time will add coherently, while integration over times longer than T_{corr} will only decrease the noise in quadrature. Thus we expect for a measurement of total time T_{meas} that

$$SNR \sim \phi\sqrt{T_{meas}T_{corr}} \qquad (10)$$

The damage, D, on the other hand, will scale as D~ ϕT_{meas}. This implies that if one tries to make up the SNR for shorter correlation times by measuring longer, then sample damage will be a limiting factor. The sample damage can be significantly reduced, however, by moving the sample to fresh spots during the measurement. The rate at which the sample can be moved is limited by the condition that the exposure time for any given spot must be longer than the expected correlation time, T_{corr}. If we move the sample to a fresh spot on a time scale roughly of order T_{corr} then the damage at each spot is given by D~ ϕT_{corr} and thus, the faster the dynamics of the sample, the less the damage from x-rays. This conclusion relies on the availability of a large sample so that many fresh spots can be exposed. The experimental station must also be equipped with a sample translator that can reposition a sample on microsecond time scales.

Furthermore, this analysis assumes, that sample damage is due to ionization and does not consider thermal loading.

In the traditional mode of performing XPCS the scattering pattern is read out as a function of time, which requires a fast detector. An alternative to performing XPCS from a sequence of individual intensity measurements is to use a split pulse scattering method. In this scheme, a short pulse is split using crystal optics into two pulses with a time delay set by an optical path length difference. These two pulse each scatter from the sample yielding speckle patterns which are simultaneously recorded on an area detector. If the sample configuration has not significantly changed during the interval, then the two speckle patterns will add together and the net contrast will be equal to the contrast obtained for each speckle pattern alone. If, however, the sample moves within this interval the speckle patterns will differ and the net contrast of the resulting sum will be lower. Thus, by measuring the contrast of the speckle pattern as a function of time delay, one can obtain the correlation function for dynamics faster than the detector can be read. The largest time delay that can be measured in this scheme is set by the largest path length difference that can be practically obtained in the beam splitter. To give a sense of scale, a $L = 3\text{mm}$ path length difference corresponds to a time delay of $\Delta T = L / c = 10$ ps.

As has been noted by Stephenson *et. al.* [3] and Grübel *et. al.* [4] a significant limitation to this beam splitting method is the need to have sufficient flux in a single pulse to create a measurable speckle while at the same time not having so much flux within a single pulse so as to destroy the sample by overheating it. The required flux per pulse depends on the atomic number of the sample, Z, and on the number of atoms scattering coherently, M_{corr}. They find, for example, that for XFEL values of 10^{15} photons/cm^2/pulse, and at energy of 8 keV, there is sufficient flux to measure samples down to values of $M_{corr} \sim 10$. For a XFELO, the expected pulse intensity is three orders of magnitude less. However, since the increased longitudinal coherence length makes a monochromator unnecessary, the effective flux delivered to the sample is only a factor of 100 less. In this case the, XFELO cannot measure down to as small as $M_{corr} \sim 10$, but would be able to measure dynamics from larger scattering regions of size $M_{corr} \sim 1000$. However, sample heating sets limits on the maximum intensity per pulse that can be delivered. Under the assumptions used in the studies of Stephenson *et. al.* it would only be possible to employ the greater flux available at XFEL's, as opposed to an XFELO, for atomic number less than around 16. Thus the advantage of XFEL's over an XFELO would only be realized for relatively low Z materials.

The analyses used by Stephenson *et. al.* and Grübel *et. al.* assume that only a single pulse with be used for a measurement. In fact, as long as the sample can be moved between pulses in order to expose a fresh spot, it should be possible to average a large number of measurements together from different pulses. Assuming, for example, that one were willing to expend 100s total integration time on a measurement, and that the pulse repetition rate was 1MHz, the signal to noise ratio could be increased by a factor of 10^4.

There are, as discussed above, a wide range of measurements, which would become possible if a XFELO were available. Here we discuss one putative experiment as an example of the kinds of new physics which could be studied. Studies of colloidal diffusion of systems such as Latex in Glycerol [1] have formed one set of important results from third generation based XPCS studies. It would be extremely useful to extend such measurements to the biological regime, which would allow measurements of the diffusion of proteins through aqueous suspension. One biologically relevant colloidal system is the lens of the eye, which contains a mixture of three types of proteins called crystallins. The concentrations of these proteins within the eye lens are close to those at which the proteins undergo a liquid-glass transition in their dynamics.

XPCS studies of dynamics of eye-lens crystallins could provide information on the viscoelastic properties of the lens and on the causes of presbyopia, a disease which leads to a stiffening of the lens with age. Previous dynamic light scattering results by Giannopoulou et. al. [12] were able to measure the dynamics of this system for a range of protein concentrations spanning the glass transition. However, light scattering is not able to probe dynamics at length scales corresponding to the inter-protein spacing, and thus cannot explore the microscopic origins of the glass transition in these systems. Current XPCS measurements at sector 8 of the Advanced Photon Source have probed the dynamics in the glassy phase [8], but the intensity of current sources is not sufficient to explore dynamics in the fluid phase. An XFELO would provide sufficient flux to measure the dynamics of this system through the glass transition and thus provide important insight on the microscopic origins of the glass transition.

Finally, we consider some of the requirements for an XPCS beamline which would be located at an XFELO.

1) **Energy.** There are two important considerations. First the energy must be high enough to permit diffraction at atomic length scales. However, broad range tunability is not generally required. The other major consideration for the energy of the beamline is x-ray damage and heating. As one goes to higher energies, the x-ray absorption decreases as E^{-3} up until the point where Compton scattering becomes more important energy loss mechanism. One problem with going to too high an energy, however, is the difficulty in stopping the x-ray beam in a detector. Thus, one needs to make a compromise between detector efficiency and sample absorption. Based on experience with current detectors, XFELO energy of around 17 keV would be a good compromise, between absorption, Compton scattering and detector efficiency. This would also allow comparison of scattering results with the Mo tube line at 17.4 keV.
2) **Optics**. The beamline optics must preserve the coherence of the beam. This mandates that beamline should have the minimum amount of optical elements. However, focusing optics will probably be necessary in order to shape the coherence area of the beam and in order to optimize the speckle size in the detector. Those elements which are required should be either highly polished (if used in reflection) or of extremely uniform density at the microscale if used in transmission.
3) **Mechanical stability**. XPCS measurements will be extremely sensitive to vibrations over time scales and length scales comparable to those expected for the sample motion. Thus a highly stable vibration free experimental platform is essential.
4) **Single pulse optics**. If single pulse speckle measurements are to be performed then it will be necessary to design a beam splitter with a variable delay path.
5) **X-ray camera with microsecond readout**. In order to measure pulse-to-pulse correlation functions it will be necessary to capture scattering images with a time resolution comparable to the pulse spacing.

In conclusion, an x-ray free electron laser oscillator would have many properties which would benefit x-ray photon correlation spectroscopy. These include complete transverse coherence, extremely long longitudinal coherence, high average intensity and very short pulse structure. XPCS measurements could take advantage of the three orders of magnitude increase in average coherent flux, allowing access to a wide range of new systems. In particular, it may become possible to study biological dynamics in aqueous suspension. The pulse structure could be used to measure dynamics on the picosecond scale. Finally, in order to take advantage of such a source, new beamlines would have to be designed which could perform sample measurements at the microsecond time scales.

I would like to thank Brian Stephenson and Alec Sandy for helpful discussions and Janae DeBartolo for the use of some figures from her Master's thesis. [13]

References

1. L. B. Lurio, et al., Phys. Rev. Lett. **84**, 785 (2000).
2. S. Dierker, **July** (1995).
3. B. Stephenson, S. Mochrie, M. Sutton, K. Nelson, F. Sette, G. Ruocco, S. Dierker, S. Sinha, and D. Schneider, in *LCLS The First Experiments*, edited by S. L. A. Center (Stanford University, Stanford, 2000).
4. G. Grübel, G. B. Stephenson, C. Gutt, H. Sinn, and T. Tschentscher, NIM **262**, 357 (2007).
5. C. Gutt, T. Ghaderi, V. Chamard, A. Madsen, T. Seydel, M. Tolan, M. Sprung, G. Grübel, and S. K. Sinha, Phys. Rev. Lett. **91**, 076104 (2003).
6. M. Leitner, B. Sepiol, L.-M. Stadler, B. Pfau, and G. Vogl, Nature Materials **8**, 717 (2009).
7. G. Grübel, A. Robert, D. L. Abernathy, In, (eds.), E. T. U. International, and Symposium, in *Eighth Tohwa University International Symposium*, edited by M. Tokuyama and I. Oppenheim, 1999), p. 158.
8. J. Debartolo, N. Karunaratne, J. Berry, C. DeCaro, L. Lurio, and G. Thurston.
9. S. Busch, T. H. Jensen, Chushkin, and A. Fluerasu, Eur. Phys. J. E **26**, 55 (2008).
10. [1]P. Falus, L. B. Lurio, and S. G. J. Mochrie, J. Synch. Rad. **13**, 253 (2006).
11. J. A. Eastman, S. U. S. Choi, W. Y. S. Li, J.L. Thompson, Appl. Phys. Lett., **78**, 718 (2001).
12. A. Giannopoulou, A. J. Aletras, N. Pharmakakis, G. N. Papatheodorou, and S. N. Yannopoulos, Journal of Chemical Physics **127** (2007).
13. J. Debartolo, Northern Illinois University, 2010.

3.4 Opportunities for a Free Electron Laser Oscillator in Nanomaterial Phonon Characterization and Complex Oxide Dynamics

Paul G. Evans
Materials Science and Engineering
University of Wisconsin-Madison, Madison, WI 53706, USA
Mail to: evans@engr.wisc.edu

3.4.1 **Introduction**

The development of a transform-limited hard x-ray free electron laser will create a large number of opportunities in the materials science and condensed matter physics of emerging electronic materials. The key characteristics of such a source are a narrow energy bandwidth, on the order of 1 meV or less, and short-duration high-repetition-rate pulses with excellent shot-to-shot reproducibility.[1] The pressing need for new characterization techniques can be illustrated using two specific problems: (i) the challenge of characterizing the dispersion of phonons across the entire Brillouin zone in nanomaterials and (ii) the problem of characterizing the dynamics of complex oxides in large non-equilibrium electric fields. The unique features of an x-ray free-electron laser oscillator will allow recent theoretical developments in both of these areas to be connected with experiments for the first time.

3.4.2 **Nanomaterial Phonon Characterization**

Using size effects and heterogeneous interfaces to manipulate the dispersion of phonons in nanostructures allows separate control of vibrational and electronic degrees of freedom in thermoelectric and high-temperature nanomaterials. [2-4] The novel mechanical and thermal properties arising from the small size of nanostructures are fundamentally different from the properties of bulk materials of the same composition. The potential to engineer the thermal properties of nanostructures is only beginning to be explored because the appropriate experimental probes for atomic-scale vibrational phenomena in nanomaterials do not yet exist.

Among the parameters that can be used to manipulate the thermal properties of nanostructures are boundary conditions, size-dependent force constants, scattering rates, surface and interface roughness, surface atom effects, and electron-phonon coupling. [2] Despite the importance of these effects, their roles in defining large-scale properties are relatively poorly known. Simulations, for example, are based on mechanical analyses or molecular dynamics simulations using bulk elastic constants or empirical potentials – without experimental evidence that these can be used at the nanoscale. [5,6] The effects of individual parameters are difficult to disentangle because lumped materials properties such as the thermal conductivity depend on all of them simultaneously. X-ray scattering techniques enabled by a transform-limited x-ray laser will allow researchers to isolate specific effects associated with phonon confinement. Hard x-ray scattering is an ideal way to probe phonons because hard x-rays couple directly to the positions of core electrons via diffraction, and via elastic or inelastic scattering.

The most important nanomaterials for thermoelectric devices are based on inorganic semiconductors. Si nanowires, for example, promise to have lower thermal conductivity than bulk Si, which in turn raises the figure of merit ZT of thermoelectric devices. [2,7] In a broader sense, Si nanostructures exhibit effects pertinent to other nanomaterials in which phonon-mediated thermal transport effects are important, including ceramics and semiconductors such as ZnO and III-V compounds. Effects linked to phonon confinement in such systems are predicted to reduce the thermal conductivity of composite materials for thermal barrier applications. [8]

The range of phonon frequencies and wavevectors relevant to the development of optimized thermal properties is defined by the fundamental phenomena of thermal conduction. As in bulk insulators and semiconductors, the thermal conduction at modest temperatures in non-metallic nanomaterials is mediated by acoustic phonons with low frequencies. [9,10] In addition to the low-energy modes relevant to transport in bulk materials, recent calculations suggest that higher frequency modes may also be important in nanowires as a result of increased boundary scattering of long-wavelength modes. [11] The discreteness arising from confinement modifies both the phonon dispersion and transport phenomena. In extremely small wires, quantized thermal conductance can limit the conductance of wires to a value proportional to the number of available phonon modes. [12] The relevant acoustic vibrational modes have been difficult to probe with traditional scattering, spectroscopy, and mechanical techniques.

It is possible to probe the vibrational properties of *bulk* materials via two different x-ray scattering techniques: thermal diffuse scattering (TDS) and inelastic x-ray scattering (IXS). Both allow the phonon dispersion to be determined quantitatively across the entire Brillouin zone. Recent advances in synchrotron x-ray optics and experimental facilities now allow TDS to probe nanostructures using tightly focused x-ray beams. [13] But the future of this approach at storage-ring-based synchrotron radiation sources may likely be limited by the indirect way that phonon energies must be deduced in TDS experiments, and the marginal flux provided these facilities.

Inelastic x-ray scattering experiments are even more limited by the flux provided by storage-ring based sources. The quantitative interpretation of IXS experiments is far more straightforward than TDS measurements. For bulk diamond-structured semiconductors, for example diamond, [14] IXS has yielded quantitatively reliable results for over a decade, but requires samples with volumes of ~10 μm^3 or more. It has proven difficult to extend IXS techniques beyond this scale because synchrotron sources provide insufficient flux in the sub-1 meV bandwidth required to capture the phonon phenomena illustrated in Figure 1. Radiation from the x-ray free-electron laser oscillator will be essentially completely monochromatic in this bandwidth regime and will thus allow experiments to proceed with far smaller sample volumes, commensurate with the volume of nanowires and other structures can realistically be produced using lithography. The high monochromatic flux of an x-ray free-electron laser oscillator will place it in a unique part of parameter space and allow revolutionary probes of the vibrational properties of nanomaterials.

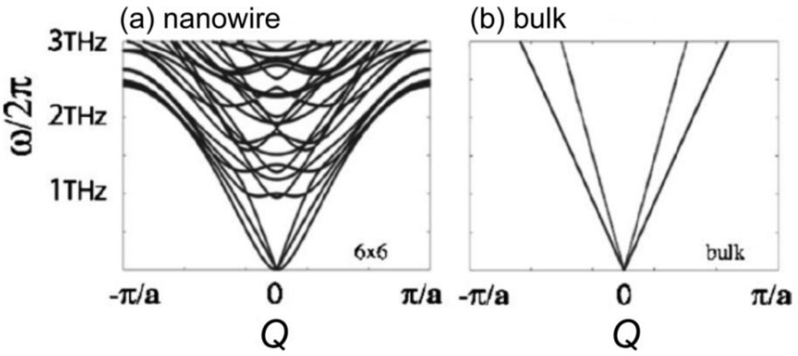

Figure 1: Phonon dispersions calculated by Becker *et al*. [6] for (a) a Si nanowire with a square cross section measuring 6 atoms along the edge bulk Si and (b) bulk Si. For reference, 1 meV is equivalent to a frequency of approximately 4 THz.

3.4.3 **Dynamics in Complex Oxides**

Recent developments in x-ray optics, scattering techniques, and epitaxial growth now make it possible to understand the properties of complex oxide insulators in regimes for which there have previously been no experimental tools. Fundamentally, studies of complex oxides under in high electric fields and at short times address the challenge of understanding the functional properties of materials at the atomic scale in highly non-equilibrium environments. [15] Recent results have shown, for example, that a very large strain of more than 2%, an extremely large elastic distortion, can be developed in ferroelectrics in response to applied electric fields. [16] First-principles predictions are now appearing in the literatures that are not testable using other techniques. [17,18] The responses of complex oxides to applied fields involve significant changes in structure that range from transitions of the crystallographic or magnetic phase, as in multiferroics, [19] to the motion of magnetic or ferroelectric domain walls. [20,21] The structural distortion associated with response to applied fields makes x-ray scattering probes an excellent match for problems in this field. In addition, complex oxides provide the ideal model systems for the development of new x-ray scattering techniques applicable to other materials. Continuous and reversible control of the properties of complex oxides has been demonstrated in only a few instances. For example, the large carrier concentrations induced by a gate electric field can lead to electronic or structural phase transitions, but this approach can be applied only to materials integrated into field-effect transistors. [22] Alternatively, the biaxial strain in epitaxial thin films grown on a piezoelectric substrate can be continuously varied by distorting the substrate, but the magnitude of the variation in strain that can be induced by the bulk substrate is typically limited to on the order of 0.1%. [23-25]

The results of structural studies of complex oxides can be compared directly with predictions emerging from first-principles theoeretical studies. The precision with which first-principles theory can be applied to the non-equilibrium properties of complex oxides is rapidly improving thanks to of recently discovered methods for working with electrically polarized materials in density function theory (DFT) calculations. [26,27] There has recently been a series of very rapid developments in first-principles theory techniques that allow the properties of materials in large electric fields to be studied using DFT. [18,28] These discoveries have resulted in the capability to perform simulations under mechanical and electrical boundary conditions that account for the stresses present in epitaxial thin films. [29]

The present synchrotron-based approach to the use of x-ray scattering to probe the dynamics of complex oxides is shown in Figure 2(a). The top electrode used to apply an electric field across a planar thin film absorbs a negligible fraction of the intensity of the incident and diffracted beams at the hard x-ray photon energies of 8-12 keV used in these diffraction experiments. Extensive studies of the fundamental properties of ferroelectric thin films have been based on the use of electric fields provided by thin film capacitors. [30-32] For example, the shift in the diffraction pattern of a $BiFeO_3$ thin film during a 12 ns electric field pulse, measured using this technique, in Figure 2(b), allows the piezoelectric properties to be readily determined. [33]

X-ray free-electron laser oscillators promise to provide the picosecond-duration pulses and total flux necessary to extend scattering techniques to the fundamental timescales of piezoelectricity and structural phase transitions. The combination of a high repetition rate, excellent pulse-to-pulse stability, and monochromaticity will allow diffraction and scattering experiments to be conducted on complex oxides driven in to non-equilibrium states and will fundamentally address the challenge of connecting theoretical developments with experiments.

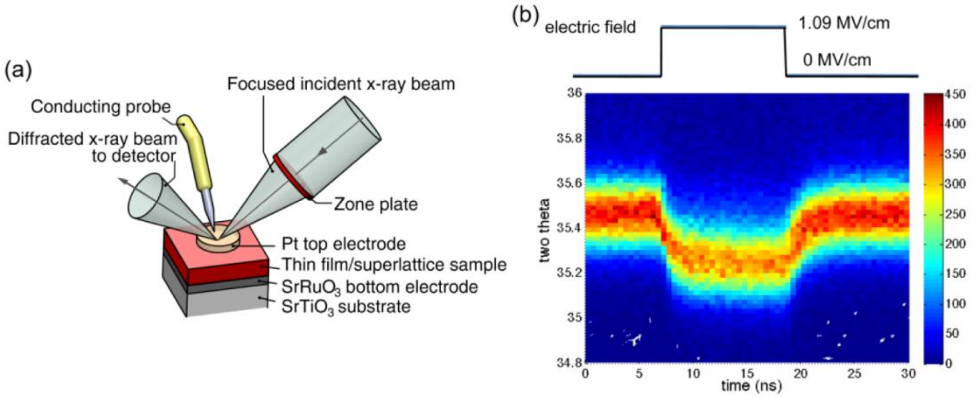

Figure 2: (a) An in situ x-ray microdiffraction probe for complex oxide capacitors. (b) Time-resolved diffraction from an epitaxial $BiFeO_3$ thin film, acquired with photon energy 10 keV. The 2θ angle of the $BiFeO_3$ thin film is decreased by piezoelectric electric expansion during the 12 ns electric field pulse, from P. Chen, *et al.*, [33].

3.4.4 References

1. "*Science Opportunities with an X-ray Free Electron Laser Oscillator*," available at http://www.aps.anl.gov/Users/Meeting/2010/Workshops/wk4_xfelo.php.
2. A. I. Boukai, Y. Bunimovich, J. Tahir-Kheli, J.-K. Yu, W. A. Goddard, and J. R. Heath, "*Silicon nanowires as efficient thermoelectric materials*," Nature **451**, 168 (2008).
3. D. G. Cahill, *et al*., "*Nanoscale thermal transport*," J. Appl. Phys. **93**, 794 (2003).
4. A. I. Hochbaum, R. Chen, R. Diaz Delgado, W. Liang, E. C. Garnett, M. Najarian, A. Majumdar, and P. Yang, "*Enhanced thermoelectric performance of rough silicon nanowires*," Nature **451**, 163 (2008).
5. T. Thonhauser and G. D. Mahan, "*Phonon modes in Si [111] nanowires*," Phys. Rev. B **69**, 075213 (2004).
6. B. Becker, P. K. Schelling, and S. R. Phillpot, "*Interfacial phonon scattering in semiconductor nanowires by molecular-dynamics simulation*," J. Appl. Phys. **99**,

123715 (2006).

7. L. D. Hicks and M. S. Dresselhaus, "*Thermoelectric Figure of Merit of a One-Dimensional Conductor*," Phys. Rev. B **47**, 16631 (1993).
8. P. G. Klemens and M. Gell, "*Thermal conductivity of thermal barrier coatings*," Mat. Sci. and Eng. A **245**, 143 (1998).
9. D. A. Broido, M. Malorny, G. Birner, N. Mingo, and D. A. Stewart, "*Intrinsic lattice thermal conductivity of semiconductors from first principles*," Appl. Phys. Lett. **91**, 231992 (2007).
10. J. Callaway, "*Model for Lattice Thermal Conductivity at Low Temperatures*," Phys. Rev. **113**, 1046 (1959).
11. N. Mingo, "*Calculation of Si nanowire thermal conductivity using complete phonon dispersion relations*," Phys. Rev. B **68**, 113308 (2003).
12. K. Schwab, J. L. Arlett, J. M. Worlock, and M. L. Roukes, "*Thermal conductance through discrete quantum channels*," Physica E **9**, 60 (2001).
13. G. Gopalakrishnan, M. V. Holt, K. M. McElhinny, J. W. Spalenka, D. A. Czaplewski, T. U. Schülli, and P. G. Evans, "*Thermal Diffuse Scattering as a Probe of Large-Wavevector Phonons in Silicon Nanostructures*," submitted (2013).
14. M. Schwoerer-Böhning, A. T. Macrander, and D. A. Arms, "*Phonon Dispersion of Diamond Measured by Inelastic X-Ray Scattering*," Phys. Rev. Lett. **80**, 5572 (1998).
15. "*Basic Energy Sciences Advisory Committee (BESAC) Grand Challenges Report, Directing Matter and Energy: Five Challenges for Science and the Imagination,*" available at http://www.er.doe.gov/bes/reports/files/GC_rpt.pdf (2007).
16. A. Grigoriev, R. Sichel, H. N. Lee, E. C. Landahl, B. W. Adams, E. M. Dufresne, and P. G. Evans, "*Nonlinear piezoelectricity in epitaxial ferroelectrics at high electric fields,*" Phys. Rev. Lett. **100**, 027604 (2008).
17. N. A. Spaldin and M. Fiebig, *"The renaissance of magnetoelectric multiferroics,"* Science **309**, 391 (2005).
18. N. Sai, K. M. Rabe, and D. Vanderbilt, "*Theory of structural response to macroscopic electric fields in ferroelectric systems,*" Phys. Rev. B **66**, 104108 (2002).
19. R. J. Zeches, M. D. Rossell, J. X. Zhang, A. J. Hatt, Q. He, C. H. Yang, A. Kumar, C. H. Wang, A. Melville, C. Adamo, G. Sheng, Y. H. Chu, J. F. Ihlefeld, R. Erni, C. Ederer, V. Gopalan, L. Q. Chen, D. G. Schlom, N. A. Spaldin, L. W. Martin, and R. Ramesh, "*A Strain-Driven Morphotropic Phase Boundary in* $BiFeO_3$," Science **326**, 977 (2009).
20. V. Chembrolu, J. P. Strachan, X. W. Yu, A. A. Tulapurkar, T. Tyliszczak, J. A. Katine, M. J. Carey, J. Stohr, and Y. Acremann, "*Time-resolved x-ray imaging of magnetization dynamics in spin-transfer torque devices*," Phys. Rev. B **80**, 024417 (2009).
21. A. Grigoriev, D.-H. Do, D. M. Kim, C. B. Eom, B. W. Adams, E. M. Dufresne, and P. G. Evans, "*Nanosecond domain wall dynamics in ferroelectric* $Pb(Zr,Ti)O_3$ *thin films*," Phys. Rev. Lett. **96**, 187601 (2006).
22. C. H. Ahn, A. Bhattacharya, M. Di Ventra, J. N. Eckstein, C. D. Frisbie, M. E. Gershenson, A. M. Goldman, I. H. Inoue, J. Mannhart, A. J. Millis, A. F. Morpurgo, D. Natelson, and J. M. Triscone, "*Electrostatic modification of novel materials*," Rev. Mod. Phys. **78**, 1185 (2006).
23. A. Herklotz, A. D. Rata, L. Schultz, and K. Dorr, "*Reversible strain effect on the magnetization of* $LaCoO_3$ *films*," Phys. Rev. B **79**, 092409 (2009).
24. C. Thiele, K. Dorr, O. Bilani, J. Rodel, and L. Schultz, "*Influence of strain on the magnetization and magnetoelectric effect in* $La_{0.7}A_{0.3}MnO_3$ */ PMN-PT(001) (A=Sr,Ca)*," Phys. Rev. B **75**, 054408 (2007).
25. A. A. Levin, T. Weissbach, A. I. Pommrich, O. Bilani-Zeneli, and D. C. Meyer, "*In situ X-ray investigation of lattice strain in* $SrTiO_3/La_{0.7}Sr_{0.3}MnO_3$ *thin films induced by piezoelectric* ${}_{0.72}Pb(Mg_{1/3}Nb_{2/3})O_3$ - ${}_{0.28}PbTiO_3$ *substrate in an external electric field*," Appl. Phys. A **96**, 575 (2009).
26. I. Souza, J. Iniguez, and D. Vanderbilt, "*First-principles approach to insulators in finite*

electric fields," Phys. Rev. Lett. **89**, 117602 (2002).

27. M. Stengel, N. A. Spaldin, and D. Vanderbilt, "*Electric displacement as the fundamental variable in electronic-structure calculations*," Nat. Phys. **5**, 304 (2009).
28. K. M. Rabe and P. Ghosez, in *Physics of Ferroelectrics: a Modern Perspective* (2007), Vol. 105, p. 117.
29. A. Roy, M. Stengel, and D. Vanderbilt, "*First-principles study of high-field piezoelectricity in tetragonal* $PbTiO_3$," Phys. Rev. B **81**, 014102 (2010).
30. A. Grigoriev, R. Sichel, H. N. Lee, E. C. Landahl, B. W. Adams, E. M. Dufresne, and P. G. Evans, "*Nonlinear piezoelectricity in epitaxial ferroelectrics at high electric fields*," Phys. Rev. Lett. **100**, 027604 (2008).
31. A. Grigoriev, R. J. Sichel, J. Y. Jo, S. Choudhury, L. Q. Chen, H. N. Lee, E. C. Landahl, B. W. Adams, E. M. Dufresne, and P. G. Evans, "*Stability of the unswitched polarization state of ultrathin epitaxial* $Pb(Zr,Ti)O_3$ *in large electric fields*," Phys. Rev. B **80**, 014110 (2009).
32. D. H. Do, P. G. Evans, E. D. Isaacs, D. M. Kim, C. B. Eom, and E. M. Dufresne, "*Structural visualization of polarization fatigue in epitaxial ferroelectric oxide devices*," Nature Mater. **3**, 365 (2004).
33. P. Chen, R. J. Sichel-Tissot, J. Y. Jo, R. T. Smith, S.-H. Baek, W. Saenrang, C.-B. Eom, O. Sakata, E. M. Dufresne, and P. G. Evans, "*Nonlinearity in the high-electric field piezoelectricity of epitaxial* $BiFeO_3$ *on* $SrTiO_3$," Appl. Phys. Lett. **100**, 062906 (2012).

3.5 Mößbauer Science and Nuclear Quantum Optics with X-ray Free Electron Laser Oscillators

Jörg Evers
Max Planck Inst. for Nucl. Phy., Saupfercheckweg 1, 69117 Heidelberg, Germany
Mail to: joerg.evers@mpi-hd.mpg.de

3.5.1 Introduction

Mößbauer science is a mature field with a multitude of diverse applications, actively pursued mostly at synchrotron sources all over the world. Next to interest in its own right, it acts as an important tool in numerous other disciplines [1]. The improvement of existing and the development of new techniques involving Mößbauer nuclei are therefore highly desirable. Novel light sources will provide a higher average flux of resonant photons, and thereby facilitate the implementation of more advanced and potentially photon hungry methods. A broad class of experiments is expected to directly benefit from this, e.g., if a better monochromatization of the incident radiation becomes feasible.

But next to the improvement of the average resonant flux, also a qualitatively different class of new experiments will become accessible, as the number of resonant photons per pulse is increased from less than one at typical synchrotron sources by several orders of magnitude. As a consequence, non-linear and quantum effects with x-rays can be exploited, fueling the field of x-ray quantum optics. In the following, it is argued that for the purpose of x-ray quantum optics, the x-ray free electron laser oscillator (XFELO) is superior to competing light sources, including the prospected seeded free-electron lasers (SFEL).

3.5.2 Nuclear Quantum Optics

3.5.2.1 *Motivation*

From the visible frequency range, it is well known that it is mandatory to exploit coherence, nonlinear light-matter coupling, and quantum effects to unleash the full power of all possible and desired techniques and applications for a given target system. For example, coherent and non-linear spectroscopy methods can lead to orders of magnitude improvement of the signal rate and better separation from the background compared, e.g., to linear absorption spectroscopy. Quantum effects promise an improvement, e.g., of the spatial resolution achieved with light beyond classical limits. The feasibility of such methods, however, is essentially determined by the availability of suitable light sources. This has motivated the development of a large variety of lasers across a broad range of the electromagnetic spectrum. For a long time, higher photon energies were largely excluded from this development, and consequently, x-ray quantum optics mostly remained a field of theoretical interest. But recent experimental progress indicates that state-of-the-art and upcoming light sources will lead to a firm establishment of quantum optical methods in the x-ray regime with Mößbauer nuclei and other target systems alike [2].

3.5.2.2 *State of the Art*

Current progress in Mößbauer science towards x-ray quantum optics is driven by the exploration of the border region between visible quantum optics and x-ray science. By now, a number of archetype quantum optical schemes could successfully be implemented with Mößbauer nuclei in the x-ray regime. Among the prominent examples are the observation of the cooperative Lamb shift [3] or electromagnetically induced transparency (EIT) [4,5]. In particular the latter is of importance, as the establishment of EIT often is regarded as a clear proof of the general suitability of a given system for quantum optics. At the same time, EIT is the foundation for many advanced applications. Also the possibility to dynamically control the light-matter interaction has already been demonstrated, e.g., by rapid switching of applied magnetic fields [6], or by dynamic modifications of the sample geometry [7]. Quantum mechanical aspects have been touched in first experiments on x-ray photon downconversion [8]. From these examples it is obvious that Mößbauer science and x-ray science as a whole can profit from well-established ideas developed in the visible frequency range.

But it is important to realize that this knowledge and technology transfer also works in reverse. In none of the above examples, the experimental success arose from a simple transfer of setups from the visible frequency range to the x-ray range. For example, EIT could be observed with two-level nuclei and a single x-ray laser field, despite the fact that usually two individually controllable laser fields and three-level atoms are required. This became possible due to a novel method of nuclear state engineering based on x-ray waveguides. The nuclear switching required a controlled rotation of a huge magnetic field (~33T) on an ns time scale, which usually is very challenging. For this, the hyperfine field in specific host materials was exploited. These and other obstacles were therefore overcome by inventing novel experimental techniques, geared towards the specific properties and requirements of Mößbauer x-ray science. Going one step further, recently, so-called spontaneously generated coherences (SGC) could be observed in

Mößbauer nuclei [9], which are coherences between nuclear states induced by the interaction with the environmental electromagnetic vacuum field alone. Such SGC have been theoretically suggested for a broad range of fascinating applications, for example, as they can lead to a suppression of spontaneous emission. But their experimental exploration so far was hindered by fundamental restrictions also in the visible domain. Again, a novel setup based on polarization-dependent engineering of light-matter interactions with x-ray waveguides and cooperative effects in large ensemble of nuclei enabled the observation and study beyond current capabilities in the visible frequency range.

Many of these new ideas and techniques developed for x-ray quantum optics potentially can be ported to other frequency ranges. Mößbauer nuclei thus form a novel platform for quantum optics with unique properties, to the benefit of quantum optics as a whole.

A second major ingredient to x-ray quantum optics with Mößbauer nuclei is a suitable theoretical modelling. It is likely that a number of interesting quantum optical effects are hidden in the vast multitude of experiments already performed with Mößbauer nuclei. But for the purpose of developing x-ray quantum optics, this is of limited use, if these effects are not unambigously identified and characterized. Usually, rather different methods are used in visible quantum optics and Mößbauer science. For example, whereas the so-called master equation as the equation of motion for the system density matrix is ubiquitous in visible quantum optics, the light-matter interaction with nuclei is often treated as a scattering problem. Recently, a quantum optical model based on master equations and the so-called input-output formalism could be developed for large ensembles of nuclei embedded in an x-ray waveguide [10]. In the respective limits, it gives results analytically equivalent to those from the previous modelling approaches. But on the one hand, it enables one to clearly identify all physical processes contributing to the system dynamics. On the other hand, it goes beyond previous models, as it encompasses non-linear light-matter interactions and treats the light field quantum mechanically. As a first application, the quantum optical modelling could be used to quantitavely identify the contributions of SGC in the nuclear scattering signal [9].

3.5.2.3 *Significance of the Light Source*

A key feature of Mößbauer nuclei is their small line width. The most commonly used ^{57}Fe has a natural line width Γ of about 5 neV, which is tiny compared to the smallest bandwidth achievable with present-day synchrotron (SR) or free electron laser (FEL) sources. As a consequence, most photons form a non-resonant background, out of which the signal typically consisting of only few photons per shot has to be extracted. In particular, all synchrotron based quantum optical experiments with Mößbauer nuclei so far have in common that they effectively operate on the single photon level. From the viewpoint of quantum optics, e.g., synchrotron radiation (SR) facilities provide weak classical light fields, with less than one resonant photon per pulse on average. By registering only the successful photon detection events in the experiment, essentially a post-selection to single-photon input pulses is achieved.

Counter-intuitively, this apparent restriction to low photon numbers is the reason why quantum optical experiments could be performed with SR at all. This can be understood as follows. One of the most important resources for quantum optics is atomic (or nuclear) coherence, i.e., a fixed phase relation between different atomic/nuclear states. For example, in EIT, coherence between two ground states is established. Because of the fixed phase relation, the two excitation channels from either of the two ground states to a common upper state can destructively interfere, such that no light is absorbed. The such-generated transparency is perfect only if the coherence between the two nuclear ground states is complete. This coherence is imprinted on the the matter by the temporal (or longitudinal) coherence of the applied light fields. While SR as a whole usually has very low temporal coherence, a single photon resonant with the nuclei within a SR pulse is temporally coherent, as evidenced by the fact that it can interfere with itself in the time domain. Therefore, quantum optical methods successfully could be implemented despite the fact that the SR as a whole has low temporal coherence.

This picture changes if a light source provides many resonant photon per pulse, as it will be possible with novel source types such as the SFEL or the XFELO, see Table 1. These compress the photons in a given shot into a smaller energy bandwidth and thus naturally increase the number of resonant photons per shot available for experiments with Mößbauer nuclei. The temporal coherence of the light source then determines, whether the different near-resonant photons within a given light pulse can interfere among each other. This temporal coherence is related to the line width of the light source, i.e., the spectral width around the resonance frequency. A finite line width acts as a source of decoherence in quantum optics, limiting the amount of matter coherence which can be established. As a direct consequence, for example, perfect transparency in EIT is only achieved if the line width of the light source is small compared to the line width of the atoms/nuclei.

While XFELO and SFEL promise a similar average resonant flux and a similiar number of resonant photons per pulse, the XFELO is expected to achive smaller bandwidths than that of the SFEL. This is due to the different structure of the XFELO pulses: Rather than having a smooth frequency distribution of a certain bandwidth as the SFEL, it consists of a number of phase-coherent modes. While the SFEL will still have a bandwidth considerably larger than the nuclear linewidth, an individual mode of the (stabilized) XFELO can achieve bandwidths which are below the natural linewidth of the nuclei. In this sense, the XFELO is superior to SFEL sources, since it does not act as a source of decoherence due to limited temporal coherence.

Apart from this advantage of a narrow line width, the XFELO also promises to achieve a high stability in terms of shot-to-shot intensity and timing fluctuations, which will be beneficial in particular for schemes exploiting non-linear light-matter interactions, dynamical control of the light-matter interaction, or synchronization to other light sources.

Table 1: Comparison of expected performance of synchrotron radiation (SR), seeded free electron lasers (SFEL) [11], and the x-ray free electron oscillator (XFELO) [12].

Parameter	***SR***	***SXFEL***	***XFELO***
Bunch separation	200ns	200ns (μ-bunch)	1 μs
Avg. Flux (ph/s/Γ)	5×10^4	2×10^8	3×10^8
Fluence (ph/pulse/Γ)	10^{-2}	6×10^3	3×10^3

3.5.2.4 *Future Perspectives*

Next to the existing experiments discussed above, a number of perspectives for nuclear x-ray quantum optics have been developed [2]. Broadly speaking these can be devided into applications of coherence, quantum effects, or enhanced control of nuclei.

A number of schemes have been suggested related to the dynamical control of the intermediate nuclear excitation state, the so-called nuclear exciton. Such excitons could be steered without any material motion, or spectrally manipulated, e.g., to enhance the light-matter interaction [13]. Building up on the dynamical switching of the light-matter interaction demonstrated in [6], alternative switching setups can lead to improved photon storage [14]. Also a control of nuclear branching ratios is possible, with applications, e.g., in the selective population of specific nuclear target states [15].

Using suitable dynamical switching, also single photon entanglement in the x-ray range has been suggested [16]. Quantum light could also be provided by down conversion [8]. A true x-ray single photon source would enable the exploration of quantum mechanical aspects of light-matter interactions in the x-ray range. After initial proof-of-principle experiments close to visible counterparts, it has been suggested that for certain applications x-ray implementations could be superior to setups in the visible frequency range, in particular due to the potentially much higher photon detection efficiency of x-rays, the low background at higher photon frequencies, as well as the large photon momentum. Current experiments have already demonstrated that x-ray quantum optical systems are exceptionally clean, in the sense that essentially no decoherence perturbs quantum mechanical coherence and interference phenomena [9].

The increased number of photons per pulse expected in XFELO or SFEL also allows reaching the strongly non-linear regime. A rough estimate based on the Kerr nonlinearity enhanced by EIT shows that already in this conceptionally rather simple system, the non-linear phase shift is expected to be of a similar order than the corresponding linear phase shift [4].

Further exploration of x-ray quantum optics is facilitated by the implementation of advanced nuclear level schemes. By exploiting the magnetic substructure together with the polarization of incident and detected light, a large variety of complex and dynamically controllable level schemes can be achieved [9,10]. A suitable polarimeter operating at the ^{57}Fe resonance frequency with exceptional polarization purity is already operational at synchrotron radiation facitility [17]. A large number of mutually coherent photons could also be used to form several independently controllable control fields, rather than the single incident beam available to present-day experiments. This would further enrich the range of accessible level schemes.

Finally, also a number of more speculative but far-fetching proposals for x-ray quantum optics have been raised. EIT together with the related reduction of the group velocity of an incident light pulse could be used to implement optical analogues of phenomena from general relativity, such as even horizons [18,19]. Also interferometric setups to explore the boundary between gravity and quantum mechanics have been suggested, as summarized in the contribution of B. W. Adams in this newsletter. Nuclear forward scattering across a large number of macroscopically separated target foils could also act as an experimental platform to study quantum transport [20]. Also x-ray optomechanics has been suggested as a promising avenue, in particular in view of recent proposals to address fundamental questions with nanomechanical resonators [21].

Despite these ideas, in particular in comparison to visible quantum optics, x-ray quantum optics still appears largely unexplored both theoretically and experimentally at this point. Nevertheless, the existing experimental progress together with the improvement in source quality expected from SFEL and XFELO make it very likely that eventually quantum optical ideas will play an important role in all areas of x-ray science.

3.5.3 Perspectives for Mößbauer Science

Next to the development of x-ray quantum optics, novel light sources will also lead to a revolution in more traditional applications of Mößbauer science [19]. All of the methods presented below require a large flux of resonant photons, and many in addition benefit from improved temporal coherence. Methods have been suggested to generate tunable light with sub-meV energy resolution based on Mößbauer nuclei [22]. This would be of considerable interest, e.g., in the study of solid state excitations, such as non-equilibrium lattice dynamics. Next to the high energy resolution, nm-scale position sensitivity could be achieved by selectively doping parts of the sample with ^{56}Fe or ^{57}Fe. Due to the long signal tail of photons scattered off of the narrow nuclear resonance, an effective separation of signal and background is achieved. Using double pulses, pump-probe experiments with high spatial, frequency and temporal resolution can be realized. It has also been suggested that the scattering function S could be measured with position- and time resolution over a large parameter range in the time domain, based on Mößbauer nuclei [23]. High time resolution can also be achieved by rotating nuclear targets, which convert the time coordinate into a spatial coordinate. This "nuclear light house effect" has been demonstrated already in proof of principle experiments [24].

In view of the greatly improved average flux of resonant photons, the substantially improved possibilities to focus and monochromatize the incident light, as well as advanced detection schemes, it is clear that Mößbauer science as a whole will benefit from novel monochromatic sources of light, opening access to a whole range of new applications.

3.5.4 References

1. W. Sturhahn, “Nuclear resonant spectroscopy”, J. Phys.: Condens. Matter 16, S497 (2004)
2. B. W. Adams, C. Buth, S. M. Cavaletto, J. Evers, Z. Harman, C. H. Keitel, A. Pálffy, A. Picon, R. Röhlsberger, Y. Rostovtsev, K. Tamasaku, “X-Ray Quantum Optics”, J. Mod. Opt. 60, 2 (2013)
3. R. Röhlsberger, K. Schlage, B. Sahoo, S. Couet, and R. Rüffer, “Collective Lamb Shift in Single-Photon Superradiance”, Science 328, 1248 (2010)
4. R. Röhlsberger, H.-C. Wille, K. Schlage, B. Sahoo, “Electromagnetically induced transparency with resonant nuclei in a cavity”, Nature 482, 199 (2012)
5. M. Fleischhauer, A. Imamoglu, J. P. Marangos, „Electromagnetically induced transparency: Optics in coherent media“, Rev. Mod. Phys. 77, 633 (2005)
6. Yu. V. Shvyd'ko, T. Hertrich, U. van Bürck, E. Gerdau, O. Leupold, J. Metge, H. D. Rüter, S. Schwendy, G. V. Smirnov, W. Potzel and P. Schindelmann, “Storage of Nuclear Excitation Energy through Magnetic Switching”, Phys. Rev. Lett. 77, 3232 (1996).
7. R. N. Shakhmuratov, F. Vagizov, and O. Kocharovskaya, “Radiation burst from a single γ-photon field”, Phys. Rev. A 84, 043820 (2011).
8. B. W. Adams [Ed.], “Nonlinear Optics, Quantum Optics, and Ultrafast Phenomena with

X-Rays: Physics with X-Ray Free-Electron Lasers", Springer, Heidelberg, 2003.

9. K. P. Heeg, H.-C. Wille, K. Schlage, T. Guryeva, D. Schumacher, I. Uschmann, K. S. Schulze, B. Marx, T. Kämpfer, G. G. Paulus, R. Röhlsberger, and J. Evers, "Spontaneously Generated Coherences in the X-ray Regime", submitted (2013)
10. K. Heeg and J. Evers, in preparation (2013)
11. G. Geloni, V. Kocharyan, E. Saldin, "Extension of self-seeding to hard X-rays >10 keV as a way to increase user access at the European XFEL", arXiv:1111.5766 [physics.acc-ph]
12. K.-J. Kim, "A Review of X-Ray Free Electron Laser Oscillator", Presentation at the ERL meeting 2011, KEK, Tsukuba, Japan
13. B. W. Adams, "Space–time control of nuclear γ-ray superradiance", J. Mod. Opt. 58, 1638 (2011)
14. W.-T. Liao, A. Pálffy, and C. H. Keitel, "Coherent Storage and Phase Modulation of Single Hard-X-Ray Photons Using Nuclear Excitons", Phys. Rev. Lett. 109, 197403 (2012)
15. A. Pálffy, C. H. Keitel, and J. Evers, "Coherent control of the cooperative branching ratio for nuclear x-ray pumping", Phys. Rev. B 83, 155103 (2011)
16. A. Pálffy, C. H. Keitel, and J. Evers, "Single-Photon Entanglement in the keV Regime via Coherent Control of Nuclear Forward Scattering", Phys. Rev. Lett. 103, 017401 (2009).
17. B. Marx, I. Uschmann, S. Hofer. R. Lotzsch, O. Wehrhan, E. Förster, M. Kaluza, T. Stöhlker, H. Gies, C. Detlefs, T. Roth, J. Hartwig and G. G. Paulus, "Determination of high-purity polarization state of x-rays", Opt. Comm. 284, 915 (2011)
18. U. Leonhardt and T. G. Philbin, "Transformation optics and the geometry of light", Prog. Opt. 53, 69 (2009).
19. J. Evers, work in progress
20. I. Pikovski, M. R. Vanner, M. Aspelmeyer, M. S. Kim, and Č. Brukner, "Probing Planck-scale physics with quantum optics", Nature Physics 8, 393 (2012)
21. G. K. Shenoy and R. Röhlsberger, "Scientific opportunities in nuclear resonance spectroscopy from source-driven revolution", Hyperfine Int. 182, 157 (2008)
22. R. Röhlsberger, E. Gerdau, R. Rüffer, W. Sturhahn, T.S. Toellner, A.I. Chumakov, E.E. Alp, "X-ray Optics for µeV-Resolved Spectroscopy," Nucl. Instrum. Methods A 394, 251-255 (1997).
23. A. Q. R. Baron, H. Franz, A. Meyer, R. Rüffer, A. I. Chumakov, E. Burkel, and W. Petry, "Quasielastic Scattering of Synchrotron Radiation by Time Domain Interferometry", Phys. Rev. Lett. 79, 2823 (1997).
24. R. Röhlsberger, T. S. Toellner, W. Sturhahn, K. W. Quast, E. E. Alp, A. Bernhard, E. Burkel, O. Leupold, and E. Gerdau, "Coherent Resonant X-Ray Scattering from a Rotating Medium", Phys. Rev. Lett. 84, 1007 (2000)

3.6 Scientific Possibilities for Nuclear Resonant Scattering with an XFEL-Oscillator

Ralf Röhlsberger
Deutsches Elektronen-Synchrotron DESY, Notkestr. 85, 22607 Hamburg, Germany
Mail to: ralf.roehlsberger@desy.de

3.6.1 Introduction

The proposed X-ray free-electron laser oscillator (XFELO) will open up completely new possibilities in the field of nuclear resonant scattering (NRS) with qualitively new applications in many fields of the natural sciences. This is mainly due to the enormous spectral flux of 10^9 ph/sec/neV anticipated at such a machine in the regime of hard x-rays. For comparison, at existing 3rd generation synchrotron radiation sources this value is about five orders of magnitude lower. From this comparison alone it becomes already clear that an XFELO will allow for experiments that are completely impossible at exisiting sources. An an XFELO, there are more outstanding properties that render such a device even more attractive for applications of NRS. Those are a) the lateral coherence of the radiation that will enable one to perform focusing with spot sizes in the range of a few 10 nm and b) the short pulse duration in the regime of a few ps that faciltitates the study of time-resolved processes in non-equilibrium dynamics. While those properties are also available at 'conventional' hard x-ray XFEL facilites, it is the intrinsic meV energy bandwidth of an XFELO that makes is particularly attractive for NRS because it obviates the need for extra meV monochromators that would be required at an XFEL. Combining all these properties of an XFELO, one arrives at applications of NRS in many areas of the natural science that are hardly possibly with any other technique. Some of them will be discussed here in more detail:

1) Dynamical properties of artificially structured materials on mesoscopic length scales via inelastic x-ray spectroscopy with μeV resolution
2) Exploring the dynamical origin of friction
3) Non-equilibrium dynamics with nanometer spatial resolution via inelastic nuclear resonant scattering in pump-probe experiments
4) Nuclear quantum optics

3.6.2 Dynamics of Artificially Structured Materials

The artificial structuring of condensed matter on (mesoscopic) length scales between 1 nm and a few μm offers outstanding possibilities to obtain materials with tailored functionality. Examples are nanocomposites consisting of metals and polymers or hybrid materials made of crystalline and amorphous phases. In all of these cases the material properties strongly vary over short length scales, thus affecting propagating excitations like phonons and leading to new dynamical properties that have no counterpart in homogeneous bulk materials. As illustrated in Fig. 1, the phonon frequencies of mesoscopically structured materials are substantially smaller than those of crystalline materials and the first Brillouin zone extends to much smaller q-values. As can be seen in the phase-space diagram in Fig. 1, a great part of the corresponding range in phase space is not covered by existing methods (grey shaded areas).

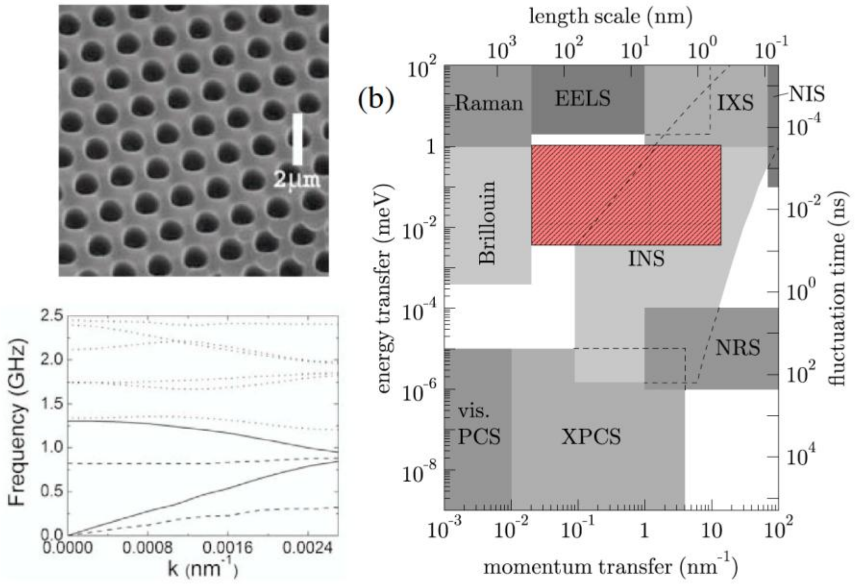

Figure 1: Left: Materials structured sructured on mesoscopic length scales between 1 nm and a few μm like phononic crystals [4] exhibit vibrational excitations in the range between μeV and meV. Right: Overview of methods for probing solid-state excitations via inelastic scattering or correlation techniques. The shaded areas indicate the range of (energy, momentum) as well as (space, time) coordinates covered by the respective technique. The hatched rectangle displays the regime in phase space that can be covered by μeV-resolved spectroscopy at an XFELO as it will provide access to a regime that is not covered by any of the other techniques. (EELS = electron energy loss spectroscopy, (X)PCS = (X-ray) Photon Correlation Spectroscopy, IXS = Inelastic X-ray Scattering, INS = Inelastic Neutron Scattering, NRS = Nuclear Resonant Scattering).

While vibrational spectroscopy in the μeV range is typically done via Brillouin light scattering, there is currently no such technique available for x-rays. This is, however, highly desirable, because visible light scattering is restricted due its small penetration depth in opaque materials and its limited range of momentum transfers. For the determination of the phonon density of states of mesoscopic structures (dimension L), the full q range up to 2π/L has to be accessible.

The best energy resolution that is currently achieved by state-of-the art inelastic x-ray spectrometers is about 1 meV. This is not sufficient to analyze the dynamical properties of mesoscopically structured materials as those shown in Fig. 1. For that reason it is necessary to develop a new type of spectrometer thatcallows for an energy resolution in the μeV range. Such a resolution can be achieved by employing the nuclear lighthouse effect at the 14.4 keV resonance of ^{57}Fe [1,2]. Nuclear resonant scattering from a sample rotating with frequencies up to 70000 s^{-1} leads to angular deflection of the resonantly scattered radiation, thus extracting a μeV wide bandpass out of the incident beam [3].

The deflected radiation can be energetically tuned over several meV by transverse displacement of the rotor relative to the beam [3]. The layout of a corresponding spectrometer is shown in Fig. 2. The proof of principle of this approach has been demonstrated in a recent experiment at the ESRF, where a photon flux of bout 10^5 s^{-1} at the sample position could be reached at an energy resolution of about 30 μeV. This photon flux is still not enough for routine inelastic scattering experiments. If operated at an XFELO, however, one expects a photon flux of 10^{10} s^{-1} at the sample position, so that IXS experiments with μeV resolution become truly feasible. Since the radiation was monochromatized via nuclear resonant scattering, the inelastically scattered radiation can be analyzed via a nuclear resonant scattering process as shown in Fig. 2. In operation, this type of spectrometer can cover a range in phase space that is marked by the purple rectangle in Fig. 1.

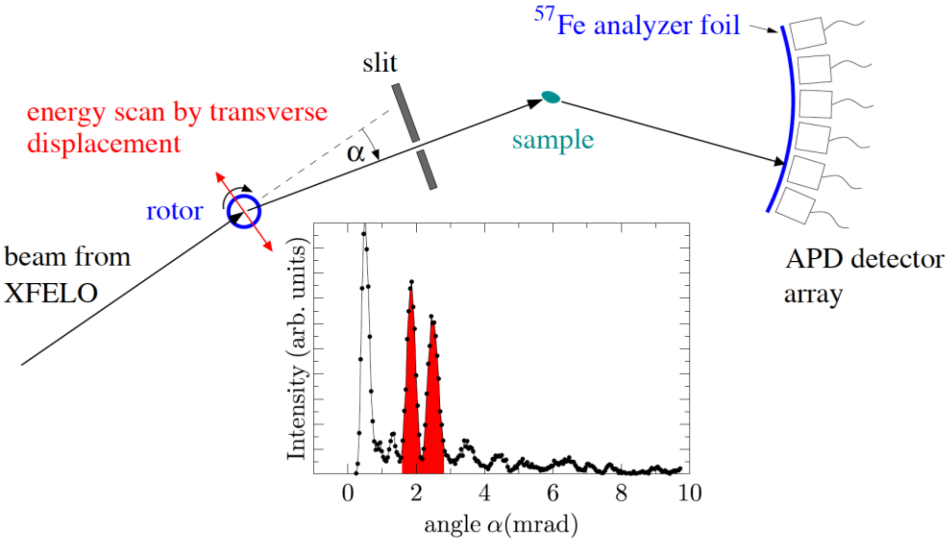

Figure 2: Scheme of a spectrometer for μeV-resolved inelastic x-ray spectroscopy based on the nuclear lighthouse effect. The beam from the XFELO passes a ^{57}Fe containing rotor that is spinning at a frequeny of several 10 kHz. A slit selects the red shaded part of the timespectrum that serves then as the primary beam incident on the sample. The energy of the deflected radiation can be tuned over several meV by transversely displacing the rotor. At an XFELO one obtains an incident flux at the sample position of about 10^{10} s^{-1} that opens a new regime of IXS experiments with μeV energy resolution.

3.6.3 Exploring the Dynamical Origins of Friction

Energy dissipation due to friction amounts to economic losses of more than 10 percent of the gross national product of the industrialized nations. A fundamental understanding of the frictional processes, resulting in the synthesis of reduced-friction materials would thus have an enormous economic impact. Despite great advances in the measurement of frictional forces on the atomic scale, the mechanisms of frictional energy dissipation, however, are not resolved to date. Friction coefficients between two materials are still empirical quantities. The reason for the lack of understanding in this field is the fact that the contact region between two materials is hardly accessible to a direct study. This region can be efficiently investigated by using a focused beam of hard x-rays from an XFELO, as shown in Fig. 3. The combination of high-resolution inelastic nuclear resonant scattering with structural x-ray probes allows one to identify the dynamical origins of friction with very high spatial resolution. Such studies will eventually reveal the mechanisms of energy dissipation on length scales from macroscopic to nanoscopic dimensions that are indispensable to understand and prepare materials with tailor-made frictional properties.

The key element for understanding friction in the real world (on macroscopic scales) is the knowledge about the vibrational properties on all length scales of the material. Once this is known, one can establish a model for the dissipation of energy along these channels and how they are excited. Particularly exciting are the answers to the following questions:

a) How can the structural properties of thin films (metallic, polymer, nanocomposites) be modified to obtain materials with significantly reduced friction ? Is there 'superlubricity' also at mesoscopic length scales?
b) What is the spatio-temporal dependence of energy dissipation during sliding friction ? What happens during different phases of stick-slip motion?
c) What are frictional properties of magnetic surfaces and how do they depend on the magnetization state? Apparently, this field is completely unexplored up to now.

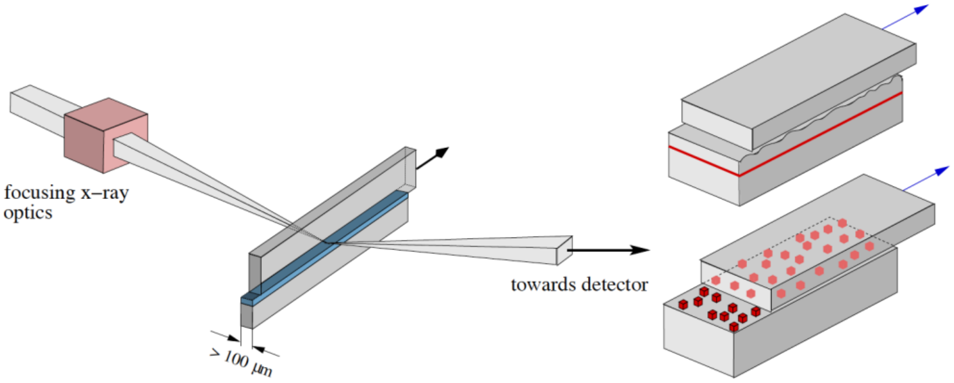

Figure 3: Left: Micro- and nanofocused beams of hard x-rays from an XFELO will be used to selectively investigate the contact area (blue) between two materials that slide relative to each other. Right: By deposition of isotopic probe layers in selected depths or decoration of the contact region with isotopic nanoparticles the frictional dynamics can be studied with very high spatial resolution.

3.6.4 Nuclear Inelastic Pump-Probe Experiments

A unique future application of inelastic nuclear resonant scattering will be the field of time-resolved (non-equilibrium) lattice dynamics: Since the incoherent signal reflects the phonon occupation number *at the very moment of excitation* this method is very suitable to be applied in pump-probe experiments, as sketched in Fig. 4. A pump pulse creates a high occupation number of phonons, where the coupling mechanism is crucial for the spectral distribution of the phonons and their corresponding lifetime: A simple heat pulse will create thermal phonons with lifetimes in the ps range or below. Highly monochromatic phonons with lifetimes of several 100 ns can be created by coupling the laser pulse to impurity resonances that decay via electronic relaxation [5]. The decay of such non-equilibrium phonon states provides valuable information about the thermal transport properties of the sample.

The spectral and temporal evolution of these phonon states can be determined as follows: If for a fixed time delay t_1 between pump and probe pulse the photon energy of the probe pulse is varied around the nuclear resonance, one obtains a snapshot of the phonon spectrum that has developed during this time interval. On the other hand, tuning the time delay between the pump and probe pulse at a fixed off-resonance x-ray energy allows one to monitor the time evolution of particular vibrational states. Using the meV beam from an XFELO, it will be possible to study non-equilibrium lattice dynamics on a ps time scale. An immediate application will be the study of the dynamics of heat-transfer on nanoscopic length scales, for example.

Due to the isotopic sensitivity of the absorption process an extremely high spatial resolution can be obtained by the use of probe layers, making this technique a rather unique application of the XFELO.

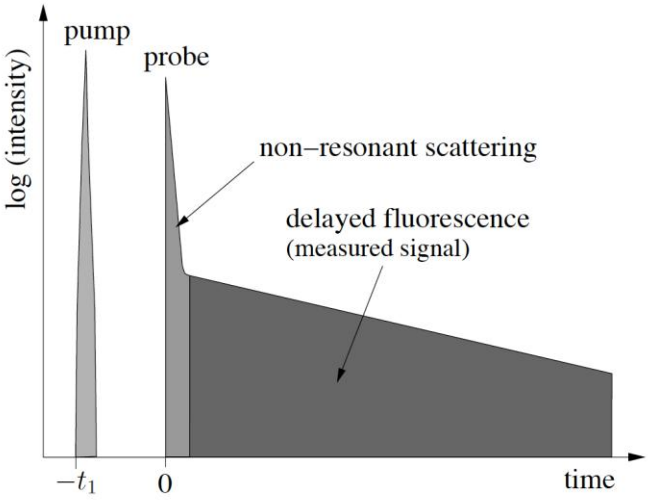

Figure 4: Inelastic nuclear resonant scattering in a pump-probe arrangement. If a pump pulse hits the sample at a time – t_1, the x-ray pulse probes the phonon states that have developed during the time interval between pump and probe pulse (Figure taken from [6].)

3.6.5 Nuclear Quantum Optics

Quantum optics is a very rich and wide field [7] that is dominantly attached to the regime of visible light due to the availablity of tunable short-pulse laser sources. Quantum optical experiments in the x-ray regime, however, are scarce mainly due to the fact that the photon number degeneracy of conventional synchrotron radiation sources is well below 1. For a recent review, see, e.g., ref. [8]. This situation will significantly change with the advent of sources like the XFELO that is expected to provide more than 10^3 photons per mode of the radiation field in one pulse. This is particularly attractive for the field of NRS, as resonant Mössbauer nuclei constitute almost ideal two-level systems that form the basis for many quantum optical phenomena [9]. Some of these are already observable at the single-photon limit. Those are the cooperative optical phenomena like superradiance and effects that are associated with it like the collective Lamb shift [10] and electromagnetically induced transparency [11]. It will be extremely interesting to explore these phenomena at higher photon number degeneracies as they are provided by sources like the XFELO. This will allow one to enter the regime of nonlinear quantum optics with potential applications for new high-resolution spectroscopies that are unthought of today but will be at the frontier of science in the future.

3.6.6 Conclusion

Nuclear resonant scattering and spectroscopy have benefitted greatly from the evolution of synchrotron-based photon sources over the past decades. Given a boost of several orders of magnitude in spectral flux as expected at an XFELO compared to existing sources, it is anticipated that completely new research areas will open up for nuclear resonant scattering techniques. A selection of them has been discussed in this article without the claim to be comprehensive. More potential areas of applications are discussed, e.g., in [12].

3.6.7 References

1. R. Röhlsberger, T. S. Toellner, W. Sturhahn, K. W. Quast, E. E. Alp, A. Bernhard, E. Burkel, O. Leupold, and E. Gerdau, Phys. Rev. Lett. 84, 1007 (2000).
2. R. Röhlsberger, K. W. Quast, T. S. Toellner, P. Lee, W. Sturhahn, E. E. Alp, and E. Burkel, Appl. Phys. Lett. 78, 2970 (2001).
3. R. Röhlsberger, E. E. Alp, E. Gerdau, O. Leupold, K. W. Quast, R. Rüffer, W. Sturhahn, T. S. Toellner, and E. Burkel, Physica B 263-264, 574 (1999)
4. T. Gorishnyy, C. K. Ullal, M. Maldovan, G. Fytas, and E. L. Thomas, Phys. Rev. Lett. 94, 115501 (2005).
5. W. A. Tolbert, W. M. Dennis, and W. M. Yen, Phys. Rev. Lett. 65, 607 (1990).
6. R. Röhlsberger, Nuclear Condensed Matter Physics Using Synchrotron Radiation, Springer Tracts in Modern Physics, Vol. 208 (Springer, Heidelberg 2004).
7. M. O. Scully and M. S. Zubairy, Quantum Optics, Cambridge 1997.
8. B. W. Adams, C. Buth, S. M. Cavaletto, J. Evers, Z. Harman, C. H. Keitel, A. Palffy, A. Picon, R. Röhlsberger, Y. Rostovtsev, and K. Tamasaku, J. Mod. Opt. (in print, 2013)
9. L. Allen and J. H. Eberly, Optical Resonance and Two-Level Systems, Wiley 1987.
10. R. Röhlsberger, K. Schlage, B. Sahoo, S. Couet and R. Rüffer, Science 328, 1248 (2010).
11. R. Röhlsberger, H.C. Wille, K. Schlage and B. Sahoo, Nature 482, 199 (2012).
12. G. K. Shenoy and R. Röhlsberger, Hyperfine Interact. 182, 157 (2008).

3.7 Nuclear-Resonance-Stabilized XFELO for Fundamental Physics and Precision Metrology

Bernhard W. Adams and Kwang-Je Kim
Argonne National Laboratory, 9700 S. Cass Ave., Lemont, IL 60439
Mail to: adams@aps.anl.gov

3.7.1 Introduction

X-ray quantum optics (XQO) is an emerging field offering perspectives ranging from fundamental physics to practical applications [1]. It builds upon the much more mature field of “visible” quantum optics (VQO) at photon energies of a few eV and below [2]. Nonetheless, there is considerable new territory to be explored due to the different ways that eV-scale photons and keV-scale photons interact with matter. Most quantum-optical experiments require light sources of very high coherence and stability, as well as a wide range of intensities. The XFELO [3-6] can meet these requirements by stabilizing the cavity relative to an external, absolute reference. Nuclear resonances are well suited for precision references because they typically occur in the x-ray wavelength region and are exceedingly sharp due to the relative isolation of nuclei from environmental perturbations [7]. The most widely known nuclear resonance is that of ^{57}Fe at 14.4 keV with a natural linewidth of about 5 neV.

When comparing different x-ray sources for their coherence and stability properties, there is a clear progression from tubes to storage rings to x-ray high-gain, single-pass free-electron lasers [8,9], to self-seeded SASE XFELs (SSS-XFEL) [10,11], to the XFELO, and, finally, to the nuclear-resonance-stabilized XFELO [12], which we will refer to as NRS-XFELO in this text. Contemporary storage ring sources emit x-rays into hundreds or thousands of transverse modes, and, depending on the monochromator, typically thousands of longitudinal modes. The mode degeneracy, i.e., the number of photons per mode is typically about 0.1-1.0. SASE XFELs emit about 10^{12} – 10^{13} photons into a single transverse mode and hundreds of longitudinal modes. Self-seeding will reduce the number of longitudinal modes to a few, or even one, but some intensity fluctuations will remain. However, there will be no coherence between pulses. A self-seeded SASE XFEL (SSS-XFEL) can provide temporal coherence for pulses shorter than a few tens of fs.

The output from an XFELO consists of pulses transmitted though the optical cavity each time the circulating, intra-cavity pulse hits one of the Bragg crystals, which is thin to transmit a few percent of the intra-cavity pulse. Each XFELO output pulse is fully coherent transversely as well as temporally—a so-called transform-limited pulse in the visible-laser community. An XFELO pulse contains about 10^9 photons, smaller by three to four orders of magnitude compared to SASE. However, the XFELO repetition rate is much higher, and the intensity stability between pulses is also much higher than SASE, even with self-seeding.

A distinguishing feature of the XFELO is that, due to the pulse recirculation, the output pulses can be coherent with each other if the cavity length can be held fixed. The output spectrum then consists of a comb of sharp lines spaced at, typically, 10 to 20 neV from each other. If left to itself, however, the cavity length will fluctuate, and other phase errors will also accumulate, so the comb lines will be effectively broadened up to their spacing, and inter-pulse coherence is lost. This can be prevented by locking the cavity length to an external reference to obtain an inter-pulse coherence commensurate with the stability of that reference. A convenient external reference is nuclear resonances, hence NRS-XFELO.

3.7.2 The Comb Structure of an XFELO and Tolerance Requirements

Consider an ideal XFELO in steady state. Electron bunches arrive at a constant interval T_e and meet the x-ray pulse circulating in the optical cavity at the undulator entrance. We write the electric field, say at just outside the cavity, of one of the output pulses, call it the 0-th pulse, as

$$E_0(t) = e^{-i\omega_{FEL}t} A(t) \ . \tag{1}$$

Here ω_{FEL} is the frequency in the middle of the XFELO bandwidth and *A(t)* is the envelope function, which we assume to be a Gaussian of rms width σ_t peaked at $t = 0$. The (*n*-1)-th pulse is from the intra-cavity pulse after circulating *n* times and its wave form is therefore displaced by *n* round-trip periods. However, we should pay attention to the fact that the round-trip periods of the pulse envelope and the pulse phase are in general different. The round-trip period for the phase is given by $T_{ph} = T_c + \Delta\phi / \omega_{FEL}$, where $T_c = L/c$ is the round trip time of the phase in the absence of the FEL interaction and $\Delta\phi$ is the phase delay due to the index of refraction of the FEL interaction [13]. The latter in radians is approximately equal to the value of the incremental gain, which is small (<0.2) and, to the first order, independent of both T_e and T_{ph}. We will therefore neglect it and simply write $T_{ph} = T_c$ in the following. The round-trip period of the pulse envelope is the same as electron bunch spacing T_e in steady state operation and should be slightly longer than T_c to compensate for the lethargy effect arising from the fact that the later part of the x-ray pulse receives more amplification [14]. For FEL gain to be effective, we must require

$$T_e - T_c << \sigma_t \, . \tag{2}$$

We now see that the electric field of the *n*th pulse is given by

$$E_n(t) = e^{-i\omega_{FEL}(t-nT_c)} A(t - nT_e) \, . \tag{3}$$

The electric field for the sum of *N* pulses in frequency representation is

$$\begin{aligned} \tilde{E}(\omega) &= \frac{1}{\sqrt{2\pi}} \int dt \, e^{i\omega t} \sum_{n=0}^{N-1} E_n(t) \\ &= \left(\sum_{n=0}^{N-1} \exp\left[in\left(\omega T_e - \omega_{FEL}(T_e - T_c) \right) \right] \right) \left(\frac{1}{\sqrt{2\pi}} \int dt e^{i(\omega - \omega_{FEL})} A(t) \right) \end{aligned} \, . \tag{4}$$

The second factor in the above gives the FEL spectral envelope while the first factor gives rise to a comb structure for large *N*, with teeth located at

$$\omega = \omega_{FEL} \frac{T_e - T_c}{T_e} + \frac{2\pi}{T_e} n \, ; n = 0, \pm 1, \pm 2, \ldots \tag{5}$$

Note the similarity of Eq. (5) with that occurring in a mode-locked optical laser [15]. For the nuclear-resonance stabilization to work, the fluctuation in frequency due to fluctuations in cavity length and electron bunch spacing should be smaller than the comb spacing $2\pi / T_e$. To see what this condition implies, we introduce a very large integer n_{FEL} as follows:

$$\omega_{FEL} = \frac{2\pi}{T_c} n_{FEL} \, . \tag{6}$$

Then Eq. (5) can be written as

$$\omega = \omega_{FEL} + \frac{2\pi}{T_e} \left(n - n_{FEL} \right) . \tag{7}$$

The tolerances on the fluctuations δT_c and δT_e are determined by the following condition:

$$|\delta\omega| = \left| \delta\omega_{FEL} - 2\pi \frac{\delta T_e}{T_e^2} \left(n - n_{FEL} \right) \right| << \frac{2\pi}{T_c} \, . \tag{8}$$

This leads to two conditions. First

$$\left|\delta\omega_{FEL}\right| = \left|\frac{\delta T_c}{T_c}\omega_{FEL}\right| = \left|\frac{c\delta T_c}{T_c}\frac{2\pi}{\lambda_{FEL}}\right| << \frac{2\pi}{T_c} \rightarrow \frac{\delta L}{\lambda_{FEL}} << 1 \cdot \tag{9}$$

Here δL is the cavity length fluctuation. Second,

$$\begin{aligned} &\left|\frac{\delta T_e}{T_e}(n-n_{FEL})\right| << 1 \rightarrow \left|\frac{\delta T_e}{\sigma_t}\frac{(n-n_{FEL})}{\sigma_n}\frac{\sigma_t\sigma_\omega}{2\pi}\right| << 1 \\ &\rightarrow \left|\frac{\delta T_e}{\sigma_t}\frac{(n-n_{FEL})}{\sigma_n}\frac{1}{4\pi}\right| << 1 \end{aligned} . \tag{10}$$

In the above, σ_ω is the rms FEL bandwidth, $\sigma_n = (T_c / 2\pi)\ \sigma_\omega$ is the corresponding spread of the comb-line numbers. In the last step, we used the fact that $\sigma_t\ \sigma_\omega = 1/2$ for a Gaussian coherent pulse. The last inequality in Eq. (10) is not difficult to satisfy; for $\sigma_t << 0.5$ ps, we can set $\delta T_e \leq 5$ fs and $|(n - n_{FEL}) / \sigma_n| \leq 0.1$, and the LHS of the last inequality becomes less than 10^{-4}.

The fact that the tolerance on the electron pulse period on the spectral comb is much more relaxed compared to that on the phase period could have been anticipated from the fact that the electron pulse period enters in the pulse envelope rather than the pulse phase, as described by Eq. (3).

3.7.3 **Cavity Stabilization**

3.7.3.1 ***Schematic***

In a specific XFELO example with an $L = 90$-m round-trip cavity, the comb lines are spaced at $\Delta E = 14$ neV from each other. A single x-ray pulse has an rms duration of about $\sigma_t = 500$ fs corresponding to the transform-limited FWHM energy bandwidth of 1.6 meV. If the cavity is left unstabilized, then thermal drift, seismic and instrumental vibrations, as well as FEL-intrinsic noise changes the phase relationship between pairs of subsequent pulses, and the modal comb will broaden the comb lines, as discussed above, until the entire 1.6-meV spectrum becomes effectively continuous. The line broadening can be reduced drastically by locking one of the spectral teeth in the comb to a nuclear resonance. Figure 1 shows schematically how the cavity stabilization is done: a nuclear-resonant sample (here ^{57}Fe) is placed in the XFELO output beam, and the resonance fluorescence and inner-shell electronic fluorescence at 6 and 7 keV are monitored as a measure of how close one of the XFELO longitudinal modes is to the resonance.

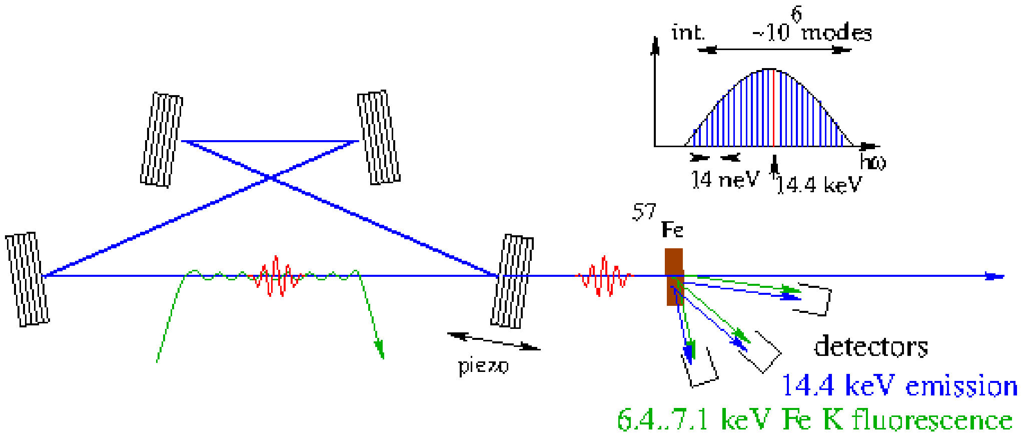

Figure 1: Schematic of the cavity-stabilization scheme. A nuclear-resonant sample (here ^{57}Fe) is placed into the XFELO output, and the nuclear-resonant and K-shell electronic fluorescence are monitored as a function of cavity tuning with a piezoelectric actuator. A feedback loop keeps one of the ca. 10^6 longitudinal modes of the XFELO on resonance with the sample.

The comb lines shift by one comb spacing if the cavity length changes by one XFELO wavelength. Therefore, the x-ray fluorescent response can be maximized by scanning the cavity length over the resonance wavelength (0.86Å for ^{57}Fe) with a piezoelectric actuator on one of the cavity mirrors. Once the maximum resonance-fluorescent response of the NR sample is found, a feedback loop can maintain it. Figure 2 shows this response over a cavity-length scan of one wavelength for the cases $\Gamma T/\hbar =$ 1,2,..5. For ideal bandwidth $\Gamma =$ 4.7 neV and $T =$ 300 ns, $\Gamma T/\hbar = 2.14$. Even taking into account some inhomogeneous line broadening to about 8 neV, $\Gamma T/\hbar = 3.64$, and the fluorescent response can resolve the 14-neV mode spacing of the NRS-XFELO.

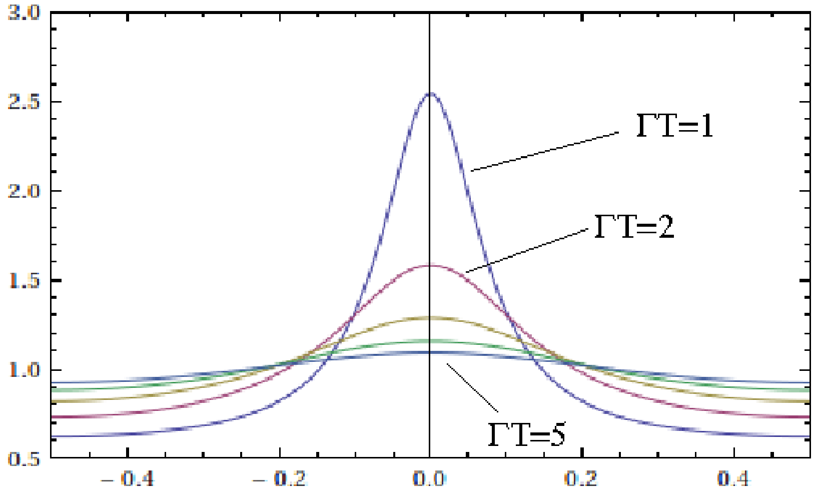

Figure 2: Signal contrast over a cavity-length scan of one x-ray wavelength.

The sample in Figure 2 should be sufficiently thick to intercept enough photons for a strong signal, yet still optically thin enough to suppress superradiant line broadening.

At an optical thickness of 0.1 and 10^9 photons per pulse in 10^6 longitudinal modes (teeth of the comb), the sample will absorb about 100 photons per pulse and will emit close to that number into 4π as 14.4-keV photons (a fraction of about 11%), and Fe fluorescence (89%). In order to measure the fluorescent response at an accuracy of 1%, one then needs to collect the signal from 100 pulses (assuming Poisson statistics). At a pulse repetition rate of 3 MHz, this means that the signal can detect deviations from the resonant condition at frequencies up to $f_{FB} \sim 30$ kHz.

Several approaches for feedback making use of the fluorescence signal will be possible. One approach is the null-detection feedback technique employed at the Laser Interferometer Gravitational-Wave Observatory (LIGO) in which the fluorescence signal is processed while one of the XFELO Bragg mirrors is given a small-amplitude oscillation [16]. The method was successfully tested in a pilot experiment with a high-resolution, six-crystal x-ray monochromator at APS Sector 30 [17]. Another approach is to use the signal from multiple longitudinal modes by moving several samples at velocities in multiples of about 0.3 mm/s. As is well known in the Mössbauer-spectroscopy community, this velocity introduces a Doppler shift equal to the 14-neV mode spacing. With this technique, one can both increase the signal strength, and thus improve the bandwidth of the feedback loop, and avoid the non-Doppler-shifted mode altogether to leave it for experiments with stabilized radiation. Furthermore, samples can be Doppler-shifted to frequencies slightly above and below a resonance to obtain sign information for the feedback loop by taking the difference of their signals. This is shown schematically in Figure 3.

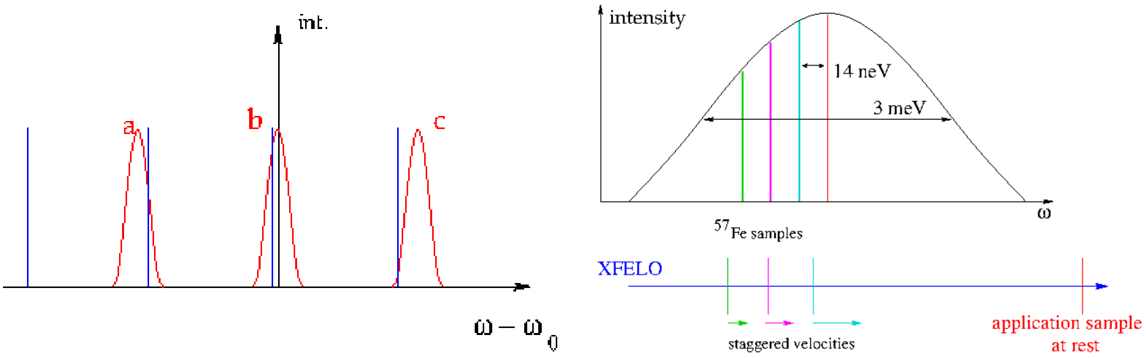

Figure 3: Using the Doppler shift on multiple samples (left) to increase the signal strength and (right) to obtain a sign signal for the feedback in addition to the maximum signal.

3.7.3.2 *Sources of Phase Noise*

There are several sources of phase noise that can degrade the lines of the output comb. Most types of phase noise occur while the intra-cavity pulse circulates in the x-ray cavity, from the fluctuation of the mirror position, the fluctuation in the gain due to the fluctuation in the electron beam parameters, etc. These phase noises are additive and lead to phase diffusion, resulting in spectral broadening as will be discussed shortly. Phase fluctuation occurring in transit through the outcoupling crystal and during the delivery to the sample will not, in general, be additive. Non-additive phase noise gives rise to a reduction in the coherent part of the signal. Here, we will assume that such noises can be controlled to an acceptable level and will not consider them further. With additive phase noise, the *n*th pass electric field in Eq. (3) is modified to

$$E_n(t) = e^{-i\psi_n - i\omega_{FEL}(t-nT_c)} A(t-nT_e) \ , \tag{11}$$

$$\psi_n = \sum_{k=0}^{n-1} \phi_k \ . \tag{12}$$

Here ϕ_k is the random phase picked up at the *k*th pass. Assuming that ϕ_k is a Gaussian random variable with an rms average σ and that each ϕ_k for different passes of k are independent, the average of the phase factor becomes

$$\left\langle e^{-i\psi_n} \right\rangle = \mathrm{e}^{-n\sigma^2/2} \ . \tag{13}$$

Since $n \approx t / T_e$ for the *n*th pass, we see that the radiation frequency becomes complex, with an imaginary part given by $\sigma^2 / 2T$ (here we simplify the time interval as T when it is not necessary to distinguish T_e and T_c), giving rise to a Lorentzian spectral shape with the half width

$$\Gamma_{eff} = \hbar\sigma^2 / 2T \ , \tag{14}$$

as discussed by Lax [18] in the analysis of a noise-driven harmonic oscillator.

In the above we have not taken into account the slow fluctuations that stay constant over several periods. It can be shown that the slow fluctuations may be taken into account by the substitution

$$\sigma^2 \rightarrow {\sigma_{eff}}^2 = {\sigma_1}^2 + 2{\sigma_2}^2 + 3{\sigma_3}^2 + \dots \ . \tag{15}$$

Here σ_q is the rms value of the fluctuation that stays constant over q periods. The sum in the above extends to $q = q_{max} = 1 / (f_{FB}T)$, where f_{FB} is the bandwidth of the feedback system controlling the fluctuation.

Let us consider specific sources of additive noise. First, there is spontaneous undulator emission, which is superposed on the radiation from the FEL gain process. The spontaneous power emitted into one transverse mode is about 10^{-8} of the FEL-beam power itself, corresponding to $\sigma^2 \sim 10^{-8}$. From Eq. (14), with $T = 300$ ns, the corresponding spectral width is about 10^{-17} eV.

Next, there are cavity-length fluctuations due to seismic vibrations of the mirror mounts. This has been studied in detail in the context of laser-interferometric gravitational-wave detectors [19]. The seismic motion amplitude exhibits strong frequency dependence, as expressed by the empirical formula for spectral power density

$$\frac{\Delta L^2[m^2]}{\Delta f[\mathrm{Hz}]} = 10^{-18}\left(\frac{10Hz}{f}\right)^4 \equiv G(f) \ . \tag{16}$$

The fluctuations that remain constant for the duration of qT will come from frequency near $f \sim 1 / (qT)$. The fluctuation from all frequencies over an interval from f_0 to $1 / T$ is then

$$\begin{aligned}\langle \delta L \rangle^2 &= \left(\frac{\lambda_{FEL}}{2\pi} \right)^2 \sigma^2 \approx \sum_{q=1}^{1/(Tf_0)} qG(1/qT) \left(\frac{1}{qT} - \frac{1}{(q+1)T} \right) \\ &\approx \int_{f_0}^{1/T} dfG(f)\frac{1}{Tf}\end{aligned} \qquad (17)$$

Requiring σ to be about 0.1 (δL ~ 1% of the x-ray wavelength), we obtain f_0 ~ 8 kHz, i.e., below the feedback-loop bandwidth determined above. Great care must be taken, however, to keep vibrations from equipment and machinery below the natural seismic level.

Heat load from x-ray absorption in the cavity mirrors couples to mechanical motion through thermal expansion. This requires detailed engineering studies, which are not available at this time. Nonetheless, a few design guidelines may be mentioned: at cryogenic temperatures the thermal expansion of diamond is drastically reduced to the 10^{-9} / K level [20, 21]. Heat conduction is greatly improved by the use of isotopically pure diamond, as is standard in the electronics industry. The heat load is pulsed at 3 MHz, and therefore mechanical resonances should be kept far from this frequency. That leaves only lower-frequency vibrations due to an envelope of the pulsed x-ray intensity.

Fluctuations in electron beam parameters will also contribute to the phase fluctuations through fluctuation in FEL gain. These effects are expected to be small but need further analysis.

3.7.4 **Applications**

3.7.4.1 ***Time and Length Standard***

Nuclear resonances are typically extremely sharp and thus hold great potential as time and length standards. An NR-XFELO would be an intense source of very narrowband radiation for use in metrology. The isotope ^{45}Sc with a 10^{-15}-eV linewidth of a resonance at 12.4 keV would match the natural linewidth of an XFELO with the above parameters for an accuracy of 10^{-19}, and other isotopes, such as ^{103}Rh (39.8 keV, 1.35×10^{-19} eV) may improve this even further. This is several orders of magnitude better than current atomic clocks. To fully make use of such an ultra-stable x-ray reference, one has to tie the x-rays to optical-wavelength standards. This can be done interferometrically, as first proposed by Shvyd'ko [22]. In that concept, a pair of sapphire crystals forms a Fabry-Perot interferometer simultaneously for x-rays and for visible light. To count x-ray fringes, the fluorescence response of resonant nuclei would be monitored, which respond only to a narrowband section of a potentially much broader incident spectrum from, e.g., a synchrotron radiation source. In a cm-long scan, about 10^8 x-ray fringes and 10^4 optical ones are counted. To reach an accuracy of 10^{-12}, corresponding to the natural linewidth of ^{57}Fe, one would then have to interpolate 10^4-fold for the x-rays, and 10^8-fold for the optical interference, i.e., measure the intensities in steps of the order of 10^{-14} m.

An NRS-XFELO offers a way of achieving the same accuracy with significantly relaxed requirements on the resolution: by scanning a standing x-ray wave over a distance of, say, 10 m, an accuracy of 10^{-12} can be reached in steps of 10^{-11} m, i.e., by interpolating 10-fold and 10^5-fold between x-ray and optical fringes, respectively. The highly collimated, single-transverse-mode output of an XFELO is needed in this scheme to eliminate geometric path errors over the 10-m scan range. In order to avoid jumping of modes leading to mis-counts of fringes, nuclear-resonant cavity stabilization of the XFELO is required. Furthermore, with isotopes exhibiting narrower resonances than ^{57}Fe, the cavity stabilization is essential to keep the radiation on-resonance all the time, and not just a fraction statistically proportional to the ratio of resonant linewidth to cavity-mode spacing (here, 14 neV).

Figure 4 shows a possible implementation with an assembly of two x-ray-focusing Fresnel zone plates and a single nucleus of ^{57}Fe embedded in a host crystal of light elements (diamond or beryllium metal) traveling along a 10-m-long standing-wave field generated by back-reflection of the output from an NR-XFELO. The distance of this assembly from the back-reflecting mirror is measured optically to 10^{-11} m, which is possible with commercial heterodyne interferometers. The left-hand zone plate focuses the incident beam to 50 nm, and the right-hand one re-collimates it and then focuses the returning beam. With an absorption cross section of 10^{-22} m^2 [7] and a flux of 10^3 resonant photons per pulse repeating at 3 MHz, a single ^{57}Fe nucleus in that focus will absorb a few thousand photons per second for a reasonably strong signal. Using a single nucleus eliminates inhomogeneous broadening, which is especially important for isotopes narrower than ^{57}Fe. Sparse sampling using pre-existing knowledge of the resonant wavelength can be employed to significantly reduce the number of fringes to be counted.

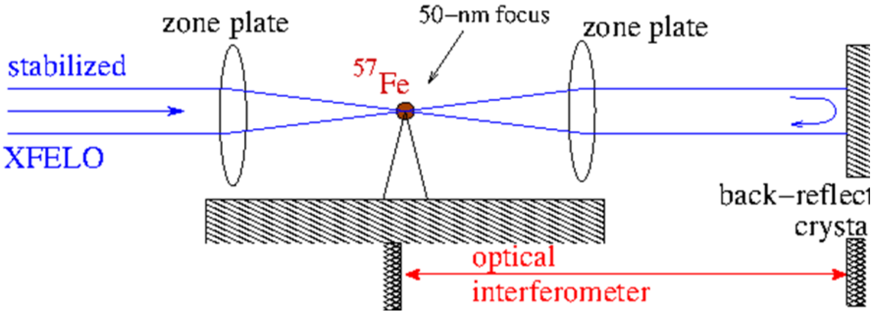

Figure 4: Schematic depiction of how to probe a meter-to-kilometer-long x-ray standing-wave field while comparing to an optical length standard. Two Fresnel zone plates generate a 50-nm x-ray focus that travels along the standing waves. A single ^{57}Fe nucleus in the focus senses the standing-wave intensity through resonance fluorescence.

For narrower-line isotopes, the scan could be extended to cover, say, 1 km. As long as the cavity stabilization is maintained, the signal from the narrow-line nucleus is of the same order of magnitude (some percent fraction of λ^2) as that from ^{57}Fe.

3.7.4.2 *Coherent Control in Quantum Optics*

In quantum optics, light is used to control matter, and the back-action of the matter on the light is measured. X-rays can significantly expand the scope of such experiments, making use of the different types of matter-light interaction (x-rays interacting with inner-shell electrons and nuclei rather than valence electrons, x-ray photons approaching the pair-production energy, and x-rays carrying significantly higher photon momentum than eV-scale photons). Especially attractive for quantum optics is the use of nuclear resonances because these offer clean two-level interactions with very little decoherence from coupling to other degrees of freedom. One may even observe spontaneously generated coherence [23]. Most experiments require well-defined light-matter interactions strengths. For example, coherent population transfer (π/2 pulses to generate 50% superposition states, or π pulses for full transfer from ground to excited state) is achieved by light pulses of a carefully controlled intensity-time integral, and with carefully defined tuning relative to a resonance. Evidently, the NR-XFELO is an ideal radiation source in such experiments. Examples are given in the next two sections. See also the article by Jörg Evers in this issue.

3.7.4.3 ***Matter-wave Interferometry***

Atomic and molecular matter-wave interferometers have become a standard tool of quantum optics, and are used in experiments ranging from studies of fundamental physics to precision measurements of magnetic or gravitational fields. In a reversal of roles compared to optical interferometers, laser standing waves act as beam splitters and mirrors through the transfer of pairs of photon momenta by absorption from one wave, and stimulated emission from the other. A limitation in these experiments is the relatively small photon momentum at the eV scale, which makes it impossible to spatially separate interfering beams for realistic beam velocities (m/s) and cross sections (sub-mm). This will be quite different with x-rays [24]. For example, the recoil velocity of a ^{57}Fe nucleus after absorption of a 14.4-keV photon is 42 m/s. It is thus easy to achieve large opening angles between the arms of a matter-wave interferometer and explore macroscopic distances of gravitational or other resonance-shifting fields. One may also think of placing a shielded region containing a vector potential inside the interferometer, similarly to experiments exhibiting the Aharonov-Bohm effect.

A very interesting possibility would be to realize a recently proposed experiment to explore the linkage of quantum physics and gravitation [25]. In this proposal, the interfering matter has a built-in clock that measures the proper time of passage through the interferometer arms. If the two arms are at different gravitational potentials, then which-way information may be extracted by reading the clock, and this should reduce or eliminate the interference-fringe contrast. Such an experiment might be realized using an NR-XFELO and molecules with two or more resonant nuclei. The nuclei fulfil the dual roles of taking up large momenta from x-ray standing waves and as built-in clocks. Making this work without incurring which-way information in the absence of gravitational red-shift requires some careful design.

A possible realization may be as follows in a combined matter-wave and Ramsey interferometer, as illustrated in Figure 5. A beam of molecules containing two ^{45}Sc atoms in the nuclear ground state g enters an x-ray standing wave tuned to the intensity of a π/2 pulse from a ^{45}Sc-NR-XFELO. Momentum is exchanged by photon absorption or stimulated emission. Several processes, all occurring in quantum superposition can lead to a net momentum transfer of zero, one, or two photon momenta in well-separated beams. In addition to the beam separation of the matter-wave interferometer, the quantum superposition of doubly exited and doubly ground-state molecules also is a Ramsey interferometer, i.e., a clock ticking at about 10^{19} Hz. The next standing wave acts as a reflector in the matter-wave interferometer while maintaining the quantum superposition of doubly excited and doubly ground-state molecules. Finally, a third standing wave acts as a recombining beam splitter of the matter-wave interferometer and an interrogator of the Ramsey interferometer. The outcome after this pulse depends on the dynamic-phase evolution between the preparation and interrogation pulses, i.e., the proper-time including gravitational red-shifts. An NRS-XFELO is essential for this to maintain coherence over the entire time of the experiment from preparation to interrogation. Furthermore, the meV bandwidth covers the range of recoil Doppler shifts. However, the line spacing of the comb must be chosen carefully to make a Doppler-shifted molecule match a line in the comb.

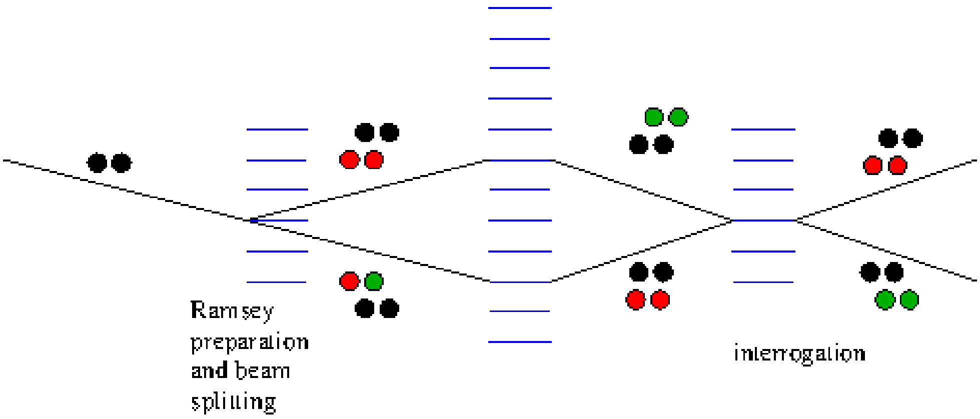

Figure 5: Schematic of a combined matter-wave and Ramsey interferometer with resonant nuclei. A beam of molecules with two resonant nuclei in their ground states (black) enters the first standing wave, which is tuned to provide a π/2 pulse for each of the two nuclei, leaving each of them in a superposition of ground (black) and excited (green or red) states (Ramsey state preparation). Photon absorption and stimulated emission also lead to momentum transfer, and thus a separation of beams. Only those molecules in which two absorption/stimulated-emission events have taken place are shown—singly-excited molecules continue on the dashed path and are discarded.

"Green" and "red" are the same excited state and are thus indistinguishable. The colors serve only to clarify the direction of momentum transfer. In the next standing wave an exchange of two photon momenta reflects the beams. Molecules taking up one or no net photon momentum are discarded. The third standing wave serves as both the analyzer of the matter-wave interferometer and the interrogator of the Ramsey interferometer.

3.7.4.4 *Decoherence in Mesoscopic Quantum Physics*

An experiment currently underway has the goal of understanding quantum decoherence in mesoscopic cases [26]. There is reason to believe that there is a transition of the character of decoherence as one goes from the microscopic world to that of real-sized cats, or other macroscopic entities, and that this goes beyond the simple argument of multiplicity of degrees of freedom. The experiment aims to trap glass spheres of about 100 nm diameter in a laser standing wave, where dielectric forces push the glass towards the intensity maxima. The spheres are then to be cooled to the vibrational ground state in the trapping potential without necessarily being cold with respect to their internal degrees of freedom. The wavefunction of the 100-nm object then has a size of a few 100 nm, corresponding to the wavelength of the light. When the trapping potential is turned off, this wavefunction can spread out over time. A laser pulse focused into this wavefunction can either lead to light scattering, thus localizing the glass sphere, or it can miss the sphere. In the latter case, the sphere then exists in a quantum superposition state of being to the left or the right of the focus, and this will lead to interference in the further evolution. X-rays can be focused much tighter than visible or UV light and can thus be used to probe the earlier time scales of the quantum evolution of the mesoscopic object. For this, one would use a glass sphere with a nanoparticle of nuclear-resonant material, such as ^{57}Fe, and an NR-XFELO tuned to this resonance. If the focused x-rays produce resonance fluorescence, the nanoparticle and thus the surrounding sphere are localized; otherwise they are not.

3.7.5 **Summary**

A cavity stabilized XFELO using nuclear resonance, NRS-XFELO, will vastly improve its coherence properties of an XFELO and thus its science reach. Realizing an NRS-XFELO appears to be within the current state of the art, at least with ^{57}Fe resonance. Extending the stabilization to narrower resonances by an order of magnitude should also be feasible. NRS-XFELOs for even narrower resonances will be quite challenging but worthwhile as they provide new scientific techniques hitherto not available in hard x-ray wavelengths, with applications in fundamental physics such as quantum gravity and the study of how decoherence emerges in mesoscopic systems.

3.7.6 **Acknowledgments**

We would like to thank Jörg Evers for helpful discussions on quantum-optical applications of the XFELO. This work was supported by the U.S. Department of Energy, Office of Science, under Contract No. DE-AC02-06CH11357.

3.7.7 **References**

1. B.W. Adams, C. Buth, S. M. Cavaletto, J. Evers, Z. Harman, C. H. Keitel, A. Pálffy, A. Picon, R. Röhlsberger, Y. Rostovtsev, K. Tamasaku, J. Mod. Opt. 60, 2-21 (2013).
2. M.O. Scully and M.S. Zubairy, *Quantum Optics*, (Cambridge University Press, 1997).
3. R. Colella and A. Luccio, Optics Comm. 50, 41 (1984).
4. K.-J. Kim, Y. Shvyd'ko, and S. Reiche, Phys. Rev. Lett. 100, 244802 (2008).
5. K.-J. Kim and Yu. V. Shvyd'ko. Phys. Rev. ST Accel. Beams 12, 030703 (2009).
6. R. R. Lindberg et al., Phys. Rev. ST Accel. Beams 14, 010701 (2011).
7. H. Fraunfelder, *The Mössbauer Effect*, (W.A. Benjamin, New York, 1963).
8. R. Bonifacio, N. Narducci, and C. Pellegrini, Opt. Commun. 50, 373 (1984).
9. P. Emma for the LCLS Team, Proc. of the 2009 Part. Accel. Conf., TH3PBI01, p. 315 (2011).
10. G. Geloni, V. Kocharyan, and E.L. Saldin, J. Modern Optics 58, 1391 (2011); G. Geloni, V. Kocharyan, and E.L. Saldin, "Cost-effective way to enhance the capabilities of the LCLS baseline," DESY 10-133, August 2010.
11. J. Amman et al., "Demonstration of self-seeding in a hard X-ray free-electron laser," Nature Photonics 6, 693 (2012); doi: 10.1038/nphoton.2012.180.
12. B.W. Adams and K.-J. Kim, in preparation.
13. C. A. Brau, *Free-Electron Lasers*, (Academic Press Inc., 1990).
14. H. Al-Abawi et al., Opt. Commun. 30, 235 (1979).
15. S. T. Cundiff and J. Ye, Colloquium: Femtosecond Optical Frequency Comb, Rev. of Modern Physics 75, (2003).
16. We thank Stan Whittcomb for discussions on this topic.
17. S. Stoupin et al., Rev. Sci. Instrum. 81, 055108 (2010).

18. M. Lax, "Classical noise V. Noise in self-sustained oscillators," Phys. Rev. 160, 290 (1967).
19. P. Saulson, http: // cgwa. phys. utb. edu/ Files/Events/ 29_ 630_ Saulson_ 0614_ Vibration_Isolation.pdf
20. S. Stoupin and Yu. V. Shvyd'ko, Phys. Rev. Lett. 104, 085901 (2010); S. Stoupin and Yu. V. Shvyd'ko, Phys. Rev. B 83, 104102 (2011).
21. See also Y.V. Shvyd'ko, these proceedings.
22. Y. V. Shvyd'ko, *X-Ray Optics*, (Springer Series in Optical Sciences, 2004).
23. K. P. Heeg, H.-C. Wille, K. Schlage, T. Guryeva, D. Schumacher, I. Uschmann, K. S. Schulze, B. Marx, T. Kämpfer, G. G. Paulus, R. Röhlsberger, and J. Evers, "Spontaneously Generated Coherences in the X-ray Regime," submitted (2013).
24. G. Huber, B. W. Adams, in "TESLA Technical Design Report, Part V," http://tesla.desy.de/new_pages/TDR_CD/PartV/xfel.pdf (2001).
25. M. Zych, F. Costa, I. Pikovski, and C. Brukner, "Quantum interferometric visibility as a witness of general relativistic proper time," Nature Communications 2, 1 (2011).
26. O. Romero-Isart, A.C. Pflanzer, F. Blaser, R. Kaltenbaek, N. Kiesel, M. Aspelmeyer, and J. I. Cirac, "Large Quantum superpositions and interference of Massive Nano-meter sized object," Phys. Rev. Letters 107, 020405 (2011).

3.8 Feasibility of X-Ray Cavities for Free Electron Laser Oscillators

Yuri Shvyd'ko
Advanced Photon Source, Argonne National Laboratory, Argonne, IL 60439, USA
Mail To: shvydko@aps.anl.gov

Abstract:

X-ray free electron laser oscillators (XFELO) will produce fully coherent x-rays with record spectral purity and average brightness in the hard x-ray regime from ≃5 keV to ≃25 keV. Feasibility studies of x-ray cavities for XFELOs are reviewed here. We discuss optical schemes of the x-ray cavities as well as technical challenges, and present results of experimental and simulation studies. The results show that the technical challenges are demonstrably solvable. No principle obstacles have been detected yet, that would hinder the feasibility of the XFELO x-ray cavities.

3.8.1 **Introduction**

An x-ray FEL oscillator (XFELO) is predicted to produce x-rays with unprecedented spectral purity and average brightness in the hard regime from ≃5 keV to ≃25 keV [1-4]. Two technologies are of critical importance for the realization of the XFELO: first, an ultra-low-emittance injector producing low intensity electron bunches at a constant repetition rate ≃1 MHz, and, second, a stable, low-loss x-ray cavity consisting of Bragg back-reflecting crystals and curved grazing-incidence collimating and focusing mirrors.

XFELO x-ray cavities are closed low-loss circuits for x-rays, comprised of Bragg reflecting diamond crystals as primary mirrors combined with grazing-incidence curved focusing and collimating mirrors for transverse mode profile control. The main challenges for the XFELO cavities are: achieving diamond crystals and grazing-incidence mirrors with high reflectivity and low wavefront distortions; stringent tolerances for angular, spatial, and heat load stability of the optical elements; and radiation damage of optical elements.

The feasibility of the x-ray cavity, and thus of the XFELO in general, was questioned by experts, because of “the mirror limitations” [5]. In the framework of R&D started at Argonne National Laboratory in 2008, the main technical challenges, including the mirrors issues, have been addressed.

Non-tunable and tunable x-ray cavities have been proposed for the XFELO [1, 2, 6]. In both cases, the main components are Bragg reflecting crystals and grazing-incidence focusing and collimating mirrors. There are two main requirements to the optical cavity and its components. First, the FEL gain should overcome the round-trip cavity loss. As a result, the cavity loss should not be more than 20%. This means that each element, the crystals and mirrors, should feature more than 96% reflectivity with minimum wavefront distortions. Second: the cavity elements have to be stable. In particular, the relative angular stability of the crystals’ orientation should be better than 10 nrad (rms), the spatial stability better than 3 μm (rms), and the temperature variations on the crystals (expressed in the units of the photon energy variations) should be less than a few meV, sometimes less than a few tenths of meV. These requirements determine the milestones for the R&D program on the feasibility of the optical cavity, which includes four main components: (i) study of the availability of high-quality crystals of high reflectivity; (ii) feasibility of grazing-incidence mirrors with $\lesssim$0.1 μrad (rms) slope error; (iii) stabilization of the optics components (angular, spatial, temperature); and (iv) damage of the optics components by XFELO x-ray beams.

The paper presents an overview of the solutions or approaches to the solutions of the principle problems.

3.8.2 Optical Schemes of X-Ray Cavities

3.8.2.1 *Two-Crystal Cavity*

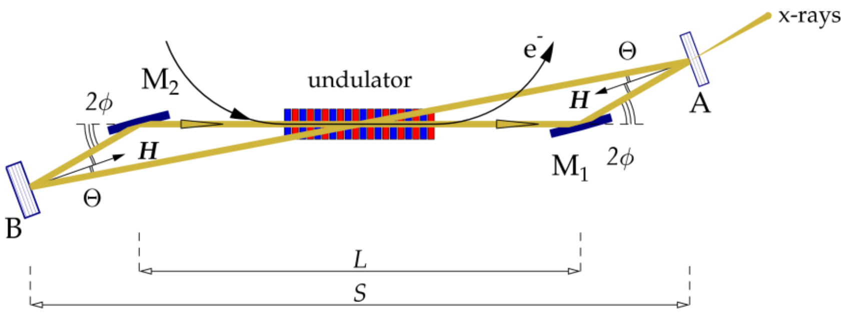

Figure 1: Scheme of an x-ray cavity with two crystals at near-normal incidence. The grazing incidence mirror M$_1$ collimates the x-ray beam, while M$_2$ focuses x-rays onto the electron bunch e$^-$ in the undulator [2]. This cavity configuration has a very restricted range of tunability because of the small grazing angle of incidence $\varphi \simeq 1$ mrad.

The basic configuration of an XFELO cavity is shown in Fig. 1. An x-ray pulse about 1 ps (rms) long is stored in an optical cavity consisting of two crystal Bragg back-reflectors A and B, and grazing-incidence mirrors M$_1$ and M$_2$. Each time the pulse arrives at the undulator entrance it meets an electron bunch, and they travel together through the undulator leading to an amplification of the x-ray pulse. The pulse energy increases exponentially as the pass number increases, assuming that the FEL gain can overcome the round-trip cavity loss. Eventually, the gain decreases due to nonlinear effects, and the FEL reaches a steady state when the gain balances the loss [1,3]. One of the crystals is made thin so that a fraction ≃5% of the intracavity power is coupled out as the output power.

The grazing-incidence curved mirror M_1 collimates the x-rays radiated from the undulator to almost parallel beam impinging upon the backscattering crystals, and thus ensures the maximum crystal reflectivity. A small grazing angle of incidence $\varphi \simeq 1$ mrad is chosen for high mirror reflectivity. Crystals are oriented so that the incident and exit x-rays at each crystal form the same angle Θ with respect to the diffraction vector $\vec{H}$, normal to the reflecting atomic planes. The angles of incidence and reflection are equal. Ellipsoidal grazing-incidence mirror M_2 closes the loop of the x-ray path and focuses x-rays onto the electron bunch e^- in the undulator. The focal length of mirrors M_1 and M_2 has to be carefully chosen to control the intracavity mode profile and optimize the coupling of the x-ray and the electron beams [3]. Line M_1M_2 passes through the XFELO undulator. The length L of the path M_1M_2 is large, much larger than the undulator length, which is typically 50 m. In examples considered in the following $L \simeq 100$ m. This value also determines the round trip flight time $2L/c \simeq 0.66$ μs and minimal repetition rate ≃1.5 MHz of the electron bunches.

The mirror is oriented so that the incident and exit x-rays are symmetric to the normal of the mirror surface. The grazing angle of incidence on the mirror is then 2Θ. The photon energy E is determined by Bragg's law $E = E_H/\sin\theta$. Here, E_H is the Bragg energy, the energy of photons reflected at normal incidence from the atomic reflecting planes with the Bragg diffraction vector $\vec{H}$. The angle of incidence Θ is complementary to the Bragg angle $\theta = \pi/2 - \Theta$. The photon energy E can be changed by changing Θ, which is accomplished by changing the distance L and reorienting the crystals to maintain Bragg reflection. However, the tuning range in this configuration is restricted by the requirement that the grazing angle of incidence $\varphi = 2\Theta$ on the mirror be much smaller than the critical angle θ_{cr} of total reflection. For photon energy $E \simeq 10$ keV, typically $\theta_{cr} \approx 1\text{-}3$ mrad. This requirement turns out to be too strict to allow practically interesting tuning ranges.

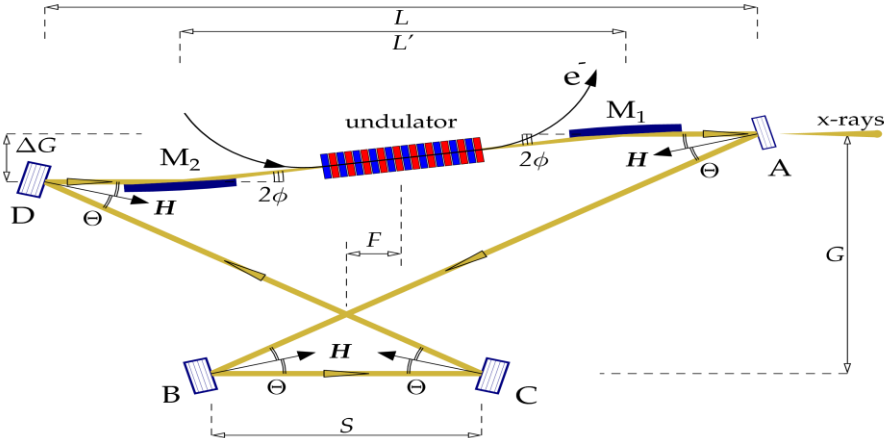

Figure 2: A scheme of a four-crystal (A,B,C, and D) x-ray optical cavity allowing a broad range of energy tuning assuming that the focusing elements are the ellipsoidal mirrors M_1 and M_2 used as collimating and focusing elements.

3.8.2.2 *Tunable Four-Crystal Cavity*

An x-ray cavity that is tunable over a broad energy range can be constructed by employing a four-crystal configuration or more than four-crystal configurations, as was proposed by Cotterill almost 40 years ago [7, 8]. Figure 2 shows how this could be adopted for the XFELO [2]. Four identical crystals A, B, C, and D are placed at the four corners of a trapezoid, so that the x-rays propagate along the zigzag path. The function of the grazing-incidence mirrors M_1 and M_2 is the same as in the case of the two-crystal cavity in Fig. 1. To change the energy of x-ray photons trapped by the cavity, the angles of incidence Θ for all four crystals have to be changed simultaneously. The positions of crystals A and D as well as of the mirrors are fixed for convenience, so that the lengths L, L', and ΔG are constant. The positions of crystals B and C are changed to adjust the same angle Θ for all crystals. The dependence of the lengths G, F, and S on Θ is determined by the requirement that the round-trip path length for x rays in the cavity is constant, i.e., independent on Θ. These dependencies of the lengths and crystal angles on photon energy are derived in [1]. The length L of the path AD is long, about 100 m for examples considered in Ref. [2]. The four-crystal geometry requires that $\Theta<\pi/4$. An equivalent crystal configuration is used in the so-called (+−−+) four-crystal x-ray monochromator, and therefore, its theory was applied to describe the single-pass spectral properties of the cavity (see, e.g., [9] for references and details).

3.8.2.3 *Tunable Multi-User Compact Cavity*

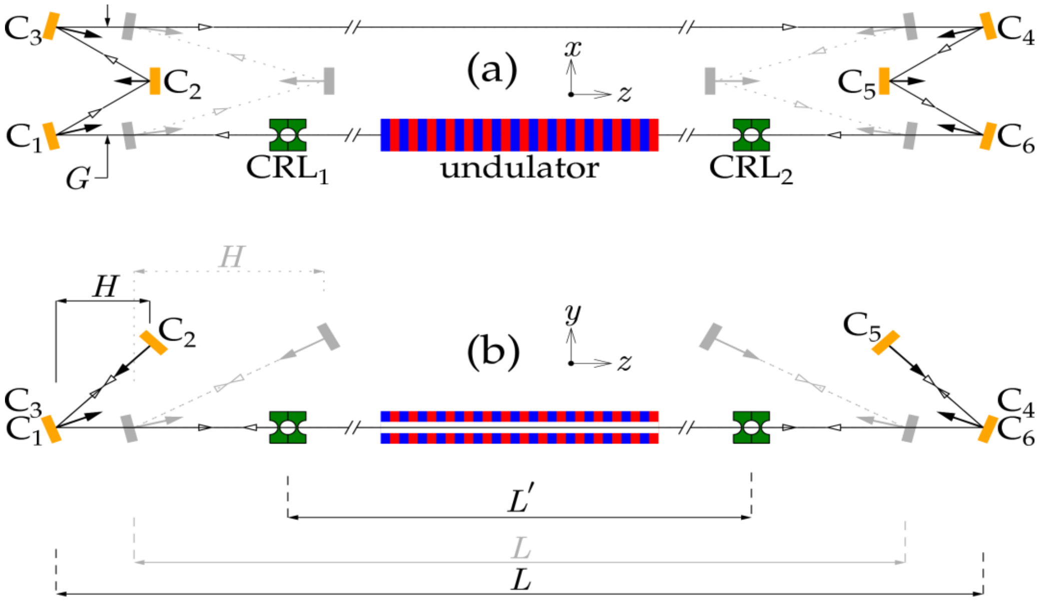

Figure 3: Schemes of a six-crystal non-coplanar x-ray cavity with crystals (orange blocks) set into Bragg reflections with Bragg angle $\Theta=65^\circ$ [6]. (a) Top view. (b) Side view. If the Bragg angle changes to $\Theta=75^\circ$ (crystals new positions are shown as gray blocks) the energy of photons circulating in the cavity changes by $\simeq$6%. A constant time of flight is ensured by changing the longitudinal size of the cavity L, keeping L', and G constant. If G=0.5 m, then H=0.38 m, and H'=0.84 m.

The tunable cavity shown in Fig. 2 is not compact. Its lateral size G is almost as large as the size L along the undulator. A tunable cavity, with a smaller lateral dimension can be designed, however, the number of crystals and Bragg reflections have to be increased to six. The crystals should be also arranged in a non-coplanar, i.e, three-dimensional, scattering geometry as shown in Fig. 3 [6]. There are two "backscattering" units comprising three crystals C_1, C_2, C_3 on one side of the undulator and C_4, C_5, C_6, on the other side of the undulator. Collimating and focusing elements are shown as CLR_1 and CLR_2. These elements could be grazing-incidence mirrors as in the schemes of Fig. 1 and Fig. 2. In the schematic shown in Fig. 3 they are presented by another possible alternative – compound refractive lenses (CRL) [10, 11].

In each backscattering unit, three successive Bragg reflections take place from three individual crystals to reverse the direction of the beam from the undulator. Assuming all the crystals and Bragg reflections are the same, the Bragg angles can be chosen in the range $30° < \theta < 90°$. Bragg angles close to $\theta=45°$ should be avoided to ensure high reflectivity for both linear polarization components, as the reflection plane orientations for each crystal change. The cavity allows for tuning of photon energy in a large spectral range by changing synchronously all Bragg angles. To ensure constant time of flight, the cavity length L and the distance between the crystals H have to be changed with θ. The lateral size G can be kept constant and small, $\lesssim 0.5$ m. In the example shown in Fig. 3, the photon energy is changed by $\simeq 1$ keV, assuming an average energy $E \simeq 15$ keV. The linear positions of the crystals are changed by less than 1 m.

Because C_1C_6 and C_3C_4 lines are fixed, the intracavity radiation power can be out-coupled simultaneously for several users at several different places in the cavity. Outcoupling through crystals C_1 and C_4 is most favorable, as the direction of the outcoupled beam does not change with photon energy. Additional outcoupling for more users through crystals C_3 and C_6 could be possible too.

Of course, such cavities are more involved. In particular, to keep total cavity losses at a low level, crystal reflectivity should be close to 97%-99%, or higher FEL gain would be required. Controls and stability are also more demanding.

3.8.3 Diamond Crystals as Bragg Reflecting Mirrors

The single-pass gain of the XFELO must overcome the radiation losses incurred in the optical cavity. The losses include those due to out-coupling of the x-rays from the cavity for the XFELO users ($\lesssim 5\%$), absorptive losses, and incoherent scattering losses in the cavity crystals and mirrors due to imperfections, relative misalignment, or temperature differences and inhomogeneities. Single-pass gain of the XFELO may be as low as 30%. This requires mirrors and crystals for the x-ray cavity, especially in four-crystal of six-crystal configurations, to have high reflectivity $R \gtrsim 0.96$. Feasibility of the crystal "mirrors" with high reflectivity is addressed in this section. Reflectivity and performance of the grazing-incidence mirrors will be discussed in Sec. 3.8.5.

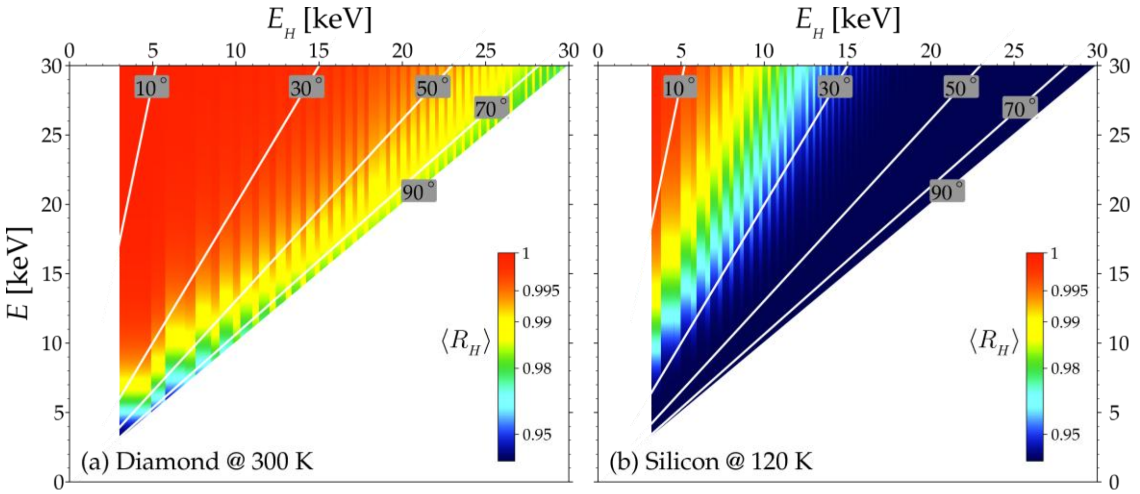

Figure 4: Color maps of averaged Bragg reflectivities $\langle R_H \rangle$ of hard x-rays from thick crystals averaged over the region of total Bragg reflection: (a) for diamond at 300 K and for comparison (b) for Si at 120 K. The averaged reflectivities are shown for all allowed Bragg reflections sorted by Bragg energies $E_H < 30$ keV, and for the incident photon energies $E > E_H$ keV. White contour lines indicate equal values of incidence angle Θ determined by Bragg's law $\sin\Theta = E_H/E$

3.8.3.1 *Reflectivity of Diamond Crystals*

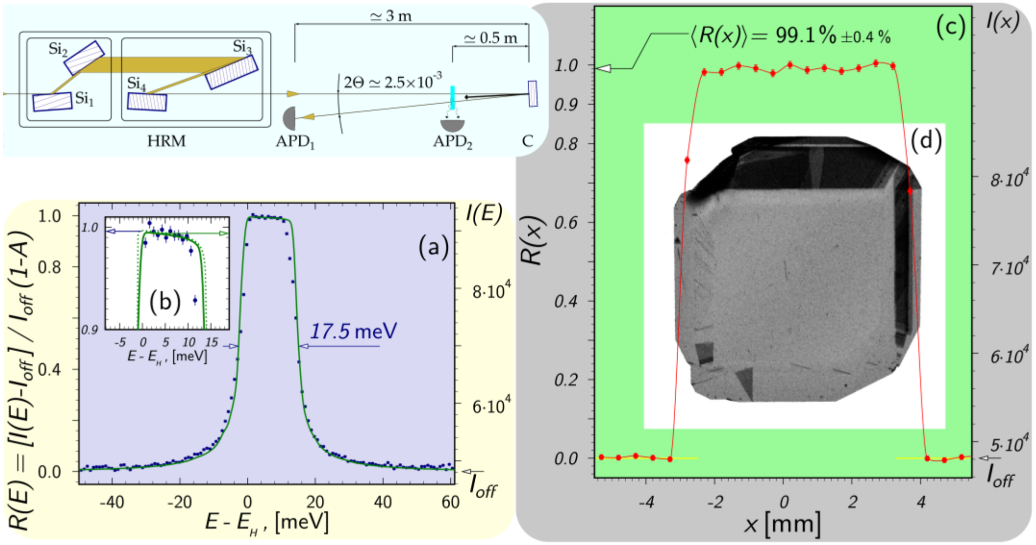

Figure 5: Nearly defect-free diamond crystal reflects more than 99% of hard x-ray photons backwards in Bragg diffraction, with a remarkably small variation in magnitude across the sample [12, 13]. (a)-(c) Reflectivity of 13.9 keV x-rays from the (8 0 0) atomic planes of a diamond crystal in Bragg backscattering, and (d) X-ray Lang transmission topogram of the diamond crystal. (top left) Scheme of the experimental layout with a specially designed monochromator with a 1 meV bandwidth [14].

Total (100%) reflection is achieved in Bragg diffraction of x-rays from crystals when the following conditions are met: first, there are no losses in the crystal due to, e.g., photoabsorption; and second, the crystal is sufficiently thick, much thicker than the extinction length L_H^{ext}.

In reality, photoabsorption always exists, and 100% reflectivity cannot be achieved. However, the peak reflectivity could be close to 100% provided the photoabsorption length L^{ph} in the crystal is much larger than the extinction length: $L^{ph} \gg L_H^{ext}$. This condition is fulfilled for crystals that have a high Debye temperature and are composed of low-Z atoms. High Debye temperatures ensure rigidity of the crystal lattice, so that a smaller number of atomic planes are required for maximum reflectivity. Low-Z atoms typically have larger photoabsorption lengths. Diamond, Be, BeO, Al_2O_3, SiC, etc., are among attractive crystals. However, diamond, due to a unique combination of superlative physical qualities, such as high thermal conductivity, low thermal expansion, high radiation hardness, and others [15] is most promising for use in XFELO cavities.

Figure 4(a) shows color maps of averaged Bragg reflectivities $\langle R_H \rangle$ of hard x-rays from thick crystals averaged over the region of total Bragg reflection: (a) for diamond at 300 K, and for comparison for Si at 120 K (b). Even under backscattering conditions when $\theta = 90°$, the averaged Bragg reflectivity of diamond can be about 99%. The peak reflectivity is even higher. In contrast, silicon crystals can feature such high reflectivity only at small Bragg angles $\theta \approx 20°$, not so interesting for XFELO cavity applications.

The high reflectivity of crystals in Bragg diffraction is intimately connected with the perfect crystal structure. There is a valid concern about availability of high-quality diamond crystals. Progress in fabrication, characterization, and x-ray optics applications of synthetic diamonds was substantial in the last two decades [16-25]. Still, the diamond crystals available commercially as a rule suffer from defects: dislocations, stacking faults, inclusions, impurities, etc. Synthetic, high-purity (type IIa, low nitrogen content) crystals grown with a high-pressure, high-temperature (HPHT) technique are generally considered to have the highest crystal quality and lowest density of defects among commercially available diamonds [21, 24, 25]. X-ray topography studies have demonstrated recently crystals with relatively large $\simeq 4 \times 4$ mm^2 defect-free areas [24-26]. Since the X-FELO beam footprint size on the crystals will be small, about 0.2 mm in diameter, *small*, high-quality single crystals look to be feasible.

Still, critical questions remains: Can the remarkably high reflectivity of diamond crystals that is predicted in theory – Fig. 4 – be achieved in practice? Is the quality of the presently available diamond crystals sufficiently high for practical use as high-reflectivity x-ray mirrors for XFELOs?

In the experimental studies performed at the Advanced Photons Source, briefly presented in Fig. 5, it was shown that the available synthetic type IIa diamond crystals indeed exhibit a high degree of perfection over the required area. By direct measurements, using hard x-rays with photon energies of E = 13.9 keV and E = 23.7 keV, it was demonstrated that nearly defect-free diamond crystals reflect more than 99% of hard x-ray photons backwards in Bragg diffraction, with a remarkably small variation in magnitude across the sample. Systematic observations of the more than 99% reflectivity eliminate high-reflectivity mirror limitations in the regime of hard x-rays, and marks an important step towards achieving x-ray cavity mirrors for XFELOs.

3.8.3.2 *Wavefront Distortions upon Bragg Reflection*

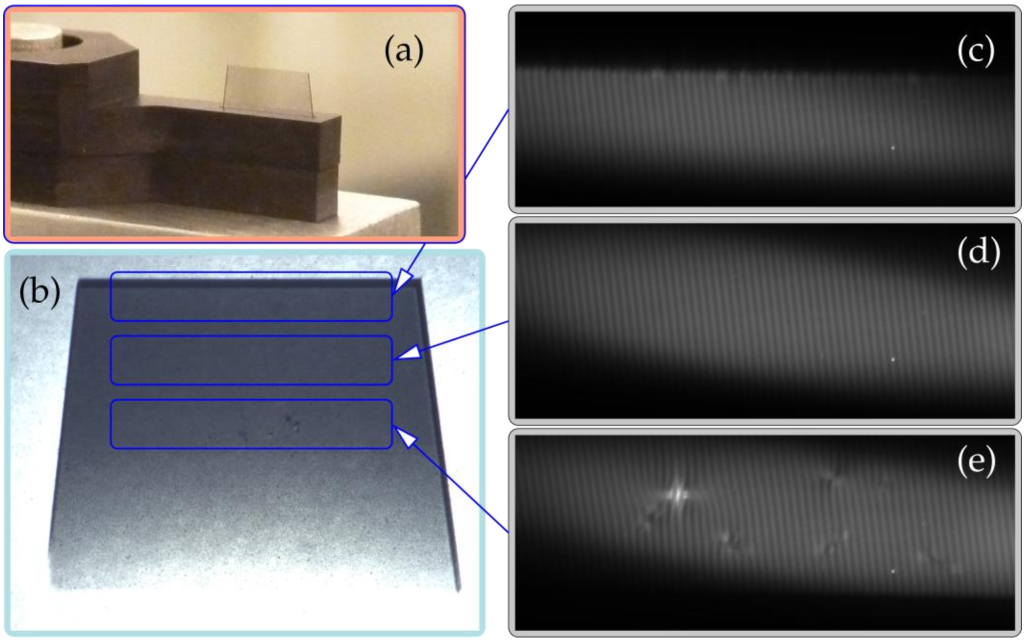

Figure 6: Wavefront Distortions upon Bragg Reflection. (a) A 0.1-mm thin diamond crystal plate in the (001) orientation in a graphite holder presently in use for self-seeding of the LCLS XFEL [27]. (b) The crystal was studied for the presence of defects by white beam topography using the (133) reflection in Laue geometry [26]. (c)-(e) The wavefront distortions upon Bragg diffraction from the (220) Bragg reflection in Laue scattering geometry were studied using a Talbot interferometer [28]. Interference fringes reveal small ≲0.5 μrad distortions in the defect-free areas (c) and (d). Crystal defects produce substantial wavefront distortions seen in (e).

XFELO cavity optics should have not only the highest reflectivity, it should also introduce minimal wavefront distortions of the radiation circulating in the cavity. The angular spread of x-rays from an XFELO with perfect x-ray cavity optics is expected to be ≃1 μrad (rms) or ≃2.4 μrad (FWHM) [1, 3]. Therefore, the real x-ray cavity optics may introduce wavefront angular variations much less than 1 μrad (rms) or 2.4 μrad (FWHM). There is a valid concern whether the available diamond crystals and crystal surface are sufficiently perfect to comply with such requirements.

With this purpose, the first wavefront measurements using a Talbot interferometer upon Bragg diffraction from a diamond crystal have been performed recently on diamond crystals from different manufacturers, such as Element6 and TISNCM [28]. In particular, a 0.1-mm-thick diamond crystal manufactured in TISNCM – Fig. 6(a) – was set into the (220) Bragg reflection in a Laue scattering geometry and showed only small wavefront distortions, with ≲0.5 μrad (FWHM) angular variation of the wavefront – Fig. 6(c)-(d) – across the defect-free area of 2×4 mm^2 – Fig. 6(c)-(d). These measurements represent more very encouraging results for the applicability of presently available diamond crystals as Bragg mirrors in XFELO cavities.

3.8.3.3 *Heat Load Problem and Thermal Stability*

The high reflectivity of crystals in Bragg diffraction is intimately connected with the perfect crystal structure. Temperature gradient $\delta T \Rightarrow$ may disrupt the perfect crystal lattice by producing gradients in crystal lattice spacing. Therefore, it may cause energy spread $\delta E/E=\beta\delta T$ of the reflection bandwidth, which may diminish the reflectivity.

To maintain high reflectivity, it is required that, when the next XFELO pulse arrives on the Bragg mirror, the energy variation of the reflection bandwidth caused by temperature gradients is much smaller than the Bragg reflection bandwidth itself. Since Bragg bandwidths are in the meV range, we require that temperature variations cause energy variations $\delta E \lesssim 1$ meV. Incident power of the XFELO pulse is $\simeq 50$ μJ/pulse [1, 3]. We assume that 2% photons are absorbed, i.e., the absorbed power is $\simeq 1$ μJ/pulse. The footprint of the beam on the crystal is $\simeq 100 \times 100\ \mu\text{m}^2$. Can such heat load cause detrimental energy variations and thus cause a problem for XFELO operations?

Figure 7 shows results of simulations of the time dependence of the crystal temperature, calculated for different offsets from the center of the beam footprint, and for different initial crystal temperatures $T(0)$ [29]. Simulations of the heat load on diamond crystal have been performed using time-dependent heat transport calculations. The temperature jumps occur every time a radiation pulse arrives at the crystal, due to almost instantaneous photoabsorption. The subsequent decay of the crystal temperature is due to the thermal diffusivity process in the crystal.

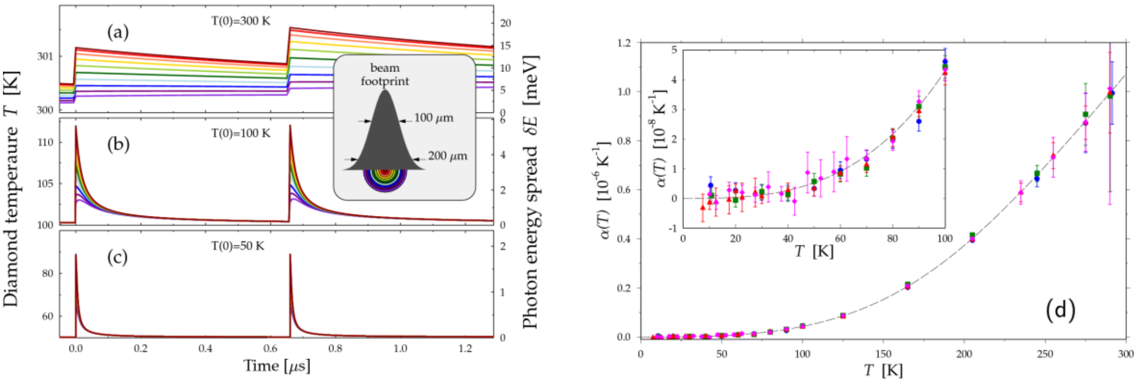

Figure 7: Temperature of the diamond crystal mirror exposed to the periodic XFELO undulator radiation pulses as a function of time [29]. Time dependencies are plotted in different colors corresponding to differing offsets from the center of the beam footprint on the crystal; the correspondence between color and transverse position is shown in the inset. The calculations are performed for three different initial diamond temperatures: (a) $T(0)=300$ K, (b) $T(0)=100$ K, (c) $T(0)=50$ K. X-ray photon energy $E=12.4$ keV, is assumed. The graph (d) shows the coefficient of linear thermal expansion in diamond measured at low temperatures [30, 31], used here to translate the temperature variation (left axis) to the photon energy variation (right axis).

The simulation results show that for diamond crystal to sustain the heat load of the radiation in the XFELO cavity, it is imperative to maintain the diamond crystal mirrors at low temperatures $T \lesssim 100$ K. In this case, the diamond has sufficient time to conduct the heat away into the bulk, so that the crystal temperature becomes completely homogeneous before the subsequent radiation pulse arrives – see Fig. 7(b)-(c). Conversely, if the crystal is maintained at room temperature – substantial temperature gradients stay behind as shown in Fig. 7(a). The favorable effect of low temperatures is due to the record high values of thermal diffusivity of diamond at $T<100$ K [15] and the extremely low linear thermal expansion coefficient of diamond at low temperatures – Fig. 7(d) [30, 31]. Isotopically enriched diamond crystals would be advantageous for such applications because of their improved thermal conductivity [32, 33].

3.8.3.4 *Dynamical Response of Crystals to Instantaneous Heating*

An XFELO x-ray pulse interacts with the Bragg reflecting crystal through diffraction and photoabsorption. The duration of the interaction, in the first approximation, is connected to the propagation time of the x-ray pulse through the crystal and to the pulse duration time. Both times are not more than 1 ps. The crucial question, related to the performance of the XFELO cavity is: Is it possible that during this short interaction time, a fast temperature change due to photoabsorption may result in a very fast deformation of the crystal lattice and therefore result in a reduced reflectivity? Assuming for simplicity the temperature rise is instantaneous, then common sense says that the deformation propagates with the longitudinal sound velocity, which is 18 μm/ns in diamond. Therefore for a 0.1-mm thick crystal the crystal deformation may take place after a few nanoseconds. This time is, however, too large to produce a negative effect on the reflectivity of the XFELO pulses.

To check this hypothesis, direct observation of the dynamics of thermal expansion using a pump-probe experiment with a laser pulse a as pump (instantaneous heating) and high-energy-resolution x-ray diffraction as a probe was performed [34]. Time evolution of the thermal expansion in the crystal lattice of diamond was studied on a time scale from 100 ps to 18 μs upon heating the crystal through its entire thickness with a penetrating 70−μJ optical laser pulse 8 ps in duration. About 26 μJ of the pulse energy were absorbed by the crystal in a spot area of 350 μm in diameter. The conditions were close to those expected for the XFELO. The results of the studies have basically confirmed the hypotheses. Crystal deformation takes place with sound velocity. No changes to the crystal reflectivity have been observed on a time scale less than 1 ns. The results are very important for the development of the XFELO x-ray cavity.

3.8.3.5 *Radiation Damage*

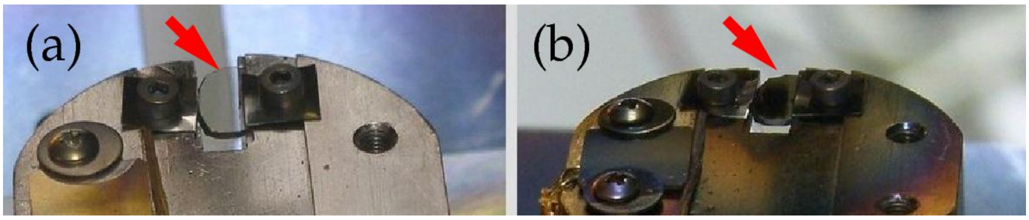

Figure 8: Diamond crystal in a water-cooled holder of a high-heat-load monochromator (HHLM) at APS. (a) Before the diamond crystal was exposed to the synchrotron beam. (b) After one year exposure to the synchrotron beam of 150 W/mm^2 power density. Blackening is observed of the crystal surface. No significant degradation in the performance of the HHLM is observed after years of operation.

The radiation delivered by the XFELO will have a very high average power density, about 4 kW/mm^2 on diamond crystals of the cavity. Diamond is known for its unique high radiation hardness. However, the power density is really high, and there is a valid concern whether such a high average power density may produce irreversible changes in the perfect crystal lattice structure and thus damage the diamond x-ray mirrors.

For comparison, the average radiation power density delivered by the most powerful undulators at third-generation synchrotron radiation sources such as the APS is about 150 W/mm^2, i.e., about 30 times less.

From the experience of operating high-heat-load double-crystal diamond monochromators exposed to direct undulator beams at the APS, it is known that some blackening appears on the surface of the first diamond crystal – Fig. 8(b). Blackening is already observable after several days of exposure. However, the blackening is not necessarily the result of the radiation damage. It maybe related to deposition of carbon or other light elements on the crystal surface from residual gasses in the UHV environment. This issue has not been studied yet. However, no significant degradation in the performance of the diamond HHLM at the APS was observed after years of operations, albeit, Bragg reflections with a broad $\simeq$0.5 eV bandwidth were in use.

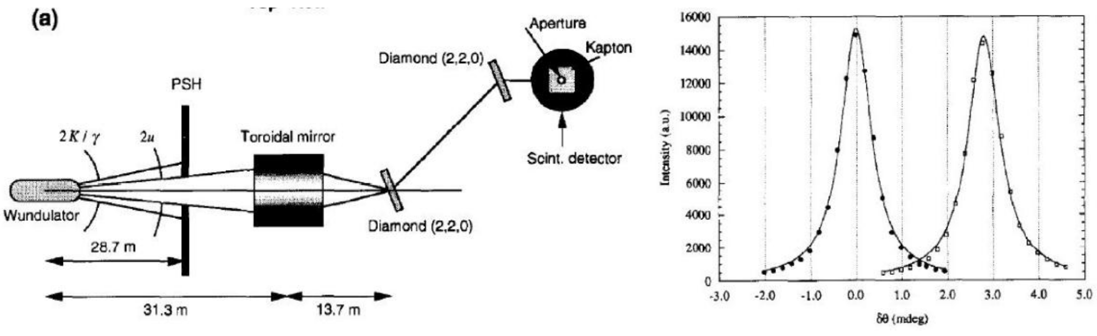

Figure 9: Performance of a water-cooled two-crystal diamond monochromator exposed to synchrotron radiation with a time-averaged power density of 3.5 kW/mm^2 [35]. (a) Layout of the experimental setup. (b) Two diamond reflection curves measured at low and high power levels.

In an experiment performed 20 years ago at the ESRF [35], the performance of the two-crystal diamond monochromator was tested under conditions very close to those expected for XFELOs. The beam from the undulator was focused to a small spot on a diamond water-cooled monochromator. Due to the focusing, the power density became 3.5 kW/mm^2. Figure 9(a) shows the layout of the setup. Figure 9(b) shows two diamond reflection curves measured with low and high power levels. No changes in reflectivity or in the reflection width were observed.

These facts may indicate that the danger of radiation damage to the diamond mirrors in the XFELO cavity is not high. However, the spectral reflection width of the XFELO mirrors is only a few meV, i.e., one to two orders of magnitude smaller that the spectral reflection widths of the diamond crystals in the double-crystal monochromators studied at the APS or ESRF. Therefore, the sensitivity of the XFELO mirrors to the damage might be higher. To ensure reliable operations of the XFELO cavity we should learn more about the radiation damage and how to mitigate this damage in diamond.

3.8.4 Focusing and Collimating Optics

Along with the high-reflectivity Bragg crystals that reflect x-rays at large angles, focusing and collimating elements are another major component of the XFELO cavity. The function of the focusing elements is to confine the radiation in the cavity and to optimize its interaction with the electron beam, i.e., to maximize the FEL gain. Much like the Bragg crystals, we require the focusing elements to have high efficiency and low losses. Grazing-incidence ellipsoidal mirrors and compound refractive lenses (CRLs), have been proposed as two of the most favorable options (see Figures 1-3 and text in Section 3.8.3). Each approach to realize the focusing and collimating optics has advantages and disadvantages. In the following we will present curved grazing-incidence mirrors as the presently preferred baseline design choice.

Grazing-incidence mirrors have the advantage of (i) being achromatic and therefore applicable to a relatively broad range of x-ray energies; (ii) having high reflectivity, i.e., low loss; and (iii) having the potential of partially reducing the heat load on the backscattering crystals. Disadvantages of the grazing-incidence mirrors include: (i) relatively complex alignment and potential source of XFELO instabilities, especially if the Kirkpatrick-Baez (KB) mirrors system [36] is considered; (ii) challenges in manufacturing mirrors with $\lesssim 0.2$ μrad (rms) figure error, which are required to avoid distortion of the x-ray beams with $\simeq 1$ μrad (rms) divergence.

To preserve the coherence and to achieve 98% efficiency in focusing (Strehl ratio = 0.98), the $\lambda/50$ Maréchal criterion has to be met for the height error $h_{rms} \lesssim \lambda/100\varphi N^{1/2}$ over the entire length of the mirror. Here N is the number of the reflective optics elements, and φ is the incidence angle. Assuming N=2, and φ=1 mrad, we obtain the estimate for the admissible height error: $h_{rms}=7\lambda$ nm, with the wavelength λ expressed in nm. This requires mirrors that have a slope error <0.1 μrad (rms), a height error <1 nm (rms), and a mid- to high-spatial roughness <0.1 nm (rms). Mirrors with such parameters are state of the art [37, 38].

Coating the mirrors with amorphous carbon is advantageous (because of the small photoabsorption in carbon) for achieving higher reflectivity and for avoiding damage due to exposure to intense XFELO radiation. An almost theoretical reflectivity of 97% from a carbon-coated KB mirror system has been demonstrated recently with 10-keV x-ray XFEL beams [39].

At present such mirrors can be fabricated in 1D parabolic (elliptical) configuration. 2D focusing or collimation is achieved using the KB-mirror system. KB system has several clear disadvantages: reduced reflectivity, complex alignment, decreased stability, and, last but not least, the KB mirrors break the coplanar scattering geometry, thereby making the cavity configuration more complex. Nevertheless, curved grazing-incidence mirrors are the only focusing element to have demonstrated the high reflectivity required for the XFELO, and therefore is the preferred baseline design choice.

3.8.5 Stability of the Optical Cavity

Reliable operation of the XFELO requires precise control of the x-ray cavity. An angular stability of 10 nrad (rms) for optical elements of the cavity is required to preserve a mode structure that develops around the optical axis [2]. Stability in the optical path length of better than ≈ 3 μm is needed to achieve sufficient gain.

There are two characteristic time scales directly related to operation of the XFELO: the x-ray cavity mode lifetime T_Q≈0.01 ms (f_Q≈100 kHz) related to the quality of the cavity, which we expect to be ≃10, and mode creation time T_G≈0.1 ms (f_G≈10 kHz) related to the time (number of passes ≃500) required to built the XFELO mode. It is anticipated that angular disturbances with amplitude ≳ 10 nrad rms do not exist in the system on such time scales. In particular, high-frequency disturbances in crystal positions and orientations can be easily eliminated by appropriate mechanical design (vibration damping). It is expected that the low-frequency disturbances that exceed 10 nrad will be compensated by a multi-channel feedback system.

A variety of technical solutions have been considered to deal with this problem. Among them, of major practical importance is stabilization by direct feedback on the signal of interest, the XFELO output, as opposed to indirect stabilization (e.g., using a visible light optics scheme with reflectors coupled to the Bragg mirrors of the cavity). An essential requirement is to stabilize several elements with several degrees of freedom. A null-detection feedback system employed at LIGO appears to be promising in achieving such a goal, because it also allows for stabilization of several optical axes with a single detector[1].

Null-detection feedback has been tested on an x-ray monochromator consisting of six crystals. It was found that an angular stability of ≈ 13 nrad (rms) can be achieved, with the characteristic correction time given by the integration time constant of the feedback loop (1 s) [40]. This number is approaching the angular stability required for the realization of the XFELO. Further improvement in stability is anticipated. Most important, in the next step, a multi-axis system with nanoradian-scale positioning resolution and a multi-axis feedback system for positioning and temperature control of the optical components of the x-ray cavity have to be designed and tested.

3.8.6 Conclusions and Outlook

X-ray cavities for XFELOs are most likely feasible. This is the main message that can be drawn from the experimental and theoretical studies performed recently and reviewed in the present paper. This builds confidence in the feasibility and success not only of the x-ray cavity, but also of the XFELO project in general.

In the next step, the "most likely" has to be removed from the message, and the feasibility of the x-ray cavity has to be demonstrated with a prototype cavity, up to the limits of the technical requirements. This is the strategic goal of the x-ray optics part of the XFELO endeavor.

3.8.7 Acknowledgments

Work was supported by the U.S. Department of Energy, Office of Science, under Contract No. DE-AC02-06CH11357. Contributions to these studies are greatly acknowledged by Kwang-Je Kim (APS), Stanislav Stoupin (APS), Ryan Lindberg (APS), Deming Shu (APS), Vladimir Blank (TISNCM), Sergey Terentyev (TISNCM), Sergey Polyakov (TISNCM), Harald Sinn (Euro-XFEL), Stan Whitcomb (LIGO), Sven

---

[1] The Laser Interferometer Gravitational Wave Observatory (LIGO) employs null-detection feedback with similar tolerance in angular stability. Dr. S. Whitcomb is acknowledged for an introduction to the null-detection feedback concept at LIGO.

Reiche (SLS), Bill Fawley (LBNL), Kurt Goetze (APS), Tim Roberts (APS), Frank Lenkszus (APS), Robert Laird (APS) and many others. Kwang-Je Kim is also acknowledged for reading the manuscript and providing valuable suggestions.

3.8.8 **References**

1. Kwang-Je Kim, Yuri Shvyd'ko, and Sven Reiche. A proposal for an x-ray free-electron laser oscillator with an energy-recovery linac. *Phys. Rev. Lett.*, 100(24):244802, Jun 2008.
2. Kwang-Je Kim and Yuri V. Shvyd'ko. Tunable optical cavity for an x-ray free-electron-laser oscillator. *Phys. Rev. ST Accel. Beams*, 12(3):030703, Mar 2009.
3. R. R. Lindberg, K.-J. Kim, Yu. Shvyd'ko, and W. M. Fawley. Performance of the x-ray free-electron laser oscillator with crystal cavity. *Phys. Rev. ST Accel. Beams*, 14:0110701, 2011.
4. K.-J. Kim, Yu. Shvyd'ko, and R. R. Lindberg. An x-ray free-electron laser oscillator for record high spectral purity, brightness, and stability. *Synchrotron Radiation News*, 25(1):25–31, 2012.
5. The European X-Ray Free-Electron Laser, Technical Design Report. ISBN 978-3-935702-17-1, DESY XFEL Project Group, European XFEL Project Team, Hamburg, Germany, July 2007.
6. Yu. Shvyd'ko. Tunable compact non-coplanar x-ray cavities for free electron laser oscillators. *to be published*, 2013.
7. R. M. J. Cotterill. Universal planar x-ray resonator. *Appl. Phys. Lett.*, 12:403, 1968.
8. R. M. J. Cotterill. Universal planar x-ray resonator. United States Patent 3518427, 1970.
9. Yu. Shvyd'ko. *X-Ray Optics – High-Energy-Resolution Applications*, volume 98 of *Optical Sciences*. Springer, Berlin Heidelberg New York, 2004.
10. A. Snigirev, V. Kohn, I. Snigireva, and B. Lengeler. A compound refractive lens for focusing high-energy x-rays. *Nature*, 384:49–51, 1996.
11. B. Lengeler, C. Schroer, J. Tümmler, B. Benner, M. Richwin, A. Snigirev, I. Snigireva, and M. Drakopoulos. Imaging by parabolic refractive lenses in the hard x-ray range. *J. Synchrotron Radiation*, 6:1153, 1999.
12. Yu. V. Shvyd'ko, S. Stoupin, A. Cunsolo, A.H. Said, and X. Huang. High-reflectivity high-resolution x-ray crystal optics with diamonds. *Nature Physics*, 6:196–199, 2010.
13. Yu. V. Shvyd'ko, S. Stoupin, V. Blank, and S. Terentyev. Near 100% Bragg reflectivity of x-rays. *Nature Photonics*, 5:539–542, 2011.
14. Stanislav Stoupin, Yuri Shvyd'ko, Deming Shu, Ruben Khachatryan, Xianghui Xiao, Francesco DeCarlo, Kurt Goetze, Timothy Roberts, Christian Roehrig, and Alexey Deriy. Hard x-ray monochromator with milli-electron volt bandwidth for highresolution diffraction studies of diamond crystals. *Rev. Sci. Instrum.*, 83:023105, 2012.
15. Mark A. Prelas, Galina Popovici, and Louis K. Bigelow, editors. *Handbook of Industrial Diamonds and Diamond Films*. Marcel Dekker, Inc., New-York, 1998.
16. Yu. Pal'yanov, Yu. Malinovsky, Yu. M. Borzdov, and A. F. Khokryakov. Use of the "split sphere" apparatus for growing large diamond crystals without the use of a hydraulic press. *Doklady Akademii Nauk SSSR*, 315:233–237, 1990.
17. Lonny E. Berman, J.B. Hastings, D. Peter Siddons, Masaki Koike, Vivian Stojanoff, and Michael Hart. Diamond crystal x-ray optics for high-power-density synchrotron radiation beams. *Nucl. Instrum. Methods Phys. Res. A*, 329:555–563, 1993.
18. H. Sumiya and S. Satoh. High-pressure synthesis of high-purity diamond crystal. *Diamond and Related Materials*, 5:1359–1365, 1996.
19. P.B. Fernandez, T. Graber, W.-K. Lee, D.M. Mills, C.S. Rogers, and L. Assoufid. Test of a high-heat-load double-crystal diamond monochromator at the Advanced Photon Source. *Nucl. Instrum. Methods Phys. Res. A*, 400:476–483, 1997.

20. J. P. F. Sellschop, S. H. Connell, R. W. N. Nilen, C. Detlefs, A. K. Freund, J. Hoszowska, R. Hustache, R. C. Burns, M. Rebak, J. O. Hansen, D. L. Welch, and C.E. Hall. Synchrotron x-ray applications of synthetic diamonds. *New Diamond and Frontier Carbon Technology*, 10:253–258, 2000.
21. H. Sumiya, N. Toda, and S. Satoh. High-quality large diamond crystals. *New Diamond and Frontier Carbon Technol.*, 10:233–251, 2000.
22. Y. Zhong, A T. Macrander, S. Krasnicki, Y S. Chu, J. Maj, L. Assoufid, and J. Qian. Rocking curve FWHM maps of a chemically etched (001) oriented HPHT type Ib diamond crystal plate. *J. Phys. D: Appl. Phys.*, 40:5301–5305, 2007.
23. M. Yabashi, S. Goto, Y. Shimizu, K. Tamasaku, H. Yamazaki, Y. Yoda, M. Suzuki, Y. Ohishi, M. Yamamoto, and T. Ishikawa. Diamond double-crystal monochromator for spring-8 undulator beamlines. *AIP Conf. Proc.*, 879:922–925, 2007.
24. R C Burns, A I Chumakov, S H Connell, D Dube, H P Godfried, J O Hansen, J Härtwig, J Hoszowska, F Masiello, L Mkhonza, M Rebak, A Rommevaux, R Setshedi, and P Van Vaerenbergh. HPHT growth and x-ray characterization of high-quality type IIa diamond. *J. Phys.: Condensed Matter*, 21:364224(14pp), 2009.
25. S.N. Polyakov, V.N. Denisov, N.V.Kuzmin, M.S. Kuznetsov, S.Yu. Martyushov, S.A. Nosukhin, S.A. Terentiev, and V.D. Blank. Characterization of top-quality type iia synthetic diamonds for new x-ray optics. *Diamond and Related Materials*, 20(5-6):726–728, 2011.
26. S. Stoupin, V.D. Blank, S.A. Terentyev, S.N. Polyakov, V.N. Denisov, M.S. Kuznetsov, Yu.V. Shvyd'ko, D. Shu, P. Emma, J. Maj, and J. Katsoudas. Diamond crystal optics for self-seeding of hard x-rays in x-ray free-electron lasers. *Diamond and Related Materials*, 33:1–4, 2013.
27. J. Amann, W. Berg, V. Blank, F.-J. Decker, Y. Ding, P. Emma, Y. Feng, J. Frisch, D. Fritz, J. Hastings, Z. Huang, J. Krzywinski, R. Lindberg, H. Loos, A. Lutman, H.-D. Nuhn, D. Ratner, J. Rzepiela, D. Shu, Yu. Shvyd'ko, S. Spampinati, S. Stoupin, S. Terentiev, E. Trakhtenberg, D. Walz, J. Welch, J. Wu, A. Zholents, and D. Zhu. Demonstration of self-seeding in a hard-x-ray free-electron laser. *Nature Photonics*, 6, 2012.
28. L. Samoylova, S. Rutishauser, C. David, J. Hartwig, P. Juranic, Yu. Shvyd'ko, H. Sinn, M. Sprung, S. Stoupin, and T. Weitkamp. Investigation of wavefront after diffraction in laue geometry on diamond. In *XTOP 2012, The 11th Biennial Conference on High Resolution X-Ray Diffraction and Imaging, O4-05*, 2012.
29. H. Sinn and Yu. Shvyd'ko. Heat dynamic simulations in dimond crystals in XFELO cavity. Unpublished, 2009-2010.
30. S. Stoupin and Yu. V. Shvyd'ko. Thermal expansion of diamond at low temperatures. *Phys. Rev. Lett.*, 104:085901, 2010.
31. S. Stoupin and Yu. V. Shvyd'ko. Ultraprecise studies of the thermal expansion coefficient of diamond using backscattering x-ray diffraction. *Phys. Rev. B*, 83:104102, 2011.
32. Lanhua Wei, P. K. Kuo, R. L. Thomas, T. R. Anthony, and W. F. Banholzer. Thermal conductivity of isotopically modified single crystal diamond. *Phys. Rev. Lett.*, 70(24):3764–3767, Jun 1993.
33. J. E. Graebner, T. M. Hartnett, and R. P. Miller. Improved thermal conductivity in isotopically enriched chemical vapor deposited diamond. *Applied Physics Letters*, 64(19):2549–2551, 1994.
34. S. Stoupin, A. M. March, H. Wen, D. A. Walko, Y. Li, E. M. Dufresne, S. A. Stepanov, K.-J. Kim, Yu. V. Shvyd'ko, V. D. Blank, and S. A. Terentyev. Direct observation of dynamics of thermal expansion using pump-probe high-energy-resolution x-ray diffraction. *Phys. Rev. B*, 86:054301, Aug 2012.

35. J. Als-Nielsen, A.K. Freund, M. Wulff, M. Hanfland, and D. Häusermann. Performance of diamond as x-ray monochromator under very high heat flux in a synchrotron beam. *Nucl. Instrum. Methods Phys. Res. B*, 94:348–350, 1994.
36. P. Kirkpatrick and A. V. Baez. Formation of optical images by x-rays. *J. Opt. Soc. Am.*, 38:766–774, 1948.
37. Shinya Morita, Hidekazu Mimura, Takashi Kimura, Daisuke Yamakawa, Weimin Lin, Yoshihiro Uehara, Satoshi Matsuyama, Hirokatsu Yumoto, Haruhiko Ohashi, Kenji Tamasaku, Yoshinori Nishino, Makina Yabashi, Tetsuya Ishikawa, Hitoshi Ohmori, and Kazuto Yamauchi. Focusing mirror for x-ray free-electron lasers. *Rev. Sci. Instrum.*, 79:083104, 2008.
38. Yukio Takahashi, Yoshinori Nishino, Ryosuke Tsutsumi, Hideto Kubo, Hayato Furukawa, Hidekazu Mimura, Satoshi Matsuyama, Nobuyuki Zettsu, Eiichiro Matsubara, Tetsuya Ishikawa, and Kazuto Yamauchi. High-resolution diffraction microscopy using the plane-wave field of a nearly diffraction limited focused x-ray beam. *Phys. Rev. B*, 80(5):054103, Aug 2009.
39. Hirokatsu Yumoto, Hidekazu Mimura, Takahisa Koyama, Satoshi Matsuyama, Kensuke Tono, Tadashi Togashi, Yuichi Inubushi, Takahiro Sato, Takashi Tanak, Takashi Kimura, Hikaru Yokoyama, Jangwoo Kim, Yasuhisa Sano, Yousuke Hachisu, Makina Yabashi, Haruhiko Ohashi, Hitoshi Ohmori, Tetsuya Ishikawa, and Kazuto Yamauchi. Focusing of x-ray free-electron laser pulses with reflective optics. *Nature Photonics*, 7:43–47, 2012.
40. Stanislav Stoupin, Frank Lenkszus, Robert Laird, Kurt Goetze, Kwang-Je Kim, and Yuri Shvyd'ko. Nanoradian angular stabilization of x-ray optical components. *Rev. Sci. Instrum.*, 81:055108, 2010.

3.9 Nanopositioning Stages to Enable XFELO Optics Mounting and Manipulating Capabilities

Deming Shu
Advanced Photon Source, Argonne National Laboratory, Argonne, IL 60439, USA
Mail to: shu@aps.anl.gov

3.9.1 Introduction

In developing an x-ray free-electron laser oscillator (XFELO), high-precision positioning techniques present a significant opportunity to support state-of-the-art coherence preserving x-ray optics. Meanwhile, the required instrument positioning performance and capabilities, such as resolution, dynamic range, repeatability, stability, and multiple axes synchronization, are exceeding the limit of commercial availability. This newsletter summarizes the current flexure-based nanopositioning stages developed for x-ray nanoprobe, high-resolution x-ray monochromators and analyzers for the Advanced Photon Source (APS) x-ray beamlines. Future nanopositioning techniques to be developed for the XFELO are also discussed.

3.9.2 Basic Nanopositioning Techniques Developed at the APS

Four major techniques have been developed for nanopositioning at the APS:

- A rotary, high-stiffness, weak-link mechanism with stacked, thin-metal sheets having 10-nrad driving sensitivity with excellent stability [1,2].

- A linear, high-stiffness, weak-link mechanism with stacked, thin-metal sheets having sub-100-pm driving sensitivity with excellent stability [1,2].
- A novel laser Doppler encoder system with multiple-reflection optics for sub-100-pm and 10-nrad-level linear and angular displacement measurement [3,4].
- A digital-signal-processor (DSP)-based, real-time, closed-loop feedback system for active relative vibration control on the nanometer scale [5].

3.9.3 Linear Weak-link Stages for Hard X-ray Nanoprobe

3.9.3.1 *Linear Weak-link Stages with Ultrahigh Positioning Resolution*

The APS has developed the hard x-ray nanoprobe beamline at APS Sector 26, which has been operated, in partnership with the Center for Nanoscale Materials (CNM), since 2008. This system covers an energy range of 3-30 keV and utilizes diffraction, fluorescence, and full-field transmission imaging to enable the study of nanoscale materials and devices. The nanoprobe has to date achieved a spatial resolution of 40-nm in scanning mode and 30-nm in full-field mode. The high spatial resolution is enabled by a combination of a high-resolution positioning system based on flexural stages, and high accuracy provided by laser interferometer-based encoders [6-8].

A nanopositioning diagnostic setup has been built to support the CNM nanoprobe instrument commissioning process and future nanopositioning instrument development at the APS. Its laser Doppler interferometer system and ultraprecision PZT-driven linear weak-link stages are the same as the initial systems applied for the CNM nanoprobe instrument. One-nanometer closed-loop positioning control is demonstrated on the two-dimensional diagnostic setup with APS-designed high-stiffness linear weak-link stages [9,10]. The 0.1-nanometer closed-loop positioning control is achieved on a one-dimensional linear high-stiffness weak-link stage test setup [11].

3.9.3.2 *Linear Weak-link Stages with Extended Travel Range*

Ball-bearing-based or roller-bearing-based linear positioning stages are capable of providing a larger travel range. However, their positioning resolution is limited by the friction of the bearing-based guiding system. Moreover, their linear motion straightness of trajectory usually is not repeatable in nanometer scale due to the roundness errors of the bearing’s rolling element and the uncertainty of the rolling ball’s or roller’s sliding effect. In the travel range of less than a few hundred microns, commercial PZT-driven flexural linear stages are available, but, it was hard to find any suitable for a travel range larger than a few millimeters with high stiffness and load capacity [12].

Linear vertical/horizontal flexural stages APS T8-31/32, with 3-mm travel range using fishbone-shaped multiple parallelogram weak-link structures as shown in Figure 1 [13], were developed at the APS for nanopositioning of a specimen holder for an multilayer Laue lenses (MLL)-based hard x-ray nanofocusing test bed at APS [14]. Table 1 shows the design specifications for the APS T8-33/34 linear vertical/horizontal flexural stages system.

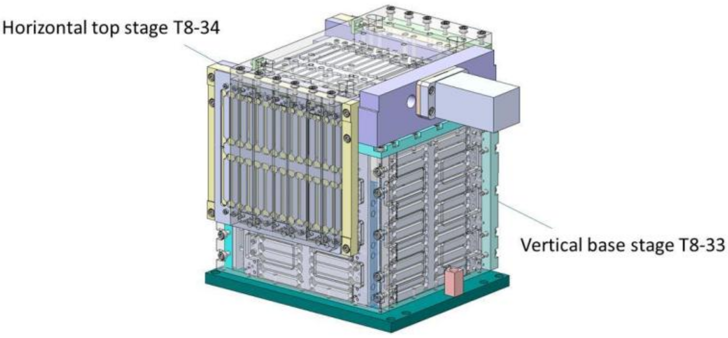

Figure 1: A 3-D model of the linear vertical/horizontal flexural stages APS T8-33/34.

Table 1: Design specifications for the APS T8-33/34 linear vertical/horizontal flexural stages system.

Parameter	***Vertical stage T8-33***	***Horizontal stage T8-34***
Overall dimensions (mm)	174 (L) x 135 (W) x 139 (H)	218 (L) x 180 (W) x 121 (H)
Travel range (mm)	3	3
Max. load capacity (kg)	4	2
Min. incremental motion (nm)	1	1
Driving mechanism	PI Nexline N-216^{TM}	PI Nexline N-111^{TM}
Encoder type	External optical sensor	External optical sensor
Stage weight (kg)	5	2

3.9.3.3 *Linear Flexure Stage with Centimeter Travel Range*

To further extend the travel range of the linear flexural stage and keep the stage compact, a prototype of a new T8-52 flexural linear stage system was designed and constructed at the APS using novel deformation-compensated flexural pivot mechanisms [15]. The prototype of the T8-52 stage is driven by the combination of a commercial PZA-12 PZT motor from Newport^{TM} mounted on the stage base and a commercial P-841.10 PZT actuator from PI^{TM} mounted on the stage carriage. The PZT motor provides 12-mm travel range with 100-nm resolution, and the PZT actuator drives the stage with sub-nanometer positioning resolution in a 15-micron travel range. The preliminary test for the prototype T8-52 stage was performed with two sets of laser interferometer systems. The results show that the stage has a ~30 micro-rad linear motion straightness of trajectory in the pitch direction within a 7-mm travel range. However, the straightness of trajectory was repeatable in ~5 micro-rad range. Figure 2 shows a photograph of the test setup for the prototype of the T8-52 flexural linear stage.

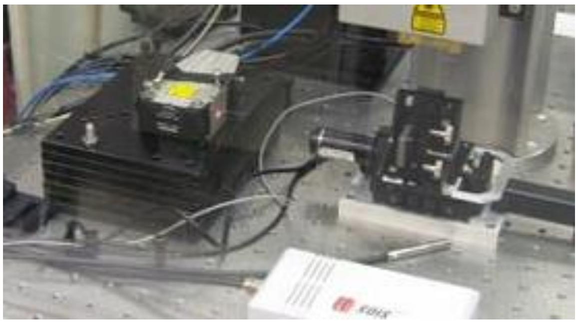

Figure 2: A photograph of the setup for the prototype of T8-52 flexural linear stage preliminary test with the Renishaw^{TM} and Sios^{TM} laser interferometer systems.

3.9.4 Angular Flexure Stages at the APS

3.9.4.1 *Horizontal Axis Angular Weak-link Stages*

The first high-stiffness weak-link mechanism with stacked thin-metal sheets was developed for the APS high-energy-resolution beamline 3-ID [16-18]. Using a laminar structure configured and manufactured by chemical etching and lithography techniques, we were able to design and build a planar-shape, high-stiffness, weak-link module for horizontal axis high-precision angular stages. The precision and stability of this mechanism allowed us to align or adjust an assembly of crystals to achieve the same performance as does a single channel-cut crystal, so we called it an “artificial channel-cut crystal.” A less-than-25-nrad-per-hour angular drift of two crystals was demonstrated in a two-hour stability test with a 1-meV bandwidth monochromatic beam [17].

Since then, more than 50 sets of such rotary weak-link mechanisms have been made for APS users in applications such as high-energy-resolution monochromators for inelastic x-ray scattering, and x-ray analyzers for ultra-small-angle scattering and powder-diffraction experiments. Their typical angular positioning resolution is 10-30 nrad with a travel range of up to 1.2 degrees [9].

The advent of the use of high-stiffness laminar weak-link mechanisms also benefits the regular monochromator design with silicon (1 1 1) or germanium (1 1 1) channel-cut crystal optics because of the improvement in the polishing quality on the crystal optical surface. Figure 3 (Right) shows a water-cooled ultra-high-vacuum (UHV)-compatible artificial channel-cut crystal monochromator. It is designed and constructed to meet the challenging stability and optical requirements of the x-ray photon correlation spectroscopy (XPCS) program at beamline 8-ID-I at the APS [19,20]. Similar UHV monochromator designs with laminar weak-link mechanisms are applied to the x-ray beamlines at APS Sector 16 (HP-CAT) [21] and at Linac Coherent Light Source (LCLS), SLAC National Accelerator Laboratory.

The applications were also expanded to the high-resolution crystal analyzer array for x-ray powder-diffraction instrumentation. An analyzer array was built for an x-ray powder diffraction instrument at APS Sector 11 as show in Figure 3 (Left). There are twelve silicon (1 1 1) or germanium (2 2 0) crystal analyzers in this array; each of them includes a PZT-driven laminar weak-link mechanism for the crystal’s fine pitch adjustment with a resolution of better than 0.05 arc-sec [22].

Figure 3 (Middle) shows a photograph of the CDFDW monochromator prototype tested at the APS beamline 30-ID. The abbreviation CDFDW stands for: C – collimating crystal, D – dispersing-element crystal (two D-crystals are used in each CDFDW), F – anomalous transmission filter, and W – wavelength-selector crystal [23]. A 0.65-meV combined energy resolution of the monochromator-analyzer pair was demonstrated in the in-line configuration, as well as sharp tails of the spectral distribution function [23,24]. A total of four angular weak-link stages and four linear weak-link stages are used in the monochromator-analyzer prototype setup.

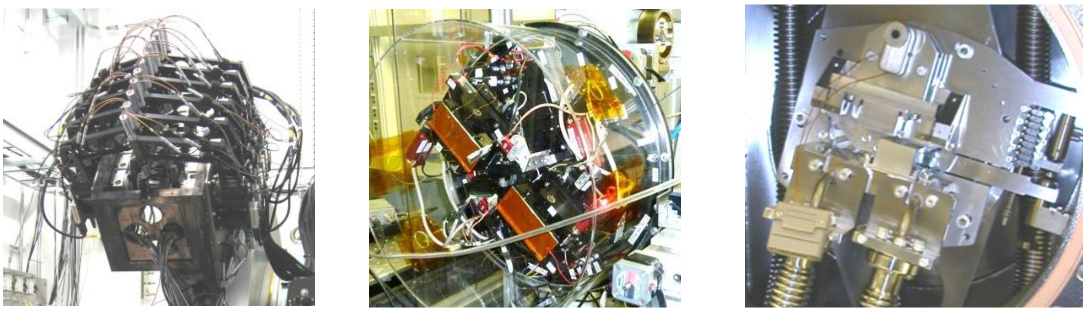

Figure 3: Left: Photograph of the analyzer array for an x-ray powder diffraction instrument at APS Sector 11. Middle: Photograph of the CDFDW monochromator prototype tested at APS Sector 30. Right: Photograph of a water-cooled UHV-compatible artificial channel-cut crystal monochromator at APS Sector 8.

3.9.4.2 *Vertical Axis Angular Weak-link Stages*

To expand the applications of the angular weak-link mechanisms to vertical axis configurations, we need to enhance their load capacity and stiffness along the rotation axis. An advanced x-ray stereo imaging instrument for particle tracking velocimetry (PTV) [25] has been developed at APS Sector 32 using the new vertical axis rotary weak-link stage. To enhance the load capacity and stiffness in a vertical axis configuration, six linear weak-link modules are mounted on the sides of the base plate and top plate, orthogonal to the angular weak-link plane, and act as a vertical stiffener for the vertical axis [25]. With this new design, 2-kg or higher vertical load capacity is achievable. The vertical axis rotary weak-link stage is mounted on top of a commercial precision rotary stage manufactured by Aerotech$^{\text{TM}}$. The PZT-actuator-driven weak-link stage extended the motor-driven rotary stage's angular displacement resolution to the ten-nanoradian-scale level in an angular travel range of 0.1-mrad.

3.9.4.3 *Multi-dimensional Alignment Apparatus*

Recent developments in hard x-ray focusing on the nanometer scale with MLLs as reported by H. C. Kang et al. have demonstrated a promising new x-ray optic for focusing hard x-rays in a few nanometers. Using tilted partial MLL structures, a one-dimensional focus as small as 16 nm with efficiencies up to 44% has been performed with 19.5-keV synchrotron radiation [26,27]. The high efficiencies should make it practical to produce a point focus using two MLLs in a crossed configuration [28]. A precision multidimensional alignment apparatus is needed for this challenging technical approach.

The first prototype of precision multi-dimensional alignment apparatus for 2-D MLL x-ray focusing was designed and constructed for an MLL test bed at APS beamline 26-ID in 2008 [14]. With this test bed, MLL demonstrated the focusing capability of hard x-rays to a 2-D focus of 25 nm horizontal x 27 nm vertical FWHM at a photon energy of 12 keV, and of 25 nm horizontal x 40 nm vertical FWHM at a photon energy of 19.52 keV [29]. Commercial flexural pivots are applied in the apparatus for tip-tilting angular adjustment as shown in Figure 4 (Left). Figure 4 (Right) shows a similar flexural-pivots-based precision alignment apparatus applied in UHV diamond-crystal monochromator for the Linac Coherent Light Source (LCLS) hard x-ray self-seeding project as the result of collaborations between the APS at Argonne National Laboratory (ANL) and the LCLS at SLAC National Accelerator Laboratory [30,31].

Figure 4: Left: Photograph of the precision multi-dimensional alignment apparatus for 2-D MLL x-ray focusing at APS Sector 26. Right: A 3-D model of the precision alignment apparatus applied in an UHV diamond crystal monochromator for the LCLS hard x-ray self-seeding project.

3.9.5 Prototype of Tip-tilting Stage with Resolution in Nanoradian Scale

Based on the experiences gained from the high-stiffness vertical-axis weak-link structure with 2-kg load capacity, a two-dimensional tip-tilting stage system Z8-53 has been designed for precision x-ray optical alignment with ultra-high motion control resolution and stability. The two-dimensional tip-tilting weak-link stage system consists of two high-stiffness weak-link stages: (1) a vertical-axis rotary weak-link stage, which is of the same design developed for PTV application, located at the top and a new horizontal-axis tip-tilting stage at the bottom; and (2) the new horizontal-axis tip-tilting stage is combined with six linear weak-link modules to enhance lateral stiffness, as shown in Figure 5 (Left). Figure 5 (Right) shows a photograph of the prototype. Table 2 summarizes the design specifications for the Z8-53 high-stiffness two-dimensional tip-tilting weak-link stage system.

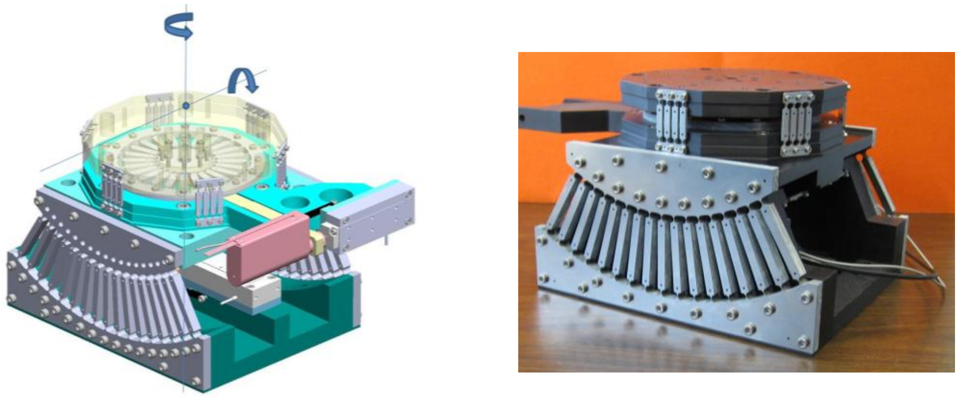

Figure 5: Left: A 3-D model of the prototype of the APS Z8-53 tip-tilting stage. Right: Photograph of the prototype.

Table 2: Design specifications for the Z8-53 2-D tip-tilting weak-link stage system.

Parameter	***Vertical-axis angular stage***	***Horizontal-axis tip-tilt stage***
Overall dimensions (mm)	236 (L) x 158 (W) x 50 (H)	212 (L) x 184 (W) x 108 (H)
Normal load capacity (kg)	2	5
Driver type	PZT and Picomotor™	PZT and Picomotor™
Encoder type	Strain sensor/optical sensor	Strain sensor/optical sensor
Angular travel range (mrad)	26	26
Min. incremental (nrad)	10	10

3.9.6 **Summary**

We briefly summarized the current flexure-based nanopositioning stages developed for x-ray nanoprobe, high-resolution x-ray monochromators and analyzers at the APS. The experiences gained from the development activities will benefit the design and development of a prototype of the two-dimensional tip-tilting stage system for a proposed XFELO project [32]. As part of the ultra-precision crystal manipulators for the XFELO cryo-cooling optical cavities, the vacuum-compatible two-dimensional tip-tilting stage system is required to have 2 – 4 kg vertical load capacity with nanoradian-level resolution and stability. Cryo-cooling mechanisms with very low vibration will also be required for the XFELO prototype development.

3.9.7 **Acknowledgments**

The author would like to thank Y. Shvyd'ko, S. Stoupin, R. Lindberg, and K-J. Kim from ANL for their help with the XFELO prototype preparation and development. The author would like to thank T. S. Toellner, E. E. Alp, J. Ilavsky, S. D. Shastri, P. L. Lee, S. Narayanan, D. Nocher, R. Ranay, and T. Buffington from ANL, and S. Kearney and J. Anton from ANL and the University of Illinois at Chicago for their help with the high-resolution x-ray monochromators and analyzers development. The authors would like to thank J. Maser, M. Holt, R. Winarski, V. Rose, C. Preissner, B. Lai, S. Vogt, G. B. Stephenson, W. Liu, L. Assoufid and the APS Optics group from ANL for their help with the x-ray nanoprobe and K-B mirror/MLL-based instruments development. The authors would like to thank A. Zholents, W. Berg, J. Quintana from ANL, P. Emma, J.

Amann, J. Hastings, Y. Feng, H. Huang, and engineers in the LCLS HXRSS team from SLAC National Accelerator Laboratory for their help with the LCLS hard x-ray self-seeding monochromator development. This work was supported by the U.S. Department of Energy, Office of Science, under Contract No. DE-AC02-06CH11357.

3.9.8 **References**

1. U.S. Patent granted No. 6,607,840, D. Shu, T. S. Toellner, and E. E. Alp, 2003.
2. U.S. Patent granted No. 6,984,335, D. Shu, T. S. Toellner, and E. E. Alp, 2006.
3. U.S. Patent granted No. 5,896,200, D. Shu, 1999.
4. U.S. Patent granted No. 6,822,733, D. Shu, 2004.
5. D. Shu, Y. Han, T. S. Toellner, and E. E. Alp, Proc. SPIE, Vol. 4771 (2002) 78-90.
6. J. Maser et al., Proc. 8th Int. Conf. X-ray Microscopy, IPAP Conf. Series 7 (July 2006) 26-29.
7. D. Shu et al., Proc. 8th Int. Conf. X-ray Microscopy, IPAP Conf. Series 7 (July 2006) 56-58.
8. U.S. Patent granted No. 7,331,714, D. Shu, J. Maser, B. Lai, F. S. Vogt, M. V. Holt, C. A. Preissner, R. Winarski, and G. B. Stephenson, 2008.
9. D. Shu, Proceedings of SRI-2009, AIP Conf. Proc. 1234, 449 (2010)
10. D. Shu and J. Maser, Proc. 9th Int. Conf. X-ray Microscopy, IOP, Journal of Physics: Conference Series 186 (2009) 012017.
11. D. Shu, Y. Han, T. S. Toellner, and E. E. Alp, Proc. SPIE Vol. 4771 (2002) 78-90.
12. D. Shu, J. Maser, Y. Chu, H. Yan, E. Nazaretski, S. O'Hara, S. Kearney, J. Anton, J. Quintana, and Q. Shen, AIP Conf. Proc. 1365 (2011) 144-147.
13. U.S. Patent granted No. 7994688, D. Shu and J. Maser, 2011.
14. D. Shu and J. Maser, Proc. SPIE, Vol. 7424 (2009) 74240D1-9.
15. D Shu, S Kearney, and C Preissner, “Design of a precision flexural linear stage system with sub-nanometer resolution and 12-mm travel range,” to be published in JPCS proceedings of SRI-2012, Lyon, France, July 2012.
16. T. S. Toellner, T. Mooney, S. Shastri, and E. E. Alp, Proc. SPIE Vol. 1740 (1992) 218.
17. D. Shu, T. S. Toellner, and E. E. Alp, Nucl. Instrum. and Methods A 467-468 (2001) 771-774.
18. E. E. Alp, T. Mooney, T. S. Toellner, and W. Sturhahn, Hyperfine Interactions 90 (1994) 323.
19. S. Narayanan, A. Sandy, D. Shu, M. Sprung, C. Preissner and J. Sullivan, J. Synchrotron Rad. 15 (2008) 12-18.
20. D. Shu, S. Narayanan, A. Sandy, M. Sprung, C. Preissner and J. Sullivan, Proc. SPIE Vol. 6665 (2007) 0O1-8.
21. W. Yang, D. Shu, E. Rod, G. Shen, and H-K. Mao, Proceedings of SRI-2008, Saskatoon, Canada.
22. P.L. Lee, D. Shu, M. Ramanathan, C. Preissner, J. Wang, M.A. Beno, R.B. Von Dreele, L. Ribaud, C. Kurtz, S.M. Antao, X. Jiao and B.H. Toby, J. Synchrotron Rad. 15 (2008) 427-432.
23. Y. V. Shvyd’ko, U. Keutgens et al., AIP Conf. Proc. 879 (2007) 737.
24. Y. V. Shvyd'ko, S. Stoupin, D. Shu, R. Khachatryan, “Angular dispersion and anomalous transmission cast ultramonochromatic x-rays,” Phys. Rev. A 84 (2011) 053823.
25. D. Shu, W-K. Lee, W. Liu, G. E. Ice, Y. Shvyd’ko, K-J. Kim, Nucl. Instrum. and Methods A 649 (2011) 114–117.
26. H. C. Kang et al., Phys. Rev. Lett. 96 (2006) 127401.
27. H. C. Kang, H. Yan et al., Appl. Phys. Lett. 92 (2008) 221114.
28. J. Maser et al., Proc. SPIE Vol. 5539 (2004) 185.

29. H. Yan et al., Optics Express, 19 (2011) 15069-15076.
30. J. Amann, W. Berg, V. Blank, F.-J. Decker, Y. Ding, P. Emma, Y. Feng, J. Frisch, D. Fritz, J. Hastings, Z. Huang, J. Krzywinski, R. Lindberg, H. Loos, A. Lutman, H.-D. Nuhn, D. Ratner, J. Rzepiela, D. Shu, Yu. Shvyd'ko, S. Spampinati, S. Stoupin, S. Terentiev, E. Trakhtenberg, D. Walz, J. Welch, J. Wu, A. Zholents, and D. Zhu, "Demonstration of self-seeding in a hard-x-ray free-electron laser," Nature Photonics, 6, 2012.
31. D. Shu, Y. Shvyd'ko, J. Amann, P. Emma, S. Stoupin, and J. Quintana, to be published in JPCS proceedings of SRI-2012, Lyon, France, July 2012.
32. K.-J. Kim, Y. Shvyd'ko, "Tunable optical cavity for an X-ray free-electron-laser oscillator," Phys. Rev. Phys. Spec. Top Accel. Beams 12 (2009) 030703.

3.10 BINP Free Electron Laser Facility – Current Status and Future Prospects

O.A.Shevchenko, V.S.Arbuzov, K.N.Chernov, E.N.Dementyev, B.A.Dovzhenko,
Ya.V.Getmanov, E.I.Gorniker, B.A.Knyazev, E.I.Kolobanov, A.A.Kondakov,
V.R.Kozak, E.V.Kozyrev, V.V.Kubarev, G.N.Kulipanov, E.A.Kuper, I.V.Kuptsov,
G.Ya.Kurkin, L.E.Medvedev, L.A.Mironenko, V.K.Ovchar, B.Z.Persov, A.M.Pilan,
V.M.Popik, V.V.Repkov, T.V.Salikova, M.A.Scheglov, I.K.Sedlyarov,
G.V.Serdobintsev, S.S.Serednyakov, A.N.Skrinsky, S.V.Tararyshkin, V.G.Tcheskidov,
N.A.Vinokurov, M.G.Vlasenko, P.D.Vobly, V.N.Volkov
BINP, Novosibirsk, Russia
Mail to: O.A.Shevchenko@inp.nsk.su

3.10.1 Introduction

The free electron laser (FEL) facility at Budker INP is being developed for more than 15 years. It is based on the normal conducting CW energy recovery linac (ERL) with rather complicated magnetic system lattice. Up to now it is the only one in the world multiorbit ERL. It can operate in three different regimes providing electron beam for three different FELs. Its commissioning was naturally divided in three stages.

The first stage ERL includes only one orbit placed in vertical plane. It serves as electron beam source for terahertz FEL which started working for users in 2003. Radiation of this FEL is used by several groups of scientists including biologists, chemists and physicists. Its high peak and average powers are utilized in experiments on material ablation and biological objects modification. The second stage ERL is composed of two orbits located in horizontal plane. The second stage FEL is installed on the bypass of the second orbit. The first lasing of this FEL was achieved in 2009. The last stage ERL will include four orbits. Its commissioning is in progress now.

In this paper we report the latest results obtained from the operating FELs as well as our progress with the commissioning of the two remaining ERL beamlines. We also discuss possible options for the future upgrade.

3.10.2 Accelerator Design

The Novosibirsk FEL facility is based on the multiturn energy recovery linac (ERL) which scheme is shown in Fig. 1. In this scheme the beam goes through the linac several times before it enters undulator. As the result one can increase the final electron energy.

Multiturn ERLs look very promising for making ERLs less expensive and more flexible, but they have some serious intrinsic problems. Particularly in the simplest scheme shown in Fig.1 one has to use the same tracks for accelerating and decelerating beams which essentially complicates adjustment of the magnetic system. This problem can be solved by using more sophisticated scheme based on two linacs [1].

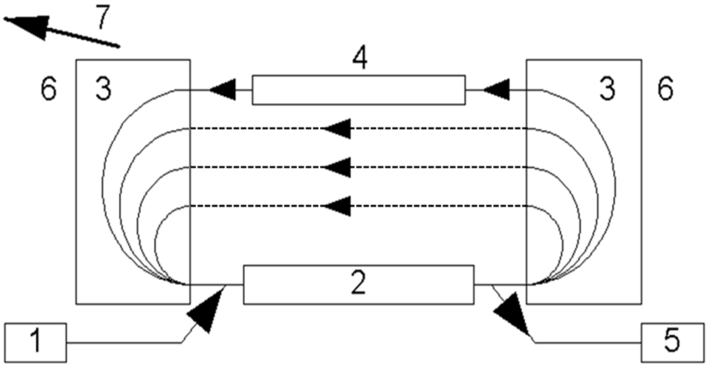

Figure 1: Simplest multiturn ERL scheme: 1 – injector, 2 – linac, 3 – bending magnets, 4 – undulator, 5 – dump.

At present the Novosibirsk ERL is the only one multiturn ERL in the world. It has rather complicated lattice as it can be seen from Fig. 2. The ERL can operate in three modes providing electron beam for three different FELs. The whole facility can be treated as three different ERLs (one-turn, two-turn and four-turn) which use the same injector and the same linac. The one-turn ERL is placed in vertical plane. It works for the THz FEL which undulators are installed at the floor. This part of the facility is called the first stage. It was commissioned in 2003 [2].

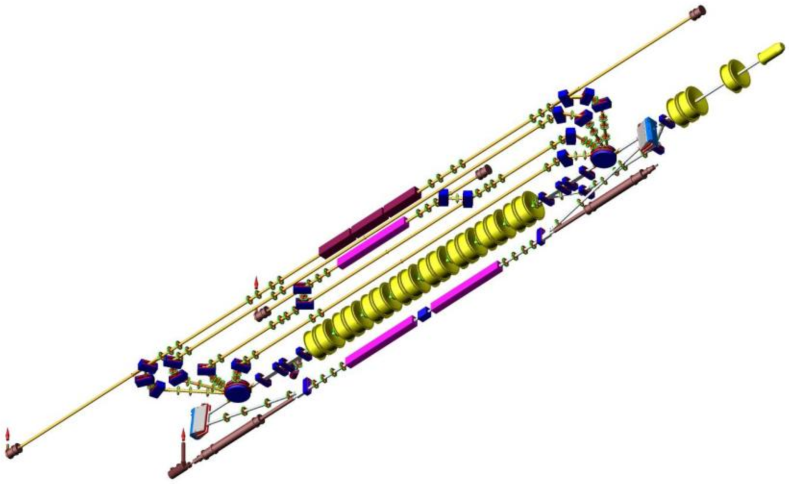

Figure 2: The Novosibirsk ERL with three FELs (bottom view).

The other two ERL orbits are placed in horizontal plane at the ceiling. At the common track there are two round magnets. By switching these magnets on and off one can direct the beam either to horizontal or to vertical beamlines. The 180-degree bending arcs also include small bending magnets with parallel edges and quadrupoles. To reduce sensitivity to the power supply ripples, all magnets on each side are connected in series. The quadrupole gradients are chosen so that all bends are achromatic. The vacuum chambers are made from aluminium. They have water-cooling channels inside.

The second horizontal track has bypass with the second FEL undulator. The bypass provides about 0.7 m lengthening of the second orbit. Therefore when the beam goes through the bypass it returns back to the linac in decelerating phase and after two decelerations it finaly comes to the dump. This part (the second stage) was commissioned in 2009. The final third stage will include full-scale four-turn ERL and FEL installed on the last track.

The basic beam and linac parameters common for all three ERLs are listed in Table 1.

Table 1: Basic ERL parameters

Injection energy, MeV	2
Main linac energy gain, MeV	10
Charge per bunch, nC	1.5
Normalized emittance, mm·mrad	30
RF frequency, MHz	180.4
Maximum repetition rate, MHz	90.2

Depending on the number of turns the maximum final electron energy can be 12, 22 or 42 MeV. The bunch length in one-turn ERL is about 100 ps. In two and four-turn ERLs the beam is compressed longitudinally up to 10-20 ps. The maximum average current achieved at one-turn ERL is 30 mA which is still the world record.

One essential difference of the Novosibirsk ERL compared to other facilities [3,4] is using of the low frequency non-superconducting RF cavities. On one hand it leads to increasing of the linac size but on the other hand it also allows to increase transversal and longitudinal acceptances which allows to tolerate longer electron bunches with large transversal and longitudinal emittances.

The location of different parts of the facility in the accelerator hall is shown in Fig. 3.

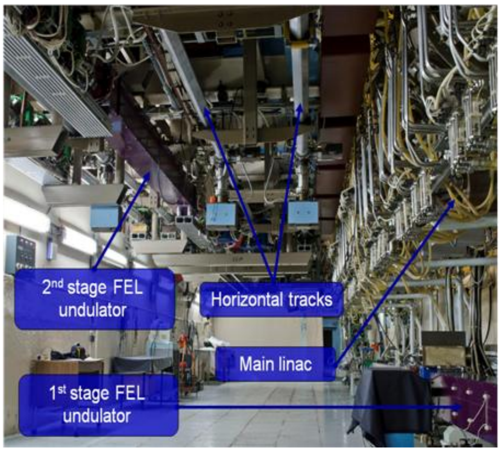

Figure 3: Accelerator hall (bottom view).

3.10.3 **The First Stage FEL**

3.10.3.1 ***Design and Basic Parameters***

The first stage FEL includes two electromagnetic undulators with period 12 cm, phase shifter and optical cavity. Undulator pole shape is chosen to provide equal electron beam focusing in vertical and horizontal directions. The matched beta-function is about 1 m. The phase shifter is installed between undulators and it is used to adjust the slippage. The optical cavity is composed of two copper mirrors covered by gold. The distance between mirrors is 26.6 m which corresponds to the round-trip frequency (and the resonance electron repetition rate) 5.64 MHz. Radiation is outcoupled through the hole made in the mirror center. The optical beamline is separated from the vacuum chamber by diamond window. The beamline pipe is filled with dry nitrogen.

The FEL generates coherent radiation tunable in the range 120-240 micron as a continuous train of 40-100 ps pulses at the repetition rate of 5.6 - 22.4 MHz. Maximum average output power is 500 W, the peak power is more than 1 MW [5,6]. The minimum measured linewidth is 0.3%, which is close to the Fourier-transform limit.

3.10.3.2 ***Operation Experience***

For the last two years about 30 experiments were carried out at the Novosibirsk THz FEL. They include: pioneering works on THz ablation; study of micro- and nanoparticles, vaccines, polymers, metamaterials; production of nanotubes and nanostructures; composite diagnostics; terahertz radioscopy, imaging, detection of concealed objects; interferomety, holography & tomography; speckle and Talbot metrology; ellipsometry; fast water vapor detection; flame and gas detonation study; impact of THz radiation on genetic materials; impact of THz radiation on cells; study of integrated proteomic response; coherent effects in gases; ultrafast time-domain spectroscopy; interaction of atoms with strong THz EM-field.

Five user stations are in operation now. Two other are in progress. The new spectrometer has been installed recently. It allows to measure continuously radiation spectrum not interrupting user experiments (Fig. 4). Other radiation diagnostics include Fourier spectrometer, thermograph, microbolometer matrix, Shottky diode together with wideband oscilloscope. The last one is used for time-resolved measurements. It allows to detect longitudinal power distribution of radiation pulses.

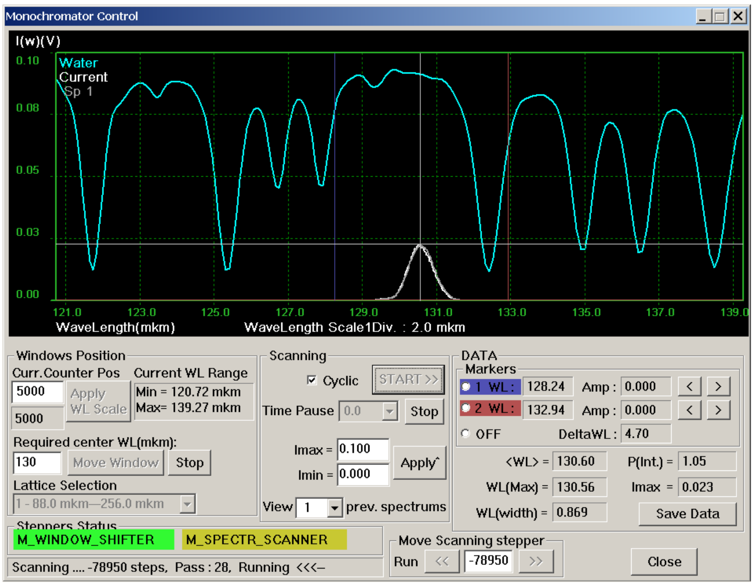

WaveLength Scale1Div. : 2.0 mkm

Curr.Counter Pos 5000

5000

Current WL Range
Min = 120.72 mkm
Max= 139.27 mkm

Required center WL(mkm): 130

Lattice Selection 1 - 88.0 mkm—256.0 mkm

☑ Cyclic

Time Pause 0.0

Imax = 0.100

Imin = 0.000

View 1 prev. spectrums

● 1 WL : 128.24 Amp : 0.000

● 2 WL : 132.94 Amp : 0.000

○ OFF DeltaWL : 4.70

<WL> = 130.60 P(Int.) = 1.05

WL(Max) = 130.56 Imax = 0.023

WL(width) = 0.869

M_WINDOW_SHIFTER M_SPECTR_SCANNER

Scanning .... -78950 steps, Pass : 28, Running <<<–

Run -78950

Figure 4: Spectrum measurement diagnostic control (white line - the measured FEL radiation spectrum, blue line - water absorption spectrum).

Recently the third harmonics lasing was obtained. It was achieved by suppression of the first harmonics lasing using aperture-decreasing scrapers installed inside the optical cavity and proper adjustment of the phase shifter. The measured detuning curves for the first and third harmonics lasing are shown in Fig. 5.

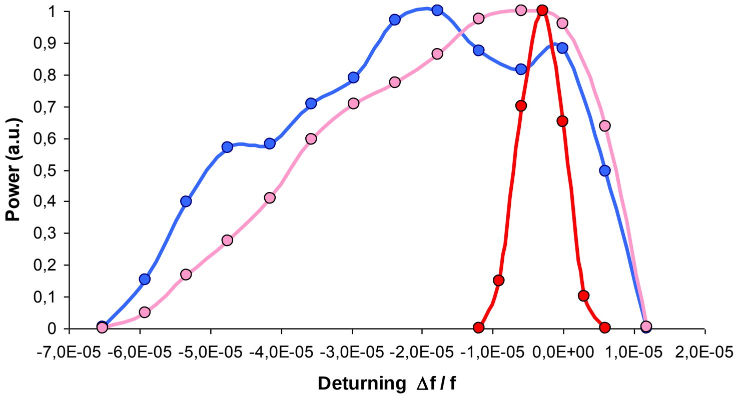

Figure 5: Normalized detuning curves for the lasing at the first (blue) and third (red) harmonics and the detuning curve for the amplified spontaneous emission at the third harmonic (pink).

3.10.4 The Second Stage FEL

The second stage FEL includes one electromagnetic undulator with period 12 cm and optical cavity. The undulator is installed on the bypass where the electron energy is about 22 MeV. Therefore the FEL radiation wavelength range is 40 - 80 micron. The undulator design is identical to the first stage one but it has smaller aperture and higher maximum magnetic field amplitude. The optical cavity length is 20 m (12 RF wavelengths). Therefore the bunch repetition rate for initial operation is 7.5 MHz.

The first lasing of this FEL was achieved in 2009. The maximum gain was about 40% which allowed to get lasing at 1/8 of the fundamental frequency (at bunch repetition rate ~1 MHz).

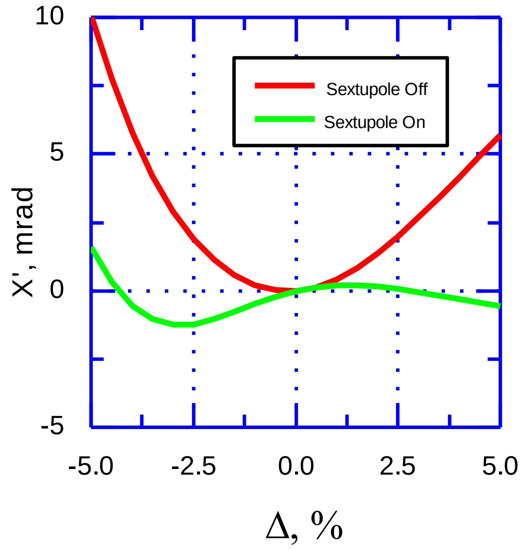

Figure 6: Compensation of quadratic dependence of the bending angle on energy by sextupoles in the first orbit bending arcs.

The significant (percents) increase of beam losses took place during first lasing runs. Therefore sextupole corrections were installed into some of quadrupoles to make the 180-degree bends second-order achromatic. It increased the energy acceptance for used electron beam (Fig. 6).

The optical beamline (Fig. 7) which delivers radiation from new FEL to existing user stations is assembled and commissioned. The output power is about 0.5 kW at the 9 mA ERL average current. Thus, the first in the world multiturn ERL operates for the far infrared FEL.

Figure 7: Optical beamlines for the first and the second stage FELs. Radiation of both FELs is delivered to the same user stations. Switching between FELs is done by retractable mirror.

3.10.5 **Third Stage ERL and FEL**

Electron beam in the third stage ERL is accelerated four times. The third FEL undulators will be installed on the last track where the beam energy is 42 MeV. In this FEL three permanent magnet undulators with period 6 cm and variable gap will be used. The wavelength range will be 5-30 microns. The scheme of the third stage ERL with FEL undulators is shown in Fig. 8. The electron outcoupling is planned to be used here [7].

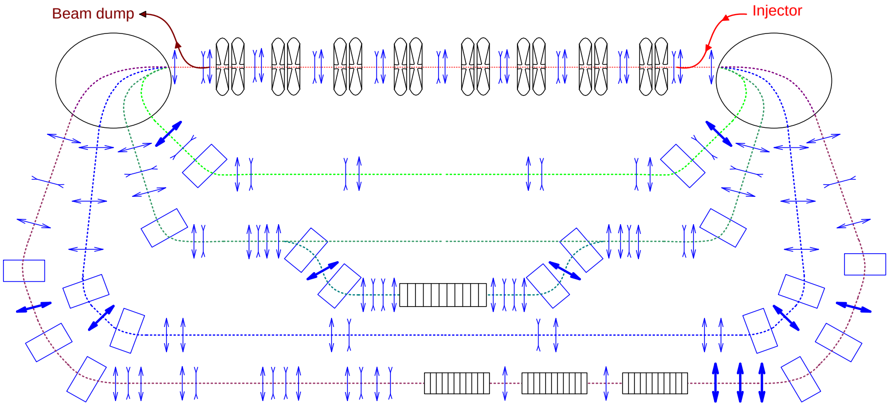

Figure 8: The third stage ERL with FEL undulators.

All magnetic system elements and vacuum chambers of the third stage ERL are assembled and installed and the first shifts for the lattice adjustment took place. By now total (from the gun to the dump) recuperation efficiency of 90% is already achieved. This allowed to obtain the repetition rate 3.75 MHz and the average current 3.2 mA which is sufficient to get lasing at the third stage FEL. The signal from the BPM installed in the accelerating structure near the dump is shown in Fig. 9. All eight peaks here correspond to the same beam at different stages – the first four are in accelerating phase and the last four - in decelerating phase. One can see that the first and the last peak amplitudes do not differ significantly. It means that the beam losses mostly take place at low energy in injector and near the dump.

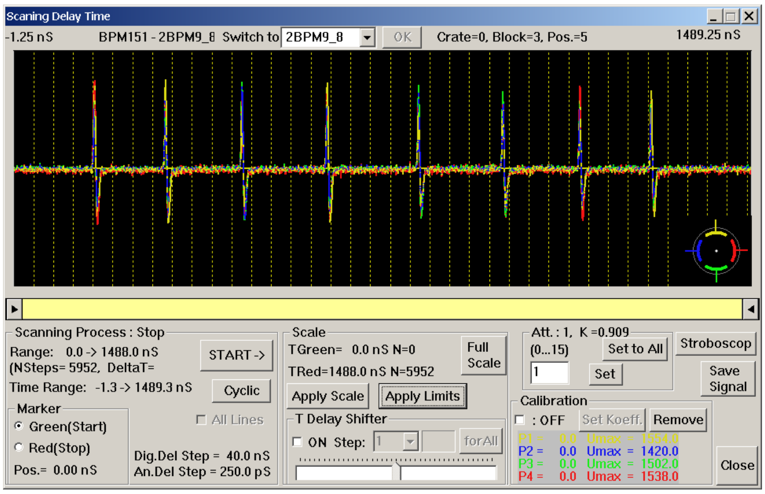

-1.25 nS   BPM151 - 2BPM9_8   Switch to 2BPM9_8   Crate=0, Block=3, Pos.=5   1489.25 nS

Scanning Process : Stop
Range: 0.0 -> 1488.0 nS
(NSteps= 5952, DeltaT=
Time Range: -1.3 -> 1489.3 nS
Marker
● Green(Start)
○ Red(Stop)
Pos.= 0.00 nS
☐ All Lines
Dig.Del Step = 40.0 nS
An.Del Step = 250.0 pS

Scale
TGreen= 0.0 nS N=0
TRed=1488.0 nS N=5952
T Delay Shifter
☐ ON Step: 1

Att. : 1, K =0.909
(0...15) 1
Calibration
☐ : OFF
P1 = 0.0 Umax = 1554.0
P2 = 0.0 Umax = 1420.0
P3 = 0.0 Umax = 1502.0
P4 = 0.0 Umax = 1538.0

Figure 9: Signal from the BPM installed in the accelerating structure.

3.10.6 Future Prospects

In the nearest future we plan to continue the third stage ERL commissioning. The third FEL undulators will be installed shortly. The optical cavity design and production is in progress now.

The other important issue which we are working on now is the operation stability and improvement of the existing FEL parameters. We plan to make some improvements of the RF system. The new power supply for the existing gun and new RF gun are being developed now. The lattice optimization is in progress. More serious modernization e.g. using the new type of undulators with variable period [8] is also considered.

3.10.7 References

1. D. Douglas, A Generic Energy-Recovering Bisected Asymmetric Linac (GERBAL), ICFA BD-Nl 26, 2001, P. 40-45.
2. A E. A. Antokhin et al. NIM A528 (2004) p.15.
3. G.R. Neil et al. Phys. Rev. Lett. 84 (2000), p. 662.
4. E.J. Minehara. NIM A483 (2002) p. 8.
5. V.P. Bolotin et al. NIM A 557 (2006) p.23.
6. E.A.Antokhin et al., Problems of Atomic Science and Technology, p.3, №1, 2004.
7. A.N. Matveenko et al., Proc. of FEL2007, p. 204.
8. N.A. Vinokurov et al., Proc. of FEL2010, p. 696.

3.11 A Program for Optimizing SRF Linac Costs

Tom Powers
Thomas Jefferson National Accelerator Facility, Newport News, VA
Mail to: powers@jlab.org

3.11.1 Introduction

Every well-designed machine goes through the process of cost optimization several times during its design, production and operation. The initial optimizations are done during the early proposal stage of the project when none of the systems have been engineered. When a superconducting radio frequency (SRF) linac is implemented as part of the design, it is often a difficult decision as to the frequency and gradient that will be used. Frequently, such choices are made based on existing designs, which invariably necessitate moderate to substantial modifications so that they can be used in the new accelerator. Thus the fallacy of using existing designs is that they will frequently provide a higher cost machine or a machine with sub-optimal beam physics parameters. This paper describes preliminary results of a new software tool that allows one to vary parameters and understand the effects on the optimized costs of construction plus 10 year operations of an SRF linac, the associated cryogenic facility, and controls, where operations includes the cost of the electrical utilities but not the labor or other costs. It derives from collaborative work done with staff from Accelerator Science and Technology Centre, Daresbury, UK [1] several years ago while they were in the process of developing a conceptual design for the New Light Source project. The initial goal was to convert a spread sheet format to a graphical interface to allow the ability to sweep different parameter sets. The tools also allow one to compare the cost of the different facets of the machine design and operations so as to better understand the tradeoffs.

3.11.2 **Software Description**

3.11.2.1 ***General structure***

The program was written in LabView in a state machine format. This allows one to separate, and/or modify the different subroutines, jump to different states, add different parameters, and/or expand the program to include different aspects of machine design. The input variables are contained in clusters of variables, one for the cavity/cryomodule parameters, one for the system cost parameters and one for the cryogenic heat loads. There is a cluster for the program outputs such as cost and design points.

3.11.2.2 ***Input / Output Parameters***

The program has two loss parameters for cryogenic losses. Static losses of each of the SRF cryo-assembly, called a cryomodule, and RF driven, or dynamic, losses. The static heat losses include the cryomodule, associated valve box, and per kilometer transfer line losses. A detailed list of the current input output parameters is given in Table 1. Figure 1 shows the user interface for modifying variables in the program while Figure 2 shows the graphical output that is available. At any given point in time all parameters for a swept variable run can be output to a tab delimited text file.

Table 1: Input/output parameter list.

SRF Parameters	***Baseline Costs***	***Outputs***
Final Linac Energy (GeV)	Cryomodule Cost ($M/unit)	Total ($M)
Gradient (V/m)	RF Power ($/W)	Construction ($M)
Frequency (Hz)	RF Control, etc. ($k/Cavity)	Cryogenic Plant ($M)
Cavities Per Cryomodule	Inter CM Girder ($k/unit)[3]	Cryomodules ($M)
Active Length Per Cavity (m)	Tunnel Civil ($k/m)	Girders ($M)
Packing Factor Tot L/Active L	AC Power ($/MW-Hour)	Tunnel, etc. Civil ($M)
Normalized Shunt Imp. (Ω/m)	5kW @ 2K Plant ($M)	10 Year Power ($M)
B_{PEAK}/E_{ACC} (mT/(MV/m))	5kW Plant Civil ($M)	Linac Length (m)
Geometry Factor (Ω)	Transfer Line ($k/m)	Num. Cryomodules
Beam Current (A)	2K Plant Margin	Num. Cavities
Beam Phase (deg)	% Increase Plant Cost @1.8K	Num. Girders, etc.
Detune Frequency Budget (Hz)	% Decrease in Eff. @1.8K	CM Dynamic Heat (W)
RF Power Margin	Linac R&D Cost ($M)	Linac 2K Heat (W)
Operating Temperature (K)	RF Wall Plug Eff.	2K With Margin
Maximum Loaded-Q	Controls AC Pwr / Girder (kW)	Q_0
Loaded-Q Uncertainty	Operations Week	Matched Q_L
Material and Treatment[1]	Power Overhead[4]	RF Power Per Cavity (kW)
Beam Transient Handling[2]	Static Heat Load/CM (W)[5]	Cryo AC Power (MW)
	Transfer Line Heat (W/km)	Non-Cryo AC Power (MW)

Notes:

1. A combination of materials and treatments were modeled in the Q_0 calculations. These were permutations of fine grain niobium and large grain niobium and vacuum baked at 120°C or not vacuum baked at 120°C.
2. The phase of the beam current can have a substantial impact on optimizing the loaded-Q and RF power requirements in an SRF Cavity. [2] Under certain circumstances the RF power requirements are substantially higher for short periods of time. There are techniques which can be used to compensate for said transients, such as slowly ramping up the beam current while the cavity tuners operate.
3. The inner cryomodule girder is the vacuum hardware, beam diagnostics hardware, and magnets that make up the common beam line hardware set between cryomodules. Also included in this item are the controls electronics and magnet power supplies.
4. The Power overhead in the baseline costs column includes items such as lighting, HVAC, and cooling tower power. An increase of 25% over the calculated electrical demand was used for this parameter.
5. The static heat load per cryomodule included the losses in the cryomodule as well as the associated valve boxes.

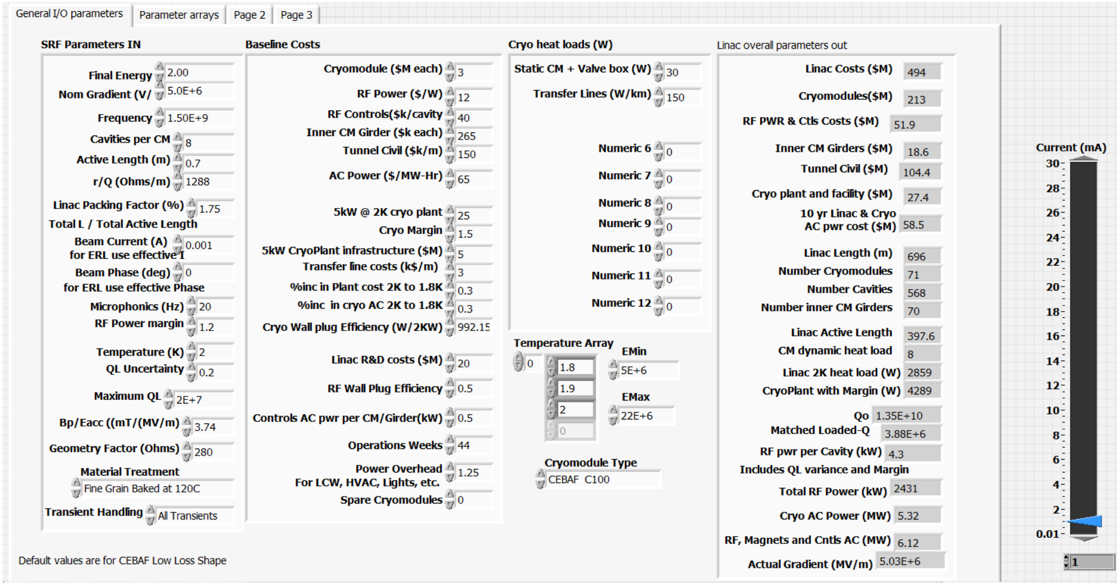

SRF Parameters IN

Final Energy 2.00
Nom Gradient (V/ 5.0E+6
Frequency 1.50E+9
Cavities per CM 8
Active Length (m) 0.7
r/Q (Ohms/m) 1288
Linac Packing Factor (%) 1.75
Total L / Total Active Length
Beam Current (A) 0.001
for ERL use effective I
Beam Phase (deg) 0
for ERL use effective Phase
Microphonics (Hz) 20
RF Power margin 1.2
Temperature (K) 2
QL Uncertainty 0.2
Maximum QL 2E+7
Bp/Eacc ((mT/(MV/m) 3.74
Geometry Factor (Ohms) 280
Material Treatment Fine Grain Baked at 120C
Transient Handling All Transients

Baseline Costs

Cryomodule ($M each) 3
RF Power ($/W) 12
RF Controls($k/cavity 40
Inner CM Girder ($k each) 265
Tunnel Civil ($k/m) 150
AC Power ($/MW-Hr) 65
5kW @ 2K cryo plant 25
Cryo Margin 1.5
5kW CryoPlant infrastructure ($M) 5
Transfer line costs (k$/m) 3
%inc in Plant cost 2K to 1.8K 0.3
%inc in cryo AC 2K to 1.8K 0.3
Cryo Wall plug Efficiency (W/2KW) 992.15
Linac R&D costs ($M) 20
RF Wall Plug Efficiency 0.5
Controls AC pwr per CM/Girder(kW) 0.5
Operations Weeks 44
Power Overhead For LCW, HVAC, Lights, etc. 1.25
Spare Cryomodules 0

Cryo heat loads (W)

Static CM + Valve box (W) 30
Transfer Lines (W/km) 150
Numeric 6 0
Numeric 7 0
Numeric 8 0
Numeric 9 0
Numeric 10 0
Numeric 11 0
Numeric 12 0

Temperature Array 0
1.8
1.9
2
0
EMin 5E+6
EMax 22E+6
Cryomodule Type CEBAF C100

Linac overall parameters out

Linac Costs ($M) 494
Cryomodules($M) 213
RF PWR & Ctls Costs ($M) 51.9
Inner CM Girders ($M) 18.6
Tunnel Civil ($M) 104.4
Cryo plant and facility ($M) 27.4
10 yr Linac & Cryo AC pwr cost ($M) 58.5
Linac Length (m) 696
Number Cryomodules 71
Number Cavities 568
Number inner CM Girders 70
Linac Active Length 397.6
CM dynamic heat load 8
Linac 2K heat load (W) 2859
CryoPlant with Margin (W) 4289
Qo 1.35E+10
Matched Loaded-Q 3.88E+6
RF pwr per Cavity (kW) 4.3
Includes QL variance and Margin
Total RF Power (kW) 2431
Cryo AC Power (MW) 5.32
RF, Magnets and Cntls AC (MW) 6.12
Actual Gradient (MV/m) 5.03E+6

Default values are for CEBAF Low Loss Shape

Figure 1: Input / Output screen of optimization program.

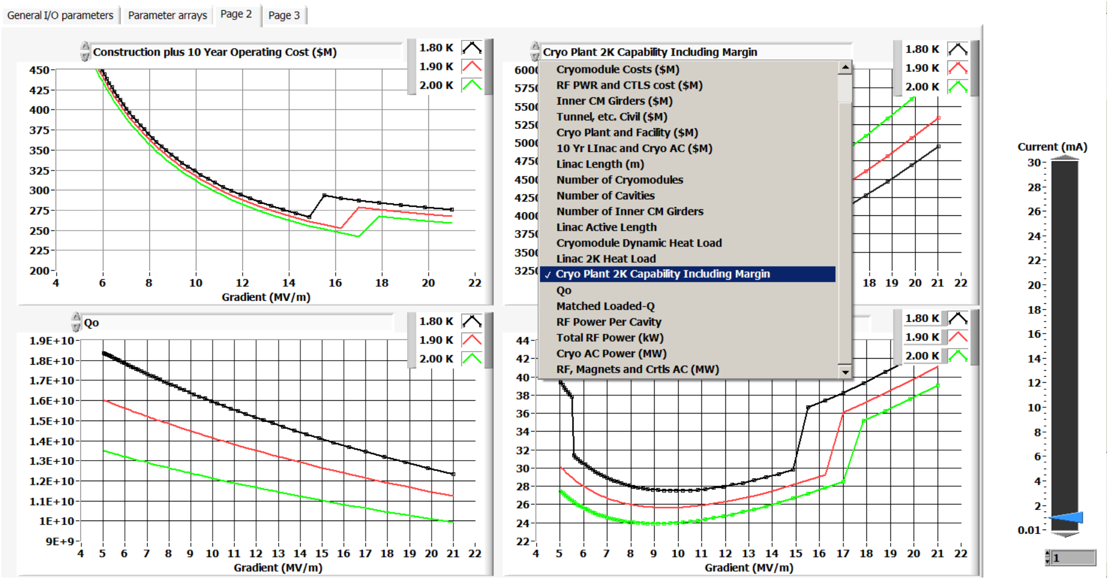

Figure 2: Graphics screen of optimization program showing method for selecting data to plot.

3.11.2.1 *Calculating Q_0*

Q_0 is calculated for each data point, and is based on a compilation of historic data. This historical data is a compilation from measurements taken in the vertical test area at Jefferson Lab, where, over the past 20 years JLAB staff has performed more than 1800 tests on superconducting cavities of various configurations and frequencies. A series of curve fits were done on these data in order to determine a Q_0 value as a function of gradient, frequency and operating temperature.[3] The analysis was limited in a number of areas due to a lack of completed data sets. It does take into account low to mid field Q-slope as well as the basic material parameters, cavity shapes, etc. It does not take into account high field slope which is an area that is currently undergoing revision. Another area that is under review is Q_0 degradation between vertical test and cryomodule installation in the accelerator, as well as long term degradation of the Q_0 in operational conditions. Figure 3, shows the value of Q_0 as a function of frequency at 16 MV/m at three different temperatures. For this data the cavity models used had the same geometry factor, and ratio of peak magnetic field to average electric field as the CEBAF low loss cavities used in the 12 GeV upgrade.

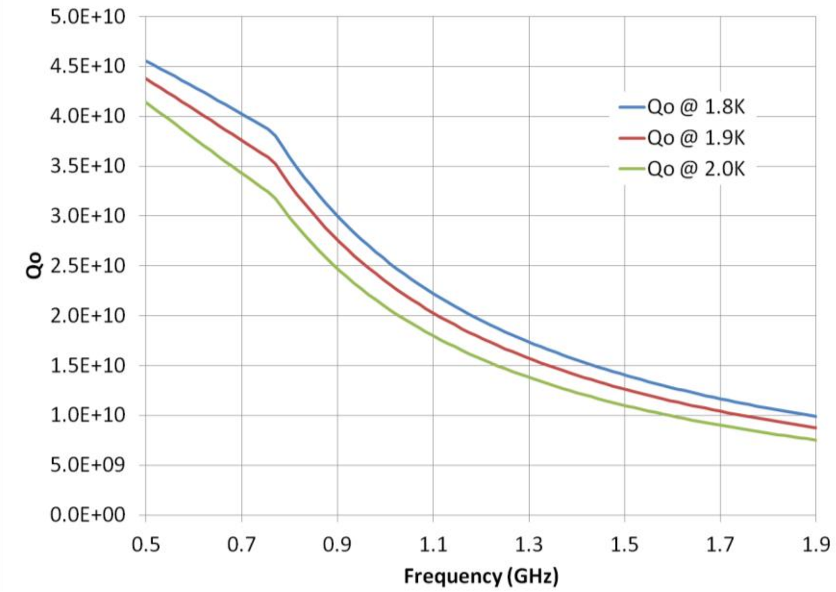

Figure 3: Q_0 as a function of frequency and temperature at 16 MV/m. All frequencies scaled from CEBAF C100 upgrade cavity.

3.11.2.2 *Calculating Loaded-Q and RF Power*

The matched loaded-Q is the loaded-Q such that the installed RF power is minimized. As discussed in the *Input/Output Parameters* section, the selected loaded-Q values depend on the whether the RF power can maintain gradient regulation under all transient beam loading conditions or only in a steady state condition. Eq. (1) provides the matched loaded-Q value under all transient conditions, while Eq. (2) gives the matched loaded-Q value under steady state conditions.

$$Q_L\Big|_{MinPower} = \frac{E}{\sqrt{\left(I_0 (r/Q)\cos\psi_B\right)^2 + \left(\pm 2\frac{\delta f}{f_0}E + I_0\,(r/Q)\sin\psi_B\right)^2}} \tag{1}$$

$$Q_L\Big|_{MinPower} = \frac{E}{\sqrt{\left(I_0 (r/Q)\cos\psi_B\right)^2 + \left(2\frac{\delta f}{f_0}E\right)^2}} \tag{2}$$

Here, E is the gradient in V/m, I_0 is the effective beam current in amperes, (r/Q) is the normalized shunt impedance in Ohms/m, γ_B is the phase of the beam current relative to the cavity gradient, δf is the difference between the RF frequency and f_0 which is the resonant frequency of the cavity. [4]

Once the matched loaded-Q is determined, it is used along with the detune frequency budget, the uncertainly in the loaded-Q and the remainder of the cavity parameters to calculate the permutations on the forward power necessary for operation at each point. The maximum value of this data set is used as the minimum RF power required. This is multiplied by the RF power margin to determine the RF power per cavity. There is no margin in the RF power for cavities operated above the design value, which is an area for future modifications to the program.

3.11.2.3 *Cryogenic Facility Costs*

Figure 4 shows the cost and efficiency estimates used for the cryogenic plant as a function of "2 K" power. The baseline plant and infrastructure costs that were used were that of the 5 kW at 2 K plant that was built as part of the CEBAF 12 GeV upgrade.[5] One major assumption is that the ratio of 50 K shield power to 2 K power is similar to that in CEBAF. Another critical aspect of the actual costs is that the plant was designed by, major components procured by, and the system integrated by JLAB staff. Were the plant to be procured as a turn-key plant the costs would likely be significantly higher. The procurement, installation and commissioning costs are scaled as the ratio of the (2 K power/5 kW)$^{0.7}$.[5] The wall plug efficiency, being the ratio of the total AC power divided by the 2 K power, was determined by plotting the efficiency achieved by several existing plants used at accelerators [6] and generating a third order fit between 800 W and 5 kW at 2K. It includes all AC power including warm compressors. Cooling towers, HVAC, lighting, etc. are included as part of a separate line item based on the overall power budget. The plant cost and efficiency was increased linearly by 30% between 2 K and 1.8 K. [5].

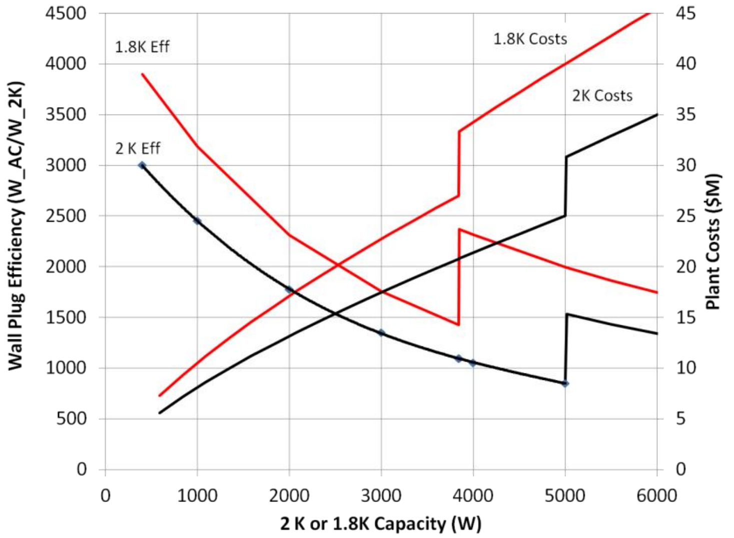

Figure 4: The wall plug efficiency and facility plant procurement costs for a helium refrigerator operated at 2.0 K and 1.8 K respectively.

The steps at 5 kW and 3.8 kW for the 2 K and 1.8 K systems were based on the practical aspect of building and shipping the components.[5] The primary issue is shipping of an assembled cold box by truck. Above these power break points the plant must be split into two sections. While one might consider using plants of different power ratings in order to reduce the cost, such plants might be less than ideal when considering standby (half power) operations, spare parts, engineering design costs, and overall maintenance costs. Based on this the model simply divides the plant into two equal sized plants. The efficiency steps up to match that of the smaller plant.

3.11.3 **Results**

3.11.3.1 ***Cost as a Function of Frequency***

One approach to the analysis of cost as a function of frequency is to maintain a constant active length of the linac. Figure 5 shows such an analysis where a 2 GeV linac was modeled with 21 cryomodules and a linac total active length of 118 m. In this model, as is often done when performing this type of optimization, cavities are not causal as it relies on a fractional number of cavities per cryomodule. Alternately one could consider using an integer number of cavities per cryomodule, which would limit the model to approximately 10 points for the same parameter sweep.

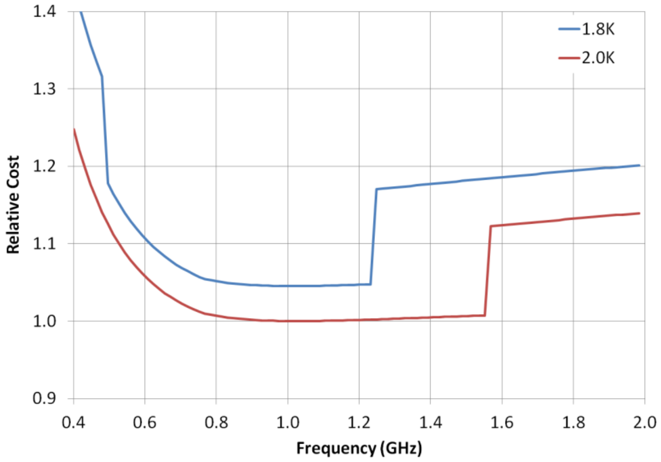

Figure 5: Relative cost of a 118 m active length, 21 cryomodule, 2 GeV linac plus 10 years of electrical power as a function of frequency and temperature.

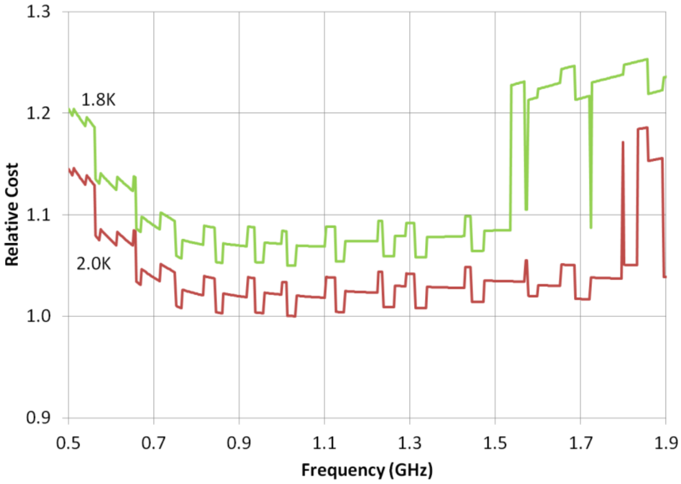

Figure 6: Relative cost of a 2 GeV linac plus 10 years of electrical power as a function of frequency and temperature for 10 – 12 m cryomodules each with a maximum of 8m of active length and an integer number of cavities.

Alternately, one can use practical cryomodules. For the results shown in Figure 6, the cryomodules were limited to 8 m of active length, resulting in 10 m to 12 m cryomodule lengths. The number of cells per cavity was varied from 4 cells at 500 MHz up to 11 cells above 1800 MHz resulting in cavities that are less than 1.2 m active length for any given cavity. This results in quantized steps in the relative costs plots. In these results, the steps are changes in the number of cryomodules. Also as one changes the frequency for a given cryomodule configuration the gradient must be reduced slightly (up to 10%) so as to provide the target machine energy. At lower frequencies the model for Q_0 currently employed does not have gradient dependence and thus there is a downward slope in the overall costs (lower cryogenic needs at lower gradients). At higher frequencies the Q_0 slope more than makes up for the reduction in gradient and the Q_0 losses increase as a function of frequency.

3.11.3.2 *Cost as a Function of Gradient*

For this model the program was set up with fixed cryomodule and cavity parameters and by sweeping the gradient, one is able to better undersand the cost drivers and implications. In actuality the program is sweeping through the number of cryomodules and calculating the average gradient such that the desired energy is achieved. Note that if the machine is run off crest, for a given number of cryomodules the gradient will have to be increased by a factor of $1/\cos(\psi_B)$ in order to provide the design beam energy gain. Figure 7 shows the relative cost of the C100 cryomodule design which was used in the 12 GeV upgrade.[7] The C100 cryomodule contains 8 cavities, each with seven cells operated at 1497 MHz, where each of the cavities has a normalized shunt impedance of 1288 Ω/m and a geometry factor of 280 Ω. This was compared to a cryomodule that could be built out of 6 cavities, of 5 cells each operated at 748.5 MHz. For this model the cavities had a normalized shunt impedance of 644 Ω/m and a geometry factor of 280 Ω.

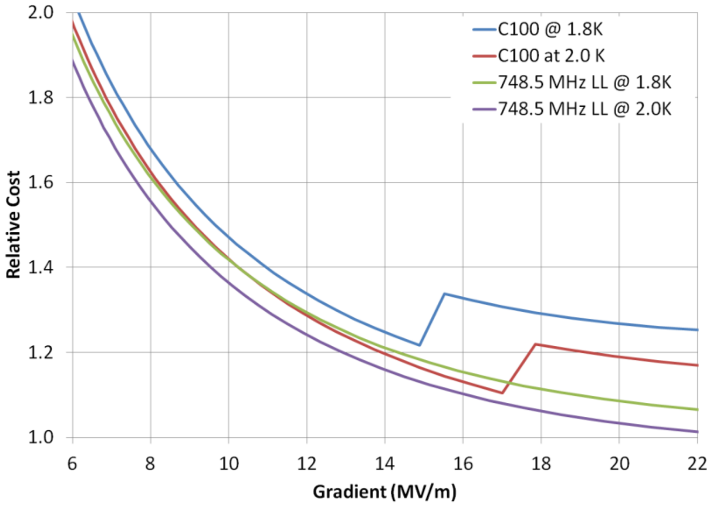

Figure 7: Relative cost of a 2 GeV linac plus 10 years of electrical power as a function of gradient and temperature.

Figure 8 shows the relative cost breakdown for the same C100 cryomodule configuration. One can see that the cost driver at the lower gradients is the cryomodule and accelerator civil construction costs. At higher gradients there is a step increase in cryogenic costs as the system exceeds a 5 kW or 3.8 kW cryogenic plant rating for 2.0 K and 1.8 K operating points respectively.

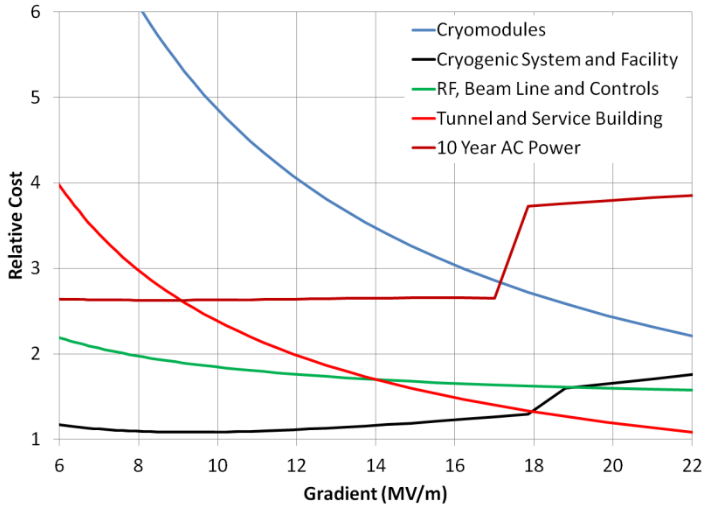

Figure 8: Relative cost breakdown for the components used in determining the cost for the C100 cryomodule operated at 2.0 K.

3.11.4 **Model Deficiencies and Future Improvements.**

The model used for the results in this paper has a number of issues which still need to be addressed. The cost estimates for items such as inner cryomodule girders, cryomodules, RF power, RF control, construction costs, etc. need to be estimated on a machine by machine, and location by location basis. Also since the current model uses a fixed number for the cryomodule unit cost, it is important to note that cryomodules with different numbers of cavities, couplers, etc. have different costs. In addition to issues like coupler selection, etc. the program does not take into account the material costs increases that occur when building cryomodules at lower frequencies.

The Q_0 data used for the analysis was taken from vertical tests. Thus there is no accounting for degradations and additional RF losses due to phenomena such as imperfect magnetic shielding, fundamental power coupler losses, and long term degradation due to new field emitters all of which occur when the cavities are installed and operated in a cryomodule. The model does not include high field Q-slope or any distribution function for field emission losses. Further analysis of state of art production data as well as data from past production runs and data from operational machines should allow us to refine the Q_0 models used. Reviewing actual costs for specific systems, hardware and constructions, as well as those included in proposals for new machines should provide us with results that are more in line with reality. In addition to addressing these issues we would like to also include more accurate distributions of gradients into the model which will affect the cryogenic losses.

3.11.5 **Conclusions**

These tools allow one to better understand the tradeoffs relating to the top level design parameters of an SRF linac. They allow one to make adjustments to the baseline costs, cavity parameters, machine packing factors, etc. on the fly and to get a quick feedback as to the impact. One surprise to the author was the major cost implications that occur when one exceeds the 18 kW at 4K helium liquefier limitations. Since this describes initial applications of a new program, any use of the results of the simulation in its current state should be done with care. For example, simple things such as inclusion of field emission onset, or Q-slope changes at lower frequencies, can dramatically change the optimum operations frequency, as both would tend to degrade high field operations. Inclusion of high field Q-slope will lead to increases in costs at the higher field levels and may lead to lower optimized field. Additionally, although the baseline cost information is felt to be reasonable, different locations will have different construction and electric power costs. Although we have made good progress in developing the tools for understanding machine cost tradeoffs more work is necessary in order to understand all of the impacts of the different parameters.

3.11.6 **References**

1. McIntosh, P., Accelerator Science and Technology Centre, Daresbury, UK, personal communication, May 2009
2. Powers, T., "RF Controls Experience with the JLAB IR Upgrade FEL," 2009 ERL Workshop, Ithaca, NY, June, 2009.
3. Ciovati, G., et. al., "Residual Resistance Data from Cavity Production Projects at Jefferson Lab," IEEE Trans. on Appl. Superconductivity, Vol 21, No. 3, June 2011.
4. Powers, T., "Practical Aspects of SRF Cavity Testing and Operations," Tutorial, SRF Workshop, Chicago, IL, July 2011.
5. Arenius, D., Thomas Jefferson National Accelerator Facility, Newport News, VA, personal communications, Feb. 2013.
6. Ganni, R., et. al., "Cryogenic Systems Improvements," Presented at The Thomas Jefferson National Accelerator Science and Technology Review, May, 2008.
7. Pilat, F., "JLAB Upgrade," Presented at Linac 12, Tel Aviv, Israel, Sept. 2012.

3.12 Simulations of a Free-Electron Laser Oscillator at Jefferson Lab Lasing in the Vacuum Ultraviolet

Michelle D. Shinn and Stephen V. Benson
Thomas Jefferson National Accelerator Facility
12000 Jefferson Ave., Newport News, VA 23606 USA
Mail to: shinn@jlab.org

Abstract:

The UVFEL at Jefferson Lab has provided a 10 eV photon beam for users by outcoupling the coherent third harmonic of the UVFEL operated at 372 nm. This can provide up to tens of milliwatts of power in the VUV. Operation of the FEL at the fundamental might enhance this power by up to a factor of 1000. With minor upgrades to the accelerator now underway and a new undulator proposed by Calabazas Creek Research, Inc. we show that we can lase in the fundamental at 124 nm. The predicted output is higher by four orders of magnitude on an average power basis and six orders of magnitude on a peak fluence basis than the Advanced Light Source at Lawrence Berkeley National Laboratory.

3.12.1 Introduction

Lasing in the vacuum ultraviolet is very difficult due to the lack of low loss optics in this wavelength range. One way to get around this limitation is to operate in the ultraviolet with a hole-coupled resonator and use the coherent third harmonic radiation naturally emitted by the FEL. This has been accomplished already at Jefferson Lab [1] but the power is rather low. If one can shorten the undulator wiggler wavelength, raise the electron beam energy, and enhance the electron beam brightness it is possible to produce gain sufficiently high for the relatively lossy mirrors in the vacuum ultraviolet.

3.12.2 FEL accelerator

3.12.2.1 *Present Accelerator Configuration*

The present accelerator for the Jefferson Lab FELs has already been described in detail in [2], so it will be described very briefly here. The accelerator source is a DC photogun operating at a nominal voltage of 350kV, which is then bunched and accelerated to ~ 10MeV with a modified CEBAF-style 2 cell booster. A merger injects this beam into a recirculating linac consisting of three cryomodules producing a total beam energy of 135 MeV.

3.12.2.2 *Proposed Upgrades*

The injector for the Jefferson Lab FEL is presently undergoing an upgrade designed to allow higher voltage from the gun and a more optimal accelerating cavity design for the booster. Though this will not reduce the emittance and energy spread dramatically at the FEL, it should reduce it by approximately 20%. The linac will also be upgraded with the replacement of one cryomodule with a new high-performance version. With this module in place the accelerator should be capable of up to 160 MeV of electron beam energy. To obtain fundamental 10 eV with the present undulator it would be necessary to increase the energy to 235 MeV. This is far beyond the capability of the present accelerating voltage. To reach 124 nm we must change the undulator as well. Calabazas Creek Research, Inc. [3] has proposed building an undulator with iron poles embedded in a solenoidal field. Their design predicts an rms field of 5.1 kG in the helical undulator with a period of 15 mm. The rms value of K would then be 0.707. Similar undulators have been built in the past by several groups.

3.12.3 FEL Oscillator

3.12.3.1 *FEL Modeling*

The availability of a pulse repetition rate of 4.678 MHz allows for the operation of the VUV-FEL as an oscillator, with a cavity length as long as ~32m. To overcome high mirror losses, the small signal gain should be high, yet the overall wiggler length is constrained to about 2 m in order for it to fit in the available space. The wiggler wavelength of 1.5 cm is short enough that an *in vacuo* device is required but the solenoid embedded design allows a helical undulator design, which permits a lower field for the same FEL gain. We are therefore assuming here a helical undulator with a period of 1.5 cm and an rms field of 5.1 kG. The bore of the wiggler would be 5 mm diameter, which would be a problem for very high average current but will not be a problem for a current of at most a few milliamperes. Such a design might have very good field quality and very low susceptibility to radiation damage. A more conventional superconducting electromagnetic undulator could achieve a similar field but with much more complexity and less flexibility in its design. A cryogenic permanent magnet wiggler could also achieve an equivalent rms field strength in a linearly polarized undulator, but would be more sensitive to radiation.

The performance of this FEL was predicted using two codes. One is a combination of the time-independent version of Genesis 1.3 to model the FEL interaction in 3-D, and the Optical Propagation Code (OPC) to model the oscillator [4,5]. OPC provides the flexibility to look at the effects of mirror figure distortions, add intra-cavity apertures, and analyze a number of other features, such as edge outcoupling, or the effect of mirror decentering and tilts. The wiggler can be placed anywhere in the cavity and the mirror ROCs can be unequal. It also allows one to evaluate the outcoupled mode and determine its profile and beam quality. The other FEL oscillator code is Wavevnm, developed by the Naval Postgraduate School. This code assumes the wiggler is located in the center of the resonator, and calculates the mirror's radii of curvatures (ROCs) based on an input Rayleigh range and waist position. Both codes treat the FEL interaction similarly in that a wiggle-averaged orbit approximation is used, i.e., the interaction is evaluated at each wiggler period and the average motion of the electrons over each period is used. In addition, the user defines a discrete mesh and the particle distribution and fields are evaluated on the mesh nodes.

For the chosen wiggler, optical cavity, and e beam parameters, simulations in Genesis 1.3 yield a single pass gain of ~3.6, insufficient for operation as a high-gain, low-*Q* oscillator [2], where a small amount of power from the output is fed back to the start to seed the next pulse. Instead, a near-concentric cavity is modeled, with the parameters given in Table 1. Power is outcoupled through a hole in the center of the mirror downstream of the wiggler. This provides an advantage in tunability, since for photon energies less than 12.4 eV, the mirrors are relatively broadband and the wavelength is controlled by the beam energy and the wiggler parameters. To add tunability, we plan to use the multiple mirror design employed on the other FELs at JLab [6] to change the coating parameters and outcoupler hole size.

The wiggler and optical cavity parameters for the Genesis/OPC simulations at 124 nm (10 eV) are shown in Table 1.

Table 1: Wiggler, electron beam, and optical cavity parameters for 124 nm operation

Parameter	Value
Wiggler period (cm)	1.5
Number of periods	120
K_{rms}	0.707
Energy (MeV)	155
Emittance (microns)	4
Energy spread (%)	0.17
Peak current (A)	180
Cavity length (m)	32.04196
Mirror radii (cm)	1.27
Mirror radius of curvature (m)	16.072
Hole radius (cm)	0.1
Mirror reflectivity (%)	80
Mirror microroughness (nm rms)	≤0.5
Slippage parameter	0.33
Nominal pulse bandwidth (FWHM)	0.2%

A few comments about the table are in order. The reflectivity at 124nm is typical, or slightly poorer (< 5%) than the value determined from curves published on manufactures websites, in order to provide a more realistic expectation of the losses encountered at this wavelength. The pulse bandwidth is an estimate based on the slippage parameter which itself is based on the electron pulse having an rms duration of 150fs. In comparing the results of the two codes, the Wavevnm simulations showed little tendency to avoid the hole, whereas the Genesis/OPC simulations showed a mode profile that was peaked slightly off center. The latter case matches our own experience. Both codes predicted a profile resembling a TEM_{01} mode, as shown in Fig. 1, with a peak roughly in the center. This is also true of the outcoupled profile. As shown in Fig. 2, the Genesis/OPC simulations indicate a peak lasing efficiency of 0.048%, an outcoupling efficiency of 27%, and an output energy per pulse of almost 5 μJ, or 23W average power at 4.678MHz.

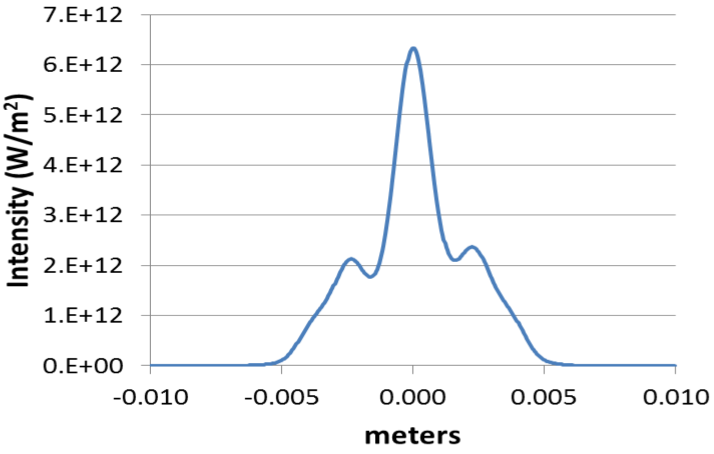

Figure 1: Transverse profile on OC mirror

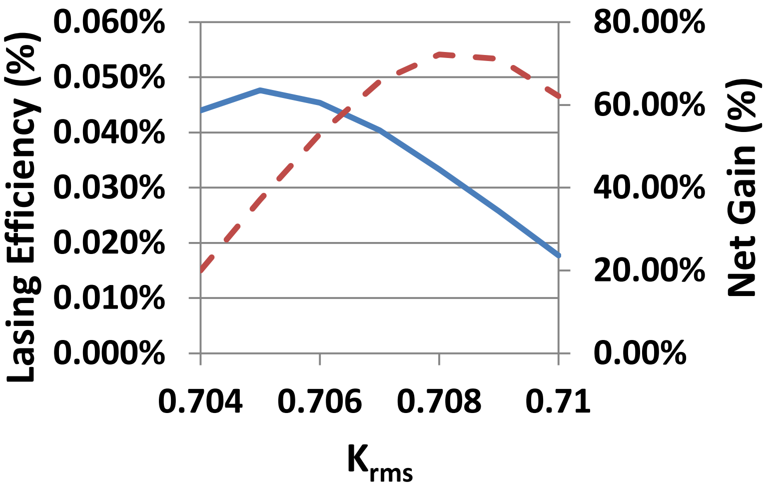

Figure 2: Lasing efficiency (solid line) and net gain (dashed line) as a function of K_{rms}

For comparison, the output at 10eV of the Advanced Light Source, operating at 500MHz with 70ps pulses, is about 3pJ/pulse with an average power of 1.6mW [2]. The measured 3rd harmonic output of the UV FEL was about 7 nJ [4]. Actual performance might be poorer when the effects of mirror thermal distortion and vibration, as well as electron beam slippage, are accounted for in the model.

3.12.4 **Optics Considerations**

Though the predicted output of the FEL makes it the highest average power laser in this wavelength range, this output is modest compared to lasers at longer wavelengths. Because the performance of the FEL is dependent on the Rayleigh range which is in turn determined by the mirror radii of curvatures, the mirror substrates will be cryo-cooled silicon, as this material is athermal, i.e., has a negligible coefficient of thermal expansion at ~120 K [7]. This material can also be superpolished to achieve a microroughness below 0.1nm, although the metal coating with protective overcoat may increase the roughness slightly. Besides the aforementioned thermal distortion of the mirrors, which can be partially compensated by deforming them [6], there are technical challenges associated with the maintenance of surface figure and finish along the periphery of the hole in the outcoupler mirror, which we believe can be met using ion milling and magnetorheological finishing.

The use of hole outcoupling in a near-concentric resonator architecture results in a low outcoupling efficiency, so the intracavity power falling on the mirrors is roughly 4 times higher than the output power. To determine whether damage to the cavity optics could be performance-limiting, consider that the mirror subjected to the highest irradiance is the high reflector (HR) mirror, since the peak intensity falling on the outcoupler mirror passes through the hole. The peak intensity on the HR is 3.46×10^8 W/m^2, on a fluence basis it is 0.1mJ/cm^2 for a 300fs pulse. This is well below the laser damage threshold of 56mJ/cm^2 estimated by using the measured damage threshold of 100mJ/cm^2 for 300fs pulses at 400nm [8] and an inverse square root wavelength dependence [9]. Thus, performance shouldn't be limited by damage to the cavity optics.

3.12.5 Conclusions

We have simulated the performance of an FEL oscillator operating in the VUV based on the existing Jefferson Lab linac and recirculator with an upgraded injector. The performance is based on 3D simulations, so 4D effects, such as slippage and bunch shape are ignored. The predicted performance is promising, with an outcoupled energy/pulse of 5μJ and an average power of 23W, making it much brighter than synchrotron light sources.

3.12.6 Acknowledgements

The authors wish to thank Gwyn Williams for his calculations of the photon flux from the Advanced Light Source as well as for discussions about VUV coatings, and to George Neil for suggesting this study. Financial support was provided by the Commonwealth of Virginia and by the U.S. DOE under Contract No. DE-AC05-06OR23177.

Authored by Jefferson Science Associates, LLC under U.S. DOE Contract No. DE-AC05-06OR23177. The U.S. government retains a non-exclusive, paid-up, irrevocable, world-wide license to reproduce this manuscript.

3.12.7 References

1. R.A. Legg, et al., “Operation and Commissioning of the Jefferson Lab UV FEL using an SRF Driver ERL”, Paper THP172, proceedings of the Particle Accelerator Conference, New York, NY (2011).
2. S.V. Benson, et al.,”A Proposed VUV Oscillator-based FEL Upgrade at Jefferson Lab”, J. Mod. Opt. **58**, 1438 (2011).
3. R. H. Jackson, M. E. Read, Thuc Bui and R. L. Ives, "Asymmetric Immersed Pole Undulators", IEEE International Conference on Plasma Science July 8-12 2012, Edinburgh, UK.
4. S. Benson, et al. “Demonstration of 3D Effects with High Gain and Efficiency in a UV FEL Oscillator”, Paper THP171, proceedings of the Particle Accelerator Conference, New York, NY (2011).
5. J. G. Karssenberg et al., “FEL-Oscillator Simulations with Genesis 1.3”, Proc. FEL’06 BESSY, Berlin, Germany, p. 407 (2006).
6. M. D. Shinn et al. “Design of the Jefferson Lab IR upgrade FEL optical cavity”, Nuclear Instruments and Methods **A507** 196 (2003).
7. P. Carpentier et al., “Synchrotron monochromator heating problem, cryogenic cooling solution”, Nuclear Instruments and Methods **A456** 163 (2001).
8. D.W. Doerr and D.A. Alexander, "Submicron patterning of aluminum films by laser ablation", *Proc. SPIE* 3874, Micromachining and Microfabrication Process Technology V, p. 62 (1999).
9. R.M. Wood, Laser-Induced Damage of Optical Materials, IOP Publishing Inc. (2003).

4 ICFA Beam Dynamics Workshop Report – Accelerators for a Higgs Factory: Linear vs. Circular (HF2012)

Alain Blondel[1], Alex Chao[2], Weiren Chou[3], Jie Gao[4], Daniel Schulte[5] and
Kaoru Yokoya[6]

[1] U. of Geneva, Geneva, Switzerland
[2] SLAC, Menlo Park, California, USA
[3] Fermilab, Batavia, Illinois, USA
[4] IHEP, Beijing, China
[5] CERN, Geneva, Switzerland
[6] KEK, Tsukuba, Japan

Mail to: chou@fnal.gov

4.1 Executive Summary

The 4th of July 2012 was a historical moment for high-energy physics (HEP). On that day, CERN announced that both the ATLAS and CMS experiments had discovered a new Higgs-like boson. In this report, we shall assume that this newly found particle will turn out to be a Higgs boson, the key signature of the Standard Model. At the ICFA meeting on July 8 in Melbourne, an ICFA Beam Dynamics Workshop "*Accelerators for a Higgs Factory: Linear vs. Circular*" (HF2012) was approved. This workshop took place from November 14 to 16, 2012 at Fermilab, USA. (conferences.fnal.gov/hf2012) Seventy-one people from 31 institutions in Asia, Europe and North America attended. The workshop agenda is in Appendix 1.

The next "big" collider after the LHC has been the subject of international HEP community planning for more than a decade. For example, at the 2001 Snowmass meeting, a number of options were considered: a linear e^+e^- collider, a circular e^+e^- collider, a Very Large Hadron Collider (VLHC) and a muon collider. Since then, however, under the direction of ICFA, a series of decisions have been made:

- It should be an e^+e^- collider;
- It should be a linear e^+e^- collider;
- It should be a cold (i.e., Superconducting RF) linear e^+e^- collider.

These major decisions have been followed by a number of significant steps. An international collaboration for the ILC, defined as a Superconducting RF linear e^+e^- collider of a center-of-mass energy (E_{CM}) 500 GeV was formed under the leadership of the Global Design Effort (GDE). Substantial progresses in design, prototyping and R&D have been made. A Technical Design Report (TDR) will be published in mid-2013, complete with a cost estimate. The Japanese HEP community has proposed to build a low-energy linear collider (E_{CM} = 250 GeV) as the first step of the ILC.

The discovery of the Higgs-like boson at the LHC has placed the focus on the need to study the properties of this new particle with high precision. Thanks to nature, the light mass of the Higgs (~126 GeV) puts a Higgs factory closer to reach. Various proposals are claimed to be able to reach the energy and luminosity of interest for a Higgs factory: a linear e^+e^- collider, either cold or warm (e.g., x-band), a circular e^+e^-

collider; a muon collider and a photon collider. They were put on the table at the HF2012 workshop as possible candidates:

(a) Linear e^+e^- colliders:
  - ILC
  - CLIC
  - X-band klystron-based

(b) Circular e^+e^- colliders:
  - Fermilab site-filler
  - LEP3
  - TLEP
  - SuperTRISTAN-40 and SuperTRISTAN-80
  - CHF-1 and CHF-2
  - VLLC

(c) Muon collider

(d) Photon colliders:
  - ILC-based
  - CLIC-based
  - Recirculating linac-based (SAPPHiRE)
  - SLC-type

The purpose of the workshop was to compare the pros and cons of these candidates mainly from the accelerator point of view but not to recommend any specific machine, which is only possible with further input from the physics side. Also it is not excluded that multiple facilities may be required to complement one another in addressing the entire breadth of Higgs physics. The comparison includes:

- ➢ physics reach
- ➢ performance (energy and luminosity)
- ➢ upgrade potential
- ➢ technology maturity and readiness
- ➢ technical challenges requiring further R&D

Cost was not included because it was too early for such a comparison at this stage. Parameter comparison tables are in Appendix 2. These tables were provided by the workshop presenters except for some obvious corrections and items derived from the data provided.

The LHC will keep collecting valuable data and it is expected that more data from the LHC will further clarify what kind of Higgs factory (or factories) will be needed.

For the candidates above (except the muon collider operating at the Higgs resonance) delivered luminosities are in units of 10^{34} $\mathrm{cm}^{-2}\mathrm{s}^{-1}$. Assuming 1×10^7 seconds a year for effective machine operation, this leads to an integrated luminosity of 100 fb^{-1} per year. Since the cross-section for Higgs production (the ZH channel for e^+e^- and s-channel for $\gamma\gamma$) is about 200 fb, the "quantum" is ~20,000 Higgs per year. The muon collider operating at the resonance has a lower luminosity (10^{31}-10^{32} $\mathrm{cm}^{-2}\mathrm{s}^{-1}$). But the cross-section of $\mu^+\mu^- \rightarrow H$ is much larger (~41 pb), which could compensate for the lower luminosity and give a comparable Higgs production rate.

Before we compare linear and circular e^+e^- Higgs factories, it will be useful to review two e^+e^- Z-factories operating at E_{CM} around 91 GeV – the circular LEP

(2.4×10^{31} $cm^{-2}s^{-1}$), and the linear SLC (3×10^{30} $cm^{-2}s^{-1}$). Both were successfully designed, constructed and operated, and both achieved important physics results: 0.5 million Z decays at the SLC over 11 years and 4 million in each of four experiments at the LEP over 7 years. The exquisite energy calibration at the LEP by resonant depolarization led to 2 MeV precision on the Z mass and width. The single most precise determination of the electroweak mixing angle $sin^2\theta_{eff}^{lept}$ at the SLC was due to 80% longitudinal electron polarization.

The SLC was the first (and only) linear collider ever built. Since then, extensive studies on linear colliders have been carried out with an impressive level of detail. The ILC and CLIC are two flagship programs. The former is based on Superconducting RF technology while the latter on two-beam acceleration. Hundreds of millions of US dollars (or equivalent) have been invested in these programs. Linear colliders are extremely challenging and complex machines, but the key technologies are claimed to be in hand. There exist well-organized international collaborations. The linear collider community will soon be reorganized by combining the ILC, CLIC and detectors together in a single organization – the Linear Collider Collaboration.

In terms of readiness, the linear e^+e^- Higgs factory is clearly the front runner. The main difficulty comes from the high cost of the project. Recently the Japan HEP community issued a report advocating building a 250 GeV (E_{CM}) linear collider in Japan as the first stage of the ILC serving as a Higgs factory.

An x-band klystron-based linear collider was previously studied in great detail in both the US and Japan. But the work was stopped after the ICFA selected SRF technology for the ILC in 2004. However, the interest in an x-band linear collider was renewed at CERN, KEK and SLAC during the discussion of a Higgs factory because its cost would be lower than a CLIC at E_{CM} = 250 GeV, and one could add a CLIC section later for an extension to higher energy.

In addition to these linear e+e- colliders, another approach not discussed at the workshop is the use of plasma (beam- or laser-driven) or dielectric wakefields to provide the acceleration field. These technologies are not mature today and face important technical challenges that require vigorous R&D, but have a large potential for Higgs factories and beyond. A plasma scheme has been published at PAC 2009 (p. 2688). An update will be presented at IPAC 2013. A comparison of this technology with other technologies for linear collider Higgs factory is a subject to be considered in the future.

Contrary to the three different technologies (SRF, two-beam and x-band) for a linear e^+e^- collider, all circular e^+e^- collider are similar. The only difference is their size. From the Fermilab site-filler (16 km) to LEP3 (27 km) to TLEP/SuperTRISTAN/CHF (40-80 km) to the VLLC (233 km), they share a number of common features.

The main limitation of a circular e^+e^- collider is that its energy is limited by synchrotron radiation ($P_{SR} \propto E^4$) and thus has no potential for an energy upgrade. (The linear colliders, on the other hand, have advocated an energy up to 3 TeV.) However, a circular e^+e^- collider could be converted to a *pp* collider in the future as the next energy frontier. This was discussed for instance in a plan presented by IHEP, China. It was proposed to begin by constructing a circular 50-70 km circumference tunnel. In Phase 1, the tunnel would host the China Higgs Factory (CHF), a 240 GeV e^+e^- collider. Then in Phase II (20-30 years in the future), when the high field superconducting magnet technology has further matured, a 100 TeV *pp* collider could be built in the same tunnel.

A noticeable feature of this plan is that it completely bypasses the ILC option and focuses the physics on either low energy (Z, W and Higgs boson studies) or very high energy (new frontier).

A main advantage of a circular e^+e^- collider of sufficiently large size is to offer a higher luminosity than a linear one at 240 GeV and below. Also, a circular collider can accommodate more than one interaction point (e.g., LEP had 4 IPs). Dozens of circular e^+e^- colliders have been built and operated in the past five decades. The technology is mature and the experience rich.

However, to meet the required energy (240 GeV) and luminosity (a few times 10^{34} $cm^{-2}s^{-1}$) of a Higgs factory, several new major technical challenges need to be met. Following the model of the B-factories and synchrotron light sources, all circular e^+e^- colliders adopted an additional circular accelerator as a full energy continuous injector (top-up injection). Due to high beam intensity and small beam size, beamstrahlung (synchrotron radiation of individual particles in the opposing beam's field) will further limit the beam lifetime. Managing this effect requires both the RF system and the machine optics (in both the arcs and the interaction region) to have large momentum acceptance (ranging from 2% to 6% depending on specific proposals). This is a nontrivial design challenge, especially in view of the equally important requirement on the optics for small emittance.

High synchrotron radiation power is another major challenge. The energy loss per turn in these machines is on the order of 10 GeV, and the beam current on the order of 10 mA. These translate to ~100 MW radiation power and must be replenished by the RF system. The major concerns are the RF power coupler, radiation shielding, radioactivation and the required wall power. Even with a 50% wall plug efficiency (which is several times higher than today's most efficient accelerator, the PSI cyclotron), one would need ~200 MW to compensate for synchrotron radiation. This is higher than the current power consumption at CERN (183 MW) and almost four times as large as that at Fermilab (58 MW). The total site power, including cryogenics, magnets, water cooling and injectors would be even higher. At a given energy, this and many other problems are easier in the machines of larger circumference.

Compared to a circular e^+e^- collider, the muon collider has the advantage of no synchrotron radiation or beamstrahlung problem due to the muon mass 207 times more than an electron. This means a muon Higgs factory would be much smaller (a circumference of 0.3 km). Even a TeV-scale collider could be accommodated in an existing campus (e.g., Fermilab). Moreover, the cross section of the s-channel resonance $\mu^+\mu^- \rightarrow H$ is about 40,000 times larger than that of e^+e^- ($\sigma_0 = 41$ pb), which provides a unique way for detailed measurement of the Higgs line shape should it be an unconventional resonance. This requires a relative beam energy spread commensurate to the expected Higgs boson width of 4 MeV – a few times 10^{-5}! The technological challenges are enormous, in particular the required 4D and 6D ionization cooling of muon beams. Simulations of the cooling processes have made substantial progress, but experimental verifications are lacking. Some critical issues (e.g., RF breakdown in a strong magnetic field) are being addressed and progress has been made towards viable solutions. The MICE international collaboration in the UK and the MAP program in the US are tackling these issues.

Photon colliders were first suggested as possible extensions of two proposed linear colliders (SLC and VLEPP). Photon colliders are based on Inverse Compton Scattering (ICS) by shooting a low energy (~1 eV) laser beam into a high energy (10s of GeV) electron beam to generate a back-scattered high energy (10s of GeV) photon beam for collisions. The advantage is that the cross section for $\gamma\gamma \rightarrow H$ is large and comparable to $e^+e^- \rightarrow ZH$ (~200 fb) but the required energy is much lower (63 GeV for a photon beam, corresponding to 80 GeV for an electron beam, compared to 120 GeV per electron beam in an e^+e^- collider). This makes a photon collider an attractive option for either a low energy linear collider (80 GeV per electron beam) or a low energy circular collider (80 GeV per beam). Furthermore, for a photon collider there is no need for positrons and only one damping ring is needed. However, the physics of a photon collider is not as comprehensive as a 240 GeV e^+e^- collider. There are also machine design issues (e.g., IR optics and removal of the spent electrons) that need to be addressed.

Several photon collider proposals were presented at the workshop. One example is ILC-based, another example CLIC-based. Their bunch structures are very different. The former has long bunch trains (727 μs) and large bunch spacing (554 ns), whereas the latter has short bunch trains (177 ns) and small bunch spacing (0.5 ns). This leads to drastically different requirements for the laser. With large spacing an optical cavity can be used, whereas a short train makes the use of a single laser shot possible. Thanks to the newly formed ICFA-ICUIL collaboration, the study of the required lasers received strong participation from the laser community. For example, the Lawrence Livermore Lab is working on a fusion project LIFE, which will use 384 laser beams for fusion ignition. Just one of these 384 lasers would be sufficient for a warm linac-based (CLIC or x-band) photon collider. However, further R&D is required for either bunch spacing scenario.

Based on the LHeC study at CERN, it was proposed to use an 80 GeV recirculating linac for a photon collider (SAPPHiRE). SLAC, on the other hand, proposed an SLC-type photon collider that uses a single linac (room temperature or superconducting) to accelerate both beams to 80 GeV.

One issue considered to be essential for inclusion in this workshop report is to give a timeline for these proposals. This is a particularly delicate exercise that the HF2012 program committee is undertaking with great hesitation. Not all proposals are at the same level of technical readiness and this is reflected in the uncertainty in the timeline. Although the workshop has addressed in depth the technical readiness of various proposals, many more issues in addition, e.g. cost, available manpower, funding profile, and international setting, will all have great impact on the timeline. Using the best information available the committee generated the timeline of various proposed Higgs factories. These are in Appendix 3.

The study on Higgs factories will continue. The ILC has finished the TDR. The CLIC has completed the CDR and is proceeding to the TDR stage. But design reports for other proposals (circular e^+e^- colliders, muon collider and photon colliders) have not yet been produced. The proponents are encouraged to move from the parameter design to conceptual design with the goal of publishing a report.

This workshop provided a useful and convenient platform for the international community to meet and discuss issues of mutual interest related to a future Higgs factory. Thus, it will be continued. The next workshop is expected to take place in late 2013. The exact dates and venue are yet to be decided.

4.2 Higgs Physics

Is the new particle discovered at the LHC the Higgs boson of the Standard Model? Or does it carry evidence for physics beyond? High precision measurements of the properties of this new particle are the next step. The session on Higgs physics [1] began with a presentation of the LHC achievements in the discovery of the Higgs boson candidate [2-3] and the present status of measurements of its properties. This was followed by an estimate of what measurements can one reasonably expect to come from LHC after the "nominal" run of 300 fb^{-1} at a center-of-mass energy of 14 TeV, or, after the high luminosity upgrade, to 3000 fb^{-1} (HL-LHC) [4-5]. The theoretical introduction described the role of the Higgs boson as a clear instrument and signal of symmetry breaking of the Standard Model and its minimal but somewhat "ad-hoc" nature, as well as the variety of scenarios that have been advocated to introduce it perhaps more naturally. This calls for a variety of measurements of Higgs properties and of other electroweak quantities. A number of scenarios for New Physics Beyond the Standard Model have been given in the literature [6-8], but a clear ansatz of the precision required to achieve their detection is still work in progress. The "Higgs factories" are accelerators-detector facilities that can do precisely that, and the following were addressed:

- the LHC itself, both "nominal mode" and HL-LHC
- the e^+e^- colliders, either linear collider projects (ILC, CLIC) or the more recent proposals of circular machines operating in the range $m_Z < E_{CM} \leq 350$ GeV
- the $\mu^+ \mu^-$ collider operating at $E_{CM} = m_H$
- a $\gamma\gamma$ collider operating just above $E_{CM} = m_H$

4.2.1 Physics Case

The Higgs boson candidate is such a special particle that it should be studied in all possible ways. However, there is still much work to do to understand quantitatively the physics case for building a Higgs Factory given that the theorists are only starting to answer the question "*how precisely should Higgs properties be measured*?" With available information effects of New Physics at the TeV scale could be of the order of a few percent, maybe up to O(5%) on Higgs couplings. A discovery (i.e. 5σ observation of a discrepancy with the Standard Model prediction) would then require precision well below a percent. How to compare or combine the information given by the LHC, e^+e^- colliders at ZH threshold, e^+e^- colliders at high energy and a $\mu^+\mu^-$ or $\gamma\gamma$ collider is still in its infancy.

A caveat to the physics discussion is in order: The main purpose of the workshop was to initiate an in-depth accelerator discussion. Nevertheless a number of important new results on the precision achievable for Higgs couplings were presented. At the same time, significant differences of views were highlighted – the most important ones are described in the following sections. It is clear that the physics discussion was only a beginning, and will need to be continued in a dedicated, broader framework with participation of experts from all proposals.

4.2.2 The LHC as a Higgs Factory

It was certainly one of the highlights of the meeting that projections showed potential of HL-LHC to reach percent precision. The cross-sections for Higgs production, shown in Figure 2.1 are very large (20 pb at 8 TeV, and increase by substantial factors when going up in energy). Numbers would be even better for the high energy option HE-LHC in the LHC tunnel with new magnets allowing 33 TeV E_{CM}, or for the super-high energy option SHE-LHC in a new, 80 km tunnel, allowing to reach 100 TeV, especially for the determination of the Higgs self-couplings as the double Higgs production increases by a factor 9 when going from 14 to 33 TeV. Assumptions on available luminosity and scaling of systematic errors were discussed extensively. LHC experiments so far have actually performed significantly better than expected.

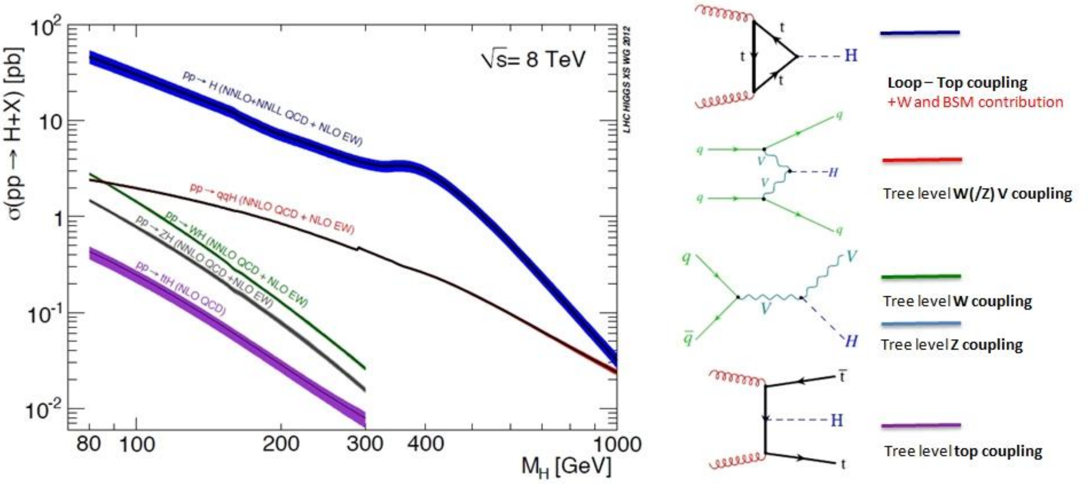

Figure 2.1: Higgs production cross-section at the LHC operating at 8 TeV center-of-mass energy. On the right are indicated the five main production mechanisms, which upon tagging can provide coupling measurements to the gluon, W, Z and top.

LHC measurements address the mass, the spin-CP properties and couplings to bosons {gamma, gluon, W, Z} and fermions (top, b, tau, muon) to a few percent. The accessible channels represent $B_{vis}\approx 98\%$ of the SM Higgs decays. The spin-CP question is expected to be settled with data available by the end of 2012. The LHC observables are cross-sections times branching ratios and can be expressed in terms of new physics as such

$$O_{if} = (\sigma \times BR)\,\{pp \to ii \to H \to ff\} = \varphi(pp \to ii)\,\frac{\sigma_{ii\to H}\Gamma_{H\to ff}}{\Gamma_H} \equiv O_{if}^{(SM)}\ \frac{\kappa_i \cdot \kappa_f}{\kappa_H} \quad ,$$

where: κ_I , κ_f , κ_H represent the ratio between the true value and the Standard Model value for initial and final state coupling to the Higgs and for the total Higgs width; and $\varphi(pp \to ii)$ is the flux factor representing the probability of finding the initial state within a pp collision of the given energy. For a selected final state, the initial state can be identified by kinematic selection. The systematic errors originate from i) various detector efficiencies and performance which tend to improve with increasing statistics, and ii) uncertainties in the flux factors.

In addition, the LHC experiments have come to the preliminary conclusion that, by identification of final states with two Higgs boson decays, an indicative measurement of the effect of the Higgs self-coupling could be obtained with HL-LHC with a precision of the order of 30% or better.

The LHC measurements provide many O_{if} observables with i= gluon-fusion, Vector-Boson-Fusion, or radiation from top, W or Z, for 7 different final states. Phenomenological predictions should be compared directly to these observables. For the sake of comparison with other facilities, projections were made in terms of κ factors, see Table 2.1, with $\Delta\kappa_x \equiv \frac{\Delta g_{Hxx}}{g_{Hxx}}$ to match the e^+e^- notations. In effect what LHC is able to determine very precisely are ratios of branching fractions. What cannot be determined is the common factor κ_H that would affect the total width, and could be changed in a global way by new undetected Higgs boson decays. For instance an increase of the total width stemming from a global factor increasing all couplings would result in an increase of the observed cross-sections, while a similar increase due to a significant invisible width would decrease them – conceptually a conspiracy could take place. The power of the variety of initial states available at the LHC is illustrated by the precisions with which the ttH coupling or gluon-gluon Higgs couplings can be determined at the LHC.

4.2.3 Higgs Physics of Electron-Positron Colliders

The most studied Higgs Factory is the e^+e^- collider. Most studies have been made of linear colliders [9-12], but the Higgs physics in e^+e^- depends only marginally on the fact that the collider is linear or circular [13-14]. It then boils down to the availability of high luminosity at the desired energies.

The specific feature is presented by the $e^+e^- \to Z\,H$ reaction, shown in Figure 2.2. The events can be detected inclusively, independently of the Higgs decay mode, by tagging e.g. a leptonic Z decay with a recoil mass equal to the Higgs mass. This cross-section is proportional to g_{HZZ}^2, while the cross-section for $e^+e^- \to Z\,H, H \to ZZ$ is proportional to g_{HZZ}^4/Γ_H, thus allowing the Higgs total width to be determined (this assumes a single resonance). In addition, the investigation of tagged ZH events can reveal invisible or exotic decays that would have escaped detection at the LHC, thus removing the ambiguity between new physics in couplings or in new decay modes. The best place to study this reaction is just below the cross-section maximum of 200 fb at E_{CM} ~ 240(±10) GeV; the chosen value depends on the energy dependence of the luminosity in a given machine. Thus in circular machines the lower end of the bracket is preferred, in linear colliders the upper end. This reaction can also be investigated at any energy where enough statistics can be collected, so that the CLIC studies [11-12] concentrate on the higher energies from 350 GeV up.

For the study of HZ, beam polarization is not essential; a high level of longitudinal electron polarization combined with 30% positron polarization can be arranged to provide a 30% increase of the rate; this was taken into account in the ILC estimates. At 240 GeV the unpolarized cross-section is 200 fb, so that collection of a million ZH events requires an integrated luminosity of 5 ab^{-1}. In most e^+e^- Higgs studies the precision is limited by the available statistics. At the linear collider, the studies of the $b\bar{b}$ and $c\bar{c}$ decays benefit from the very small beam spot size at the IP and from the specific time structure of the accelerator that allows operation of the vertex detectors in a pulsed mode. Whether this quality can be preserved on a circular machine with a collision rate between 10 kHz and 1 MHz and in the presence of synchrotron radiation needs further study.

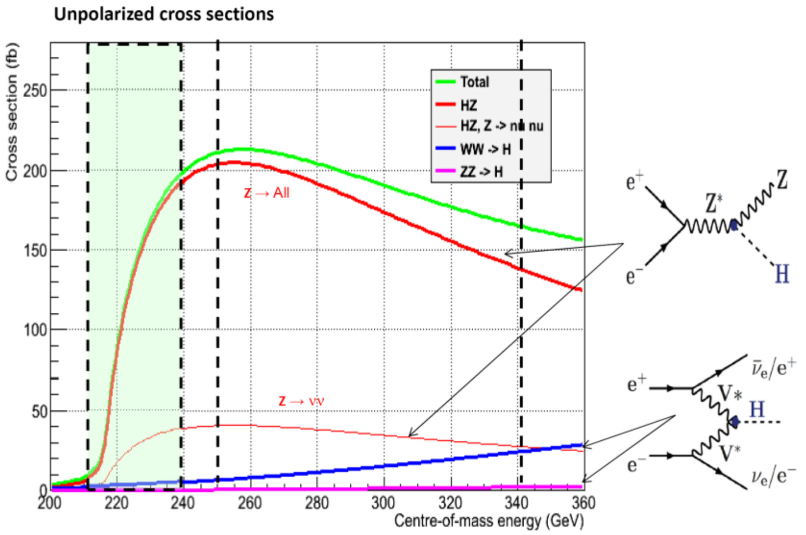

Figure 2.2: Unpolarized Higgs boson production cross-sections at low energy e^+e^- colliders. The regions of interest for the direct study of the Higgs boson are: 1) the threshold region, between 210 GeV and 240 GeV; 2) the region of cross-section maximum around 240-250 GeV and the regieon up to the $\bar{t}t$ threshold (340-350 GeV).

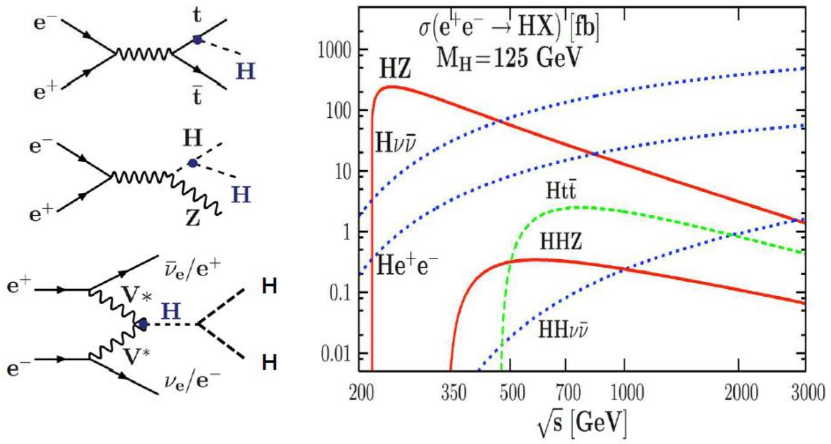

Figure 2.3: High energy $\bar{t}tH$ and HH cross-sections in e^+e^- colliders. Note the two to three orders of magnitude lower cross-sections compared to the ZH process.

The e^+e^- colliders can also collect high statistics of Higgs decays at higher center-of-mass energies, where the most abundant production mechanism is Vector-Boson Fusion $e^+e^- \to \overline{\nu_e} W^+ \nu_e W^-$, $W^+W^- \to H$, Figure 2.3. This reaction in combination with the ZH measurements can improve significantly the determination of the Higgs width. At high energies, the reactions $e^+e^- \to t\bar{t}\,H$ (above 475 GeV) and $e^+e^- \to \overline{\nu_e}\,\nu_e HH$ (in the TeV range) can give a handle on the Higgs coupling to the top quark and on the Higgs self-coupling. Here the longitudinal beam polarization is useful (although not essential) as a means of controlling the backgrounds and enhancing the signal.

There are different views on the need for an e^+e^- Higgs factory to run at energies higher than the ZH maximum. Everyone agrees that reaching 350 GeV E_{CM} is a definite bonus, allowing the study of the reaction $e^+e^-\to\overline{\nu_e}\,\nu_e H$ and of direct top quark pair production. This is possible for the ILC, CLIC and, although close to their limit, for the larger circular machines such as CHF and TLEP. The relative merits of running above 350 GeV *for Higgs physics alone* depend on the machine considered. While the linear collider proponents emphasize that the study of the Higgs-top coupling and the triple Higgs coupling require an e^+e^- machine at least up to 1 TeV, the proponents of circular machines argue that these measurements will in all likelihood be performed, earlier, at the HL-LHC with a precision similar to what is advertised for, e.g., the 1 TeV ILC – this was rather new information at the time of the workshop. Running only above 350 GeV as advocated by CLIC proponents is another possible strategy that remains to be fully evaluated. The Higgs self-coupling is an extremely difficult measurement, the best reported sensitivity (very preliminary, 11%) would be from CLIC running at 3 TeV for 2 ab^{-1}. A further physics case beyond H(126) for a Linear Collider at an energy above 350 GeV may come from the discovery of one or more new particles at the LHC in the coming years.

In addition e^+e^- colliders are unique for the precision measurements of quantities sensitive to new particles through electroweak radiative corrections (EWRCs). These provide important tests of the completeness of the Standard Model and of the Higgs mechanism. This can be best done by revisiting the Z peak with a high luminosity machine. TLEP claims 10^{36} $cm^{-2}s^{-1}$ (TeraZ). The main question there is how one could take advantage of these potentially huge statistics to improve on the LEP measurements, some of which are already at the limit of systematics.

In this context, the availability of longitudinal beam polarization is extremely valuable for the measurement of the inclusive and exclusive beam polarization asymmetries A_{LR} and $A^{f}_{FB,Pol}$. This is straightforward in a linear collider and has been advocated for obtaining a measurement of the weak mixing angle $\sin^{2}{}_{\mathrm{eff}}{}^{\mathrm{lept}}$ with a precision of a few 10^{-5}. If longitudinal polarization could be achieved with colliding beams in a circular machine at the Z peak, a small fraction of the advertised luminosity would allow these measurements to reach an extremely interesting level of accuracy.

The availability of very precise energy calibration, as available from the transverse polarization in a circular machine using resonant depolarization, would allow a new measurement of the Z mass and width with ten-fold precision improvement, or better, over the present errors of about 2 MeV. The W pair threshold would offer a measurement of the W mass with better than 1 MeV precision if a measureable level of transverse polarization can be achieved at ~80 GeV per beam.

4.2.4 Physics of $\mu^+\mu^-\to$ Higgs

A muon collider [15-18] can do everything that an e^+e^- collider of the same energy can do, with some advantages in terms of precise knowledge of the center-of-mass energy distribution, which can be extracted exquisitely from (g-2) spin precession detected from the decay electrons. However, a $\mu^+\mu^-$ collider has the additional feature that the coupling of muons to the Higgs is m_μ/m_e times larger than for electrons, leading to a useable cross-section of 40 pb for the s-channel production $\mu^+\mu^- \to H(126)$. The study of the resonance requires a machine of precisely $E_{beam} = m_H/2$ with a precision of better than $\Gamma_H = 4.2$ MeV. The demand on both reproducibility and beam energy spread is thus very stringent. The energy spread can in principle be reduced to 3×10^{-5} by emittance exchange but this is done at the expense of transverse emittance and the luminosity is expected to be around 10^{31} cm^{-2}s^{-1}.

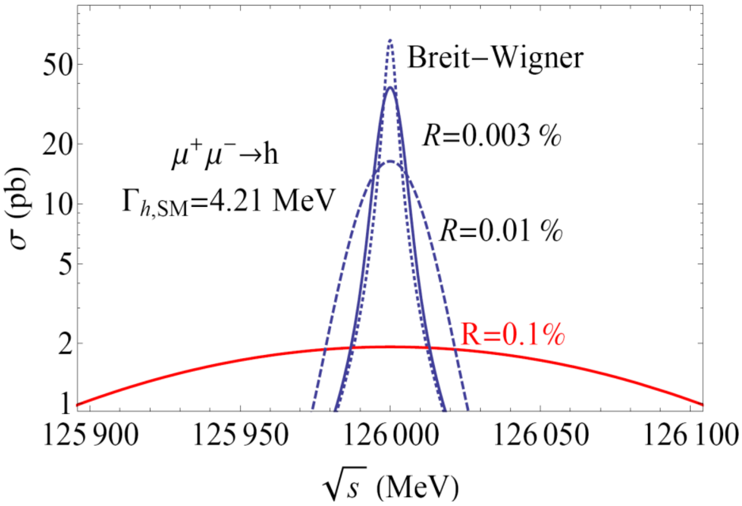

Figure 2.4: Direct measurement of the Higgs decay width Γ by using muon beams of high energy resolution.

About 2300 Higgs decays would be observed for one year of running (100 pb^{-1}). Then the Higgs boson mass can be obtained with a precision of 0.1 MeV, the line shape width directly with a precision of 0.2 MeV (5%), the peak cross-section with a precision of 2-3%, from which the Higgs width can be extracted with a relative precision of 3% and the muon coupling to 1.5%.

In conclusion, the muon collider Higgs factory is unique in its ability to check that the Higgs boson is a single resonance of the expected line shape; the Higgs mass can be determined with a precision of a 0.1 MeV, and the muon coupling to the percent level. Unless a significantly higher luminosity can be achieved, all other measurements seem to be better done with a hadron or e^+e^- collider. Studies are going on to increase the luminosity at the $\mu^+\mu^- \to H(126)$ resonance to 10^{32} cm^{-2}s^{-1}. At higher energies, the muon collider retains its potential as a unique tool to study, via the s-channel resonance, the line shape of possible heavier neutral Higgs bosons, or to investigate very high energy lepton collisions.

4.2.5 Physics of $\gamma\gamma \to$ Higgs

The photon collider can be seen as an add-on to a linear collider [19] or as a dedicated machine [20]. The reaction of interest is the direct s-channel $\gamma\gamma \to H$ which has a cross-section of 200 fb. The Higgs cross-section is enhanced for photons of circular polarization in the J=0 state, so the use of a polarized laser allows a significant enhancement of signal over the background. The use of linearly polarized photons allows selection of specific CP states.

The unique attribute of the photon collider is the initial coupling to a pair of photons. Higgs can be observed in e.g. the $\gamma\gamma$ or $b\bar{b}$ final state, following which, using the $b\bar{b}$ partial width measured at another machine, the $H \rightarrow \gamma\gamma$ partial width can be extracted in absolute terms to a precision of 1%. This quantity is of particular interest because this decay proceeds through an inclusive loop that can potentially reveal heavier particles into which the Higgs cannot decay directly. Experimentation would have to be developed to control the luminosity spectrum at the appropriate level of precision.

4.2.6 Higgs Physics Summary

The main purpose of the workshop was to initiate an extended accelerator discussion. It is clear that the physics discussion was only a start, and will need to be continued in a dedicated, broader framework. However a number of important results on the Higgs couplings were already presented.

The relative precisions on Higgs couplings to various particles that were presented for the various proposals are listed in Table 2.1. The table is not yet fully complete but a few conclusions can already be drawn.

- HL-LHC will already be a Higgs factory, able to perform precise measurements on the relative values of the $\gamma\gamma$, gluon-gluon, $t\bar{t}$, W and Z couplings.
- An e^+e^- Higgs factory operating at ZH maximum with the anticipated luminosity for the ILC or LEP3 will access the Higgs boson physics observables that will not be accessible at the LHC (total width, invisible width, and ccbar decay), and allow some improvements over the precision available at the HL-LHC for a few of the other couplings (see Table 2.1), in particular the $b\bar{b}$ coupling.
- To attain the sub-percent precision measurements sensitive to new physics at the TeV scale it is of interest to pursue investigation of accelerators that could give significantly higher luminosities at ZH threshold and below. These are the proposed large circular colliders such as CHF or TLEP.
- Unfortunately, none of the proposed facilities is able to make a very significant measurement of the Higgs self-coupling[2]; investigation of this important question may have to wait for a higher energy collider beyond the LHC/ILC/CLIC.

It should also be emphasized that testing the closure of the Standard Model by precision measurements at the Z peak or the W threshold is one of the important tasks for a next generation lepton collider.

---

[2] The most significant prospects come from the CLIC studies. Recent and preliminary indications are that a precision of 22% at 1.4 TeV or 11% at 3 TeV could be attained with 1.5 ab^{-1} (resp 2 ab^{-1}) integrated luminosity [12].

Table 2.1: Expected performance on the Higgs boson couplings from the LHC and e^+e^- colliders, as compiled from the Higgs Factory 2012 workshop. Many studies are quite recent and still ongoing.

Accelerator → Physical Quantity ↓	**LHC** 300 fb^{-1} /expt	**HL-LHC** 3000 fb^{-1} /expt	**ILC** 250 GeV 250 fb^{-1} 5 yrs	**Full ILC** 250+350+ 1000 GeV 5yrs each	**CLIC** 350 GeV (500 fb^{-1}) 1.4 TeV (1.5 ab^{-1}) 5 yrs each	**LEP3, 4 IP** 240 GeV 2 ab^{-1} (*) 5 yrs	**TLEP, 4 IP** 240 GeV 10 ab^{-1} 5 yrs (*) 350 GeV 1.4 ab^{-1} 5 yrs (*)
N_H	1.7×10^7	1.7×10^8	6×10^4 ZH	10^5 ZH 1.4×10^5 Hνν	7.5×10^4 ZH 4.7×10^5 Hνν	4×10^5 ZH	2×10^6 ZH 3.5×10^4 Hνν
m_H (MeV)	100	50	35	35	100	26	7
$\Delta\Gamma_H / \Gamma_H$	--	--	10%	3%	ongoing	4%	1.3%
$\Delta\Gamma_{inv} / \Gamma_H$	Indirect (30%?)	Indirect (10% ?)	1.5%	1.0%	ongoing	0.35%	0.15%
$\Delta g_{H\gamma\gamma} / g_{H\gamma\gamma}$	6.5 – 5.1%	5.4 – 1.5%	--	5%	ongoing	3.4%	1.4%
$\Delta g_{Hgg} / g_{Hgg}$	11 – 5.7%	7.5 – 2.7%	4.5%	2.5%	< 3%	2.2%	0.7%
$\Delta g_{Hww} / g_{Hww}$	5.7 – 2.7%	4.5 – 1.0%	4.3%	1%	~1%	1.5%	0.25%
$\Delta g_{HZZ} / g_{HZZ}$	5.7 – 2.7%	4.5 – 1.0%	1.3%	1.5%	~1%	0.65%	0.2%
$\Delta g_{HHH} / g_{HHH}$	--	< 30% (2 expts)	--	~30%	~22% (~11% at 3 TeV)	--	--
$\Delta g_{H\mu\mu} / g_{H\mu\mu}$	< 30%	< 10%	--	--	10%	14%	7%
$\Delta g_{H\tau\tau} / g_{H\tau\tau}$	8.5 – 5.1%	5.4 – 2.0%	3.5%	2.5%	≤ 3%	1.5%	0.4%
$\Delta g_{Hcc} / g_{Hcc}$	--	--	3.7%	2%	2%	2.0%	0.65%
$\Delta g_{Hbb} / g_{Hbb}$	15 – 6.9%	11 —2.7%	1.4%	1%	1%	0.7%	0.22%
$\Delta g_{Ht\,t} / g_{Htt}$	14 – 8.7%	8.0 – 3.9%	--	5%	3%	--	30%

(*) The total luminosity is the sum of the integrated luminosity at four IPs.

Comments on Table 2.1:

- For the LHC:
  Measurements at the LHC are extracted from final state Higgs decay cross-sections. Since there is no tagged Higgs channel at the LHC there is an unknown overall scaling factor that can be taken as either an unknown total width normalization or an uncertainty in invisible channels. Except for invisible width limits, the precisions given in the table were obtained under the assumption that there is no invisible decay mode of the Higgs boson so that the total width is the sum of the observed partial ones. One can alternatively, and without model dependence, interpret these numbers as precision of the relative couplings. The first set of numbers corresponds to the hypothesis in which the systematic errors remain the same as in today's LHC results; the second set of numbers corresponds to the assumption that experimental systematic errors scale down with statistics, while the systematic errors of theoretical nature (flux factors) could be reduced by a further factor of two – this second assumption is considered the most realistic at the moment, but does not take into account possible improvement in the detectors. Except for g_{HHH}, the estimated precisions are for one single LHC experiment.
- For the the e^+e^- facilities – The quoted integrated luminosities and the expected sensitivities are based on the following assumptions:
  (a) All luminosity numbers were taken at face value from the proponents of the various facilities (Tables 8.1 and 8.2). Some are optimistic, others conservative. The integrated luminosities correspond to the total delivered by each facility. It is the sum of two experiments sharing one IP at ILC, or the sum over four experiments for LEP3 and TLEP. Operating time of 10^7 seconds per year was assumed.
  (b) The integrated luminosities for the ILC and CLIC were based on a model with slow initial build-up for machine operation.
  (c) The numbers of Higgs for the CLIC do not include the effects of beam polarization except for the HHH coupling studies.

4.3 Linear e^+e^- Colliders

4.3.1 **Introduction**

ILC R&D has been based on a truly global international collaboration. In its RDR and TDR phases, the Global Design Effort (GDE) has been the global working force on ILC accelerator R&D with about 130 participating institutions (http://www.linearcollider.org). The core technology for ILC of 2×10 km linacs is Superconducting RF (SRF) technology. It features seventeen thousand 1.3 GHz SRF cavities with accelerating field of 31.5 MV/m in 1,700 cryomodules and is based on over 20 years worldwide R&D efforts. The TDR was completed at the end of 2012. The volume covering accelerators consists of two parts: Part I: R&D, Part II: Baseline Reference Report. Based on the TDR, staging scenarios to start with a Higgs factory of 250 GeV extendable to 1 TeV are proposed.

CLIC is an international collaboration of 44 institutions from 22 countries. CLIC has a staged design to reach a center-of-mass energy of 3 TeV. Different from conventional klystron powered linac, CLIC adopts a drive beam scheme to produce the main linac RF (distributed klystron scheme), with a drive beam current ~100 times greater than the accelerated beam current. In 2012, CLIC has published a CDR in three volumes: Vol. I: The CLIC accelerator and site facilities, Vol. II: Physics and detectors at CLIC, Vol. III: CLIC study summary. The feasibility of the CLIC scheme has been established. The CLIC staging scenarios include a first stage at 500GeV that can be used as a Higgs factory. Higher energy stages will still contribute to the Higgs studies, e.g. to the measurement of the Higgs self-coupling and the coupling to WW.

The main advantage of the linear collider is that the cost grows as $A+B\times E_{CM}$, thus "only" linearly with energy; the main drawback is that both A and B are very large. The challenge is to achieve reliably very high bunch intensities and very small beam sizes for the two beams simultaneously and to collide them. There are specific proposals (ILC and CLIC) which have been designed to the point that the main technologies are in hand, although the level of readiness are somewhat different. International collaborations have been set-up and organized. The luminosity grows linearly with energy with a value of 2×10^{34} $cm^{-2}s^{-1}$ at $E_{CM} = 500$ GeV. The luminosity can be doubled by increasing the RF power by a factor of about 1.5 at a capital cost increase of several percent. The machine delivers beam to one IP. High level (80%) of any type of beam polarization is readily available for electrons, whereas a lower level (30%) is achievable for positrons. Beam energy calibration relies on accurate beam spectrometers with a relative precision of a few 10^{-4}. Beamstrahlung induces a broadening and some uncertainty in the center-of-mass energy, but this is not of great importance for Higgs physics. The collision environment features electromagnetic residues which have been carefully studied. The beam comprises 5 bunch trains per second which allows the use of very thin detectors operating in a pulsed mode. There exists a proposal to establish a linear collider in Japan starting with a center-of-mass energy of 250 GeV.

Compared with other types of Higgs factory, linear e^+e^- Higgs factories have the following features:

- Advantages:
  - ➢ Extensive design and prototyping work have been done.
  - ➢ Key technologies are in hand after large investment for R&D.
  - ➢ There exist well-organized international collaborations led respectively by the ILC GDE and CLIC Collaboration (soon to be combined in the Linear Collider Collaboration).
  - ➢ It is an important step towards high energy e+e- collisions.
  - ➢ Polarized beams (e^- 80%, e^+ 30%) can be created.
  - ➢ It is the front runner (in terms of readiness).
- Challenges:
  - ➢ High cost
- Specific issues:
  - ➢ ILC
    - ✧ Final Focusing System (FFS)
    - ✧ Positron source for a Higgs factory needs 10 Hz operation of the electron linac for e+ production, or the use of an unpolarized e+ beam as a backup scheme
  - ➢ CLIC
    - ✧ Accelerating structure

- ✧ Industrialization of major components
- ✧ From CDR to TDR

The KEK x-band e^+e^- / $\gamma\gamma$ Higgs Factory is based on CLIC-type cavities and the existing conventional RF technology. An optical FEL can also be used to produce high-energy photon beams for a $\gamma\gamma$ collider. In the first stage of operation ($e^+e^- \rightarrow$ Z, WW and $\gamma\gamma \rightarrow$ H) the proposed facility could be built on the KEK site. If the initial operational mode is with photon beams, then there is no need for an e+ source or a positron damping ring. The total length of the two linacs would be short, about 3.6 km at E_{CM}(ee) ~ 250 GeV.

The machine-detector interface (MDI) for ILC 500 GeV and CLIC 3 TeV has been studied. The requirements for MDI are to provide reliable collisions of ultra-small beams (~few nanometers), with an acceptable level of background.

4.3.2 ILC-based Higgs Factory

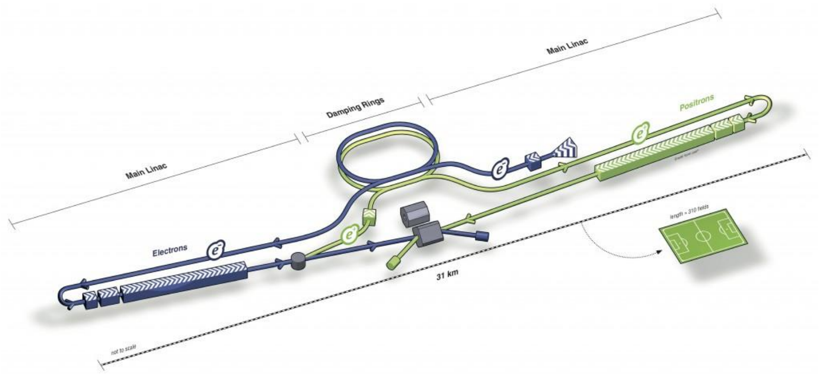

Figure 3.1: Layout of the ILC.

ILC is in the advanced design stage. (Figure 3.1) The Technical Design Report (TDR) was completed at the end of 2012. The official printed version will appear in June in 2013 after a few review steps. The TDR concentrates on the design of a machine of center-of-mass energy E_{CM} = 500 GeV and does not describe in detail the design as a Higgs Factory. However, the technology for the Higgs Factory is obvious. Up to the center-of-mass energy 500 GeV ILC can adapt to any staging scenarios required by physics. The difference is only the lengths of the linac and the tunnel. The estimated cost of the 250 GeV Higgs Factory is 67% of the cost of the 500 GeV collider and is 75% if the tunnel for 500 GeV is constructed. The required total site power is about 120 MW and 125 MW, respectively. (The power for 500 GeV operation is 160 MW.) In the present scope of ILC, when going beyond E_{CM} = 500 GeV, an R&D is planned for higher accelerating gradients for cost savings. Even without higher gradient the cost increase for the 1 TeV machine is around 10% of the 500 GeV machine.

In the case of $E_{CM} < 300$ GeV, 10Hz operation (5 Hz for collision and 5 Hz for positron production) is planned in the baseline design because the positron production in the undulator scheme is somewhat inefficient when the electron energy $E_{CM}/2$ is lower than 150 GeV. (Figure 3.2) This does not cause any problem technically, but is not very elegant. The 10 Hz operation requires an extra length of electron linac corresponding to $150 - 250/2 = 25$ GeV and extra electric power ~25 MW. Thus, if 10 Hz operation is avoided, the construction cost ~3% and the operation power ~25 MW can be saved compared with the values quoted in the TDR. A possible way to avoid 10 Hz operation is to adopt the electron-driven, conventional method. This is a proven design. The only change in physics is that the positron is unpolarized.

In all cases the luminosity presented in Table 8.1 assumes 1312 bunches per pulse. This can be upgraded by a factor of 2 by adding about 50% more RF system.

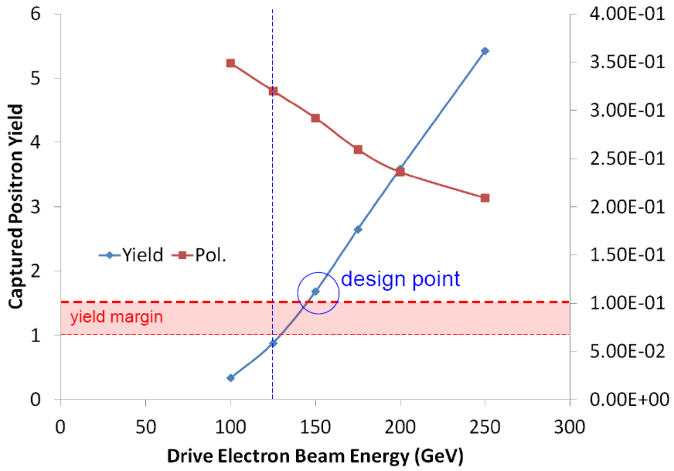

Figure 3.2: Positron yield (blue) and polarization (red) as a function of the drive electron beam energy.

There are a few items that require final steps of R&D.

First, the target for the positron production still needs several months or 1-2 years of further study. However, the design of the backup scheme, which uses conventional electron-driven system, has been completed. If ILC has to start construction in 2013, this backup scheme can be adopted. The only disadvantage is that positron polarization would not be available.

Second, the test of the final focusing system is still going on at KEK-ATF2. There have been delays, including that due to the 2011 earthquake, but no fundamental problem is expected. The latest operation in December 2012 achieved a vertical beam size ~70 nm (Figure 3.3), which differs from the design (37 nm) by only a factor of two. Further study is being planned in 2013. [21]

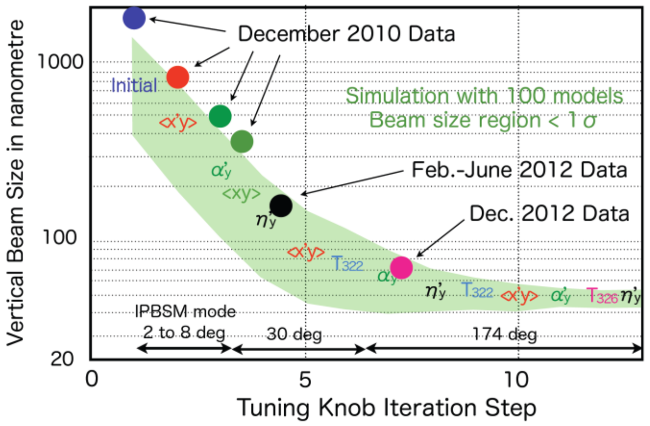

Figure 3.3: Vertical beam size from the ATF2 experiment.

4.3.3 CLIC-based Higgs Factory

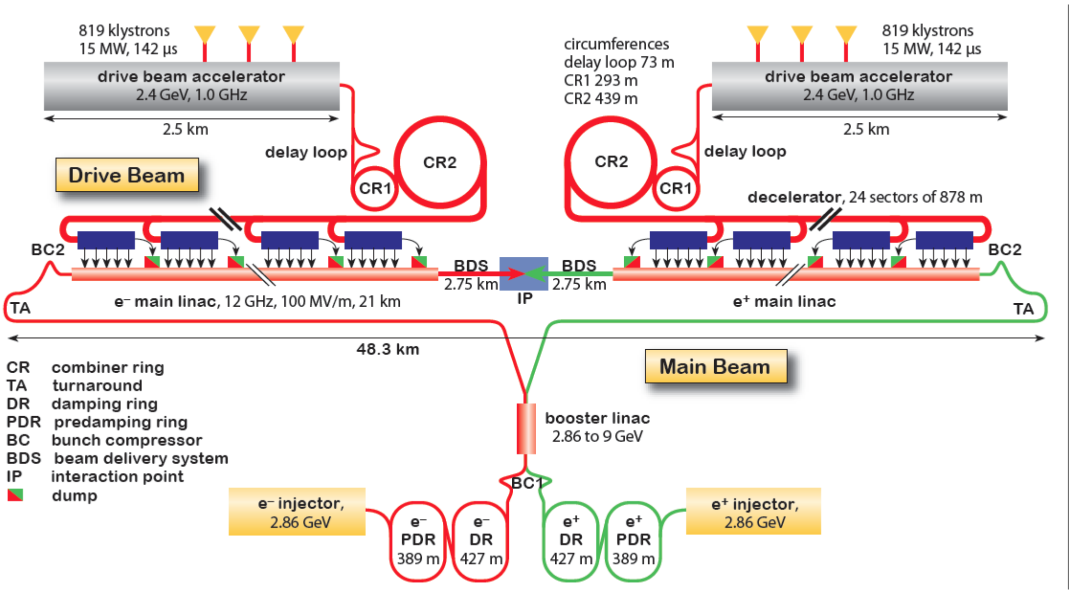

Figure 3.4: Layout of the CLIC.

Figure 3.4 shows the layout of the CLIC. The CLIC baseline design proposes building in stages of increasing energy. The choice of these stages will have to be fixed taking into account future LHC results. Currently two example scenarios exist, named A and B, in order to illustrate the staging strategy. Scenario A has stages at 500 GeV, 1.4 TeV and 3 TeV, while scenario B has stages of 500 GeV, 1.5 TeV and 3 TeV. Scenario A provides higher luminosity at 500 GeV, while scenario B has a lower integrated cost for the three stages. Each of the energy stages contributes to the Higgs studies. Table 3.1 lists the parameters of the 500 GeV and 3 TeV stages of scenario A.

It is possible to operate each energy stage of CLIC at a lower than nominal energy. This can be achieved by operating the main linac at a reduced gradient, i.e. by reducing the drive beam current. The main bunch charge also needs to be reduced in this mode in order to preserve the same beam quality. At certain reductions of the gradient it is possible to increase the length of the drive and main beam pulses. The resulting increased number of bunches per beam pulse allows an increase in luminosity. The main and drive beam complex is fully prepared for this type of operation. The power consumption at lower than nominal collision energy is somewhat lower than at 500 GeV, the exact value depends on the collision energy.

The CLIC physics study group envisages performing the Higgs measurements at a center-of-mass energy of 500 GeV or 350 GeV, rather than at 250 GeV. The total number of Higgs that can be expected at different center-of-mass energies is shown in Figure 3.5 for the $e^+e^- \to ZH$ and $e^+e^- \to \nu\nu H$; the parameters for 250 GeV and 350 GeV are given in Table 3.1.

If large importance was attributed to the operation at 250 GeV, one could also consider adding an extraction line in the main linac, to extract the beam at 125 GeV. This would result in somewhat increased luminosity. The same luminosity would be obtained if CLIC were built for this collision energy only. However this is currently not foreseen since it delays the program at higher energies.

The feasibility of the CLIC concept has been established with the studies documented in the CDR. In particular the drive beam concept has been proven at a test facility (CTF3) and very high gradients have been achieved experimentally. Specific challenges as the unprecedented alignment and stability tolerances have been successfully addressed experimentally. The main remaining challenges are to develop a technical design, based on the conceptual design. This includes an optimization of the accelerator components and systems and preparation for industrial procurement. In particular small series production of accelerating structures is important.

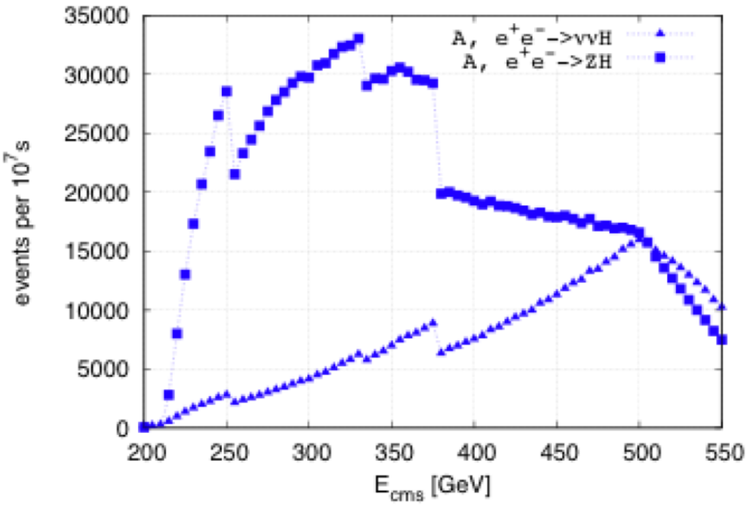

Figure 3.5: The rate of Higgs bosons produced in the 500 GeV stage of CLIC scenario A operated at different center-of-mass energies. The design is slightly modified with respect to the CDR: the same number of wigglers has been installed in the damping ring as for the 3 TeV case. The quality of the luminosity spectrum is in all cases similar or better than at 500 GeV.

Table 3.1: The luminosity at different energies for scenario A. The effective cross section for Higgs production and the number of Higgs per 10^7 sec is also given. It has been calculated based on a parameterization of the cross section derived with Wizzard2 [22] and adding the beam-beam and initial state radiation with GUINEA-PIG. Polarisation has been neglected, which increases the rate for $e^+e^- \rightarrow \nu\nu H$ by 80%.

Design E_{CM} [GeV]	**500**			**3000**
Operating at E_{CM} [GeV]	**250**	**350**	**500**	**3000**
L [10^{34} cm^{-2}s^{-1}]	1.37	2.13	2.3	5.9
$L_{0.01}$ [10^{34} cm^{-2}s^{-1}]	1.04	1.30	1.4	2.0
σ ($e^+e^- \rightarrow \nu\nu H$) [fb]	20.4	32.4	67.6	415
σ ($e^+e^- \rightarrow ZH$)) [fb]	208.2	141.3	70.1	4.6
$e^+e^- \rightarrow \nu\nu H$ per10^7 sec	2,795	6,901	15,548	244,850
$e^+e^- \rightarrow ZH$ per10^7 sec	28,551	30,097	16,123	2,714

4.3.4 X-band Klystron-based Higgs Factory

An X-band e^+e^- / $\gamma\gamma$ Higgs factory studied at KEK is a conventional klystron-based facility. Linear accelerators are based on CLIC-type cavities and the existing RF technology (XL4 klystrons, ScandiNova modulators, SLED II system). A two-beam scheme could be implemented at a later stage as a test facility for CLIC. An optical FEL can be used to produce high-energy photon beams for a $\gamma\gamma$ collider. In the first stage of operation ($e^+e^- \to$ Z, WW and $\gamma\gamma \to$ H), the proposed facility can be built on the KEK site. If the initial operational mode is with photon beams, then there is no need for an e+ source or a positron damping ring. With a crossing angle of ~25 mrad for both e^+e^- and $\gamma\gamma$ beams, only a single set of beam dump lines would be required. For some processes, the required center-of-mass energy is considerably lower at the proposed facility than at an e^+e^- collider. The rich set of final states in e^+e^- and $\gamma\gamma$ collisions is instrumental for measuring the properties of the Higgs boson.

4.3.5 Machine-Detector Interface

The Machine Detector Interface (MDI) for linear e^+e^- colliders, such as ILC and CLIC, allows for essentially full solid angle acceptance. Beam parameter measurements (energy, polarization, luminosity) allow control of beam-beam effects on physics analyses. MDI magnet technologies are well into development, such as a compact SC magnet for the ILC, and a hybrid permanent magnet for the CLIC. The risks to machine performance due to single pass collisions of nm-size bunches will be controlled via IP luminosity feedback, especially advantageous is IP feedback for the ILC bunch structure.

4.4 Circular e^+e^- Colliders

4.4.1 Introduction

A number of proposals exist for Higgs factories based on a circular e^+e^- collider with a center-of-mass energy of 240 GeV and in some cases extending to 350 GeV or 500 GeV. Circular colliders have been successfully used for lower energy machines in the past and the concept and technology are well developed. The highest energy facility was LEP2, which reached a maximum center-of-mass energy of 209 GeV. Circular colliders allow for more than one interaction point and potentially could provide more luminosity than linear colliders of equal energy. However their energy reach is limited and a number of issues may compromise their performance as will be detailed below. The proposals are in a very early stage with no design reports, which makes it difficult to evaluate them. A brief summary of the advantages and challenges of circular e^+e^- colliders in general are given below:

- Advantages:
    - ➢ At 240 GeV and below, a higher luminosity than a linear collider when the ring is sufficiently large
    - ➢ Based on mature technology and rich experience
    - ➢ Some designs can use existing tunnel and site

  - ➢ More than one IP
  - ➢ Tunnel of a large ring can be reused as a *pp* collider in the future
- Challenges:
  - ➢ Beamstrahlung limiting beam lifetime and requiring lattice with large momentum acceptance
  - ➢ RF and vacuum problems from synchrotron radiation
  - ➢ A lattice with low emittance
  - ➢ Efficiency of converting wall power to synchrotron radiation power
  - ➢ Limited energy reach
  - ➢ No comprehensive study; design study report needed

4.4.2 Circular e^+e^- Colliders Considered

The main parameters for the different proposals considered at the Workshop are listed in Table 8.2.

The driving parameter of a circular collider accelerator design is its circumference, which is in some cases determined by external constraints and in some cases by a cost optimization. Otherwise the design strategy is fairly similar for all proposals. Based on the choice for the ring circumference, the colliders can be grouped as follows:

- LEP3 has a circumference of 26.7 km in order to be installed in the existing LHC tunnel, leading to a serious cost reduction. However, installation of LEP3 for concurrent operation with the LHC is complicated and unlikely.

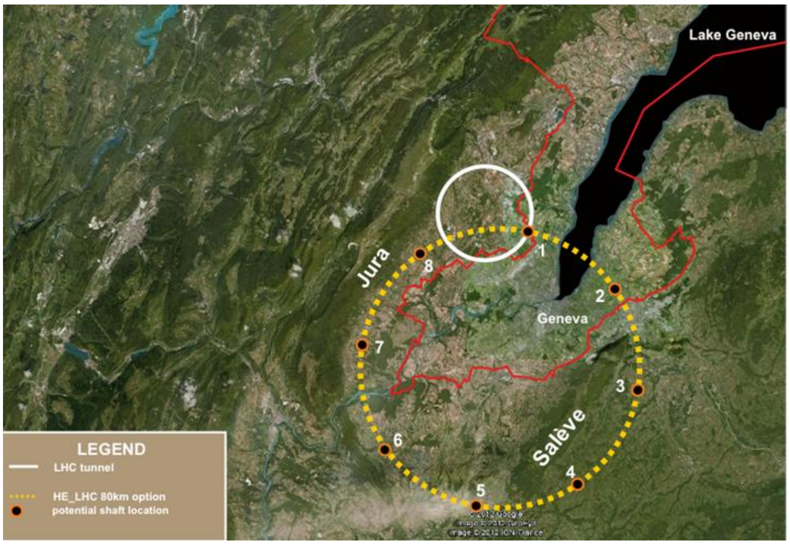

Figure 4.1: Sketch of LEP3 (white circle) and TLEP (yellow circle).

- As its name suggests, the Fermilab site-filler would fit on the Fermilab site. It therefore is limited to a smaller circumference than the other designs of about 16 km. It is conceivable to later reuse this machine as an injector for a very large hadron or lepton collider with a very large circumference in excess of 200 km.

Figure 4.2: Left: Fermilab site-filler; Right: SuperTRISTAN.

- TLEP, the different versions of SuperTRISTAN and the IHEP Higgs Factory as well as VLLC use larger circumferences on the order of 40 to 233 km with the aim to optimize the machine performance and to be able to reach 350 GeV and in the case of VLLC with 233 km circumference also 500 GeV. In these cases one can conceive of installing a hadron collider in the same tunnel at a later stage. This collider could have proton energies a factor of a few higher than LHC, the exact value depending on the size of the ring and the magnet technology used. One could even contemplate lepton-hadron collisions.

4.4.3 Technical Challenges

The main challenges of the various proposals are fairly similar. Basically, the storage ring collider technology is well established, so the technical issues have been based on well-established accelerator physics and technologies of the past including the LEP2, the B-factories and the circular synchrotron light sources. A possibility that some unforeseen technical issues are waiting around the corner, although present, is relatively small. Some of the issues below, however, are critical because they require various degrees of extrapolations from past experience, and because at this time there has been very little conceptual design or R&D work devoted to these circular colliders.

4.4.3.1 *Energy Reach and Upgradability*

The proposed center-of-mass energy is 240 GeV for all machines. For the larger rings TLEP and SuperTRISTAN also 350 GeV is proposed. It is considered that reaching higher energies further would lead to a strong increase in the cost of the projects and is therefore not practical or even forbidding. In particular the potential to increase the energy of an existing circular collider will be very limited. Operation at the Z peak and W pair threshold can be envisaged with luminosities 2-5 orders of magnitude higher than in the LEP.

The energy that can be reached with a circular e^+e^- collider is determined by the size of the ring and the installed RF voltage, which are both important cost factors. The circulating beams emit synchrotron radiation. The average energy loss E_{loss} of each particle per turn is given by $E_{loss} = 88\ \text{keV}\ (E/\text{GeV})^4/(\rho/\text{m})$, for a beam energy E and bending radius ρ. For example, a 120 GeV electron in the LEP/LHC tunnel would emit about 7 GeV per turn. This loss needs to be compensated with accelerating RF with a total voltage exceeding the loss. In order to reach a higher energy, either the RF voltage or the radius, or both, has to be increased. A simple cost model can be applied to conclude that the RF voltage and the cost of accelerator are expected to scale as E^2. Circular colliders are therefore basically machines operating between the Z peak and the 240 GeV ZH cross-section maximum, possibly up to the top threshold at 350 GeV. They become highly unpractical approaching the level of 500 GeV, and impossible substantially above 500 GeV. The decision on whether or not to go in the direction of circular colliders depends critically on what required center-of-mass energy is needed to explore the Higgs coupling constants. Without this critical input, no useful decision can be made.

For the larger rings, one can however reuse the tunnel to install a hadron machine later, in a similar fashion as the LHC has been installed in the LEP tunnel. This would provide a path to future projects. For the Fermilab site-filler one can conceive using it as an injector for a larger ring. LEP3 does not provide an upgrade path but rather exploits existing infrastructure.

4.4.3.2 *Synchrotron Radiation*

The luminosity of a circular collider increases with the circulating beam current, which in all proposals is several mA. The current is limited in all proposals by the total power of the emitted synchrotron radiation, which is typically set to about 100 MW (LEP2 went up to 20 MW). The main challenges are to limit the power consumption by obtaining good efficiency for the transfer from wall plug power into beam power and to deal with the impact of the intense radiation on the vacuum and the RF. In addition, power requirements other than compensation for synchrotron radiation, such as for cryogenics, magnets, water cooling, injectors etc., need to be taken into consideration and optimized.

Compared to LEP2 the synchrotron radiation is more intense and in some designs also the critical energy is higher, which might cause a significant radiation hazard and this issue needs to be evaluated and solved.

A larger ring circumference obviously allows both increasing the beam current linearly with the radius for the same radiation power and reducing the installed RF voltage inversely with the radius. As a result the luminosity will increase linearly with the bending radius. With beam lifetime included (see section 4.3.6 Beamstrahlung), the luminosity gains with the bending radius even more rapidly than linearly.

4.4.3.3 *RF System*

The RF system must provide the high accelerating voltage to overcome the synchrotron radiation loss with sufficient overvoltage to provide an acceptable quantum lifetime. It must also provide the high power to be transferred with high efficiency to the beam. The RF system must be shielded against the strong synchrotron radiation.

Distribution of the RF stations requires a conceptual design to minimize the orbital saw-tooth effects, especially in the cases when e^+ and e^- beams occupy the same vacuum chamber.

An optimal choice of the RF frequency needs to be made. An efficient RF power coupler for the needed system also needs to be worked out in a conceptual design of the collider. Note that the ILC cavities (1.3 GHz) have not been designed for this high average power and that the coupler R&D would need to be redone. At 700 MHz, however, the work done for the high power proton machines can be readily applied.

When a large ring is operated at a relatively low beam energy E at a fixed synchrotron radiation power, the required beam current can become large and increase as $1/E^4$. (For example in the case when the TLEP is operated at the Z-pole, the beam current exceeds 1 Ampere.) Since the RF section is very long compared with existing rings, possible collective instabilities should be studied. The RF section length can be made shorter at low energies in view of the total voltage required, but the demand to the power coupler would be even more severe when the total synchrotron radiation power is fixed.

4.4.3.4 *Vacuum System*

The raw synchrotron radiation power per meter will be much higher than LEP2 although lower or comparable to that of the B-factories. Although some other parameters will require much extrapolation from existing colliders, most of the vacuum system issues such as the higher-order mode cooling are expected to be within our engineering capacity. The one most significant exception might be the radioactivation by the high critical energy (~1.5 MeV) and high power synchrotron radiation. It is possible that this consideration may drive the entire vacuum chamber design.

4.4.3.5 *Beam-beam Effects*

Much of the past experience in operating the LEP and the B-factories has been incorporated into the proposals of the circular Higgs factories. The achieved beam-beam parameter of 0.083 per IP (Figure 4.3) with 4 simultaneously operating IPs at LEP2 [23] provided a solid basis for the design of the new colliders. However, not all past experiences have been consistent and there remains a need to continue the study and identify and understand the underlying beam dynamics. Keeping in mind the critical impact of beam-beam effects on the luminosity, the new operating regime of beamstrahlung and collision point optics, it is still critical to fully understand the beam-beam effects in order to optimize the design. On the other hand, one possibility on the optimistic side could be that the beam-beam parameter value might be substantially increased due to the much enhanced synchrotron radiation damping.

With high RF voltage, it is expected that the synchrotron tune of the electron beam will be high. Together with the small β_y at the interaction point, which leads to large hour-glass effect, it may generate potentially harmful beam dynamics effects.

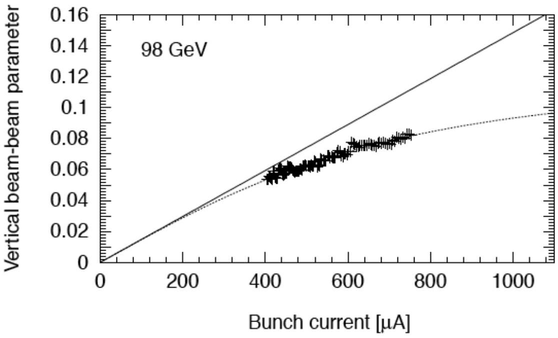

Figure 4.3: Vertical beam-beam parameter measured at LEP2.

4.4.3.6 *Beamstrahlung*

The strong beam-beam forces also lead to the emission of energetic photons, i.e. beamstrahlung, which reduces the beam particle energy and leads at each collision to the development of a low energy tail in the beam. (Figure 4.4) [24] The effect is weaker than the beamstrahlung in the linear colliders and does not affect the collision energy spread significantly. However, due to the limited energy acceptance of the machine, particles in this tail can be lost thus reducing the luminosity lifetime. In order to keep the beam longer than a typical refill time of once per minute, less than one particle in ~10^6 must be lost per bunch crossing. A lattice and RF energy acceptance of 2-6% is required and the beam parameters need to be adjusted to reduce beamstrahlung; this could potentially result in a reduction of luminosity.

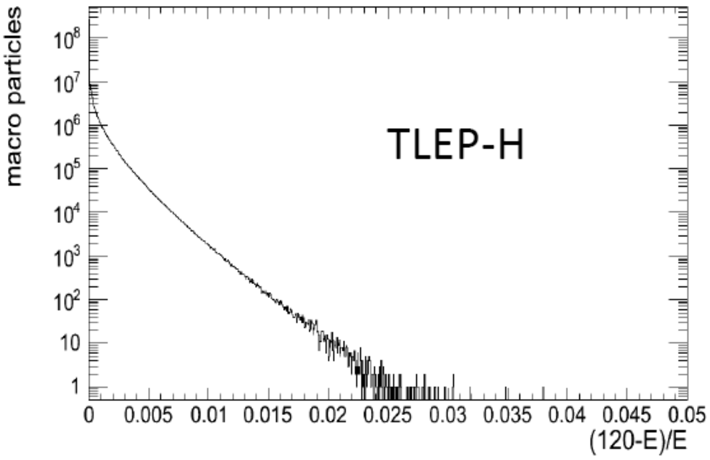

Figure 4.4: Simulation of the particle spectrum after one collision due to the beamstrahlung effect at TLEP. An energy acceptance of 2% is necessary.

4.4.3.7 *Lattice Design*

The lattice design is challenging, since small beta-functions at the interaction point and a large distance between the interaction point and the first quadrupole magnet are required together with a large energy acceptance to reduce the impact of beamstrahlung on the luminosity lifetime.

Decisions need to be made on whether the collider will consist of a single ring or a double ring. It also requires an early decision on colliding beams head-on or at an angle.

Special and dedicated efforts must be invested in the interaction region design because of its complexity, its direct impact on the optimization of beam-beam effects and luminosity, and its impact on the final energy acceptance. Diagnostics need to be planned carefully in this region.

Also important is the machine-detector interface that impacts on the accelerator performance, the detector performance, and the expected detector noise background level. Due to synchrotron radiation and other backgrounds, the IP vacuum chamber may require a small size that compromises high precision flavor tagging.

A significant development was made during the workshop in terms of an idea to increase the energy acceptance due to the interaction region optics. Further effort to consolidate this idea as well as further optimization will be needed in this important area in order for the circular collider design to be completed.

Lattice design for the regular cells is less of an issue, particularly when considering the experiences gained in low-emittance light sources.

4.4.3.8 *Emittance Control*

Various effects can disturb the small beam emittance required for the collider operation. In addition to beamstrahlung, these include dynamic aperture and nonlinear optical effects, intrabeam scattering, electron-cloud, higher-order-mode heating with short bunches, coherent synchrotron radiation instability, etc.

An important issue is to control the ratio of vertical and horizontal emittance in the collider ring. It is necessary that this ratio be minimized before the beam-beam collisions blow up the beam due to beam-beam effects. A large number of error tolerances, as well as diagnostics tools and correction mechanisms, will need to be established to assure a small value for this emittance ratio. Operational experience gained at synchrotron radiation facilities can be very helpful here as well.

4.4.3.9 *Top-up Injection*

Due to high luminosity and the beamstrahlung effect, the beam lifetime would be limited. In order to keep the luminosity nearly constant during a production cycle, a second ring as an injector would be added for the top-up injection scheme, which was successfully employed at PEP-II and KEKB. (Figure 4.5) The positron production rate should be appropriate. An optimized injection scheme needs to be worked out in a conceptual design.

Large synchrotron tune helps to separate the instability modes for the transverse mode coupling instability (TMCI). However, TMCI is more important for the larger rings and lower energies, such as the case for the top-up ring at injection.

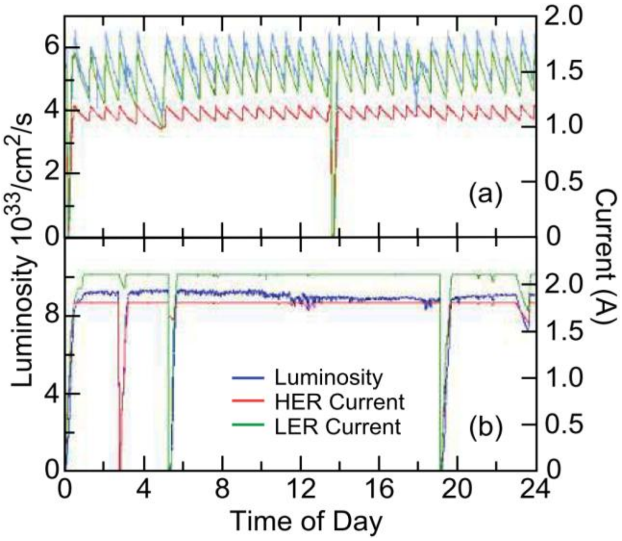

Figure 4.5: PEP-II operation: top – without top-up injection; bottom – with top-up injection.

4.4.3.10 *Polarization*

In electron storage rings, polarization builds up by the Sokolov-Ternov effect. At high energies the beams will have difficulty reaching transverse polarizations due to their large energy spread. Therefore one should not expect to have polarized beams at

120 GeV or above in any of the proposed circular machines. Other means of beam energy calibration have to be devised. As seen in the physics section, this is not a big loss for the Higgs boson physics. Obtaining transverse polarization at the Z peak was achieved in LEP for the energy calibration, and this should not be difficult in the machines under discussion, especially since great efforts will be dedicated to achieving small vertical emittances. It would be of great benefit for the physics to have i) longitudinal polarization for colliding beams at the Z peak, and ii) availability of transverse polarization at the W threshold (E_{beam} = 80-85 GeV) for calibration purposes. Both are uncertain at this point and need to be studied. Additional hardware such as movable spin rotators (as in the HERA) or polarization wigglers as in the LEP would probably be necessary.

4.5 Muon Collider

4.5.1 **Introduction**

A unique feature of a muon collider is its large cross-section in s-channel resonance for Higgs production. This cross-section is proportional to the mass squared of the colliding particles. Since the mass of a muon is about 200 times that of an electron, the cross-section of $\mu^+\mu^- \to H$ is about 40,000 times larger than that of $e^+e^- \to H$. This makes a muon collider particularly attractive to serve as a Higgs factory.

The muon collider has a number of other advantages as well as challenges when compared to other types of Higgs factory. They are summarized below:

- Advantages:
  - Large cross section $\sigma(\mu^+\mu^- \to H) = 41$ pb in s-channel resonance will compensate for low luminosity (to compare to $e^+e^- \to ZH$ at 0.2 pb)
  - Small physical size footprint
  - No synchrotron radiation problem
  - No beamstrahlung problem
  - Unique way for direct measurement of the Higgs line shape and total decay width Γ
  - Exquisite energy calibration
  - A path to very high energy lepton-lepton collisions
- Challenges:
  - Muon 4D and 6D cooling needs to be demonstrated
  - Need small center-of-mass energy spread (0.003%)
  - RF in a strong magnetic field
  - Background from constant muon decay
  - Significant R&D required towards end-to-end design and firming up luminosity figures
  - Cost unknown (not much cheaper than a TeV muon collider)

Presently there are two main muon collider R&D programs in the world. One is the Muon Accelerator Program (MAP) in the U.S. coordinated by Fermilab. Another is the Muon Ionization Cooling Experiment (MICE) in the U.K. carried out by an international collaboration.

4.5.2 The Muon Collider as a Higgs Factory

The layout of a muon collider is shown in Figure 5.1. It consists of six stages:

- Proton driver – a high beam power (~4 MW), short beam pulse (~3 ns) proton accelerator. It can be either a rapid cycling synchrotron or a combination of a linac, an accumulator and a compressor.
- Target system – a mercury jet target and a solenoid for generating and capturing high flux pion beams.
- Front end – for pion decay to muon and phase rotating the muon beam for reducing the momentum spread.
- Cooling – a key part of the muon collider. It uses a complex magnet-RF system for ionization cooling to reduce the longitudinal and transverse emittance of the muon beam by several orders of magnitude.
- Acceleration – a number of options including linac, recirculating linac, rapid cycling synchrotron and FFAG.
- Collider ring – two muon beams, one μ^+ another μ^-, each of 63 GeV, colliding for Higgs production via the s-channel resonance.

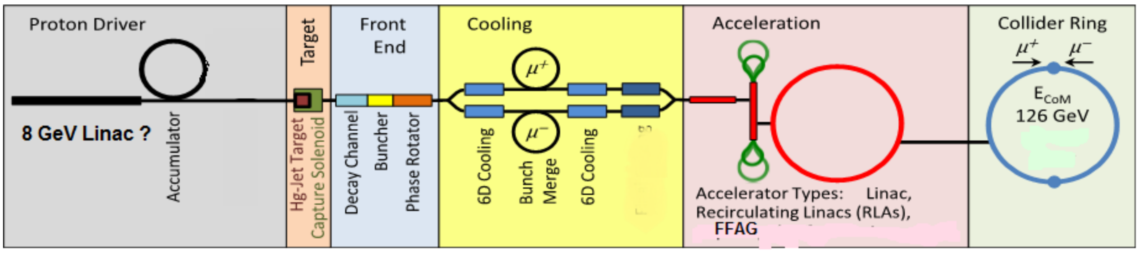

Figure 5.1: Layout of a muon collider.

The most demanding part is the cooling. As shown in Figure 5.2, the 6D cooling requires a total reduction of a factor of 10^6 in beam emittance (10^4 in the transverse phase space and 10^2 in the longitudinal phase space). And this has to be done rapidly (~msec) before the muons decay. The R&D involves a number of frontier technologies such as high temperature superconducting (HTS) high field magnets and high gradient low frequency superconducting RF (SRF). (It should be noted that for a Higgs factory, the requirement for the high field magnets is less demanding than that for a TeV-scale collider because the final cooling stage is not needed.) The breakdown of an RF cavity in a strong magnetic field is an example of the many challenging issues that a muon collider would have to solve before it can become a viable option for a Higgs factory. The Muon Accelerator Program (MAP) is making good progress in this direction.

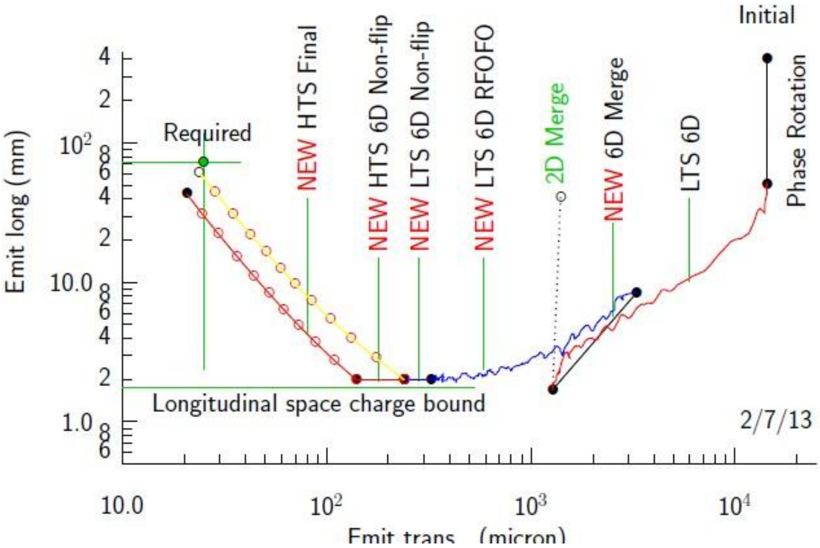

Figure 5.2: Muon cooling procedure.

When the muon collider serves as a Higgs factory, the longitudinal emittance is more important than the transverse one as high energy resolution of the muon beam is required for direct measurement of the Higgs total decay width Γ (see Sec. 2.4). Therefore, the cooling can end at the point where there is the smallest longitudinal emittance. The price to pay for this simplification is a lower luminosity due to larger transverse emittance. The design luminosity for a muon Higgs factory is 10^{31}–10^{32} cm^{-2}s^{-1}, which is about 2-3 orders of magnitude less than for an e^+e^- collider. Fortunately, however, this is compensated by the large cross-section (~41 pb, to be compared to 0.24 pb for $e^+e^- \rightarrow ZH$) so the number of Higgs produced per year is comparable for the two types of Higgs factory.

As a muon is ~200 times heavier than an electron, the synchrotron radiation and beamstrahlung of a 63 GeV muon beam become irrelevant, and the ring size can be quite small (300 m), which is a big advantage of a muon collider.

An interesting feature of a muon beam is its energy can be calibrated precisely. With a polarization as small as 10%, the muon energy can be determined by measuring the oscillation frequency of the electrons (from muon decay) to an accuracy of ~0.1 MeV.

The parameters of a muon Higgs factory are listed in Table 8.3.

4.6 Photon Colliders

4.6.1 Introduction

The idea of a photon collider (γγ collider) dates back to 1981 and much significant work has been done since then. The photon collider is based on Inverse Compton Scattering ICS) as illustrated in Figure 6.1. The discovery of the "Higgs-like" boson brought about renewed interest to this concept. The advantage is that the cross section for $\gamma\gamma \rightarrow H$ is large and comparable to $e^+e^- \rightarrow ZH$ (~200 fb) but the required energy is much lower (63 GeV for a photon beam, corresponding to 80 GeV for an electron beam, compared to 120 GeV per electron beam in an e^+e^- collider). This makes a photon collider an attractive option for either a low energy linear collider (80 GeV per electron beam) or a low energy circular collider (80 GeV per beam). Furthermore, for a photon collider there is no need for positrons and only one damping ring is needed.

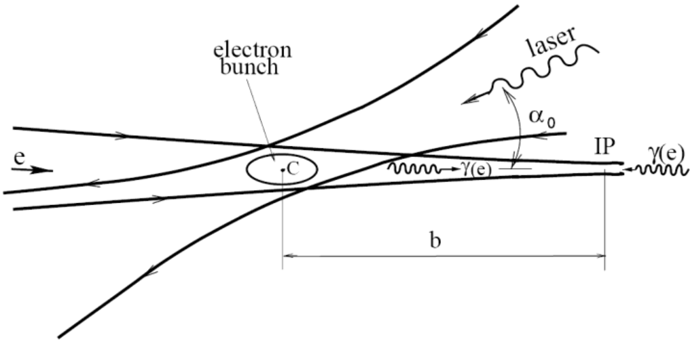

Figure 6.1: Illustration of the Inverse Compton Scattering.

Several possibilities of γγ colliders were presented in the workshop, including:

(1) ILC-based
(2) CLIC-based (CLICHÉ)
(3) NLC-type
(4) SLC-type
(5) SAPPHiRE
(6) Energy-Recovery Linac-based (This was not presented at the workshop, see Ref. [25])

From a physics point of view these concepts can be classified into two categories:

(a) Those which focus on s-channel Higgs production at $E_{\gamma\gamma\ CM}$ = 126 GeV;
(b) Those which are extendable to higher energies.

Among the above concepts (1), (2) and (3) belong to (b); (4), (5) and (6) to (a). The concepts in (a) include an arc for electrons of several tens of GeV so that they cannot be extended to higher energies in a realistic sense.

The concepts above can also be classified into two from the viewpoint of the distance between the bunches, namely,

(A) Those which are based on a normal-conducting linac so that the distance between bunches is of the order of a nanosecond;
(B) Those which are based on a superconducting linac with the bunch distance of order of a micro-second.

Among the above concepts (2) and (3) belong to (A), and (1), (4), (5), (6) to (B). ((4) belongs to (A) if a normal-conducting linac is used.) The requirements on the laser are quite different between these two categories.

The common features in all cases are:

- The primary electron beam must be highly polarized (≥ 80%) for obtaining a narrow energy spread of the photon beam.
- The laser flush energy at the conversion point must be several Joules (except (6), which requires one order of magnitude less), although the exact value depends on the electron bunch length.

Here we briefly describe these concepts. The proposed parameters are summarized in Table 8.4.

The linear collider-based ones – (1), (2) and (3) – are relatively obvious, so they are omitted here.

SLC-type: Uses 85 GeV pulsed normal-conducting or superconducting linac (or 45 GeV pulsed superconducting linac, twice-recirculating) to produce two ~80 GeV electron beams and the arcs of 1km radius to bend them as in SLC. No damping rings. For the laser, the ILC-type optical cavity or FEL is suggested.

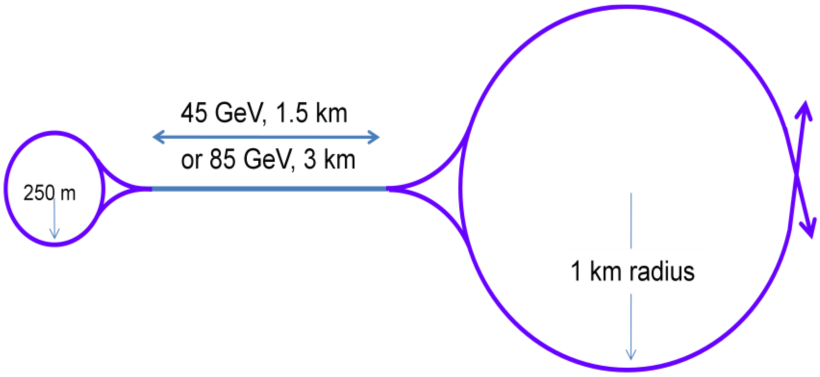

Figure 6.2: SLC-type photon collider.

SAPPHiRE: Uses recirculating CW linac (two 11 GeV linacs, 4 turns) with 80 GeV arcs and FNAL-A0-type flat-beam gun (but must be of higher intensity and polarized). No damping rings. The acceleration part of this scheme is an Energy Recovery Linac but the energy is not recovered when used as a photon collider.

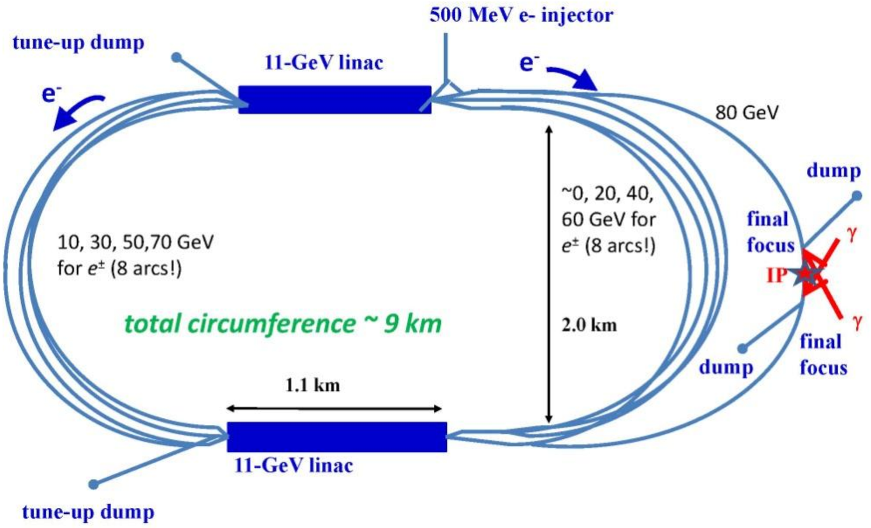

Figure 6.3: Layout of SAPPHiRE.

Energy Recovery Linac-based: Uses two 50 GeV CW SC linacs with 50 GeV arcs. The laser flush energy, and therefore the e-γ conversion efficiency is much lower than in (5). The luminosity is partly restored by the much higher beam current. The merit of the low conversion efficiency is that the energy of the electrons that did not interact with laser photons can be recovered in the ERL configuration.

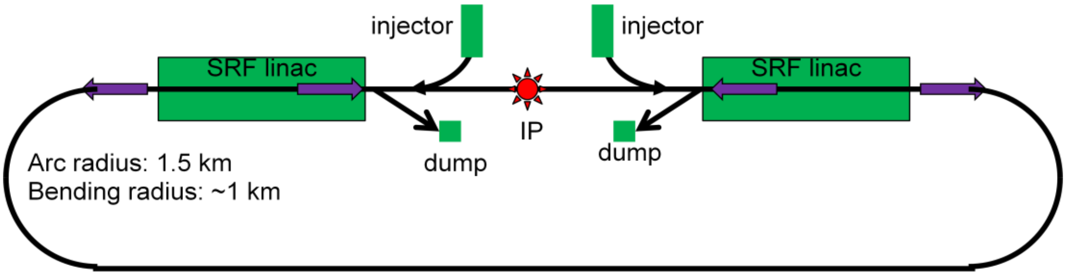

Figure 6.4: Energy-recovery linac-based photon collider.

Generally speaking, the γγ Higgs factory has the following advantages:

- The colliding γ beams have high polarization.
- The required primary beam energy is relatively low (category (a)) so that the cost may be lower.
- It can be added to a linear collider (category (b)).
- The positron beam is not needed (category (a)).
- The damping ring, which is necessary for positron, may be omitted. Then, however, the electron gun must provide low emittance and high polarization.
- It allows access to CP property of the Higgs

The challenges are:

- The physics is not as comprehensive as it would be in a 240 GeV e^+e^- collider. (for category (a))
- Background coming from the wide energy spectrum of the photons.
- The design of the interaction region is complex.
- High power laser technology is required.

4.6.2 **Required R&D for Photon Colliders**

Category (B) needs a laser repetition rate on the order of MHz with flush energy several Joules. This is unrealistic. Hence, an optical cavity to accumulate weak laser pulses is indispensable. The required parameter range are: Q-value O(1000), the optical path length O(100m), stored energy O(10J). The Q-value has already been reached but the present state-of-the art for the other two parameters is path length O(1m) and stored energy O(1mJ). Thus, intensive R&D is needed for the optical cavity. (Figure 6.5)

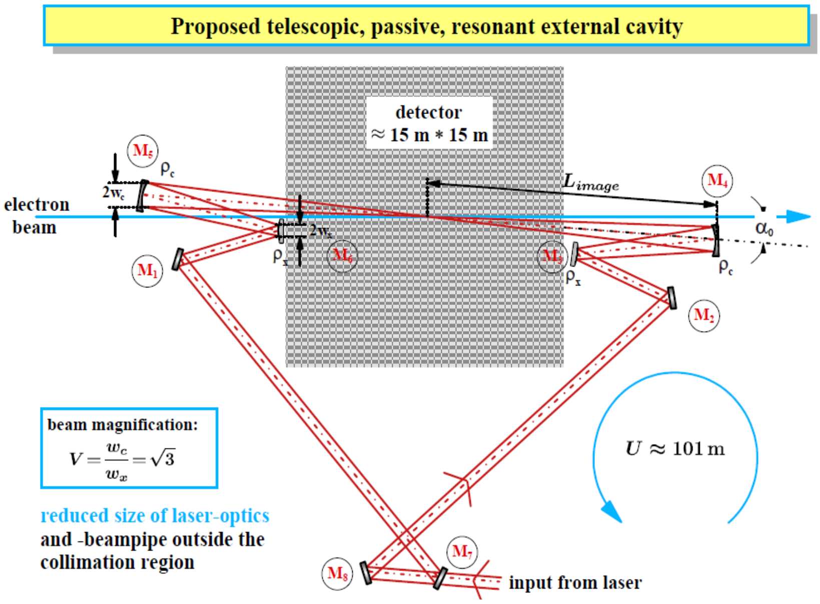

Figure 6.5: Sketch of an optical cavity in the interaction region.

Category (A) requires the laser flush energy O(kJ), split into some hundred sub-pulses of several Joules each, repeated at several tens of Hz. This sort of lasers may be available from inertia fusion technology such as LIFE. (Figure 6.6) However, it is not clear when they become available and when the technology to split the kJ pulse into sub-pulses becomes ready. For the R&D of laser systems required to implement a photon collider, the commitment of both the accelerator and laser communities is necessary.

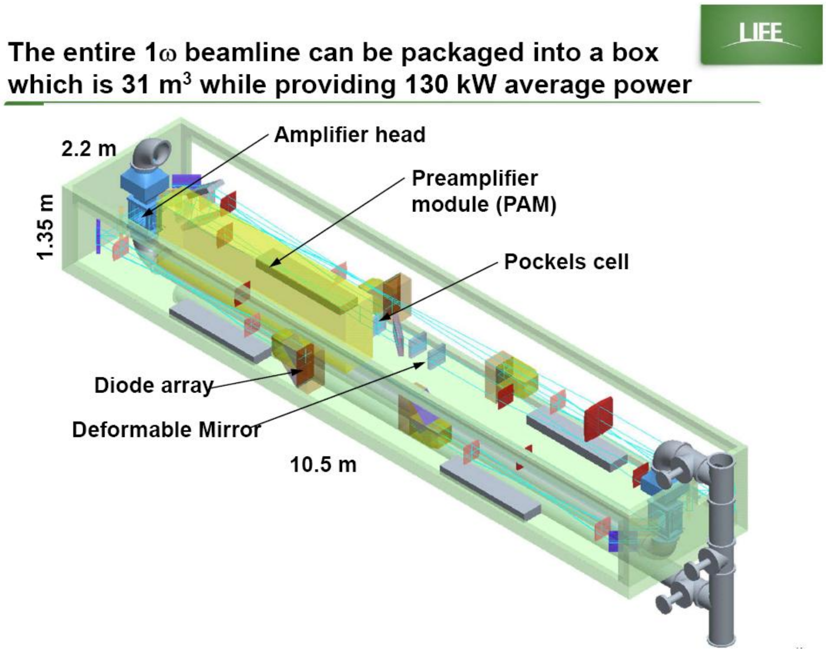

Figure 6.6: One of the 384 laser beam lines for the inertia fusion project LIFE at the Lawrence Livermore Laboratory.

Some of the proposals, including both (A) and (B), suggest the possibility of using an FEL. However, to produce several Joule pulse demands the energy extraction from electron beams with extremely high efficiency (≥ 10%). A tapered FEL is a possibility but this also requires R&D of many years including a demonstration. SAPPHiRE suggests a possibility of using the primary electron beams as the FEL driver, but this requires even more difficult R&D.

All the proposals of category (a) omit damping rings so they demand a low-emittance, highly polarized electron beam. The polarized RF gun is a possibility, but the achievement of this technology will require years of R&D. (4) allows larger emittance compared to (5) and (6) but requires larger bunch charge.

In all cases detailed design reports are still missing. The report should include:

- Design of the laser system
- Design of the polarized gun system
- More detailed design of the linac system for (4), (5) and (6). (In particular the cryogenics system for (6) may be very demanding.)
- More detailed design of the arcs and the entire geometry, which are to be reflected in the cost estimate.
- Cavity specification with power couplers
- Total power consumption
- Detailed design of the interaction region including the final-focus lattice and the path of the laser beams. (It is quite likely that the required laser flush energy would increase after detailed studies in particular for (4), (5) and (6). Relatively serious studies have already been done for (1), (2) and (3), though not at the level of a technical design.) (6) must also include the recovery path of the disrupted electrons.
- Background studies including realistic photon spectrum and the effects of the spent electrons.
- Estimated length of the R&D time. Those of category (a) are limited to s-channel Higgs production only. Therefore timely construction is essential. For those of category (b) there is a possibility of starting the machine as an e^+e^- collider (around 240 GeV) and converting it later to a $\gamma\gamma$ collider when the technology becomes mature. (If one wants to start (b) as an s-channel Higgs machine for saving the initial cost, the situation is similar to (a) though polarized RF gun would not be needed.)

4.7 Acknowledgments

This workshop was endorsed by the ICFA and received strong support from the Fermilab Director’s Office. The authors want to express their sincere gratitude to all the speakers and participants for their well-prepared excellent presentations and dynamic and stimulating discussions. The comments, suggestions and feedback we received from the world HEP community before, during and after the workshop were encouraging and most valuable for writing this report.

4.8 Appendices

4.8.1 Appendix 1 – Agenda

Wednesday, November 14, Room One West		
08:00 – 09:00	Registration	
	Session 1: Introduction and physics (Chair: Alain Blondel)	
09:00 – 09:05	Welcome (5’)	Pier Oddone (Fermilab)
09:05 – 09:30	Strategy for Higgs study (20’)	Young-Kee Kim (Fermilab)
09:30 – 10:10	Higgs at the LHC (30’)	Fabio Cerutti (LBNL)
10:10 – 10:55	Higgs beyond the LHC – theories (30’)	Chris Quigg (Fermilab)
10:55 – 11:15	Coffee (20’)	
11:15 – 12:00	Higgs beyond the LHC – experiments (30’)	Patrick Janot (CERN)
12:00 – 12:30	Accelerators for a Higgs factory (20’)	Stuart Henderson (Fermilab)
12:30 – 14:00	Lunch	
	Session 2: Linear e+e- Higgs factories (Chair: Jie Gao)	
14:00 – 14:45	ILC as a Higgs factory (30’)	Nick Walker (DESY)
14:45 – 15:30	CLIC as a Higgs factory (30’)	Daniel Schulte (CERN)
15:30 – 16:00	Group photo & Coffee (30’)	
16:00 – 16:45	SLC- & NLC-type Higgs factory (30’)	Tor Raubenheimer (SLAC)
16:45 – 17:30	Machine-detector interface for the ILC and CLIC (30’)	Marco Oriunno (SLAC)
17:30 – 19:30	Reception (Wilson Hall, 2nd floor)	

Thursday, November 15, Room One West		
	Session 3: Circular e+e- Higgs factories (Chair: Daniel Schulte)	
09:00 – 09:40	LEP3 and TLEP (25’)	Frank Zimmermann (CERN)
09:40 – 10:05	SuperTristan (15’)	Katsunobu Oide (KEK)
10:05 – 10:30	Fermilab site-filler (15’)	Tanaji Sen (Fermilab)
10:30 – 11:00	Coffee (30’)	
11:00 – 11:25	IHEP Higgs factory (15’)	Qing Qin (IHEP)
11:25 – 12:05	LBNL/SLAC ring and lattice issues (25’)	Yunhai Cai (SLAC)
12:05 – 12:30	Topping up injection (15’)	John Seeman (SLAC)
12:30 – 14:00	Lunch	
	Session 4: Limits for circular e+e- colliders (Chair: Alex Chao)	
14:00 – 14:30	Beamstrahlung – calculations and cure (20’)	Valery Telnov (BINP)
14:30 – 15:00	Beamstrahlung – simulations (20’)	Marco Zanetti (MIT)
15:00 – 15:30	Scaling law (20’)	Kaoru Yokoya (KEK)
15:30 – 16:00	Coffee (30’)	
16:00 – 16:30	Beam-beam tune shift (20’)	Jie Gao (IHEP)
16:30 – 17:00	Synchrotron radiation – RF (20’)	Andy Butterworth (CERN)
17:00 – 17:30	Synchrotron radiation – vacuum (20’)	Nadine Kurita (SLAC)
18:30 – 20:30	Dinner (Users Center – Chez Leon)	

	Friday, November 16, Room One West	
	Session 5 (Chair: Weiren Chou)	
	5A: Low emittance rings	
09:00 – 09:45	Light sources (30’)	Riccardo Bartolini (Diamond)
09:45 – 10:30	Colliders (30’)	Yoshihiro Funakoshi (KEK)
10:30 – 11:00	Coffee (30’)	
	5B: Muon collider as a Higgs factory	
11:00 – 11:20	Physics of $\mu\mu \rightarrow$ Higgs (15’)	Tao Han (U. of Pittsburgh)
11:20 – 12:05	Muon collider (30’)	David Neuffer (Fermilab)
12:05 – 12:30	Background and machine-detector interface (15’)	Ron Lipton (Fermilab)
12:30 – 13:45	Lunch	
	Session 6	
	6A: $\gamma\gamma$ collider as a Higgs factory (Chair: Kaoru Yokoya)	
13:45 – 14:10	Physics of $\gamma\gamma \rightarrow$ Higgs (15’)	Mayda Velasco (Northwestern U.)
14:10 – 14:45	$\gamma\gamma$ collider (25’)	Tohru Takahashi (Hiroshima U.)
14:45 – 15:10	Laser for CLIC-based $\gamma\gamma$ collider (15’)	Andy Bayramian (LLNL)
15:10 – 15:30	SAPPHIRE (15’)	Frank Zimmermann (CERN)
15:30 – 16:00	Wine & Cheese (30’)	
	6B: Summary Talks (Joint with the Wine & Cheese Seminar) (Chair: John Campbell)	
16:00 – 16:25	Higgs factory – physics (25’)	Alain Blondel (U. of Geneva)
16:25 – 17:00	Higgs factory – accelerators (35’)	Weiren Chou (Fermilab)
17:00	Adjourn	

4.8.2 Appendix 2 – Parameter Comparison Tables

At the workshop a set of parameter tables were compiled with input from the proponents of each proposal. There are four parameter tables, one for each category of Higgs factory, namely,

- Linear e^+e^- colliders
- Circular e^+e^- colliders
- Muon collider
- Photon colliders

Each table contains two parts:

- Top level parameters, including:
  - Center-of mass energy
  - Luminosity
  - Number of interaction points (IP)
  - Number of Higgs per year per IP
  - Machine size (length or circumference)
  - Power consumption
  - Polarization
  - Energy upgrade limit

  These parameters are common to all Higgs factories and can be used for cross comparison.
- Other important parameters:
  These can be different for different categories of Higgs factory. They can be used for comparing different machines in the same category.

These tables were provided by the workshop presenters except for some obvious corrections and items derived from the data provided.

Table 8.1: Parameters of Linear e^+e^- Colliders (Note: The CLIC 250 GeV numbers are for the 500 GeV machine operating at 250 GeV)

		Linear e+e- collider						
		ILC			**CLIC**			**X-band**
					A+	**A**	**A/B**	**Klystron-based**
Top Level Parameters								
Energy (center of mass)	GeV	250	500	1000	250	500	3000	
Luminosity (per IP)	10^{34} cm^{-2} s^{-1}	0.75	1.8	4.9	1.37	2.3	5.9	
No. of IP		1	1	1	1	1	1	
No. of Higgs per year (per IP)	1000	23	49		34	44	446	
Size (length or circumference)	km	21	31	48	13.2	13.2	48.3	
P(wall)	MW	128	162	301	235	272	589	
Polarization								
e-	%	80	80	80	80	80	80	
e+	%	30	30	30	0	0	0	
Other Important Parameters								
Geometric luminosity	10^{34} cm^{-2} s^{-1}	0.37	0.75	2.61	0.82	1.42	4.29	
Pinch enhanced luminosity	10^{34} cm^{-2} s^{-1}	0.75	1.8	4.9	1.37	2.3	5.9	
Linac accelerating gradient	MV/m	31.5	31.5	31.5/45	40	80	100	
No. of particles per bunch	10^10	2	2	1.74	0.34	0.68	0.372	
Number of bunches per pulse		1312	1312	2450	842	354	312	
Bunch distance	ns	554	554	366	0.5	0.5	0.5	
Average current / beam	mA	0.0210	0.0210	0.0273	0.0229	0.0193	0.0093	
Peak current / beam	A	0.0058	0.0058	0.0076	1.0894	2.1787	1.1919	
Pulse repetition rate	Hz	5	5	4	50	50	50	
Beam power per beam	MW	2.63	5.25	13.66	2.87	4.82	13.95	
Normalized emittance εx,n	mm-mrad	10	10	10	0.66	2.4	0.66	
Normalized emittance εy,n	mm-mrad	0.035	0.035	0.03	0.025	0.025	0.02	
βx IP	mm	13	11	11	8	8	4	
βy IP	mm	0.41	0.48	0.23	0.1	0.1	0.07	
σx, IP	nm	729	474	335	150	200	40	
σy, IP	nm	7.66	5.90	2.70	3.2	2.3	1	
σz, IP	mm	0.3	0.3	0.225	0.072	0.072	0.044	
sigma_E IP (electron)	%	0.19	0.124	0.085	0.3	0.3	0.3	
sigma_E IP (positron)	%	0.152	0.07	0.047	0.3	0.3	0.3	
Full crossing angle	mrad	14	14	14	18.6	18.6	20	
Average number of photons		1.176	1.700	2.250	0.7	1.3	2.1	
δB beam-beam	%	0.953	4.500	10.500	1.5	7	28	
Upsilon (average)		0.0201	0.0616	0.203	0.0515	0.207	5.49	

Table 8.2: Parameters of Circular e^+e^- Colliders

		Circular e+e- collider							
		LEP3	**TLEP**		**Super-**	**Fermilab**	**IHEP Ring**		**SLAC/LBNL**
					TRISTAN	**Site-filler**	**IHEP-50km**	**IHEP-80km**	**Ring**
Top Level Parameters									
Energy (center of mass)	GeV	240	240	350	240	240	240	240	240
Luminosity (per IP)	10^{34} cm^{-2} s^{-1}	1	4.9	0.65	1	0.52	2.5	3.85	1
No. of IP		2 (4)	2	4	1	1	2	1	1
No. of Higgs per year (per IP)	1000	20		100		13	100	200	
Size (length or circumference)	km	26.7	81	81	40	16	49.78	69.88	26.7
P(wall)	MW	200	200	200	100	200	300	300	200
Polarization									
e-		0	0	0	0	0	0	0	0
e+		0	0	0	0	0	0	0	0
Other Important Parameters									
Bending radius	km	2.6	9	9	5.4	1.753	6.2	7.8	2.6
Ne	10^{10} per bunch	100	50	75	67	80	70	60	8
nb (number of bunches) per beam		4	80	12	8	2	26	52	50
I(beam)	mA	7.2	24.3	5.4	6.5	5	17.5	21.3	7.2
ΔE(synch)	GeV/turn	6.99	2.1	9.3	3.5	10.5	3	2.35	6.99
P(synch) per beam	MW	50	50	50	22.5	50	51.8	50	50
Critical energy of synch. rad.	MeV	1.47	0.43	1.32	0.71	2.19	0.62	0.49	1.47
εx,n	mm-mrad	5870	2210	6850	9400	5321	3053	3358	1010
εy,n	mm-mrad	23	12	34	9.4	27	21.14	16.67	5.05
beta_x IP	mm	200	200	200	200	200	280	200	50
beta_y IP	mm	1	1	1	1	2	1	1	1
σx, IP	nm	71000	43000	63000	89000	67319	60000	53479	14663
σy, IP	nm	320	220	320	63	476	300	266	2.64
σz, IP	mm	3.1	1.7	2.5	1.2	2.85	1.6	1	1.5
sigma_E, IP	%	0.23	0.15	0.22	0.14	0.28	0.13	0.12	0.2
Full crossing angle	mrad	0	0	0	0	0	0	0	0
Beam lifetime due to radiative Bhabha	sec	1080	1920	3240		1080	960	600	
b-b tune shift x		0.09	0.1	0.05	0.032	0.067	0.102	0.08	0.036
b-b tune shift y		0.08	0.1	0.05	0.083	0.095	0.073	0.08	0.07
Damping partition number (x)		1.5	1	1	1	1.5	1	1	1
Damping partition number (y)		1	1	1	1	1	1	1	1
Damping partition number (z)		1.5	2	2	2	1.5	2	2	2
Longitudinal damping time	turns	26	57	19	35	11	41	51	15
RF Voltage	GV	12	6	12	8.3	12	9	12	12
Momentum compaction									0.000024
Synchrotron oscillation tune		0.19	0.12	0.12	0.23	0.192	0.392	0.364	0.135
Average number of photons		0.6	0.5	0.51	3.2	0.36	0.5	0.48	0.24
δB beam-beam	%	0.03	0.035	0.035	0.02	0.022	0.038	0.057	0.0088
Upsilon(max)		0.00231	0.00348	0.00353	0.00320	0.00212	0.00371	0.00570	0.00186

Table 8.3: Parameters of Muon Collider

		Muon collider	
		Muon-Low L	**Muon-High L**
Top Level Parameters			
Energy (center of mass)	GeV	126	126
Luminosity (per IP)	10^{34} cm^{-2} s^{-1}	0.001	0.01
No. of IP		2	2
No. of Higgs per year (per IP)	1000	5	50
Size (length or circumference)	km	0.3	0.3
P(wall)	MW	100	125
Polarization			
μ+, μ-		10%	10-20%
Energy upgrade limit		10 TeV	10 TeV
Other Important Parameters			
Bending radius	km	0.04	0.04
Nmu	10^{10} per bunch	200	500
nb (number of bunches)		1	1
Normalized emittance εx,n	mm-mrad	400	200
Normalized emittance εy,n	mm-mrad	400	200
βx IP	mm	60	40
βy IP	mm	60	40
σx, IP	nm	200000	120000
σy, IP	nm	200000	120000
σz, IP	mm	60	40
sigma_E, IP	%	0.003	0.003
Luminosity life time	sec	0.00066	0.00066
Repetition rate	Hz	15	15

Table 8.4: Parameters of Photon Colliders

		$\gamma\gamma$ collider						
		ILC-based		CLIC-based		Recirculating linac-based	SLC-based	Thin Target
		ILC (x=4.46)	ILC (x=1.97)	CLIC (x=4.46)	CLIC (x=4.46)			
Top Level Parameters								
Energy (center of mass)	GeV	126 (lum. peak)	126 (lum.peak)	126	126	132 (max $\gamma\gamma$)	130	
Luminosity (per IP)	10^{34} cm^{-2} s^{-1}	0.03	0.12	0.36	0.65	0.06	1	0.15
definition of luminosity		$\gamma\gamma$ > 125 GeV	$\gamma\gamma$ > 125 GeV	$\gamma\gamma$ > 0.6ECM	$\gamma\gamma$ > 0.6ECM	$\gamma\gamma$ > 125 GeV		$\gamma\gamma$ > 0.6ECM
No. of IP		1	1	1	1	1	1	1
No. of Higgs per year (per IP)	1000	5	10			10 to 20	5	
Size (length or circumference)	km	~14?	~16?			9	12	
P(wall)	MW	~100?	~100?	150?	300?	100	150	
Polarization								
e-		80%	80%	80%	80%	90%	80%	80%
γ		93% (lum. peak)	86% (lum. peak)	100%	100%	90%		
Energy upgrade limit		0.8Ee- (typical)	0.8Ee- (typical)			?	260	
Other Important Parameters								
Drive electron energy	GeV	83	110	80?	80?	80	80	100
Ne	10^{10} per bunch	2	2	0.4	0.68	1	5	1.5
nb (number of bunches per pulse)		2860	2860	1694	2124	CW	1000	CW
bunch distance	μs	0.33	0.33	0.5(154) x 4(11)	0.5(354) x 24(6)	5	1	1
electron I(beam)	mA	0.045	0.045	0.11		0.3	10	2.4
Pulse repetition rate	Hz	5	5	100	50	CW	10	CW
electron P(beam)	MW	3.8	5.0	8.6		50	8	480
Electron beam								
εx,n	mm-mrad	10	10	1.4	1.4	5	6	5
εy,n	mm-mrad	0.03	0.03	0.05	0.05	0.5	5	0.5
beta_x CP	mm	4.5	4.56			5		
beta_y CP	mm	5.3	6.0			100		
beta_x IP						5	0.5	
beta_y IP						0.1	0.5	
σx, CP	nm	535	460			400	140	385
σy, CP	nm	32	29	0.3	0.3	440	125	320
σz, CP	mm	0.35	0.35			0.03	200	0.1
sigma_E IP	%	0.22 in ML	0.22 in ML	0.351	0.351	<0.1	0.5	
Laser beam								
wavelength	μm	0.351	1.054	0.351		0.35		0.395
Flush energy	J	9	9			5		0.075
Rayleigh length	mm	0.63	0.63			0.3		
σx, CP	nm	4200	7300			2800		
σy, CP	nm	4200	7300			2800		
σz, CP	mm	0.45	0.45			0.15		
IP<->CP distance	mm	1.4	1.5			0.6		2
Laser-beam crossing angle	mrad					0		20
γ beam								
n_gamma		1.0e10 (primary)	1.6e10 (primary)	9.60E+10	1.63E+11	8.30E+09		3.20E+09
σx, IP	nm	480	430			400		
σy, IP	nm	10	7			18		

4.8.3 Appendix 3 – Timelines

Listed below are our best estimates or, sometimes, “guesstimates” of the timeline of various proposals for a Higgs factory. For each proposal, we shall identify a date of completion of its experimental program (not a date for completion of the facility).

1. LHC

The LHC dates are the most readily available. The date for completion of “nominal LHC” at 14 TeV with ~300 fb^{-1} is assumed to be 2021, which is the beginning of the LHC long shut down of 2022-2023. The High Luminosity running is assumed to last until 2030 for an integrated luminosity of 3000 fb^{-1}. There is a possibility that this may be extended by a few years. A further extension to even higher energies by replacing the LHC magnets by 16-20 T peak field magnets in situ (HE-LHC) would take quite a few years after that date; similarly the timescale to fill an 80 km long tunnel with 20 T magnets (SHE-LHC) is also very uncertain.

2. Linear e^+e^- colliders

The ILC dates were hinted at in the statement of interest of Japanese colleagues at the European Strategy ESPP workshop in Krakow (September 2012). It is stated that the project is ready to go. The Technical Design Report with cost estimate will be published in June 2013. Assuming a decision is taken within the next couple of years, and after due process it is assumed in the TDR that the construction time is around 9 years, this having to include the construction of a new lab infrastructure; the main uncertainty here comes from the availability of the appropriate funding level. A commissioning time of one year is assumed. Thus, it is assumed the physics run could begin around 2025. Five years of continuous running at 250 GeV E_{CM} is, according to the ILC documents, necessary to reach 250 fb^{-1}, by a date which we estimate to be around 2030. The upgrade and additional running at 350 GeV, 500 GeV and 1 TeV lead to a completion date around 2040-2045.

The current planning for the CLIC foresees a development phase until 2016, which allows taking a decision on the next high energy frontier project to be taken in 2016-2017, based on the LHC results. In the preparation phase until 2022 the technical designs would be finalized, the industrial procurement prepared and the site authorisation would be obtained to be ready for construction starting from 2023 and finishing by 2030. So data could be taken as the LHC programme reaches completion.

3. Circular e^+e^- colliders

Compared with the linear colliders, the circular Higgs factory proposals are much less construction ready. The ILC, for example, has its TDR completed with accurate cost estimate. In contrast, the circular proposals have yet to form the study groups that line up to produce CDRs. Cost estimates for the circular options are even further in the future.

As the circular Higgs factories are in their infancy, it is difficult to make reasonable predictions. Consider the cases of LEP3 and TLEP. It took 13 years from the first CERN yellow report in 1976 to the LEP start-up, of which 6 years from ground-breaking to first collisions. The first step is to produce a conceptual design study report. Given the significant interest raised at the workshop and the available worldwide expertise this should take two years, reaching a decision point following which 2-3 more years would be necessary for a TDR. The following is a possible CERN scenario; we expect a similar time scale for other circular Higgs factory proposals.

Assuming a decision in the few years following the next CERN strategy update in 2018, construction could possibly start in 2021 when the main components of the LHC upgrade are acquired. Construction of an 80 km tunnel should be at least similar to that of the LEP ring (tunnelling technology has made progress in recent years), thus at least 6 years. The components of the machine need to be developed and built in parallel. In a new ring the installation and commissioning is assumed to be straightforward and takes two years. Thus data-taking could possibly start around 2030 leading to 5 years worth of precision results not earlier than 2035. A full program on TLEP including polarized beams at the Z peak and exploration at the WW and ttbar thresholds would probably take another 10-15 years. The increase of complexity (double ring, larger RF system, longer vacuum chamber) with respect to LEP is a source of significant uncertainty in this number. LEP3 in the LHC tunnel is a fall back in case the funding for the larger projects does not come forth, but because of the need to install the machine in the LHC tunnel itself, it is difficult to expect an earlier time scale than that of TLEP. A new ring of similar circumference as LEP3 could probably be built faster at another site.

4. Muon collider

For the muon collider, the MAP program will deliver its feasibility study in 2018. By that time it is also important that the MICE experiment is completed. The CDR/TDR process could then take place lasting probably at least 5 years to which the approval process needs to be added. The cost is unknown. The committee shall not venture a guesstimate of a date for muon colliders in this report. An update of the muon collider timeline by the MAP collaboration is expected to be available during Snowmass 2013.

5. Photon colliders

A photon collider can either be seen as an add-on to a linear collider, in which case one could contemplate operation sometimes in the active life (2030-2045) of the ILC. If a dedicated machine were to be built, a CERN time scale would probably place it starting construction in 2022 with possibly a somewhat faster timescale than TLEP because of the smaller tunnel, leading to the completion of 5 years of statistics sometimes between 2030 and 2035.

4.9 References

1. Presentations by F. Cerutti (Higgs at the LHC), C. Quigg (theory introduction) P. Janot (Higgs beyond the LHC – experiments) and A. Blondel (Higgs Factory – Physics) at the ICFA beam dynamics workshop, Accelerators for a Higgs Factory: Linear vs. Circular (HF2012), Fermilab, 14-16 November 2012, https://indico.fnal.gov/conferenceDisplay.py?confId=5775
2. CMS, "Observation of a new boson at a mass of 125 GeV with the CMS experiment at the LHC", Phys.Lett. B716 (2012) 30-61
3. ATLAS, "Observation of a New Particle in the Search for the SM Higgs Boson with the ATLAS Detector at the LHC", ibid 1-29
4. CMS, "CMS at the High-Energy Frontier", ESPP Contribution #177
5. ATLAS, "Physics at a High-Luminosity LHC with ATLAS", ATL-PHYS-PUB-2012-004 (2012), ESPP Contribution #174
6. R.S. Gupta, H. Rzehak, J.D. Wells, "How well do we need to measure Higgs boson

couplings?", arXiv:1206.3560 (2012)

7. M.E. Peskin, "Comparison of LHC and ILC capabilities for Higgs boson coupling measurements",arXiv:1207.2516 (2012)
8. H. Baer et al., "Physics at the International Linear Collider", in preparation, see http://lcsim.org/papers/DBDPhysics.pdf
9. J.E. Brau et al., "The physics case for an e+e- linear collider", ESPP Contribution #69
10. C.F. Duerig, "Determination of the Higgs Decay Width at the ILC", talk given at the LCWS12 (Oct. 2012)
11. CLIC CDR, P. Lebrun et al, CERN 2012-005, arXiv :1209.2543
12. Physics and Detectors at CLIC, L. Linssen et al, CERN-2012-003, arXiv:1202.5940; T. Lastovicka and J. Strube , "Higgs self-coupling study at CLIC", talk given at the LCWS12 (Oct. 2012); CLIC e+e- Linear Collider Studies. Additional input on the Higgs self-coupling complementing submission ID 99, January 21st, 2013.
13. A. Blondel et al, LEP3: A High Luminosity e+e- Collider to study the Higgs Boson, ESPP contribution 138, arXiv:1208.0504v2 (2012)
14. P. Azzi et al., "Prospective studies for LEP3 with the CMS detector", arXiv 1208.1662 (2012) ESPP contribution 171.
15. V. Barger et al., "Physics at Higgs Factories", Snowmass-2001-E110 (2001)
16. B. Autin, A. Blondel and J. Ellis, "Prospective Study of Muon Storage Rings at CERN", CERN-99-02 (1999)
17. D.M. Kaplan, "From Neutrino Factory to Muon Collider", arXiv:1102.1591 (2011) and references therein
18. T. Han and Z. Liu, "Direct Measurement of the Higgs Width at a Muon Collider", arXiv:1210.7803 (2012)
19. D. Asner et al., "Higgs Physics at a gg collider based on CLIC", arXiv:hep-ex/0111056 (2001)
20. S.A. Bogacz et al., "SAPPHIRE: A small $\gamma\gamma$ Higgs factory", arXiv:1208.2827 (2012)
21. International Linear Collider – Technical Design Report, Volume 3 Accelerator, Part 1, 3.6 ATF2 Final-Focus Experiment, to be published.
22. Jan Strube, private communication.
23. R. Assmann, private communication.
24. V. I. Telnov, arXiv:1203.6563 [physics.acc-ph]
25. Y. Zhang, JLAB-TN-12-053 (Oct. 31. 2012)

5 Workshop and Conference Reports

5.1 XFELO 2013 Workshop Report – Part A: Sciences

Hyunjung Kim[1] and Hiroshi Kawata[2]
[1] Sogang University, Seoul 121-742, Korea
[2] KEK, 1-1 Oho, Tsukuba, 305-0801, Japan
Mail to: hkim@sogang.ac.kr,

5.1.1 Introduction

In this XFELO Workshop 2013, the potential applications of exciting XFELO sciences were presented and discussed based on the prominent characteristics of XFELO, such as (i) full coherence in both transverse and longitudinal directions, (ii) ultrafine bandwidth, and (iii) higher repetition rate and (iv) higher stability compared to SASE type XFEL with or without self-seeding, which will be referred to SXFEL in the following. Although the pulse intensity of XFELO is less than three to four orders of magnitude smaller than that of an SASE pulse, the peak spectral brightness is comparable since the XFELO bandwidth is correspondingly narrower.

5.1.2 Possible Scientific Area

Significant extension and improvement of scientific techniques developed in third generation x-ray facilities will be achieved. Such techniques are inelastic x-ray scattering, Mössbauer spectroscopy, hard x-ray photoemission, nm resolution hard x-ray imaging, imaging and dynamics based coherent x-ray scattering. Some of the selected and detailed expectations and specifications discussed during this workshop are listed below for each scientific area.

5.1.2.1 *High Resolution Spectroscopy: Inelastic X-ray Scattering*

Since the XFELO promises to offer 10^4 times more intensity than the typical third generation synchrotron sources and at least 10^2 more than the SXFEL, high resolution inelastic scattering (IXS) experiments with 0.1 meV resolution will be easily achieved. In other words, the much higher brilliance available from XFELO can overcome small cross sections of IXS. Small samples and disordered systems will be more feasible to investigate. By working in the frequency domain, a method to achieve attosecond time resolution without actually using attosecond pulses was presented . In fact, it is claimed that with an XFELO and optimized conditions the time resolution could be 1000 times better than than from pump probe technique with SXFEL.With high longitudinal coherence, e.g., standing wave inelastic scattering would be possible for studying non crystalline materials.

5.1.2.2 *High Resolution Spectroscopy: Mössbauer Spectroscopy*

The whole field of Mössbauer spectroscopy can benefit from an XFELO. This motivates the long-term goal of establishing quantum optical methods in the hard x-ray regime. A few examples in this direction are a coherent dynamical control scheme based on a rapid rotation of an externally applied magnetic field, which could suppress the decay of excited nuclei due to quantum interference, the measurement of the cooperative Lamb shift in a large ensemble of nuclei, the observation of an archetype quantum optical effect with nuclei, and the observation of so-called spontaneously generated coherences. The XFELO could allow accessing a qualitatively different parameter regime for x-ray quantum optics with nuclei. The XFELO provides narrow-band fully coherent transform limited pulses. The full temporal coherence allows the use of all resonant photons in a single pulse collectively for manipulation of the nuclei. The large number (10^3) of photons per pulse will make it possible to explore a qualitatively different dynamics which could not be studied with third generation sources providing single photon per pulse. In particular, the intensity of such a pulse is enough to induce non-linear effects. Other target systems for x-ray quantum optics could be inner-shell electrons of atoms. Advance in instrumentation and techniques will further facilitate the approach of inner-electron target systems.

5.1.2.3 *Hard X-Ray Photoemission Spectroscopy (HXPS, HAXPES)*

Hard x-ray photoemission spectroscopy (HXPS) will benefit from the highly coherent beam in longitudinal direction. More information from the bulk structure could be obtained, making HXPS a more versatile tool for any new material or multilayer nanostructure.

5.1.2.4 *X-ray Microscopy and Phase Contrast Imaging*

In general, nm focusing should be available by XFELO. Here also highly coherent longitudinal beam will make more variety of the samples accessible for investigation.

5.1.2.5 *Dynamics and Imaging with Coherent X-rays*

Considering the stability achievable in XFELO, traditional X-ray photon correlation spectroscopy can be applied for studying 2D dynamics with microsecond time scale with proper 2D detector development. Highly coherent flux make dynamics and related speckle analysis available for reaching atomic resolution, in general, i.e., by wide angle scattering measurement. Biological samples will have benefit. Coherent beam at high energy will be useful for various sample systems. Anomalous coherent x-ray diffraction imaging (CDI) e.g., at 2meV resolution with full coherence can be feasible. High resolution CDI, CDI combined with pump-probe technique, as well as Bragg CDI at wide angle can be readily accomplished.

5.1.2.6 *Time-Resolved Studies*

For pump-probe X-ray diffraction and scattering studies, XFELO may be comparable to or even better than XFEL. To realize pump-probe experiment with high repetition XFELO light source, there are two important developments. One is the synchronization procedure should be developed. Some of the techniques have already been developed by using COM system at the level of sub-femto second. The other is a high repetition and also high power pump light source. The latter might be possible to use coherent THz light which is produced by the accelerator itself.

5.1.3 Insights to New Scientific Areas

The XFELO might be a big step forward in terms of coherence since the XFELO will have full longitudinal coherence. Full longitudinal coherence will be available in seeded SXFELs but they exhibit significant intensity fluctuations. With full longitudinal coherence, the gap between time-domain and energy domain techniques in the study of dynamics can be closed.

A future possibility of an extreme stabilization of an XFELO by tying its output to a narrow nuclear resonance line such as ^{57}Fe can be explored. This nuclear resonance (NR) stabilized XFELO even has coherence between pulses. The extreme stabilized XFELO will have applications to nuclear resonance metrology, x-ray quantum optics, and fundamental sciences such as quantum gravity. Nonlinear optics in x-ray regime such as four-wave mixing and stimulated Raman scattering can be tested. Development of nanometer-sized x-ray sources may be reasonable to investigate.

5.1.4 Conclusions

The XFELO is unique in providing full coherence, high average intensity, and high stability to study the areas which have not been accessible so far. For example, the XFELO characteristics are suitable for many X-ray quantum optics experiments.

While the commonly used key parameters are on the same level for XFELO and seeded XFEL, there are important advantages of the XFELO in terms of high repetition and better stability. If the XFELO can indeed be stabilized so that the linewidth of the individual modes becomes smaller than the nuclear linewidth, the perturbations to the coherent dynamics can be neglected.

Finally, we note that the demands of quantum optics in visible laser have continued to be a strong driver for the development of better instrumentation and optics. It would be desirable to have a similar driver in the X-ray spectral region as well. The advance in X-ray instrumentation will benefit X-ray science as a whole. An example case is the diamond mirrors which are studied in the context of the development of the XFELO, but which can be used for many other applications as well.

This enables contacts with new user communities, thus stimulating novel scientific approaches.

5.1.5 Acknowledgement

This report summarizes the presentations on XFELO sciences during the workshop, by Hiroshi Kawata, Giulio Monanco, Hyunjung Kim, Yu Gan, Charles Fadley, Changwook Lee, Hyotcherl Ihee, Jung Ho Je, Do Young Noh, Jörg Evers, Bernhard Adams.

5.2 XFELO 2013 Workshop Report – Part B: XFELO R&D Issues (Accelerator and X-ray Optics)

Nikolay Vinokurov[1,2], Chung-Jong Yu[3]
[1] Budker Institute of Nuclear Physics, Novosibirsk, Russia
[2] Korea Atomic Energy Research Institute, Daejeon, Korea
[3] Pohang Accelerator Laboratory, Pohang, Korea
Mail to: nikolay.vinokurov@gmail.com

5.2.1 **Introduction**

The XFELO consists of three parts: accelerator, which provides the electron beam with necessary parameters, magnetic and vacuum system, including undulator, and x-ray resonator.

5.2.2 **Components**

5.2.2.1 ***Accelerator***

The accelerator, required for the XFELO (6-7 GeV, CW operation) is very expensive (more than $1B). To build such an accelerator it needs to have the reasonable package of its applications (scientific case). On the other hand, a proper accelerator – energy recovery linac (ERL) - is discussed in many countries to use it as the next generation x-ray source. Therefore it is natural to include the XFELO into the bigger project of the ERL-based x-ray source, as discussed by H. Kawata's talk. This x-ray source will provide high-brightness subpicosecond periodic x-ray pulses with both XFELO (one beamline) and spontaneous undulator radiation sources (several beamlines). On the other hand, the unique parameters of radiation of the XFELO increase significantly the scientific importance of the ERL-based x-ray source. Therefore the XFELO is a strong reason to build this big installation.

5.2.2.2 ***SRF***

The most complicated and expensive part of the ERL is the RF system. The superconducting (SC) RF technology was reviewed in the talk of G. Neil (TJNAF). It is worth noting, that the unique electron accelerator CEBAF is the only example of the routine and reliable operation of large number of SC accelerating modules. These accelerating modules are also used in small ERL at the same laboratory. Therefore it is preferable to use the CEBAF RF system as a prototype for the ERL-based x-ray source one. The overall cost of 6 GeV accelerating system is about $1B. It may be decreased twice for 4-pass (2 accelerations and 2 decelerations) ERL.

5.2.2.3 ***Gun***

The electron gun, which is capable to provide low (of the order of .1 mm·mrad) normalized emittance at about ten pC charge per bunch and few mA average current, is under development at KEK/JAEA (as discussed by H. Kawata's talk) and also at Cornell. These guns as well as the well-proven JLAB ERL gun are a good prototype. However, it is desirable to build the test gun and hundred-MeV pre-accelerator (or even a small injection ERL) in advance, as measurements of so low slice emittances require complicated techniques and have to be performed at high enough energies. Such a test facility is under construction at KEK (See Kawata's talk)

5.2.3 **Magnet and Vacuum**

The magnetic and vacuum systems of an XFELO are within the state of art. More advanced schemes, like master oscillator plus power amplifiers, mentioned in the talk of K.-J. Kim (ANL), may be used at ERL.

5.2.4 **Optics**

5.2.4.1 ***Mirrors***

The x-ray resonator issues are crystal reflectivity (including the radiation heating problem), focusing and mechanical precision of the crystal mounts. They were addressed in talks of V. Blank (TISNCM), Y. Shvydko (ANL) and D. Shu (ANL). The reflectivity degradation due to heating may limit the intracavity power. The contribution of spontaneous undulator radiation to the forward crystal heating has to be considered.

The required spatial and the angular stability can be met by the weak-link mechanism actively used at the APS. The recent results of the TISNCM diamond as a self-seeding crystal and a wide-offset monochromator in LCLS indicated that it is a promising candidate as the resonator crystal while the effect of high-repetition-rate x-ray pulses are unknown. The answer would be found in a few years after the long-term use of the diamond. This crystal also showed a good indication of preserving wavefront. We may get useful ideas on the optics issues from other super-precise installations, like optical detectors of gravitational waves (described in the talk of K. Arai, Caltech).

5.2.4.2 ***Stabilization***

The nuclear resonance stabilization of the XFELO spectrum, described in the talk of B. Adams, looks very promising. The development of the next-generation time standard (superprecise x-ray clock) has huge application field (both basic research and applied metrology).

5.2.4.3 ***Tests***

The test of high-quality (long decay time) x-ray resonator, pumped by undulator radiation, at existing storage rings (APS, PLS …) may be useful for tests of all these issues and nuclear resonance stabilization technique.

5.2.5 **Scale**

The sizes of the ERL-based facility are about 1km×1km, and the cost scale is $2B. The typical time of creating of such installation is 10 years (at least 5 years for a proposal approvals and initial R&D, and at least 5 years for technical design, prototyping, component production, building and assembly). Therefore it would be appropriate to make a proposal for considering this ERL as possible next decade accelerator project (which does not overlap in time and interfere with accelerating projects, which are under way now) and including it to a "list of future installations".

Very preliminary estimate for the R&D program total cost is $75M for 5 years. It consists of $50M for the infrastructure plus an early budget of $5M. The majority of the initial infrastructure cost of $50M will be for an SCRF beam facility with low emittance injector, and the yearly R&D will be divided into x-ray optics and SCRF R&D, together with collaboration with other institutions.

5.2.6 **Participants in the XFELO Workshop**

XFELO2013 Participants List

Written on 2013-02-19

No	Name	Position / Affiliation	E-mail
1	Bernhard Adams	Physicist at Argonne National Laboratory *Hobbies: Photography (insects in flight, laser, high voltage), languages*	adams@aps.anl.gov
2	Changwook Lee	Assistant Professor, School of Nano-Bioscience and Chemical Engineering, Ulsan National Institute of Science and Technology (UNIST)	changwook@unist.ac.kr
3	Charles Fadley	Distinguished Professor of Physics, Dept. of Physics, University of California Davis, Advanced Light Source Professor, Materials Sciences Division, Lawrence Berkeley National Laboratory, *Aspiring Gangnam Style Dancer*	chuckfadley@gmail.com
4	Chung-Jong Yu	Leader of X-ray Beamline Operation Group 1, PAL	cjyu@postech.ac.kr
5	Deming Shu	Senior Engineer for Precision Instrumentation, Advanced Photon Source, Argonne National Laboratory	shu@aps.anl.gov
6	Do Young Noh	Professor of Physics and Photon Science, Gwangju Institute of Science and Technology (GIST), Director of the Center for Extreme Light Applications	dynoh@gist.ac.kr
7	Eun-San Kim	Professor, Dept. of Physics, Kyungpook National University (KNU), Korea	eskim1@knu.ac.kr
8	George Neil	Associate Director, Thomas Jefferson National Accelerator Facility, Chair of Future Light Source Subgroup of ICFA Beam Dynamics Group, *An Avid Marathoner*	neil@jlab.org
9	Giulio Monaco	Scientist, European Synchrotron Radiation Facility	gmonaco@esrf.fr
10	Hiroshi Kawata	Head of ERL Project Office, Dept. of Future Accelerator and Detector Technologies, KEK and also Professor, Photon Factory, Institute of Materials Structure Science, KEK	hiroshi.kawata@kek.jp
11	Hyotcherl Ihee	Professor, Dept. of Chemistry, KAIST (Korea Advanced Institute of Science and Technology), Group Leader, Chemical Reaction Study, Center for Nanomaterials and Chemical Reactions, Institute for Basic Sciences (IBS)	hyotcherl.ihee@kaist.ac.kr
12	Hyunjung Kim	Professor, Dept. of Physics, Sogang University, Seoul	hkim@sogang.ac.kr
13	In Soo Ko	XFEL Project Director, PAL; Professor, Dept. of Physics, POSTECH	isko@postech.ac.kr
14	Joerg Evers	Head of a research group working on X-ray quantum optics, MPI, Heidelberg, *likes hiking and is an aspiring windsurfing amateur*	joerg.evers@mpi-hd.mpg.de
15	Jung Ho Je	Professor, Dept. of Materials Science and Engineering, Pohang University of Science and Technology (POSTECH)	jhje@postech.ac.kr
16	Koji Arai	Senior Research Fellow, LIGO Project, California Institute of Technology, *Hill-climbing Cyclist*	karai@caltech.edu
17	Kwang-Je Kim	Argonne Distinguished Fellow, Argonne National Lab.; Professor, Univ. of Chicago; Distinguished Guest Professor, POSTECH	kwangje@aps.anl.gov
18	Nikolay Vinokurov	Head of laboratory at Budker Institute of Nuclear Physics (BINP, Russia) Director of Center for Quantum-Beam based Radiation Research at Korea Atomic Energy Research Institute (Daejeon, Korea)	nikolay.vinokurov@gmail.com
19	Vladimir Blank	Director, Technological Institute for Superhard and Novel Carbon Material (TISNCM), Troitsk (New Moscow), Russia	vblank@ntcstm.troitsk.ru
20	Young Il Joe	Graduate Student, Abbamonte Research Group, University of Illinois at Urbana-Champaign	jojo978@gmail.com
21	Yu Gan	Graduate Student, Abbamonte Research Group, University of Illinois at Urbana-Champaign	ygan1129@gmail.com
22	Yuri Shvydko	Senior Physicist, Advanced Photon Source, *Kimchi Lover*	shvydko@aps.anl.gov

5.3 Workshop on Accelerator R&D for Ultimate Storage Rings

Yi Jiao
Institute of High Energy Physics, CAS, Beijing, China
Mail to: jiaoyi@ihep.ac.cn

5.3.1 Introduction

The Workshop on Accelerator R&D for Ultimate Storage Rings was held on October 30 to November 1, 2012, at the Hongluoyuan Hotel in Huairou District, north of Beijing, near the site of a new campus for the Chinese Academy of Sciences and potentially a future state-of-the-art storage ring. The Institute of High Energy Physics (IHEP) in Beijing hosted this international workshop because it is seeking special support from the national funding agency to conduct R&D related to the new 5-GeV, 1.2 to 1.5-km circumference storage ring-based light source. About 60 accelerator physicists and engineers from several international light sources attended. The workshop website is found at http://usr2012.ihep.ac.cn/.

The co-chairs of the workshop were R. Hettel (SLAC) and Q. Qin (IHEP). The International Advisory Committee (IAC) members included K. Balewski (DESY), A.W. Chao (SLAC), H. Ding (IOP), M. Eriksson (MAX-Lab), R. Gerig (ANL), X.M. Jiang (IHEP), H. Ohkuma (Spring-8), P. Raimondi (ESRF), and Z. Zhao (SINAP). IAC members contributed to working with the Science Program Committee (SPC) members to select and finalize the topics and speakers and to preparing the close-out presentations of the workshop.

It is well known that the interest in realizing the next generation of diffraction-limited, so-called “ultimate” storage ring (USR) light sources is growing and several laboratories, including SLAC, SPring-8, ESRF, IHEP/Beijing and possibly other laboratories are considering implementing them in their strategic plans for the next decade. The design of these machines, which have electron emittances of < ~100 pm in both transverse planes, have been discussed in the last two ICFA Future Light Source Workshops and have been the topic of study by individual groups. It is acknowledged that R&D is required in various accelerator physics and engineering areas before such machines can actually be implemented, especially as the emittance is reduced towards 10 pm. These rings will most likely use compact magnet and vacuum chamber technology similar to that being developed for the MAX-IV storage ring, now under construction.

The purpose of this workshop was to bring together accelerator experts from diverse light source facilities having common interest in developing these new sources to focus on accelerator physics and engineering challenges for USRs and to identify areas requiring R&D. The charge for the workshop is listed below.

5.3.2 Charge to the Workshop

- Survey conceptual designs and compare the performance goals for USRs worldwide;
- Identify technical challenges and R&D requirements associated with:
    - Ring dimensions and lattice design,
    - Collective effects, impedances and lifetime,

  - Injection methods,
  - Accelerator component and system design (magnets, vacuum chambers, instrumentation, feedback systems, etc.),
  - Beam stability,
  - Insertion devices and damping wigglers;
- Prioritize R&D topics and define critical studies that should begin imminently.

5.3.3 Scientific Program

The workshop was organized with an opening introductory session that included presentations on the science case and performance goals for diffraction-limited storage ring light sources. Q. Qin (IHEP) introduced the workshop charge, H. Ding (IOP) presented the scientific cases for USR, Y. Dong (IHEP) presented the highlights of the science of USR, and R. Hettel (SLAC) overviewed the USR design and performance requirements.

This was followed by several topical sessions, interspersed with discussion sessions, organized to identify issues in lattice design, accelerator physics, injection, accelerator engineering, instrumentation and feedback systems, and insertion devices relative to the present state-of-the-art. While possible avenues of solution were discussed in some cases, the identification of these issues was the primary purpose of the workshop. The presentations can be found at the Workshop website:

http://indico.ihep.ac.cn/conferenceOtherViews.py?view=standard&confId=2825.

In the session of lattice design, talks were presented for the low-emittance designs in the laboratories worldwide, including Max-Lab, ESRF, SPring-8, LBNL, SOLEIL, IHEP, LNLS, SLAC, ANL, DLS and BINP. In the session of accelerator physics, talks were spread over beam collective effects, propagation of ultra-short bunch in USRs and potential lasing, RF optimization, coupling correction, dynamic aperture optimization, bunch length manipulation, “round” beam production. In the session of injection, the talks covered topics such as single-shot top-up injection, pulsed multipole injection, swap-out injection and longitudinal injection. In the session of accelerator engineering, the talks were presented about magnets, vacuum system, alignment, RF system, kicker magnets, field mapping and power consumption. In the session of instrumentation and feedback system, talks were given about orbit feedback, beam size stabilization and high-resolution orbit and photon BPM development. In the session of insertion devices, the talks covered topics such as insertion devices (IDs) for USRs, ID commissioning, X-ray optics, ID dynamic effects and simulation codes.

5.3.4 Conclusion

The Workshop on Accelerator R&D for Ultimate Storage Rings has helped to more clearly define USR accelerator design issues and the areas where R&D are needed. In this workshop several important R&D topics were addressed or advised:

- USR storage ring configuration optimization, based on targeted spectral brightness, coherence, special operating modes (e.g. short bunches, lasing), and almost certainly the most significant factor: available funding;
- Methods to create “round” beams, such as operating with equal horizontal and vertical tunes, using skew quadrupoles, solenoids and other methods;

- Further improvement of the performance capabilities to make USRs more “FEL-like”, such as lasing at soft X-ray energies using single-pass FEL undulators located in switched bypasses, potentially lasing at hard X-ray energies in X-ray FEL oscillators;
- Flexible beam manipulation in USR, including emittance exchange and partitioning, bunch length manipulation with more than one frequency RF cavities;
- Reliable and efficient injection into USRs;
- Strong interconnection and system integration of the accelerator technologies for magnets, vacuum, RF and stability;
- R&D on new IDs those benefit USRs, including damping wigglers, cryogenic permanent magnet undulators, superconducting undulators and variable

6 Recent Doctorial Theses Abstracts

6.1 Optics Design of Intrabeam Scattering Dominated Damping Rings

Fanouria Antoniou
Mail to: Fanouria.Antoniou@cern.ch

Graduation date: January 8th, 2013
University: NTUA (National Technical University of Athens), Greece
Supervisors: Prof. E. Gazis and Dr. I. Papaphilippou

Abstract:
A e^+/e^- linear collider, the Compact Linear Collider (CLIC) is under design at CERN, aiming to explore the terascale particle physics regime. The collider has been optimized at 3 TeV center of mass energy and targets a luminosity of 10^{34} cm^{-2} s^{-1}. In order to achieve this high luminosity, high intensity bunches with ultra low emittances, in all three planes, are required. The generation of ultra low emittance is achieved in the Damping Rings (DR) complex of the collider. The large input beam emittances, especially the ones coming from the positron source, and the requirement of ultra low emittance production in a fast repetition time of 20 ms, imply that the beam damping is done in two stages. Thus, a main-damping ring (DR) and a pre-damping ring (PDR) are needed, for each particle species. The high bunch brightness gives rise to several collective effects, with Intra-beam scattering (IBS) being the main limitation to the ultra-low emittance. This thesis elaborates the lattice design and non-linear optimization of a positron pre-damping ring and the lattice optimization of a damping ring, under the influence of IBS. Several theoretical models, describing this effect, are discussed and compared for different lattices, while two multi-particle tracking algorithms are bench-marked with the theoretical models. Finally, IBS measurement results, at the Swiss Light Source (SLS) and the Cornell electron storage ring Test Accelerator (Cesr-TA), are presented and compared with theoretical predictions.

7 Forthcoming Beam Dynamics Events

7.1 SLAC Summer School on Electron and Photon Beams

SLAC National Accelerator Laboratory is offering for the first time a Summer School on Electron and Photon Beams for senior undergraduate students, graduate students and post-docs. The school will be held at SLAC from July 22nd to July 26th, 2013. The goal of the school is to introduce students and post docs to the physics and technology of high brightness electron and coherent X-ray beams, a growing field of research with applications in areas like synchrotron radiation, X-ray free-electron lasers, atomic and molecular science at the femtosecond-Ångstroms scale.

Scholarships to cover the cost of travel and/or lodging are available for some of the participants. You will find a more detailed description of the school on the school web site: http://slac.stanford.edu/sssepb/ .

The school organizing committee would be grateful if you could bring this information to the attention of students and post-docs in your institution and encourage them to attend the school.

Organizing Committee Chair: Claudio Pellegrini
Contact: sssepb@slac.stanford.edu

7.2 53rd ICFA Advanced Beam Dynamics Workshop (ABDW) Energy Recovery Linacs (ERL) 2013

Tentative dates: September 9-13, 2013.
Venue: Budker Institute of Nuclear Physics, Novosibirsk, Russia.
Web-site: http://ssrc.inp.nsk.su/Conf/ERL2013/

The workshop continues the chain of the ERL workshops (the latest was the 50th ABDW ERL 2011, KEK, Japan). The aim of the workshop is further development of ERL physics, technology and applications. In particular, the issues of beam stability, halo, emittance requirements and limitations, subsystems (RF, injectors, lattices) have to be considered. Also, the ERL applications, operation experience and project statuses have to be discussed.

The oral (invited and distributed) and poster session will be organized for the workshop. About 100-120 participants are expected.

Proceedings will be published electronically at the JACoW site.

International Organizing Committee

G. N. Kulipanov, BINP (Chair)
S. Benson, TJNAF
I. Ben-Zvi, BNL
R. Hajima JAEA
G. Hoffstaetter, Cornell
H. Kawata KEK
K-J. Kim, ANL and the U. of Chicago
J. Knobloch, HZB

S. Smith , STFC/DL/ASTeC
Yu. Shatunov, BINP

International Program Committee

R. Hajima, JAEA (Chair)
W. Anders, HZB
D. Angal-Kalinin, STFC/DL/ASTeC
I. Bazarov, Cornell U.
S. Belomestnykh, BNL
J. Bisognano, SRC-U. Wisconsin-Madison
M. Borland, ANL
D. Douglas, JLAB
B. Dunham, Cornell U.
P. Evtushenko, JLAB
T. Furuya, KEK
C. Hernandez-Garcia, JLAB
G. Hoffstaetter, Cornell U.
A. Jankowiak, HZB
T. Kamps, HZB
D. Kayran, BNL
K-J. Kim, ANL and the Univ. of Chicago
E-S. Kim, Kyungpook Natl. U.
J. Knobloch, HZB
Y. Kobayashi, KEK
M. Liepe, Cornell U
V.N. Litvinenko, BNL
K. Liu, Peking U.
P. McIntosh, STFC/DL/ASTeC
A.Matveenko, BESSY II
L. Merminga, TRIUMF
J. Michael Klopf, Jefferson Lab
L. Militsyn, STFC Daresbury Lab
N.Nakamura, KEK
S. Sakanaka, KEK
O. A. Shevchenko, BINP
T. Smith, Stanford U.
J. Teichert, HZDR
A. Tribendis, BINP
N. Vinokurov BINP
J. Wang, IHEP

Local Organizing Committee Chair and JACoW representative

M. Kuzin, BINP

Workshop Scientific Secretary

Ya. Getmanov, BINP

7.3 The 14th International Conference on Accelerator and Large Experimental Physics Control Systems (ICALEPCS 2013)

The 14th International Conference on Accelerator and Large Experimental Physics Control Systems (ICALEPCS 2013) is scheduled for October 6-11, 2013 in San Francisco, California (USA) and is hosted by the National Ignition Facility at the Lawrence Livermore National Laboratory (https://www.llnl.gov/). Managers, scientists, engineers and decision makers of preeminent world-class science laboratories and facilities will discuss big-science control and information systems.

Abstract submission is now open for ICALEPCS2013. Instructions on how to submit your abstract can be found on the conference website via

http://icalepcs2013.org/abstracts/index.php

You are kindly invited to submit your abstract before 1st April 2013.

ICALEPCS (http://www.icalepcs.org) is a series of biennial conferences that rotates between three major areas of the world: America (including North, Central and South America), Asia (including Oceania) and Europe (including Russia, the Near East and Africa) and is well established as the largest conference dedicated to control systems for accelerators and large experiments in physics.

The high standard that has been reached by the conference is widely recognized. The conference series is endorsed by the European Physics Society/Experimental Physics Control Systems (EPS/EPCS); the Physical Society of Japan (JPS); and the Association of Asia Pacific Physical Societies (AAPPS).

We are pleased to invite all those involved worldwide in the field of controls and those interested in following the latest trends in control systems for accelerators and experimental physics systems, large and small (particle accelerators, particle detectors, telescopes and nuclear fusion facilities, etc.). Please visit our home page (http://www.icalepcs2013.org/) for more details.

Scientific Program Chair: Peg Folta
Conference Chair: Chris Marshall
Local Organizing Committee: http://icalepcs2013.org/committees/organizing.php.

7.4 COOL'13

We are pleased to announce that the next International Workshop on Beam Cooling and Related Topics, COOL'13, will take place at the Alpin Palace Hotel in Murren, Switzerland from 10th to 14th June 2013.

This is the 9th workshop in the series which was first held in Montreux, Switzerland in 1993 and has been a bi-annual event since 2001. The workshop will highlight the latest developments in the field of particle beam cooling and will provide a perfect opportunity for accelerator physicists, engineers and students to meet and interact in a quiet and relaxed environment.

At an elevation of 1650 m, perched on a high, sunny terrace facing the famous Eiger, Monch and Jungfrau, Murren is located amidst some of the world's most spectacular scenery. Coming by train from one of the airports (Bern, Zurich, Basel, Geneva) Murren is reached by a mountain railway or by aerial cableways running from the Lauterbrunnen valley into the centre of the car-free village. Murren has remained a charming little village rich of traditions and has managed to escape over-development despite being famous in the history of winter sports.

A program of invited oral presentations is being developed by the International Program Committee and will be published in due course at the workshop website

https://cool-13.web.cern.ch/COOL-13

Please bookmark the site and visit it regularly for updates on the program and for useful information concerning the workshop.

Prospective participants should take note of the deadlines for abstract submission (15th February 2013), early registration (3rd May 2013) and hotel reservation (10th May 2013). Delegate registration will open in January and proposals for hotel accommodation will be published on our website.

Abstract and paper submission as well as delegate registration will be handled via the JACoW Scientific Programme Management System (SPMS) at

https://oraweb.cern.ch/pls/cool2013/profile.html

The proceedings will be published at the JACoW site

http://www.jacow.org

shortly after the workshop. We would like to take the opportunity to invite you to update your JACoW profile if you no longer wish to receive communications on this and future COOL workshops.

We are excited to welcome you to this unique location for COOL'13 and are looking forward to meeting you at the workshop.

The Local Organising Committee:

Pavel Belochitskii	Alexandre Frassier
Flora Berrenger	Lars Varming Joergensen (Editor)
Madeleine Catin (Secretary)	Bertrand Lefort
Tommy Eriksson	Gerard Tranquille (Chair)

7.5 SRF 2013

We are pleased to invite you to attend the 16th International Conference on RF Superconductivity, SRF 2013, to take place on September 23-27, 2013 in Cite Universitaire, downtown Paris, France. Please note this important conference in your calendar and bookmark the conference website.

http://www.srf2013.fr/

RF superconductivity is now the key technology of many accelerators for particle physics, nuclear physics and, increasingly, light sources. SRF 2013 will cover the latest advances in the science, technology, and applications of superconducting RF. The program will consist of invited review talks, poster sessions and 'hot-topic' discussion sessions (and also our traditional boat tour, trademark of this conference). An industrial exhibition will also take place during the conference.

We will continue the tradition of providing a vivid forum for SRF scientists, engineers, students and industrial partners to present and discuss the latest developments in the science and technology of superconducting RF for particle accelerators.

Special tutorials will be held from Sept. 19-21 in GANIL, Caen. These are designed to provide an in-depth overview of SRF related subjects for scientists and engineers new to the field. It will also give the attendees a unique opportunity of visiting the GANIL accelerator facilities, especially the Spiral2 linac which will be under assembly at this time.

The proceedings will be published through JACoW. Only contributions presented as a talk or in the poster sessions will be included in the proceedings.

We invite you to log on to your JACOW account and activate the SRF mailing-list checkbox in your personal profile to ensure that you will receive updates on the SRF Conference in the future.

https://oraweb.cern.ch/pls/jacow/profile.new_account

Registration and call for contribution will open 1st February 2013. We invite you to visit regularly www.srf2013.fr website to find latest information.

Conference Chairwoman: Claire Antoine
Conference Chairman: Sebastien Bousson
Conference contact: contact@srf2013.fr

7.6 ICFA Mini-Workshop on Space Charge (SPACE CHARGE 2013)

This workshop will be held at CERN in Geneva, Switzerland from 15-19 April, 2013. High intensity beams have always caught the attention of the accelerator community. The present development of the field is being pushed by projects and major upgrade programs to existing facilities. We refer for example to the FAIR project at GSI, and the LIU upgrade at CERN. The need for advanced understanding of space charge dominated machines and the unavailability of both CERN and GSI accelerators as of early 2013, sets a convenient time window (April 2013) to organize a meeting of reviewing the state of the art in our field. This workshop would serve as a forum for the urgent issues of the upcoming year.

Workshop co-chair: G. Franchetti (GSI) g.franchetti@gsi.de,
F. Schmidt (CERN) frank.schmidt@cern.ch
Workshop website: https://indico.cern.ch/conferenceDisplay.py?confId=221441

7.7 35th International Free-Electron Laser Conference (FEL'13)

The 35th International Free-Electron Laser Conference (FEL'13) is scheduled for August 26-30, 2013 in New York, New York (USA) and is hosted by the Collider-Accelerator Department at the Brookhaven National Laboratory (http://www.bnl.gov/). Managers, scientists, engineers and decision makers from world-class science laboratories and facilities will discuss scientific, technological, and user aspects of free-electron lasers.

Abstract submission is now open for FEL'13. Instructions on how to submit your abstract can be found on the conference website via (http://www.c-ad.bnl.gov/fel2013/AbstractSubmission.htm). You are kindly invited to submit your abstract before 15th April 2013.

FEL'13 (http://www.c-ad.bnl.gov/fel2013/) is the annual event for the FEL community to present and discuss progress and new ideas on the physics and technology of free electron lasers. The conference will take place at the Marriott Marquis Hotel in Manhattan, New York. The conference sessions will be held from Monday to Thursday, with the last day of the conference dedicated for a day-long tour to Brookhaven National Laboratory and Long Island.

All scientists and project managers involved in various FEL projects and leading technology are invited to present their research to the community. The Scientific Program of the conference will consist of invited talks and contributed presentations, either in the form of oral presentations or posters.

Scientific Program Chair: Vitaly Yakimenko
Conference Chair: Vladimir Litvinenko
Local Organizing Committee: http://www.c-ad.bnl.gov/fel2013/localOrganization.htm

7.8 The 17TH Pan-American Synchrotron Radiation Instrumentation Conference

Dates: June 19-21, 2013
Venue: National Institute of Standards and Technology (NIST) in Gaithersburg, Maryland, USA
Conference web-site: http://pml.nist.gov/sri2013

Conference co-chairs: Peter Revesz, CHESS
Gwyn Williams, JLAB
Uwe Arp, SURF/NIST

Participating Organizations

- Advanced Light Source
- Advanced Photon Source
- Center for Advanced Microstructures & Devices
- Cornell High Energy Synchrotron Source
- Canadian Light Source
- Jefferson Lab
- Linac Coherent Light Source
- Laboratório Nacional de Luz Síncrotron
- National Synchrotron Light Source
- Synchrotron Radiation Center
- Synchrotron Ultraviolet Radiation Facility
- Stanford Synchrotron Radiation Lightsource

Plenary Session Topics

- IR and Vacuum-Ultraviolet
- Detectors
- Future Optics

Session Topics

- Sources & Insertion Devices
- Beamline Components
- Coherence
- Spectroscopy
- Microscopy, Imaging
- Applications

Sample Environment
Timing

Related Events

Monday, June 16, 2013

Metrology
High Pressure
Facility Upgrades & High Brightness Sources
Talbot Interferometry for imaging and wavefront characterization.

Tuesday, June 17, 2013

50 Years of Atomic Physics with Synchrotron Radiation
Detectors
Photoemission Spectroscopy – the upcoming decades

Background

Synchrotron Radiation Instrumentation meeting offers an opportunity for networking and interactions for the community working between the accelerator and the scientific users at the major facilities. It is a critically important meeting, and is usually peppered with facility updates, accelerator news and examples of the science motivating the field. The Pan-American SRI-2013 meeting is the 17th in a series that started at SURF/NIST in 1979, and has run every 2 years since then. The 2005 USA National Meeting scheduled at CAMD in Baton Rouge, Louisiana, had to be cancelled due to Hurricane Katrina. It was ultimately held in 2007, with the Canadian Light Source hosting the meeting the following year. The last Pan-American meeting was held in 2010 and was hosted by Argonne. An International SRI meeting series has run every 3 years since 1982, the most recent being hosted by Soleil and ESRF in Lyon, France, in 2012.

Sponsors

Cornell University
Cornell High Energy

Jefferson Lab
Thomas Jefferson

NIST SURF III
National Institute of Standards and Technology

7.9 The Third Low Emittance Ring Workshop

Under the auspices of the EuCARD2 project, we are happy to announce the third Low emittance ring workshop to be held in Oxford in July 8th-10th 2013, hosted by the John Adams Institute for Accelerator Science.

The workshop brings together different accelerator communities working on the design of ultra low emittance lattices such as synchrotron light sources, damping rings and test facilities for linear colliders and HEP circular colliders. The aim of the workshop is to review the present development s in design of ultra low emittance lattices, the experience and the challenges with the operation of low emittance synchrotrons and the main technological problems. The merging of different accelerator communities is expected to foster ideas exchange and the collaboration both on theoretical, experimental and design issues. Areas for common R&D programmes will be explored. The workshop will profit from the experience of colleagues who have designed, commissioned and operated lepton ring colliders and synchrotron light sources as well as from the ones involved in future low emittance upgrade programmes of existing rings.

Workshop sessions will include:
- Low emittance lattice design and tuning
    - algorithms and optimisation tools
    - nonlinear beam dynamics
    - novel injection schemes
    - beam based tuning techniques and model calibration
    - beam loss management and Top-Up operation
- Collective effects
    - Intrabeam scattering
    - Electron cloud
    - Machine impedance effects and minimisation
    - Coherent synchrotron radiation
- Low emittance ring technology
    - IDs and magnets
    - Kickers
    - Diagnostics and instrumentation
    - Vacuum
    - Engineering integration

Suggestions for presentations should be sent to one of the organisers:

Riccardo Bartolini, JAI / Diamond Light Source (r.bartolini1@physics.ox.ac.uk)
Susanna Guiducci, INFN (susanna.guiducci@lnf.infn.it)
Yannis Papaphilippou, CERN (ioannis.papaphilippou@cern.ch)

7.10 First Circular for PSTP2013

7.10.1 Workshop Introduction

This is the first announcement for the XVth International Workshop on Polarized Sources, Targets, and Polarimetry (PSTP2013) which will be held at the University of Virginia, Charlottesville, Virginia, USA on September 9th to September 13th, 2013, organized jointly by the University of Virginia and Jefferson Laboratory. This workshop continues a series whose last few meetings were at St. Petersburg, Russia (2011), Ferrara, Italy (2009), Brookhaven, USA (2007) and Tokyo, Japan (2005). PSTP2013 is sponsored by Jefferson Laboratory, the University of Virginia and the International Spin Physics Committee.

7.10.2 Program

The topics to be discussed are:

Polarized Ion Sources
Polarized Electron Sources
Polarized Positron Sources
Polarized Gas Targets
Polarized Solid Targets
Proton, Electron, and Ion Beam Polarimetry
New Initiative
Applications of Spin

It is expected that all submitted papers will be presented in plenary sessions, with parallel sessions used only if the submissions exceeds the available schedule. The program will also include a poster session. The Proceedings will be electronically published by Proceedings of Science (http://pos.sissa.it/), with a limited number of soft-cover paper copies to be made available to the registrants.

7.10.3 **Registration**

The website for PSTP2013 is at http://faculty.virginia.edu/PSTP2013/. The poster for the Workshop is available for download at the above Website. Registration for the Workshop will be available soon and the fee will be $400 and $200 for students and retired persons. After July 15, 2013, the Registration Fee will be $450 and $225 respectively. The Registration Fee will be payable on-line, by credit card; at the Workshop site it can be paid for in cash or by credit card. Details will be available soon on the Workshop Web site. The e-mail address for the Workshop organizers is pstp2013@virginia.edu.

7.10.4 **Travel and Accommodation**

Charlottesville is served by a small airport with links to major International airports such as Washington Dulles, Charlotte, NC, Atlanta, GA and others. The Richmond airport is also an option, about 70 miles from Charlottesville and convenient by rental car. Accommodation will be in local hotels with a University of Virginia negotiated rate. Attendees will make their own reservations. Further information about travel to Charlottesville can be found at the PSTP website.

7.10.5 **Visas**

The recommendation of our International Departments for those having to apply for visas is to apply as early as you can. The Local Organizing Committee will supply Invitation Letters to those who request them.

7.10.6 **Local Organizing Committee Members**

Don Crabb – UVA (Co-Chair)
Matt Poelke – Jlab (Co-Chair)
Gordon Cates – UVA
Donal Day – UVA
Slava Derbenev – Jlab
Dave Gaskell – Jlab
Chris Keith – Jlab
Yousef Makdisi – BNL
Kent Paschke – UVA
Vadim Ptitsyn – BNL
Anatoli Zelenski – BNL

7.10.7 International Spin Physics Committee (ISPC)

R. Milner – MIT (Chair)
E. Steffens - Erlangen (Past-Chair)
M. Anselmino – Torino
E. Aschenauer – BNL
A. Belov – INR Moscow
F. Bradamante* – Trieste
E.D. Courant* – BNL
D.G. Crabb* – Virginia
A.V. Efremov* – JINR
G. Fidecaro* – CERN
H. Gao – Duke
W. Haeberli* – Wisconsin
A.D. Krisch* – Michigan
P. Lenisa – Ferrara
B.-Q. Ma – Peking
A. Martin – Trieste
N. Makins – Illinois
A. Masaike* – Kyoto
A. Milstein – Novosibirsk
M. Poelker – Jlab
R. Prepost – Wisconsin
C.Y. Prescott* – SLAC
T. Roser – BNL
N. Saito – KEK
H. Sakai – Tokyo
V. Soergel* – Heidelberg
H. Stroeher – Juelich
O. Teryaev - Dubna
W.T.H. van Oers* – Manitoba

* Honorary Member

8 Announcements of the Beam Dynamics Panel

8.1 ICFA Beam Dynamics Newsletter

8.1.1 Aim of the Newsletter

The ICFA Beam Dynamics Newsletter is intended as a channel for describing unsolved problems and highlighting important ongoing works, and not as a substitute for journal articles and conference proceedings that usually describe completed work. It is published by the ICFA Beam Dynamics Panel, one of whose missions is to encourage international collaboration in beam dynamics.

Normally it is published every April, August and December. The deadlines are 15 March, 15 July and 15 November, respectively.

8.1.2 Categories of Articles

The categories of articles in the newsletter are the following:

1. Announcements from the panel.
2. Reports of beam dynamics activity of a group.
3. Reports on workshops, meetings and other events related to beam dynamics.
4. Announcements of future beam dynamics-related international workshops and meetings.
5. Those who want to use newsletter to announce their workshops are welcome to do so. Articles should typically fit within half a page and include descriptions of

the subject, date, place, Web site and other contact information.

6. Review of beam dynamics problems: This is a place to bring attention to unsolved problems and should not be used to report completed work. Clear and short highlights on the problem are encouraged.
7. Letters to the editor: a forum open to everyone. Anybody can express his/her opinion on the beam dynamics and related activities, by sending it to one of the editors. The editors reserve the right to reject contributions they judge to be inappropriate, although they have rarely had cause to do so.

The editors may request an article following a recommendation by panel members. However anyone who wishes to submit an article is strongly encouraged to contact any Beam Dynamics Panel member before starting to write.

8.1.3 How to Prepare a Manuscript

Before starting to write, authors should download the template in Microsoft Word format from the Beam Dynamics Panel web site:

http://www-bd.fnal.gov/icfabd/news.html

It will be much easier to guarantee acceptance of the article if the template is used and the instructions included in it are respected. The template and instructions are expected to evolve with time so please make sure always to use the latest versions.

The final Microsoft Word file should be sent to one of the editors, preferably the issue editor, by email.

The editors regret that LaTeX files can no longer be accepted: a majority of contributors now prefer Word and we simply do not have the resources to make the conversions that would be needed. Contributions received in LaTeX will now be returned to the authors for re-formatting.

In cases where an article is composed entirely of straightforward prose (no equations, figures, tables, special symbols, etc.) contributions received in the form of plain text files may be accepted at the discretion of the issue editor.

Each article should include the title, authors' names, affiliations and e-mail addresses.

8.1.4 Distribution

A complete archive of issues of this newsletter from 1995 to the latest issue is available at

http://icfa-usa.jlab.org/archive/newsletter.shtml.

This is now intended as the primary method of distribution of the newsletter.

Readers are encouraged to sign-up for electronic mailing list to ensure that they will hear immediately when a new issue is published.

The Panel's Web site provides access to the Newsletters, information about future and past workshops, and other information useful to accelerator physicists. There are links to pages of information of local interest for each of the three ICFA areas.

Printed copies of the ICFA Beam Dynamics Newsletters are also distributed (generally some time after the Web edition appears) through the following distributors:

Weiren Chou	chou@fnal.gov	North and South Americas
Rainer Wanzenberg	rainer.wanzenberg@desy.de	Europe++ and Africa
Toshiyuki Okugi	toshiyuki.okugi@kek.jp	Asia**and Pacific

++ Including former Soviet Union.

** For Mainland China, Jiu-Qing Wang (wangjq@mail.ihep.ac.cn) takes care of the distribution with Ms. Su Ping, Secretariat of PASC, P.O. Box 918, Beijing 100039, China.

To keep costs down (remember that the Panel has no budget of its own) readers are encouraged to use the Web as much as possible. In particular, if you receive a paper copy that you no longer require, please inform the appropriate distributor.

8.1.5 **Regular Correspondents**

The Beam Dynamics Newsletter particularly encourages contributions from smaller institutions and countries where the accelerator physics community is small. Since it is impossible for the editors and panel members to survey all beam dynamics activity worldwide, we have some Regular Correspondents. They are expected to find interesting activities and appropriate persons to report them and/or report them by themselves. We hope that we will have a “compact and complete” list covering all over the world eventually. The present Regular Correspondents are as follows:

Liu Lin	Liu@ns.lnls.br	LNLS Brazil
Sameen Ahmed Khan	Rohelakan@yahoo.com	SCOT, Oman
Jacob Rodnizki	Jacob.Rodnizki@gmail.com	Soreq NRC, Israel
Rohan Dowd	Rohan.Dowd@synchrotron.org.au	Australian Synchrotron

We are calling for more volunteers as Regular Correspondents.

8.2 ICFA Beam Dynamics Panel Members

Name	**eMail**	**Institution**
Rick Baartman	baartman@lin12.triumf.ca	TRIUMF, 4004 Wesbrook Mall, Vancouver, BC, V6T 2A3, Canada
Marica Biagini	marica.biagini@lnf.infn.it	LNF-INFN, Via E. Fermi 40, C.P. 13, Frascati, Italy
John Byrd	jmbyrd@lbl.gov	Center for Beam Physics, LBL, 1 Cyclotron Road, Berkeley, CA 94720-8211, U.S.A.
Yunhai Cai	yunhai@slac.stanford.edu	SLAC, 2575 Sand Hill Road, MS 26 Menlo Park, CA 94025, U.S.A.
Swapan Chattopadhyay	swapan@cockroft.ac.uk	The Cockcroft Institute, Daresbury, Warrington WA4 4AD, U.K.
Weiren Chou (Chair)	chou@fnal.gov	Fermilab, MS 220, P.O. Box 500, Batavia, IL 60510, U.S.A.
Wolfram Fischer	wfischer@bnl.gov	Brookhaven National Laboratory, Bldg. 911B, Upton, NY 11973, U.S.A.
Yoshihiro Funakoshi	yoshihiro.funakoshi@kek.jp	KEK, 1-1 Oho, Tsukuba-shi, Ibaraki-ken, 305-0801, Japan
Jie Gao	gaoj@ihep.ac.cn	Institute for High Energy Physics, P.O. Box 918, Beijing 100039, China
Ajay Ghodke	ghodke@cat.ernet.in	RRCAT, ADL Bldg. Indore, Madhya Pradesh, 452 013, India
Ingo Hofmann	i.hofmann@gsi.de	High Current Beam Physics, GSI Darmstadt, Planckstr. 1, 64291 Darmstadt, Germany
Sergei Ivanov	sergey.ivanov@ihep.ru	Institute for High Energy Physics, Protvino, Moscow Region, 142281 Russia
In Soo Ko	isko@postech.ac.kr	Pohang Accelerator Lab, San 31, Hyoja-Dong, Pohang 790-784, South Korea
Elias Metral	elias.metral@cern.ch	CERN, CH-1211, Geneva 23, Switzerland
Yoshiharu Mori	mori@rri.kyoto-u.ac.jp	Research Reactor Inst., Kyoto Univ. Kumatori, Osaka, 590-0494, Japan
George Neil	neil@jlab.org	TJNAF, 12000 Jefferson Ave., Suite 21, Newport News, VA 23606, U.S.A.
Toshiyuki Okugi	toshiyuki.okugi@kek.jp	KEK, 1-1 Oho, Tsukuba-shi, Ibaraki-ken, 305-0801, Japan
Mark Palmer	mark.palmer@cornell.edu	Wilson Laboratory, Cornell University, Ithaca, NY 14853-8001, USA
Chris Prior	chris.prior@stfc.ac.uk	ASTeC Intense Beams Group, STFC RAL, Chilton, Didcot, Oxon OX11 0QX, U.K.
Yuri Shatunov	Yu.M.Shatunov@inp.nsk.su	Acad. Lavrentiev, Prospect 11, 630090 Novosibirsk, Russia
Jiu-Qing Wang	wangjq@ihep.ac.cn	Institute for High Energy Physics, P.O. Box 918, 9-1, Beijing 100039, China
Rainer Wanzenberg	rainer.wanzenberg@desy.de	DESY, Notkestrasse 85, 22603 Hamburg, Germany